

University of South Wales



2053171

FRACTURE CHARACTERISTICS OF  
CONCRETES AND CEMENT-STABILIZED SOIL

by

C.W.A. YIM B.Sc.

Thesis presented in fulfilment of the requirement  
for the Degree of Master of Philosophy  
Council for National Academic Awards, London, 1986.

Department of Civil Engineering and Building,  
The Polytechnic of Wales, July, 1986.

Collaborating Establishment, Transport and Road  
Research Laboratory, Berkshire, United Kingdom.

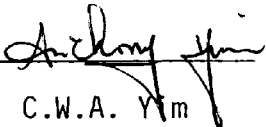
謹獻給親愛的家人

感謝你們一直以來

支持和勸勉鼓勵萬分多謝

CERTIFICATION OF RESEARCH

This is to certify that, except when specific reference to other investigations is made, the work described in this thesis is the result of the investigations of the candidate.




C.W.A. Yim

(Candidate)

17<sup>th</sup> September, 1986

(Date)

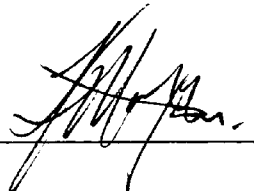


J. Davies

(Director of Studies)

17.9.1986

(Date)



T.G. Morgan

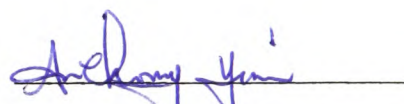
(Supervisor)

17/9/'86.

(Date)

DECLARATION

This is to certify that neither this thesis, nor any part of it, has been presented, or is being currently submitted, in candidature for any degree at any other Academic Institution.

  
C.W.A. YIM  
(Candidate)

LIST OF CONTENTS

	<u>PAGE NO.</u>
CERTIFICATION OF RESEARCH	i
DECLARATION	ii
ACKNOWLEDGEMENTS	viii
SUMMARY	1
LIST OF SYMBOLS	3
CHAPTER 1	
INTRODUCTION	5
CHAPTER 2	
REVIEW OF LITERATURE	10
2.1	10
Introduction	
2.2	10
Griffith Theory	
2.3	12
Irwin's modification to the	
Griffith theory	
2.4	14
Linear Elastic Fracture Mechanics (LEFM)	
2.4.1	14
The Stress Intensity Factor K Approach	
2.4.2	18
The Strain Energy Release Rate $\mathcal{G}$ Approach	
2.5	20
Application of the finite element method	
in LEFM	
2.6	24
Application of the LEFM to cementitious	
materials	
2.7	33
Review of the Mode II Compact Shear (CS)	
specimens	

		<u>PAGE NO.</u>
CHAPTER 3	APPLICATION OF THE FINITE ELEMENT METHOD IN LEFM	48
3.1	Introduction	48
3.2	The Finite Element Program	49
3.3	Determination of K from finite element solutions	50
3.3.1	Chan's Displacement Method	50
3.3.2	Woo's Displacement Method	52
CHAPTER 4	MATHEMATICAL MODELLING FOR 100mm CS SPECIMENS USING PAFEC FINITE ELEMENT PROGRAM	62
4.1	Introduction	62
4.2	Finite element modelling for 100mm double-notched cubes	63
4.2.1	A convergence study of element-mesh size	66
4.2.2	Stress analysis of the specimen	67
4.2.3	Comparison of the Mode I and Mode II stress intensity factors for $H/W = 0.5,$ $0.4$ and $0.3$	70
4.2.4	Determination of the calibration coefficients of the Mode II stress intensity factors for $H/W = 0.5, 0.4$ and $0.3$	72

	<u>PAGE NO.</u>
4.2.5 . Comparison of the boundary collocation method to the finite element methods	75
4.2.6 Conclusions	76
4.3 Finite element modelling for 100mm single-notched cubes	79
4.3.1 A convergence study of element-mesh size	79
4.3.2 Comparison of the Mode I and Mode II stress intensity factors	80
4.3.3 Determination of the calibration coefficients of the Mode II stress intensity factors	82
4.3.4 Conclusions	82
4.4 Finite element modelling for 150mm double-notched cubes	83
4.4.1 A convergence study of element-mesh size	84
4.4.2 Comparison of the Mode I and Mode II stress intensity factors for $H/W = 0.53, 0.4$ and $0.6$	85
4.4.3 Determination of the calibration coefficients of the Mode II stress intensity factors for $H/W = 0.53, 0.4$ and $0.26$	88



	<u>PAGE NO.</u>
4.4.4	Conclusions 88
CHAPTER 5	AN EXPERIMENTAL INVESTIGATION INTO THE MODE II FRACTURE TOUGHNESS OF MORTAR AND SOIL-CEMENT 132
5.1	Introduction 132
5.2	General properties of mortar and compact shear fracture test procedures 134
5.3	Trial tests on 100mm mortar cubes and prisms 137
5.4	Development of test equipment 139
5.4.1	Test series one - using Departmental made compressive platens 139
5.4.2	Test series two - using INSTRON compressive platens 142
5.5	Determination of fracture toughness for 100mm double-notched mortar cubes - Test series three 146
5.6	Determination of fracture toughness for 100mm single-notched mortar cubes - Test series four 153
5.7	General properties of soil-cement and compact shear fracture test procedures 156

	<u>PAGE NO.</u>	
5.8	Determination of fracture toughness for 100mm double-notched soil-cement cubes - Test series five	160
5.9	Determination of fracture toughness for 100mm single-notched soil-cement cubes - Test series six	163
CHAPTER 6	CONCLUSIONS AND FUTURE WORK	213
6.1	Conclusions	213
6.1.1	Finite element modelling for 100mm double-notched cubes	213
6.1.2	Experimental investigation (mortar)	215
6.1.3	Experimental investigation (soil-cement)	218
6.1.4	Finite element modelling for 100mm single-notched cubes	219
6.1.5	Experimental investigation (mortar)	220
6.1.6	Experimental investigation (soil-cement)	221
6.1.7	Finite element modelling for 150mm double-notched cubes	221
6.2	Future work	223
REFERENCES		226
APPENDIX	(Publications)	232

### ACKNOWLEDGEMENTS

The Candidate wishes to express his gratitude to Dr. J. Davies, his Director of Studies, and Mr. T.G. Morgan, his Supervisor, for their constant help and encouragement.

The Candidate is grateful to Mr. R.D. McMurray, his Head of Department, for allowing the use of departmental facilities. The financial assistance of The Polytechnic of Wales and the efforts of Mr. B.W. Preece, Deputy Head of Department in securing the research assistantship is gratefully acknowledged.

He is also grateful to the technical staff of the Department of Civil Engineering and Building for their valuable help in performing the experimental work. He is particularly pleased with the help given by the Staff of the Polytechnic Computer Centre.

Finally, he is appreciative of Mrs. M.W. Ellis for typing this illegible manuscript patiently.

## SUMMARY

Application of fracture mechanics to the cracking and failure of concrete under stress has been receiving considerable attention. Most of these investigations have been directed towards the determination of the critical stress intensity factor or fracture toughness of concrete, mortar, or cement paste, failing in tension. Studies on an experimental determination of fracture toughness for concrete subjected to a compressive stress field have limited report so far.

This project applies the concept of linear elastic fracture mechanics to investigate the Mode II shear type of failure of mortar and soil-cement. Fracture studies are particularly important in mortars and other cement composites as these materials are generally weak in shear. The fracture toughness is determined using both the stress intensity factor  $K$  approach and the strain energy release rate  $G$  approach. Both experimental and numerical methods are applied to determine the fracture toughness ( $K_{IIC}$ ) and results are compared on a range of specimen geometries.

The numerical work was carried out on 100mm double-notched, single-notched and 150mm double-notched cubes and their stress intensity factors were determined using the displacement approach of the finite element method. The results of the numerical analysis indicate that with decreasing notch spacing and increasing notch depth the shear failure mechanism assumes the greater significance.

The experimental work consisted of a series of fracture tests which were carried out on 100mm double-notched and single-notched cubes applied to both mortar and soil-cement. The standard 100mm concrete cube was modified and a testing arrangement developed which would appear to be suitable for the testing of cement composites for fracture mechanics purposes in the Mode II type of failure. All these tests were carried out on the INSTRON testing machine. The fracture toughness values were determined using the strain energy release rate utilizing the 'pop-in' load  $P_1$  corresponding to the appearance of the first crack introduced on the load-displacement curves. The experimental results confirmed that linear elastic fracture mechanics can be applied to mortar and soil-cement.

Good correlation between the stress intensity factor  $K$  approach and the strain energy release rate  $\mathcal{G}$  approach is obtained provided correction for the machine/specimen interaction or the machine stiffness characteristics is applied to experimental results.

LIST OF SYMBOLS

$\tau$	shear stress
$\sigma$	tensile stress
$U_o$	elastic energy
$U_a$	change in the elastic energy
$U_s$	change in the elastic surface energy
$S_e$	elastic surface energy of a material
$S_p$	plastic strain work
$\left. \begin{array}{l} \sigma_x, \sigma_y, \sigma_z \\ \tau_{xy}, \tau_{yz}, \tau_{xz} \end{array} \right\}$	rectangular components of stress
$E$	Young's modulus
$G$	shear modulus
$\nu$	Poisson's ratio
$\theta$	Polar angle with the origin located at the crack tip
$r$	radial distance measured from the crack tip
$\chi$	radial distance measured towards the crack tip
$\left. \begin{array}{l} U_x \\ U_y \\ w \end{array} \right\}$	components of crack surface displacement
$\left. \begin{array}{l} U'_x(x,0) \\ U'_y(x,0) \end{array} \right\}$	components of crack surface displacement along $(x,0)$
CS	compact shear

a	notch depth
H	notch spacing
W	width of a cube
b	thickness of a specimen
B	vertical distance between two notch tips
A	crack surface area
R	crack resistance
C	compliance of a body (= displacement/load)
WD	work done
Y(a/W)	calibration coefficient
P	applied load
$P_1$	'pop-in' load
$P_{max}$	failure load
$G_I, G_{II}, G_{III}$	strain energy release rate in Mode I, Mode II and Mode III type of failure respectively
$G_{IC}, G_{IIC},$ $G_{IIIC}$	} critical strain energy release rate in Mode I, Mode II and Mode III type of failure respectively
$K_I, K_{II}, K_{III}$	Stress intensity factor in Mode I, Mode II and Mode III type of failure respectively
$K_{IC}, K_{IIC},$ $K_{IIIC}$	} Critical stress intensity factor in Mode I, Mode II, Mode III type of failure respectively
$K_{LT}$	latent fracture toughness

## CHAPTER 1

### INTRODUCTION

For the engineering application of linear elastic fracture mechanics to the prediction of the strength and life of cracked structures, a knowledge of the crack tip stress intensity factor is necessary. This information, combined with an experimentally determined critical stress intensity factor and the crack growth rates for the structural materials, made such predictions possible.

In the development of basic fracture mechanics concepts, extensive research has been carried out analysing the Mode I type of failure on both metallic and non-metallic materials, mainly steel and concrete. Although limited analytical work has been done on the Mode II type of failure, little has been experimentally verified on cementitious materials.

The object of this study is to determine the Mode II fracture toughness of mortar and soil-cement using both the stress intensity factor  $K$  approach and the strain energy release rate  $G$  approach. This includes the development of a mathematical model which satisfies the Mode II type of fracture failure conditions. The Mode II stress intensity factors are predicted using the computer program suite, PAFEC. The results are verified experimentally by means of the compression tests on the INSTRON testing machine.

The critical literature review on numerical methods in determining stress intensity factors shows that the finite element



method is the best choice because it can provide approximate solutions of finite cracked bodies when exact solutions are difficult or impossible to obtain. In this project the displacement approach of the finite element method used by Chan et al is adopted for analysing 100mm double-notched cubes and the one used by Woo et al is adopted for 100mm single-notched and 150mm double-notched cubes. Instead of using a fine triangular element mesh around the crack tip as demonstrated by Chan, a coarse mesh of quadrilateral isoparametric elements with four crack tip elements at the crack tip is used on all specimen geometries.

A compact shear specimen has been adopted and modified for a Mode II fracture study in this project. This includes numerical analysis and experimental work.

#### (1) Finite element analysis

It is important in the initial stage of this study to establish a mathematical model which satisfies the Mode II type of fracture failure conditions before full scale experiments are operated. Three main geometries have been used in this study. They are 100mm double-notched, 100mm single-notched and 150mm double-notched cubes with notches cut in both the upper and lower faces. The 100mm double-notched cubes include three configurations differ according to the spacing  $H$  of the notches, these being 50 , 40 and 30mm. The upper notches are 10mm deep, whereas the lower notches vary from 25mm to 60mm in 5mm increments. The single-notched cube

has the same variation of notch depths as the double-notched cube except the top notch is 6mm off-centre to the bottom one. The 150mm double-notched cubes include H=80, 60 and 40mm with the upper notches being kept at 15mm deep, whereas the lower notches vary from 30mm to 80mm in 5mm increments.

The aims of this analysis are :

1. to represent a cube into a mathematical model which meets the loading and boundary conditions,
2. to study the capabilities of various finite elements,
3. to carry out a convergence study in order to find the suitable finite element mesh size,
4. to study the stress profiles along the line of action of the load,
5. to compare  $K_{II}$  and  $K_I$  values,
6. to determine the calibration coefficients  $Y(a/W)$ ,
7. to compare the finite element methods with the boundary collocation method in the determination of stress intensity factors.

## (2) Experimental analysis on 100mm cubes

The aims of this experimental analysis are :

1. to develop a testing arrangement which is suitable for the testing of cement composites in the Mode II type of failure,

2. to determine a suitable test geometry,
3. to find an acceptable method of evaluating the load-displacement curves for the determination of fracture toughness for mortar and soil-cement.

The experimental work is divided into two main parts :

Part A : mortar

The general properties of mortar have been determined, these include :

- (a) the bulk density,
- (b) the standard compressive (100mm) cube strength test,
- (c) the standard static modulus of elasticity test.

A testing arrangement has been determined for the Mode II type of fracture failure. The fracture tests in compression include using

- (a) the existing Departmental made compressive platens (Test series one),
- (b) the INSTRON compressive platens and a load rig (Test series two).

The fracture toughness values have been determined by using both the stress intensity factor  $K$  approach and the strain energy release rate  $G$  approach for :

- (a) 100mm double-notched cubes (Test series three),
- (b) 100mm single-notched cubes (Test series four).

#### Part B : soil-cement

The general properties of soil-cement have been determined, these include :

- (a) the bulk density,
- (b) the optimum dry density and moisture content,
- (c) the compressive (100mm) cube strength test.

The fracture toughness values have been determined by using both the stress intensity factor  $K$  approach and the strain energy release rate  $G$  approach for :

- (a) 100mm double-notched cubes (Test series five),
- (b) 100mm single-notched cubes (Test series six).

## CHAPTER 2

### REVIEW OF LITERATURE

#### 2.1 INTRODUCTION

A highly intriguing problem in the theory of Elasticity is that which involves the stress concentration in the region around a void or notch. This also becomes a design problem when thin structural members of higher strength steel or other structural materials, sensitive to fatigue and brittle fracture, are used. As engineers need to predict the strength of cracked structures, in order to design against sudden failure, the science of fracture mechanics has grown into a major field of study in engineering mechanics.

The type of fracture which occurs in engineering materials is either ductile or brittle. In ductile fracture, failure takes place following the plastic deformation of the material particularly where shear and sliding takes place at  $45^{\circ}$  to the direction of principal stresses. In brittle fracture there is little or no plastic deformation prior to failure and the type of fracture which occurs is largely dependent upon the nature of the material and loading.

#### 2.2 GRIFFITH THEORY

The first successful analysis of fracture problems was that of Griffith (1) in 1920. He investigated the propagation of brittle cracks in glass.

Griffith stated that crack propagation will occur if the energy released upon crack growth is sufficient to provide all the energy

that is required for crack growth.

He then considered an infinite plate, containing a unit-thickness crack of length  $2a$  and subjected it to uniform tensile stress,  $\sigma$ , applied at infinity (Figure 2.1). The total energy of the cracked plate was found to be

$$U = U_o + U_a + U_s \quad (2.1)$$

where

$U_o$  = elastic energy of the loaded uncracked plate

$U_a$  = change in the elastic energy caused by  
introducing the crack in the plate

$U_s$  = change in the elastic surface energy caused by  
the formation of the crack surfaces

He used a stress analysis in order to show the elastic energy is

$$U_a = \frac{\sigma^2 \pi a^3}{E} \quad (\text{for plane stress}) \quad (2.2)$$

and the elastic surface energy is

$$U_s = 2(2aS_e) \quad (2.3)$$

where  $S_e$  is the elastic surface energy of the material.

Substituting equations (2.2) and (2.3) into (2.1) gives

$$U = U_o - \frac{\sigma^2 \pi a^3}{E} + 4aS_e \quad (2.4)$$

where the decrease in elastic energy of the plate is shown as a negative sign.

The equilibrium condition for crack extension is obtained by substituting

$$\frac{d}{da} U = 0$$

$$\frac{d}{da} \left( -\frac{\sigma^2 \pi a^2}{E} + 4aS_e \right) = 0 \quad (2.5)$$

$$\frac{2 \sigma^2 \pi a}{E} = 4S_e \quad (2.6)$$

$$\sigma a^{\frac{1}{2}} = \left( \frac{2 E S_e}{\pi} \right)^{\frac{1}{2}} \quad (2.7)$$

Crack extension in truly brittle materials occurs when equation (2.7) has a constant critical value.

### 2.3 IRWIN'S MODIFICATION TO THE GRIFFITH THEORY

Equation (2.6) may be rearranged in the form :

$$\sigma^2 \frac{\pi a}{E} = 2S_e \quad (2.8)$$

For a small crack extension, the elastic energy per unit crack surface area is represented by the energy release rate

$$\mathcal{G} = \sigma^2 \frac{\pi a}{E} \quad (2.9)$$

and the increased surface energy is represented by the crack resistance

$$R = 2 S_e \quad (2.10)$$

Before unstable crack growth occurs,

$$\mathcal{G}_c = R$$

If  $R$  is a constant,  $\mathcal{G}$  must exceed a critical value  $\mathcal{G}_c$ .

Thus fracture occurs when

$$\sigma^2 \frac{\pi a}{E} \geq \sigma_c^2 \frac{\pi a}{E} = \mathcal{G}_c = R \quad (2.11)$$

where  $\sigma_c$  is the stress required to fracture a plate with a crack of size  $2a$ .

Irwin (2) and Orowan (3) independently suggested that the Griffith theory for truly brittle materials could be modified and applied to both brittle materials and metals that exhibit plastic deformation. They recognized that a material's resistance to crack extension was

$$\mathcal{G} = \sigma^2 \frac{\pi a}{E} = 2(S_e + S_p) = R \quad (2.12)$$

where  $S_p$  = plastic strain work



For relatively ductile materials  $S_p \gg S_e$

i.e.  $R$  is mainly plastic energy and the surface energy can be neglected.

## 2.4 LINEAR ELASTIC FRACTURE MECHANICS (LEEM)

The principle of linear elastic fracture mechanics states that the stress intensity factor is used as the characterizing parameter for crack extension.

### 2.4.1 The Stress Intensity Factor $K$ Approach

Irwin (4) demonstrated that there are three types of failure conditions due to a local mode of deformation on the crack plane. They can be classified as follows :

#### Mode I - the opening mode (Figure 2.2a)

The displacements of the crack surfaces are perpendicular to the plane of the crack. They are pulled apart in the  $y$ -direction, but the deformations are symmetric about the  $x$ - $z$  and  $x$ - $y$  plane.

Paris and Sih (5) used the Westergaard method (6) of stress analysis of cracks to derive the displacement and stress equations corresponding to the three displacement modes with reference to Figure 2.3 for notations, the crack tip displacement and stress fields under plane strain conditions were found to be

$$\sigma_x = \frac{K_I}{(2\pi r)^{\frac{1}{2}}} \cos \frac{\theta}{2} \left[ 1 - \sin \frac{\theta}{2} \sin \frac{3\theta}{2} \right]$$

$$\sigma_y = \frac{K_I}{(2\pi r)^{\frac{1}{2}}} \cos \frac{\theta}{2} \left( 1 + \sin \frac{\theta}{2} \sin \frac{3\theta}{2} \right)$$

$$\tau_{xy} = \frac{K_I}{(2\pi r)^{\frac{1}{2}}} \sin \frac{\theta}{2} \cos \frac{\theta}{2} \cos \frac{3\theta}{2}$$

$$\sigma_z = \nu(\sigma_x + \sigma_y)$$

$$\tau_{xz} = \tau_{yz} = 0 \quad (2.13)$$

$$u_x = \frac{K_I}{G} \left( \frac{r}{2\pi} \right)^{\frac{1}{2}} \cos \frac{\theta}{2} \left( 1 - 2\nu + \sin^2 \frac{\theta}{2} \right)$$

$$u_y = \frac{K_I}{G} \left( \frac{r}{2\pi} \right)^{\frac{1}{2}} \sin \frac{\theta}{2} \left( 2 - 2\nu - \cos^2 \frac{\theta}{2} \right)$$

$$w = 0$$

### Mode II - the sliding mode (Figure 2.2b)

The displacements of the crack surfaces are in the plane of the crack and perpendicular to the leading edge. The two crack surfaces slide over each other in the x-direction, but the deformations are symmetric about the x-y plane and anti-symmetric about the x-z plane. The crack tip displacements and stresses were found to be :

$$\begin{aligned}\sigma_x &= \frac{K_{II}}{(2\pi r)^{\frac{1}{2}}} \sin \frac{\theta}{2} \left( 2 + \cos \frac{\theta}{2} \cos \frac{3\theta}{2} \right) \\ \sigma_y &= \frac{K_{II}}{(2\pi r)^{\frac{1}{2}}} \sin \frac{\theta}{2} \cos \frac{\theta}{2} \cos \frac{3\theta}{2} \\ \tau_{xy} &= \frac{K_{II}}{(2\pi r)^{\frac{1}{2}}} \cos \frac{\theta}{2} \left( 1 - \sin \frac{\theta}{2} \sin \frac{3\theta}{2} \right)\end{aligned}\tag{2.14}$$

$$\sigma_z = \nu (\sigma_x + \sigma_y)$$

$$\tau_{xz} = \tau_{yz} = 0$$

$$U_x = \frac{K_{II}}{G} \left( \frac{r}{2\pi} \right)^{\frac{1}{2}} \sin \frac{\theta}{2} \left[ 2 - 2\nu + \cos^2 \frac{\theta}{2} \right]$$

$$U_y = \frac{K_{II}}{G} \left( \frac{r}{2\pi} \right)^{\frac{1}{2}} \cos \frac{\theta}{2} \left[ -1 + 2\nu + \sin^2 \frac{\theta}{2} \right]$$

$$w = 0$$

### Mode III - the tearing mode (Figure 2.2c)

Crack surface displacements are in the plane of the crack and parallel to the leading edge of the crack. The crack surfaces slide over each other in the z-direction, but the deformations are anti-symmetric about the x-y and x-z plane. The crack tip displacements and stresses were found to be

$$\begin{aligned}\tau_{xy} &= -\frac{K_{III}}{(2\pi r)^{\frac{1}{2}}} \sin \frac{\theta}{2} \\ \tau_{yz} &= \frac{K_{III}}{(2\pi r)^{\frac{1}{2}}} \cos \frac{\theta}{2}\end{aligned}\tag{2.15}$$

$$\sigma_x = \sigma_y = \sigma_z = \tau_{xy} = 0$$

$$w = \frac{K_{III}}{G} \left(\frac{2r}{\pi}\right)^{\frac{1}{2}} \sin \frac{\theta}{2}$$

$$u = v = 0$$

In equations (2.13), (2.14) and (2.15)  $G = E/2(1+\nu)$  is the shear modulus,  $E$  is Young's modulus,  $\nu$  is Poisson's ratio. The polar coordinate  $r$  is the radial distance measured from the crack tip and  $\theta$  is the polar angle. The above equations have been obtained by neglecting higher-order terms in  $r$ . They can be regarded as a good approximation in the region where  $r$  is small compared to other planar ( $x$ - $y$  plane) dimensions such as the crack length. The stresses, which tend to infinity as  $r$  approaches zero (i.e. at the crack tip) are products of geometrical position  $(2\pi r)^{-\frac{1}{2}} f(\theta)$ . The singularity of the order  $r^{-\frac{1}{2}}$  in the stress-field equations is a controlling feature in the relationship of stress concentrations to stress intensity factors.

The parameters  $K_I$ ,  $K_{II}$  and  $K_{III}$  are known as the stress intensity factors corresponding to the three fracture modes. It is

important to notice that the stress intensity factors are not dependent on the coordinates,  $r$  and  $\theta$  ; they control the intensity of the stress fields but not the distribution for each mode. Dimensional considerations of equations (2.13), (2.14) and (2.15) show that the stress intensity factors must contain the magnitude of loading factors linearly for linear elastic bodies and must also depend upon the configuration of the body including the crack size. Therefore, stress-intensity factors may be interpreted as parameters, reflecting the redistribution of stress in a body due to the introduction of a crack. The critical value of the stress-intensity factor  $K_C$  is considered to be a material property and is termed as the fracture toughness.

Modes I and II, which are symmetric and skew-symmetric with respect to the crack plane can be analysed as plane-extensional problems of the theory of elasticity. Mode III can be regarded as the pure shear (or torsional) problem. The superposition of these three modes is sufficient to describe the most general case of crack tip deformation and stress fields.

#### 2.4.2 The Strain Energy Release Rate $\mathcal{G}$ Approach

Irwin (4) demonstrated that if a crack is extended by amount " $da$ " , the work done by the stress field ahead of the crack when moving through the displacements corresponding to a crack of length  $(a + da)$  is formally equivalent to the change in strain energy  $\mathcal{G} da$  , equations (2.13), (2.14) and (2.15) can be generalized as :

$$\sigma_{ij} = \frac{K}{(2\pi r)^{\frac{1}{2}}} f_{ij}(\theta)$$

so that the stress intensity factor can be written as :

$$K = \sigma (\pi a)^{\frac{1}{2}} f(a/w) \quad (2.16)$$

where  $f(a/w)$  is a dimensionless parameter that depends on the geometries of the specimen and crack.

Substituting equation (2.16) into (2.11) gives the critical strain energy

$$\mathcal{G}_c = \frac{K_c^2}{E} \quad (\text{Plane stress}) \quad (2.17)$$

$$\mathcal{G}_c = \frac{(1-\nu^2)}{E} K_c^2 \quad (\text{Plane strain})$$

$$\mathcal{G}_I = \frac{(1-\nu^2)}{E} K_I^2$$

$$\mathcal{G}_{II} = \frac{1-\nu^2}{E} K_{II}^2 \quad (2.18)$$

$$\mathcal{G}_{III} = \frac{1-\nu^2}{E} K_{III}^2$$

where  $\mathcal{G}_I$ ,  $\mathcal{G}_{II}$  and  $\mathcal{G}_{III}$  are the energy release rate contributors of Mode I, Mode II and Mode III respectively.

Under linear elastic fracture mechanics conditions the prediction of crack growth and fracture is the same for both the energy balance and elastic stress field approaches.

## 2.5 APPLICATION OF THE FINITE ELEMENT METHOD IN LEFM

A rigorous determination of the crack tip stress intensity factor requires an exact solution of the elasticity problem formulated for the cracked structure. Applying the classical theory of elasticity to actual problems is very difficult to solve. The application of the boundary-collocation method is also limited, due to the inability to handle problems of a general nature and the need to satisfy convergence criteria. Numerical techniques such as the finite element method, although approximate, have been shown to yield satisfactory results for stress analysis problems in general. The finite element method is the most appropriate for obtaining approximate stress intensity factors whenever exact solutions are not available.

The crack tip stress intensity factors can be estimated from the numerical solution by one of the following approaches :

### (a) Energy Release Rate Method

This method requires the computation of total strain energy from the element stresses and strains. This can be done automatically and the strain energy included in the output. The energy release rate of a cracked body loaded by forces  $P$  as shown in Figure 2.4 can be expressed as :

$$G = \frac{P^2}{2b} \left( \frac{\partial c}{\partial a} \right) \quad (2.19)$$

where  $b$  is the thickness and  $c$  (= displacement/load) is the compliance of the body.

The energy release rate is approximated by obtaining energy values for two slightly different crack lengths, subtracting, and dividing by the incremental crack length. Since, as previously stated, the energy release rate is directly related to the stress intensity factor, it is a simple computation to find  $K$ . In theory this method should not require extremely small elements at the crack tip, but in practice the element size is important.

#### (b) The J-integral Method

Rice (7) has shown that the value of the line integral is

$$J = \int_{\Gamma} \left( W \, dy - T \frac{\partial u}{\partial x} \, dS \right) \quad (2.20)$$

where  $\Gamma$  is an arbitrary contour surrounding the crack tip as shown in Figure 2.5.  $W$  is defined as the strain energy density,  $T$  is the traction vector defined according to the outward normal along  $\Gamma$  and  $u$  is the displacement vector.

Rice (7) has demonstrated that the line integral is proportional to the square of the crack tip stress-intensity factor. For plane strain conditions :

$$K_I = \left[ \frac{JE}{1-\nu^2} \right]^{\frac{1}{2}} \quad (2.21)$$



In evaluating the integral of equation (2.20) for the finite element solution over a path surrounding the crack tip, an estimate of the crack tip stress-intensity factor can be obtained by using equation (2.21).

The advantage of this method is that no extrapolations are required. The accuracy of this method is independent of mesh configuration and depends only on the accuracy of the evaluation in evaluating the J-integral. It is also applicable to any crack geometry, including combined mode loading. The disadvantage is that for a single element representation it is difficult to estimate the degree of error in the estimated value.

### (c) The Stress Method

The stress approach involves a correlation of the finite element nodal point stresses with the crack tip stress equations. For plane strain conditions and making use of the Westergaard (6) stress equations on the  $\theta = 0$  plane, equation (2.13) gives

$$K_I = (2\pi r)^{\frac{1}{2}} \sigma_y \quad (2.22)$$

equation (2.14) gives

$$K_{II} = (2\pi r)^{\frac{1}{2}} \tau_{xy} \quad (2.23)$$

The validity of the Westergaard stress equations in the finite element analysis applies to element size  $r = 0.001a$  (where  $a$  is the crack length) around the crack tip area.

Chan et al (8) used a very fine triangular element mesh in order to produce a better estimate of  $K$ . The element size around the crack tip was in the order of 0.001 of the crack length. Nodal point stresses in the vicinity of the crack tip were substituted into equations (2.22) and (2.23) and values of  $K$  were evaluated. Since stresses are derivatives of displacements, there is more scatter in data point, and the extrapolation is less reliable.

#### (d) The Displacement Method

The displacement approach for determining the stress intensity factors is similar to the stress method. The nodal point displacements are correlated with the Westergaard displacement equations on the crack surface where  $\theta = \pi$ . For plane strain conditions

equation (2.13) gives

$$K_I = \frac{(2\pi)^{\frac{1}{2}}}{4(1-\nu^2)} \frac{U_y}{r^{\frac{1}{2}}} \quad (2.24)$$

equation (2.14) gives

$$K_{II} = \frac{(2\pi)^{\frac{1}{2}}}{4(1-\nu^2)} \frac{U_x}{r^{\frac{1}{2}}} \quad (2.25)$$

The Westergaard displacement equations are valid in the finite element analysis for elements of size  $r = 0.1a$  around the crack tip area.

The stress-intensity factors  $K$  can be evaluated accordingly by substituting nodal displacements  $U$  into equations (2.24) and (2.25).

Woo et al (9) employed a coarse finite element mesh to determine the stress intensity factors of a cracked body by using a conic-section simulation model (10). This method makes use of an elliptic displacement functions which are satisfied by the introduction of an equivalent ellipse obtained through simulating the actual crack surface displacement as a part of a parabola or a hyperbola.

As the finite element method provides better approximate solutions of finite crack bodies, further study on the application of finite element method to obtain stress intensity factors is made in Chapter 3.

## 2.6 APPLICATION OF LEFM TO CEMENTITIOUS MATERIALS

Many different theories have been put forward to explain the fracture mechanisms in concrete. In recent years attention has been directed to the application of fracture mechanics to investigate crack propagation in concrete. Fracture mechanics does not explain the micro-mechanism of fracture but deals with the relationships between stress, energy and size of crack, for example, and enables a quantitative analysis of the failure to be made. Here two categories of stress failure in concrete-like materials will be discussed. These are tensile and compressive failure.

### Mode I Failure of Cementitious Materials

Most of the limited research on the application of the energy concept of fracture mechanics to concrete, has been carried out on flexure or tensile specimens. Tensile fracture in concrete is not limited to one crack, however, but to several of microcracks which cover the entire highly stressed zone. In this situation the energy required increases about ten-fold by the newly formed microcrack surfaces. This is analogous to the large energy associated with the plastic deformation of metals. Heterogeneity in concrete undoubtedly complicates the detailed study of fracture mechanics insofar as it creates non-uniform energy requirements for crack propagation. A crack encountering an aggregate particle or an otherwise stronger zone may go around it or through it; but in either event the energy demand is normally increased.

Glucklich (11) has suggested that the energy requirement curve for crack propagation is not a straight line for concrete, but a curve with an ascending slope. There is an increase in the energy demanded as the crack arrest mechanism due to heterogeneity. This corresponds to the "slow crack growth" stage observed in some experiments. The criteria for slow crack growth is that a crack will always propagate to balance the total energy.

Kaplan (12) was the first to report measurements of fracture toughness for concrete. He performed experiments on beam flexure specimens in direct and indirect tension to show that the microcracks occurred in concrete when loaded.

Swamy (13) summarised some of the investigators' test geometries and their calculated fracture toughness values which can be used to compare with other researchers' works.

Visalvarich et al (14) employed four methods to determine the critical strain energy release rate for a double cantilever beam. The materials used were mortar, fibre reinforced concrete and asbestos cement. The four methods used were :

- (a) analytical methods to determine the stress intensity factor
- (b) the compliance measured strain energy technique
- (c) the "quasi-static" energy measuring technique and
- (d) the "off-set" fracture energy technique that takes into consideration the permanent deformation (or offset) at unloading.

In a linear-elastic body when fracture occurs by unstable crack propagation, the strain energy release rate of the material was determined using equation (2.19)

$$G = \frac{P^2}{2b} \frac{dc}{da}$$

where

P = applied load

b = thickness of the cantilever beam

c = compliance of the specimen

a = crack length

$G$  was based on experimentally determined compliance of a specimen.

Or using (2.17)

$$G_K = \frac{K^2}{E}$$

where  $G_K$  was based on known  $K$ .

For the material showing stable crack propagation, the fracture energy was evaluated from the "quasi-static" fracture energy method. This method assumes that when the load is released to zero no permanent deformation remains. The strain energy was

$$U_R = \frac{D}{bda} \quad (2.26)$$

where  $D$  is the shaded area of the load-deformation curve shown in Figure 2.6a.

For the material experiencing a slow, stable crack growth and a significant permanent or residual deformation such as concrete, the energy required to extend a crack was taken into consideration. This was done by using the unloading and reloading technique. For each loading cycle, a straight line fitting the reloading path was drawn. The area under the load-deformation curve and between two subsequent straight lines, corresponding to the successively recorded crack lengths, was used to determine the fracture energy

$$U_{IR} = \frac{A}{bda} \quad (2.27)$$

where  $A$  is the shaded area of the load-deformation curve shown in Figure 2.6b.

It was concluded that the concepts of linear elastic fracture mechanics were applicable to asbestos cements and plain mortar. The fracture energies, determined from the compliance measurement and from the quasi-static energy technique, underestimated the true fracture energy of mortar and steel fibre reinforced mortar. The fracture energy which accounted for the existence of the permanent deformation at unloading was found to represent the actual energy of mortar and fibre reinforced concrete. The critical stress intensity factor for plain mortar was determined as  $1.3\text{MNm}^{-3/2}$ .

#### Mode II Failure of Cementitious Materials

Studies on an experimental determination of fracture toughness for concrete subjected to a compressive stress field were reviewed as follows.

Glücklich (11) has indicated that the tensile stresses existing at the ends of an inclined crack can extend the crack and release strain energy (see Figure 2.1). These crack extensions will be parallel to the direction of compression as this is the only direction without a normal compressive stress.

It has been suggested that the strain energy release rate may be independent of crack length, in a compressive stress field, so that the strain energy released by crack formation  $U$  is

$$U = \frac{\pi b a (\sigma_{\text{comp}})^2}{2E} \quad (2.28)$$

where  $b$  and  $a$  are crack dimensions shown in Figure 2.7.

Hence

$$\delta = \frac{\partial u}{\partial c} = \frac{\pi b (\sigma_{\text{comp}})^2}{2E} \quad (2.29)$$

and with the involvement of crack length.

$$\delta_c = \frac{\pi a (\sigma_{\text{comp}})^2 \sin^2 \phi \cos^2 \phi (1-\nu^2)}{E} \quad (2.30)$$

Whether  $\delta_c$  is independent of crack length or not (equations (2.29) and (2.30)), it can be shown that in a compressive field, cracks are inherently more stable than cracks in a tensile field. Further tensile cracks developed in a compression test are easily arrested and the tendency is for progressive cracking to occur with increasing load. Thus, final fracture is delayed by the development of many cracks parallel to the axis of loading and the stress-strain curve has a much greater curvature than in a tension test.

Knox (15) performed tests on standard 100mm concrete cubes under three loading conditions :

- (a) hardboard packing
- (b) rubber packing            and
- (c) no packing

These are illustrated in Figure 2.8.

- (a) The cube was tested in compression with hardboard packing interposed between the specimen and the platens of the test machine. It was found that the path of propagation of the secondary crack running from the initial crack was dependent



on tensile opening displacement and shear sliding displacement, the actual path being a combination of both modes. If conditions are such that the Mode II displacement predominates, failure will occur along the line of the initial crack as shown in Figure 2.8a. The critical crack inclination was found to be  $30^{\circ}$ .

- (b) It was observed that when concrete failed in compression with rubber strip packing interposed between the specimen and the machine platens, then a true tensile splitting mechanism was obtained from the first crack to propagation (see Figure 2.8b).
- (c) It was observed that propagation of the most critical cracks under Mode I and Mode II conditions occurred when standard compression tests (with no packing) were used as shown in Figure 2.8c. The application of increasing stress caused the formation of numerous stable cracks which eventually linked up and caused absolute failure of the specimen.

Desayi (16) investigated the fracture of mortar and concrete prisms with preformed centrally inclined notch of different depths and inclinations as shown in Figure 2.9. The prisms were tested under compression conditions. The fracture toughness of the materials were determined using the strain energy release rate method. Two expressions for the strain energy release rate for both crack-dependent and crack-independent were used. They were :

For crack-independent, equation (2.29)

$$\mathcal{G} = \frac{\pi b \sigma_c^2}{2E}$$

and

For crack-dependent, equation (2.30)

$$\mathcal{G} = \frac{\pi a \sigma_c^2 \sin^2 \phi \cos^2 \phi (1-\nu^2)}{E}$$

The critical strain energy release rate  $\mathcal{G}_c$  values of the prisms were found to be in the range of 0.135 to 0.347 mmN/mm<sup>2</sup> for mortar and 0.135 to 0.474 mmN/mm<sup>2</sup> for concrete when the crack-independent  $\mathcal{G}$  equation (2.29) was used. When the crack-dependent  $\mathcal{G}$  equation (2.30) was used,  $\mathcal{G}_c$  values were in the range of 0.043 to 0.173 mmN/mm<sup>2</sup> for mortar and 0.054 to 0.232 mmN/mm<sup>2</sup> for concrete.

Desayi concluded that the cracks initiated at the tips of the notches and propagated in the direction of loading. The ultimate load and the ultimate strain were found to gradually reduce as the notch length increased.

Watkins (17) investigated the Mode II shear failure of soil-cement cubes (Figure 2.10). The numerical analysis was carried out by the compliance method as proposed by Dixon et al (18). The stress intensity factor is determined as

$$K_{II} = \frac{5.11}{2BW} (\pi a)^{\frac{1}{2}} \quad \text{for } 0.3 \leq a/w \leq 0.5 \quad (2.31)$$

The direct compression test was carried out by loading the specimen in a direction perpendicular to that of compaction. For the specimen of  $H/W = 0.4$  and  $0.3 \leq a/w \leq 0.5$ , the  $K_{IIC}$  values with no correction for slow crack growth were found to be in the range of 0.42 to 0.43  $\text{MN m}^{-3/2}$ . The  $K_{IIC}$  values by using Chisholm and Jones' equation (19) were in the range of 0.42 to 0.45  $\text{MN m}^{-3/2}$ . By using the strain energy release rate method, they were found to be in the range 0.44 to 0.47  $\text{MN m}^{-3/2}$ .

Liu (20) and Watkins et al (21) investigated the fracture behaviour in a short shear beam in plain concrete. The finite element method has been employed to analyse the shear behaviour of the test specimen under in-plane shear conditions. The Mode II stress intensity factor was determined using the strain energy release rate method demonstrated by Dixon and Strannigan (18) as

$$K_{II} = 0.22 \frac{P}{Ba} (\pi c)^{\frac{1}{2}} \quad (2.32)$$

Details are shown in Figure 2.11.

The experimental work confirmed the numerical analysis that shear failure took place in the specimens with  $a/w$  ratio between 0.1 and 0.25. All specimens failed between the two slots, and a crushed zone was observed at the crack tip. The  $K_{IIC}$  values were reported to be in the range 0.50 to 0.55  $\text{MN m}^{-3/2}$ .

## 2.7 REVIEW OF THE MODE II COMPACT SHEAR (CS) SPECIMENS

A compact shear (CS) specimen was introduced by Chisholm and Jones (19) for the study of a Mode II shear failure. The Mode II stress intensity factors for a pair of "through-the-thickness" edge cracks in a finite isotropic plate as shown in Figure 2.12. An elastostatic analysis has been carried out in terms of the complete Williams (22) stress function employing both even and odd components and the results of the numerical analysis have been verified by comparison with a photoelastic analysis. The Williams stress function  $\chi(r,\theta)$  which satisfies the biharmonic equation can be expressed as :

$$\begin{aligned} \chi(r,\theta) = & \sum_{m=1}^{\infty} \left( B_{2,2m-1} \left\{ r_j^{m+\frac{1}{2}} \left[ \cos(m-\frac{3}{2})\theta_j - \left(\frac{2m-3}{2m+1}\right) \cos(m+\frac{1}{2})\theta_j \right] \right\} \right. \\ & + B_{2,2m} \left\{ r_j^{m+1} \left[ \cos(m-1)\theta_j - \cos(m+1)\theta_j \right] \right\} \\ & + B_{4,2m-1} \left\{ r_j^{m+\frac{1}{2}} \left[ \sin(m-\frac{3}{2})\theta_j - \sin(m+\frac{1}{2})\theta_j \right] \right\} \\ & \left. + B_{4,2m} \left\{ r_j^{m+1} \left[ \sin(m-1)\theta_j - \left(\frac{m-1}{m+1}\right) \sin(m+1)\theta_j \right] \right\} \right) \end{aligned} \quad (2.33)$$

where

- $B_{2,m}$  = the coefficients of the even stress function (opening mode) series
- $B_{4,m}$  = the coefficients of the odd stress function (sliding mode) series
- $r,\theta$  = the polar coordinate directions with the origin located at the crack tip

$m$  = the  $m$ -th term in the eigen-function expansion

$J$  = the  $J$ -th boundary point

The polar stresses obtained by partial differentiation of equation (2.33),  $\chi(r,\theta)$  are given as :

$$\sigma_{\theta} = \frac{\partial^2 \chi}{\partial r^2} \quad (2.34)$$

and

$$\tau_{r\theta} = - \frac{\partial}{\partial r} \left( \frac{1}{r} \frac{\partial \chi}{\partial \theta} \right)$$

Near the crack tip as  $r \rightarrow 0$  for  $\theta = 0$  and  $m = i$

equation (2.34) becomes

$$\sigma_{\theta} = B_{2,1} r^{-\frac{1}{2}} \quad (2.35)$$

The Westergaard equations from equation (2.13) for these conditions reduce to

$$\sigma_y = \frac{K_I}{(2\pi r)^{\frac{1}{2}}} \quad (2.36)$$

Therefore,

$$K_I = (2\pi)^{\frac{1}{2}} B_{2,1} \quad (2.37)$$

Similarly,

$$K_{II} = (2\pi)^{\frac{1}{2}} B_{4,1} \quad (2.38)$$

In addition, to satisfy the biharmonic equation the Williams' stress function must satisfy the boundary conditions along the crack surface. For the problem under consideration the normal and shearing stresses are zero for  $\theta = \pm\pi$ , i.e.  $\sigma_{\theta}$  and  $\tau_{r\theta} = 0$ . The remaining boundary requirements expressed in terms of the stress function and its normal derivatives are along the boundaries AB, BC, CDE and EO'F as shown in Figure 2.13. The undetermined constants  $B_{i,k}$  with  $i = 2,4$  and  $k = i$  to  $m$  are obtained by constructing a matrix of coefficients  $[C]$  from the Williams' stress function and its normal derivative for each boundary point of the specimen. It is expressed as :

$$[C] [B] = [L] \quad (2.39)$$

The product of this coefficient matrix  $[C]$  and a column matrix  $[B]$  of unknown constants is set equal to a column matrix containing the boundary values for the non-dimensionalised stress function  $\chi/P$  and its normal derivative. The solution in matrix form is

$$[B] = [C]^{-1} [L] \quad (2.40)$$

The numerical result for  $h = 2.44\text{cm}$  with  $W = 9.5\text{cm}$  for a bilinear centre-line stress distribution is shown in Figure 2.14. The numerical solution was verified by comparison with a photoelastic

analysis. The specimen was made of hysol epoxy resin 4290-CPS with dimensions  $h = 2.44\text{cm}$ ,  $W = 9.5\text{cm}$  and  $a/w$  ratio between 0.4 and 0.8 . It was loaded in a photoelastic experiment to study the isochromatic fringe patterns resulting from the Mode II crack tip stress distribution. The results are shown in Figure 2.14. The experiment verifies the accuracy of the Boundary-collocation solution for the Mode II stress-intensity factors.

The stress-intensity factor is non-dimensionalized by dividing  $B_{4.1} (2\pi)^{\frac{1}{2}}$  by  $\sigma a^{\frac{1}{2}}$  where  $\sigma$  is the applied stress  $P/bh$  . The plot of Figure 2.14 reveals that for  $0.3 \leq a/w \leq 0.7$  the expression

$$K_{II} = \frac{PW^{\frac{1}{2}}}{bh} \left(\frac{a}{w}\right)^{\frac{1}{2}} = \sigma a^{\frac{1}{2}} \quad (2.41)$$

is valid to within 2% . Beyond this range a least-squares approach is necessary to determine the best fit. At an  $a/w$  ratio of 0.8

$$K_{II} = (1.08) \sigma a^{\frac{1}{2}} \quad (2.42)$$

Agarwal et al (23) performed fracture toughness tests in shear Mode II on short glass fibre composites as shown in Figure 2.15. Equal and opposite forces parallel to the plane of the crack and perpendicular to the crack front were applied through the gripping area. It was found that a large gripping area will give rise to an undesirable bending moment on the specimen and too small an area will cause crushing. The critical strain energy release rate  $\mathcal{G}_{IIC}$  values were obtained by the compliance method. The  $\mathcal{G}_{IIC}$  values were found to be independent of crack length and were less than half of that in Mode I and Mode III.

This specimen is rejected in this study because it has been restricted in terms of thickness and gripping area in order to produce the Mode II displacement condition.

Richard (24) introduced a new compact shear (NCS) specimen for a pure shear loading test as shown in Figure 2.16 for brittle materials. A loading frame is used to apply equal and opposite forces (in tension) to the specimen. The crack length has been limited to  $0.55W \leq a \leq 0.65W$  because in this range  $K_I$  is less than 3% of  $K_{II}$ . The author intends to determine the  $K_{IIc}$  values of different brittle materials.

Leslie Banks-Sills et al (25) presented a specimen from which a narrow region of nearly uniform pure shear can be obtained under tensile loading as shown in Figure 2.17. It is found from the finite element analysis that direct stress  $\sigma_{xx}$  is approximately 4% of the shear stress  $\sigma_{xy}$  in the region surrounding the crack. Photoelastic study shows  $K_{II}$  is 140 times larger than  $K_I$ . The author concluded that the opening mode in this sample is negligible and a Mode II deformation is dominant.

This test is not used in this study as the loading frame and the test specimen are not easily adopted for tests in concrete.

Riddle et al (26) modified the compact shear specimen used by Jones and Chisholm (27) as shown in Figure 2.18. The thickness of the specimen in the crack tip region was one-half of the thickness of the material in the loading hole region, so that if plastic deformation occurs in the specimen, it happens in the region near



the crack tip and not at the loading holes. The  $K_I/K_{II}$  ratio varies from 0.3 for the shortest crack to 0.083 for the longest crack. Stress intensity solutions for the compact shear specimen were evaluated using a J-integral method and pure Mode II loading condition was achieved. This method is restricted by the direction of tensile loading through the loading holes as shown in Figure 2.18.

Anandarajah et al (28) studied the Mode II failures of adhesive joints with both thin and thick adhesive layers on the compact shear specimen under tensile load conditions as shown in Figure 2.19. The compliance method was used to determine the critical strain energy release rate  $G_{IIC}$ , which was strongly dependent upon the thickness of the adhesive layer and the crack length. This compact shear specimen is not adopted in this study because the Mode II failures have not been achieved.

Wang et al (29) investigated the fracture behaviour of a random short fibre sheet moulding compound (SMC) components subjected to pure shear (Mode II) loading. The uniform shear-stress field in the test was introduced by clamping the ends of the specimen into the grips subjected to the tensile loading as shown in Figure 2.20 for both centre crack and edge crack. It was concluded that a Mode II shear loading has been achieved and the  $K_{IIC}$  values appeared to be independent of crack configuration and crack lengths.

This test method is not used in this project because the specimen has been restricted in the 'sheet' form and a tensile load load frame is necessary to achieve the Mode II failure.

Most of the compact shear specimens discussed have produced a pure Mode II type of failure. The restrictions are high to achieve such failure conditions as simple geometries are limited in their thickness and loading conditions while the complex geometry is restricted to be tested with an equally complex load frame. Above all, the specimens were tested in the tensile loading conditions; which were achieved using specially designed load frames.

The simple compact shear specimen proposed by Watkins (17) has been adopted for fracture studies in this project because (a) the specimen can be readily prepared and modified from 100mm standard cubes and (b) tests are to be carried out under direct compression load.

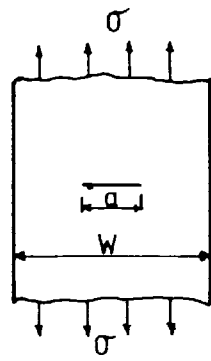


Fig. 2-1 A through-cracked plate  
(Griffith's model [1])

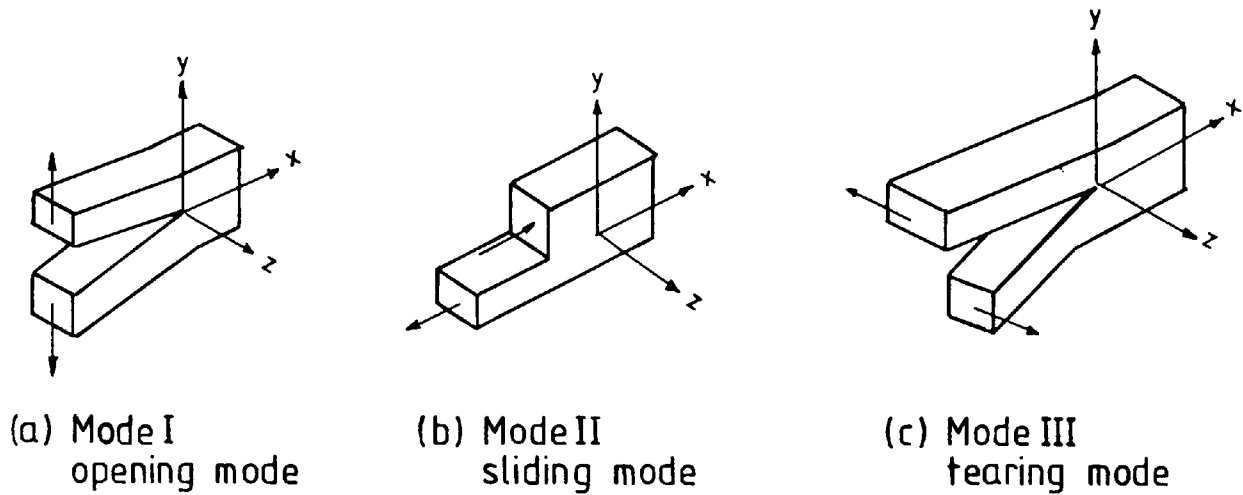


Fig. 2-2 The three modes of crack surface displacements.

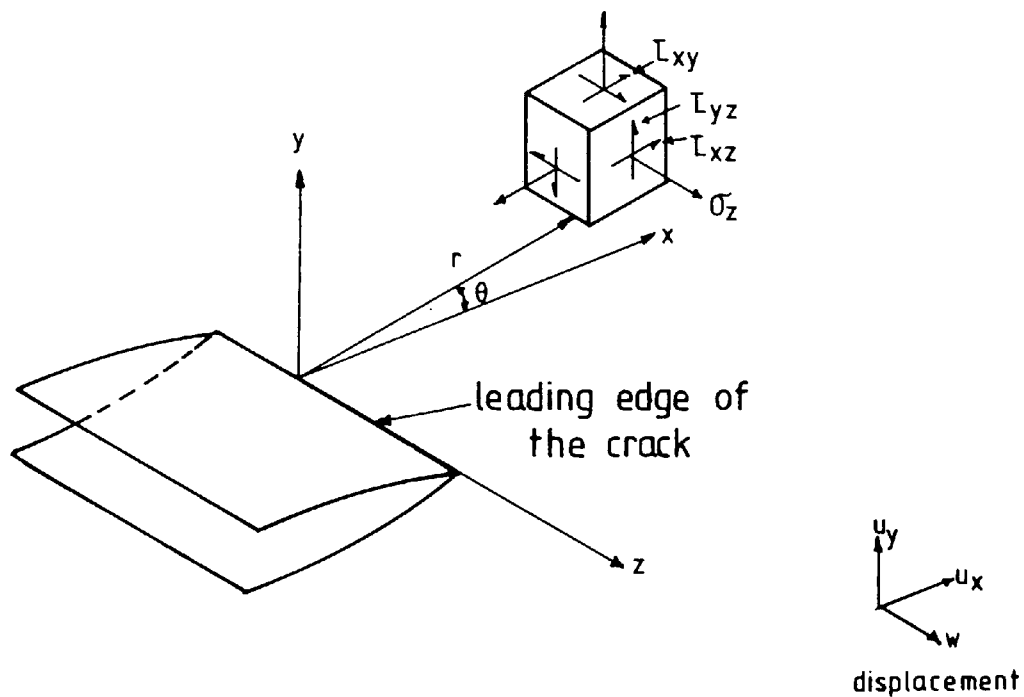


Fig. 2-3 Coordinates measured from the leading edge of a crack & the stress components in the crack tip stress field.

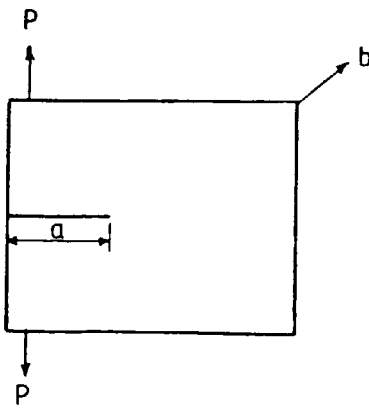
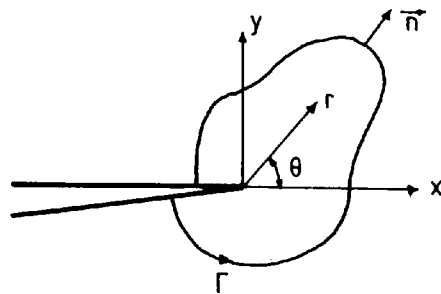
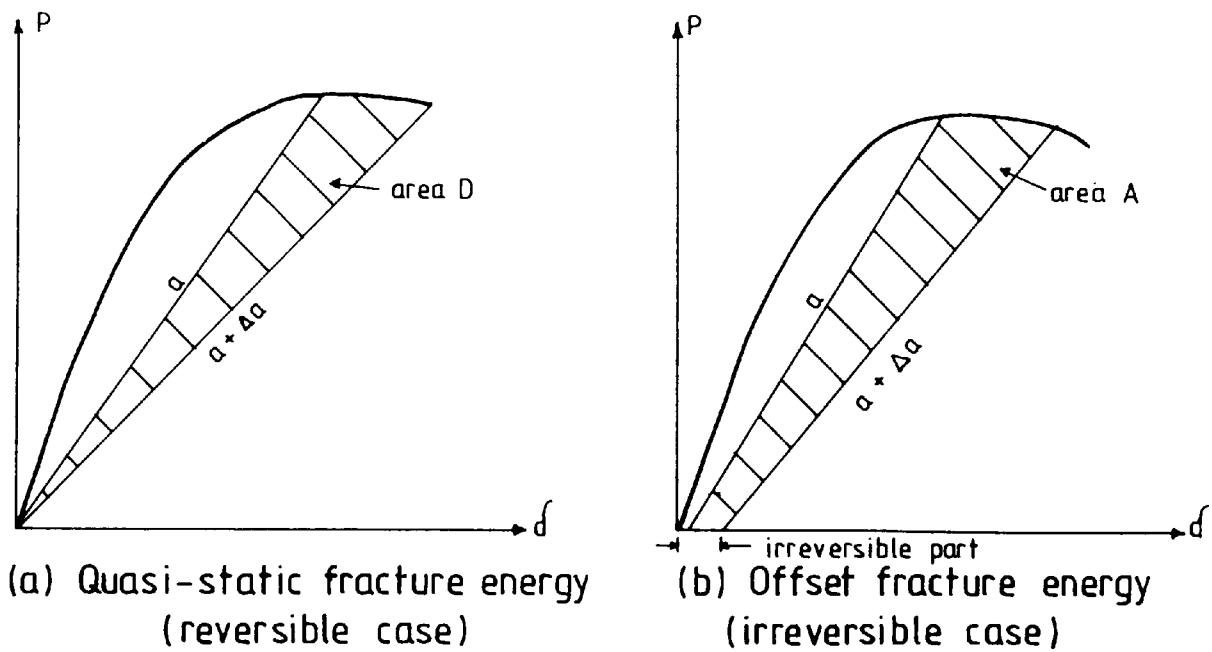


Fig. 2-4

Fig. 2-5 Crack tip contours & typical contour  $\Gamma$   
(Rice's model [7])Fig. 2-6 Load-displacement curves  
(Visalvanich [14])

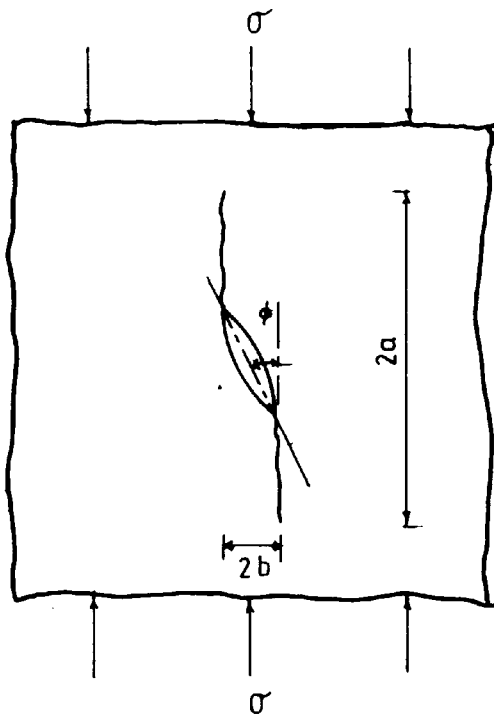


Fig. 2.7 Propagation of a skew elliptical crack in a compressive field (Glücklich's model [11] )

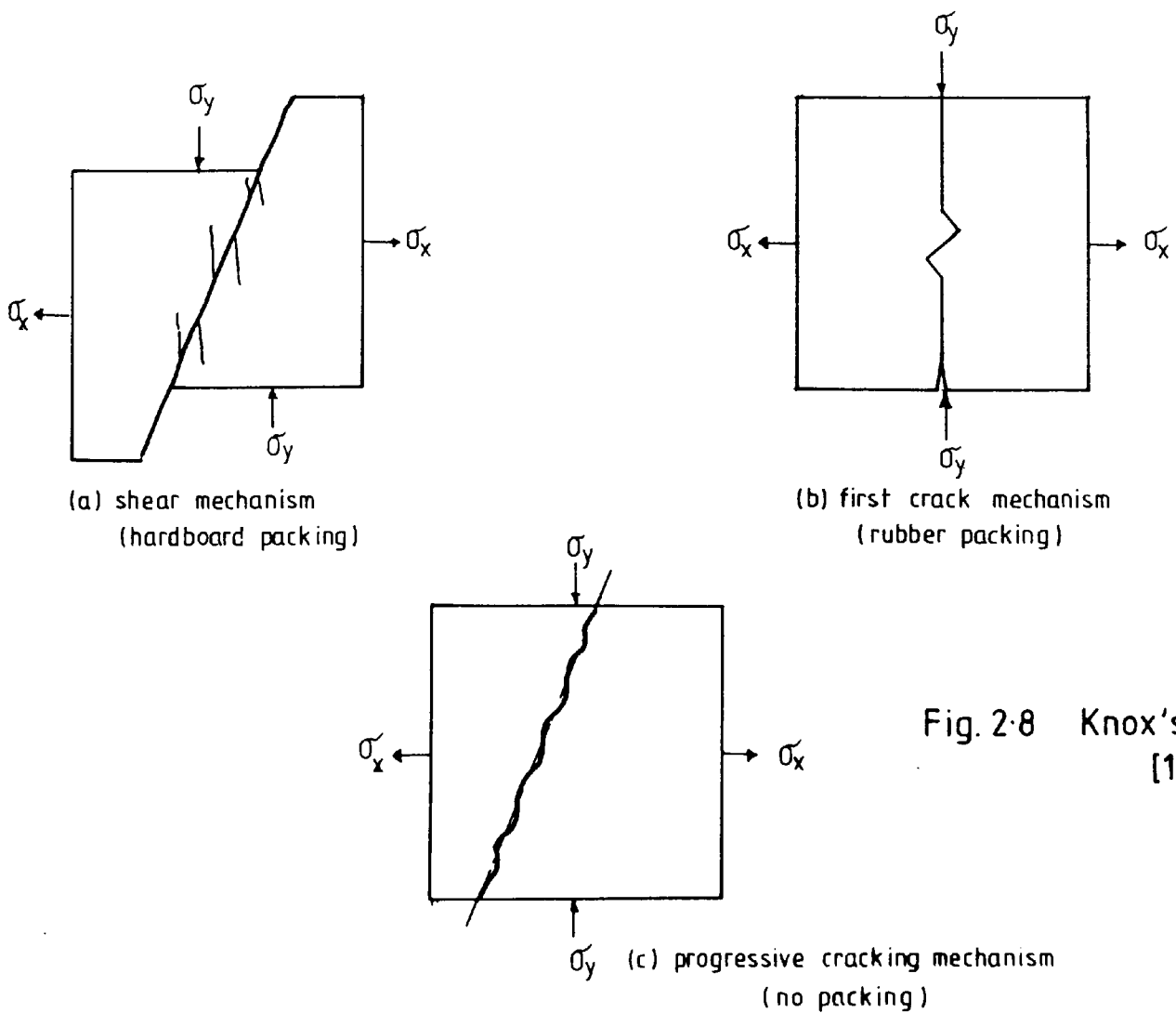


Fig. 2.8 Knox's model [15]

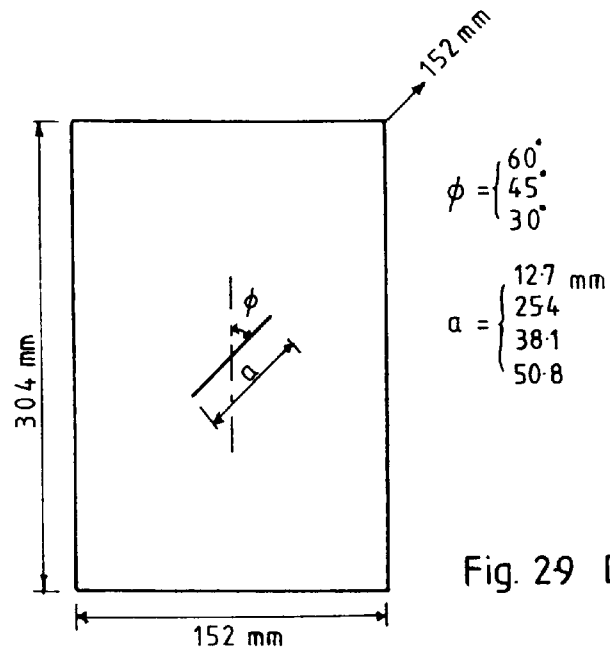


Fig. 29 Desayi's model [16]

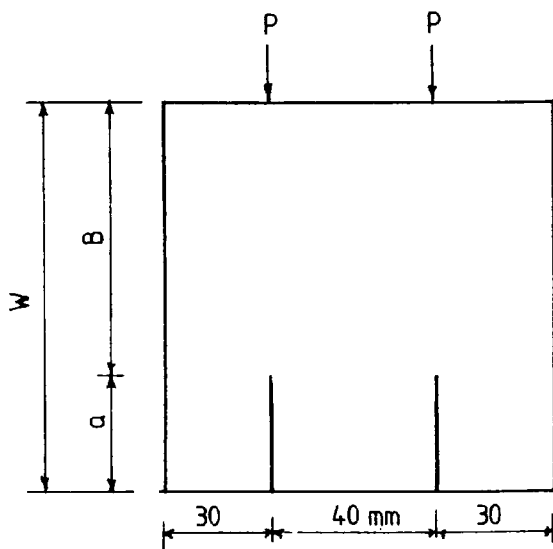


Fig. 2-10 Watkins' model [17]

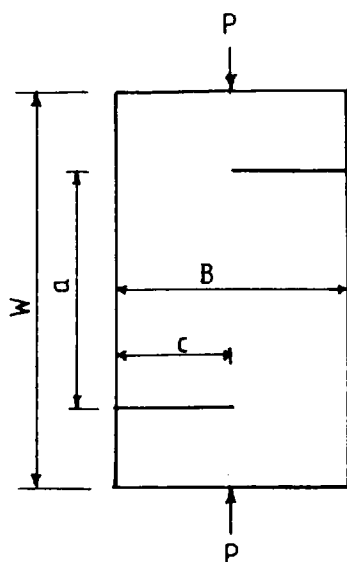


Fig. 2-11 Liu's model [20]

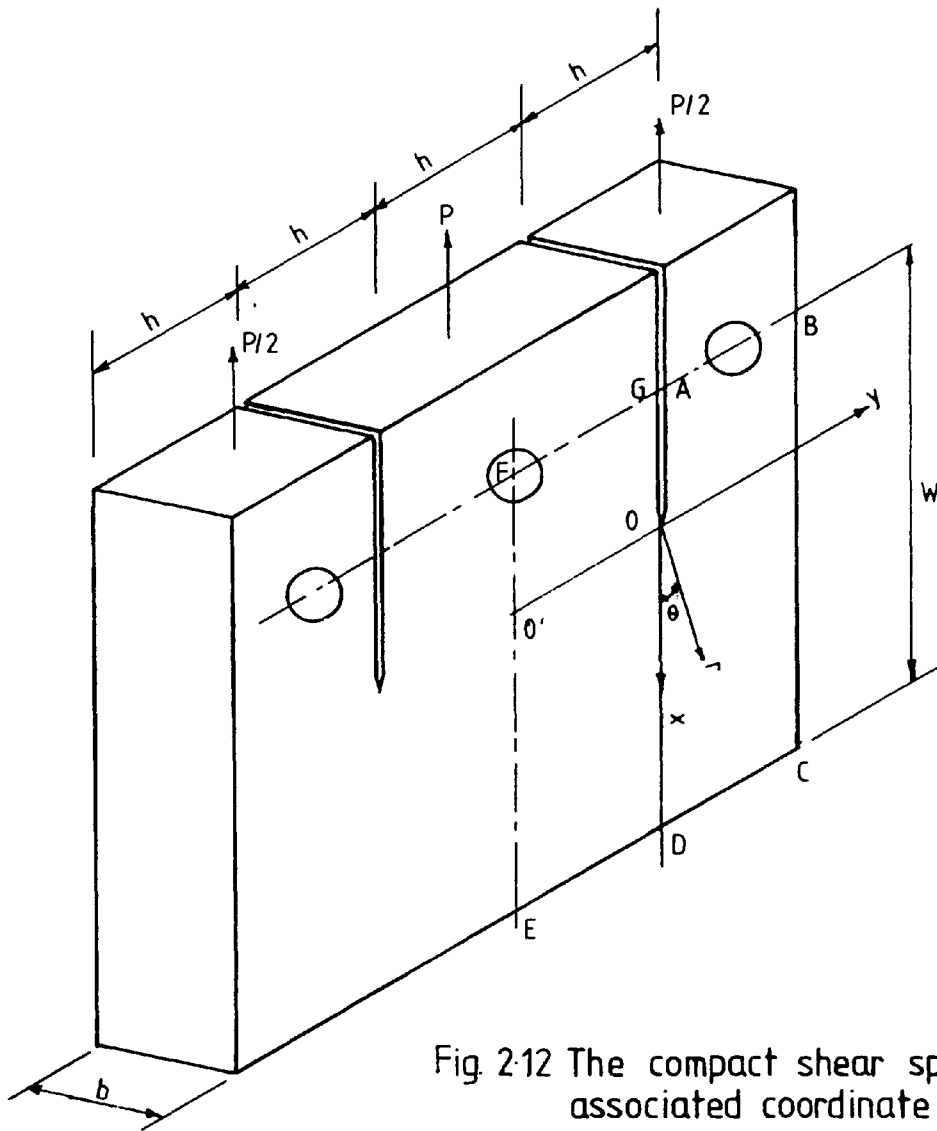


Fig. 2.12 The compact shear specimen & associated coordinate system for Mode II loading.

( Chisholm & Jones' model [19] )

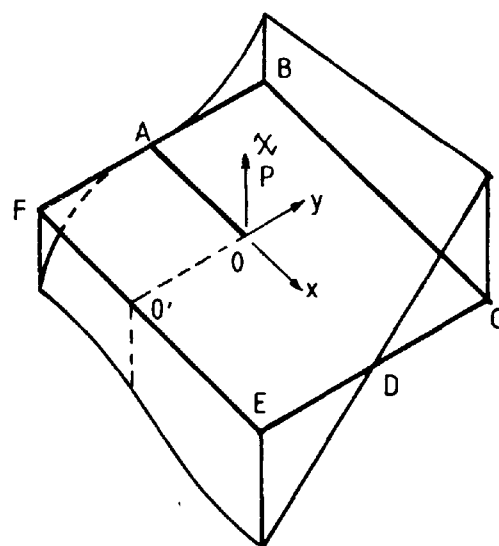


Fig. 2.13 The stress function for a bilinear stress along E-F.

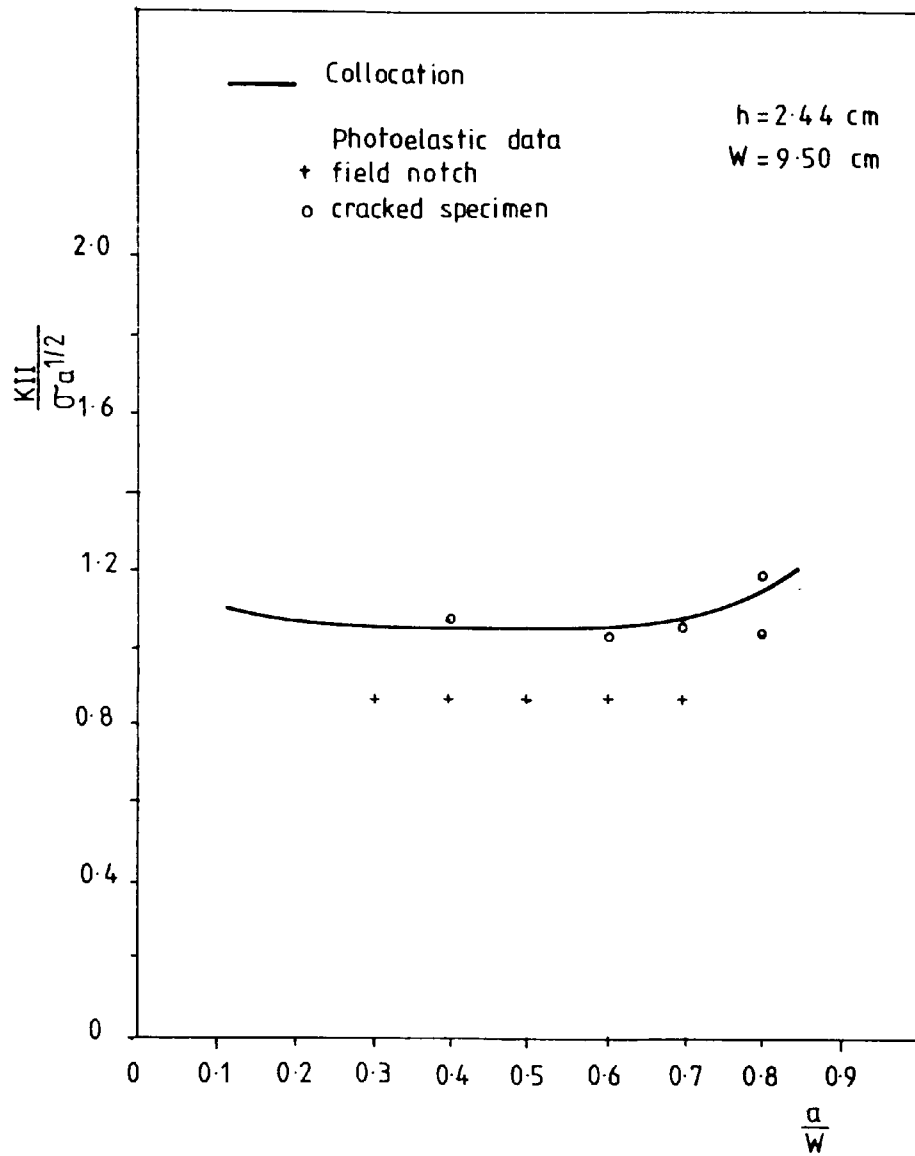


Fig. 2.14 Comparison of collocation results  
 with photoelastic data.  
 (Chisholm & Jones [17])



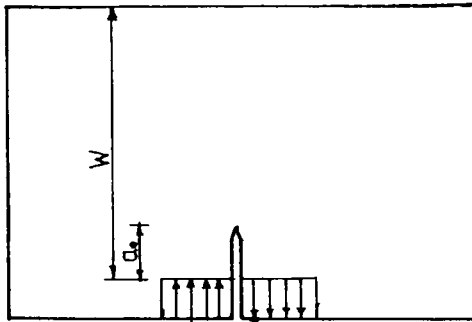


Fig. 2-15 Agarwal et al model [23]

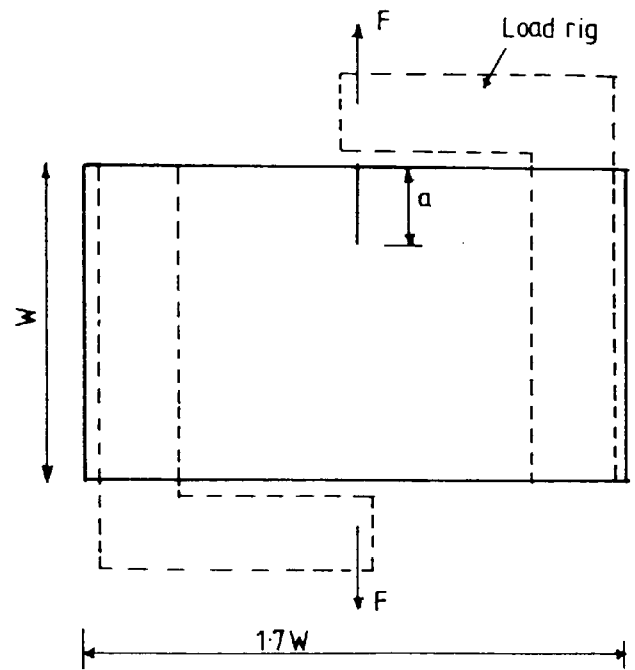


Fig. 2-16 Richard's model [24]

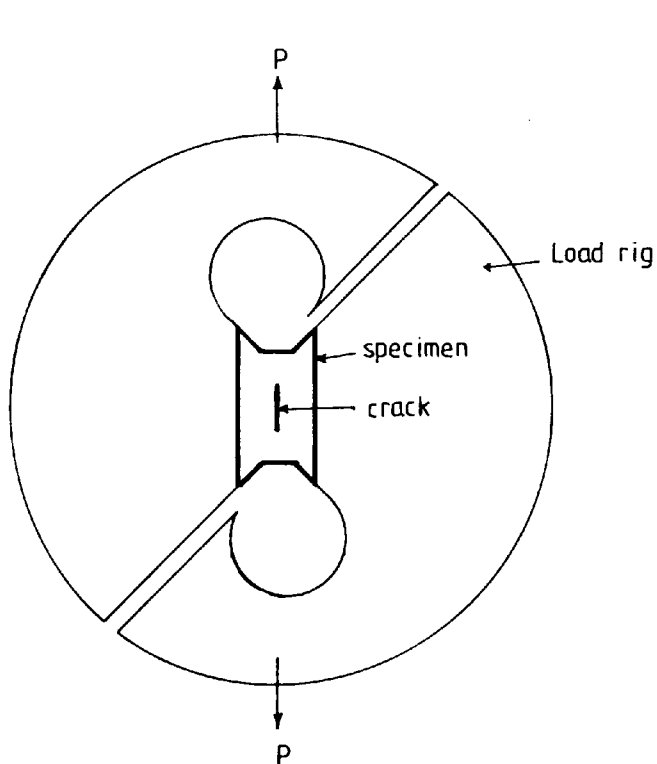


Fig. 2-17 Leslie et al model [25]

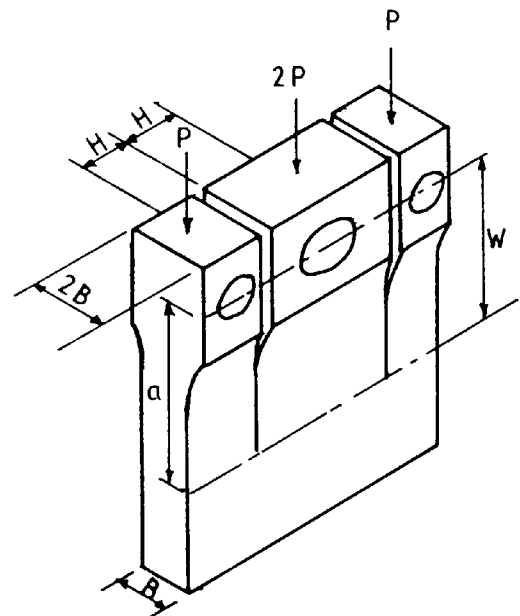


Fig. 2-18 Riddle et al model [26]

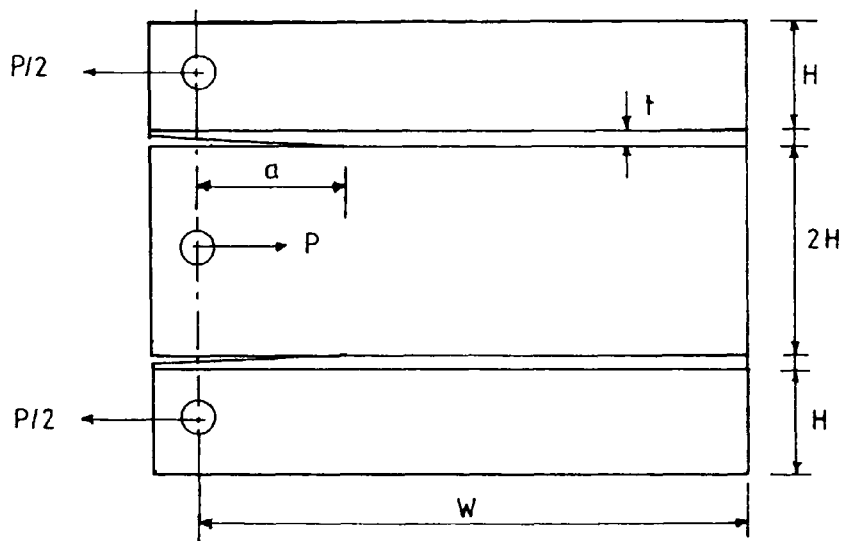


Fig. 2-19 Anandarajah model [28]

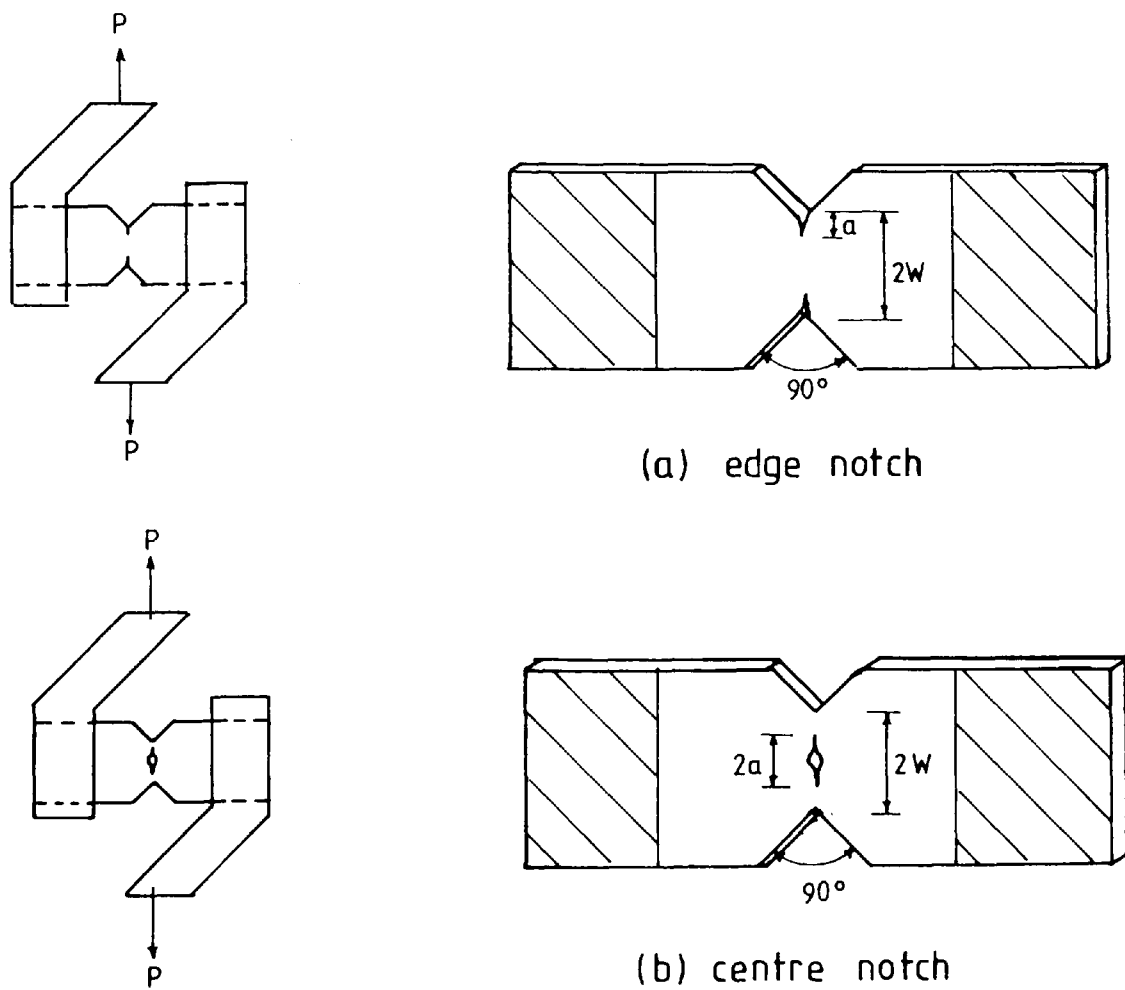


Fig. 2-20 Wang et al [29]

## CHAPTER 3

### APPLICATION OF THE FINITE ELEMENT METHOD IN LEFM

#### 3.1 INTRODUCTION

The finite element method is based on a technique of minimizing the total potential energy of an elastic body. The body is divided into a number of small elements connected at nodal points. In a plane problem, each node has two degrees of freedom, namely, the displacements in the  $x$  and  $y$  directions. The stiffness matrix for each element must be defined in terms of the strain energy, which is related to unknown displacements. Therefore it is necessary to assume a displacement function in terms of the nodal coordinates in order to construct a stiffness matrix for each element. For plane elasticity problems there are two formulations commonly in use. One is derived from a linear displacement function and the other from one of the possible forms of a quadratic function.

The coefficients of the displacement function in both cases are determined by substituting linear or quadratic functions for the nodal coordinates in terms of the variables  $x$  and  $y$ . Since there are more terms in a quadratic function, an element using this function does require more nodal points. The quadratic element, therefore, normally employs nodes at the centre of each side as well as the corner nodes. Thus a triangular element has six nodes and a quadrilateral element requires eight.

The solution process may be divided into three basic stages :

- (a) Determination of the stiffness matrix for each element.  
This matrix relates each nodal force (a vector) to the nodal displacement (also a vector) via the element stiffness matrix.
- (b) Combination of the element stiffness matrices into an overall assemblage stiffness for the complete problem.
- (c) Solution of the problem using the overall stiffness matrix to obtain unknown forces and displacements from the known boundary conditions.

### 3.2 THE FINITE ELEMENT PROGRAM

The finite element suite used in this study is PAFEC (level 5.1) (30). The program is written in FORTRAN language and is operated on a VAX 11/785 computer. The program is general purpose for solving both plane stress and plane strain problems.

The suite provides a wide range of element types to solve various kinds of structural problems. Three related quadrilateral elements together with 8 noded crack tip elements applied at the crack tip only (Figure 3.1) are employed to study the mesh size effects and general capabilities in determining the stress-intensity factors of a cracked body.

The element can be generated automatically and is operated by specifying the element types, spacings and material properties.

Facilities of the PAFEC interactive graphic suite also include comprehensive data checking, mesh correction and display of intermediate results such as distorted shape, principal stresses or vector contours etc.

The execution procedures of the program are summarised in a flow chart as shown in Figure 3.2.

### 3.3 DETERMINATION OF K FROM FINITE ELEMENT SOLUTIONS

A problem inherent in the finite element method is that the stress intensity factor  $K$  is not a direct result of the computations. Therefore the stress intensity must be indirectly deduced from the available output. The most commonly accepted method of doing this is the displacement method. The two displacement approaches demonstrated by Chan et al (8) and Woo et al (9) will be discussed here in detail.

#### 3.3.1 Chan's Displacement Method

Chan et al (8) employed the Westergaard's displacement equations to correlate the finite element nodal point displacements. Under plane strain conditions, equations (2.24) and (2.25) give Mode I and Mode II stress-intensity factors as

$$K_I = \frac{(2\pi)^{\frac{1}{2}} E}{4(1-\nu^2)} \cdot \frac{U_y}{r^{\frac{1}{2}}}$$

and

$$K_{II} = \frac{(2\pi)^{\frac{1}{2}} E}{4(1-\nu^2)} \cdot \frac{U_x}{r^{\frac{1}{2}}}$$

where  $U_x$ ,  $U_y$  are the displacements in the x and y directions respectively,  $r$  is a distance measured from a crack tip.

If the substituted displacements were the exact theoretical values then the value of the  $K^*$  obtained as  $r$  approaches zero is the exact value of  $K$ . Since the finite element displacements are rather inaccurate at an infinitesimal distance from the crack tip, this limiting process is not suitable. Instead a tangent extrapolation of the  $K^*$  curve is used to estimate the value of  $K$ .

Chan et al (8) evaluated the stress-intensity factor for a single edge-cracked plate using both the finite element method and the collocation method. The compact tension (CT) geometry is as shown in Figure 3.3 with  $a/W = 0.5$  and  $H/W = 0.6$ . The finite element curves were calculated from the displacement analysis using a fine triangular element mesh with element size  $r = 0.001a$  around the crack tip. The Williams' stress function was used in the collocation process and the comparison of both methods is shown in Figure 3.4. The element curve rapidly approaches a constant slope as  $r/a$  increases with a sudden drop near  $r/a \rightarrow 0$ . This indicates that the displacement method requires less refinement of element size at the crack tip. The best estimate of the stress-intensity factor is obtained by extrapolating the constant slope portion of the  $K_I$  curve back to the vertical axis as shown in Figure 3.4.

A convergence graph of the  $K_I$  values produced by the finite element method and the collocation method is shown in Figure 3.5. It can be seen that the agreement between the two methods is very good.

It is seen that the displacement method can produce a good estimate of  $K$  with a dense element mesh around the crack tip.

### 3.3.2 Woo's Displacement Method

The conic-section simulation model (9,10) has been used to compute the stress intensity factors directly from the finite element analysis. The method makes use of the technique of mapping the nodal displacement function. A satisfactory finite element method used to analyse the stress field near a crack tip of an elastic body should represent the  $r^{-\frac{1}{2}}$  type of elastic stress singularity. Woo et al (9) employed the conic-section simulation model of the determination of stress intensity factors using isoparametric finite element analysis with quarter point singular crack tip elements around the crack tip.

Figure 3.6 depicts a crack in a semi-infinite plate subjected to uniform tensile stress  $\sigma_0$  remote from the crack in a direction inclined at an angle  $\beta$  to that of a crack. The Mode I and Mode II stress intensity factors are given by

$$\begin{aligned} K_I &= \sigma(\pi a)^{\frac{1}{2}} \\ K_{II} &= \tau(\pi a)^{\frac{1}{2}} \end{aligned} \tag{3.1}$$

where  $\sigma$  and  $\tau$  are the stress components in the region normal to and along the crack respectively.

The cracked surface displacements under plane stress conditions were found to be

$$u_x(x,0) = -\frac{1-\nu}{E} \sigma_0 x \quad (3.2)$$

$$u_y(x,0) = \frac{2\sigma_0}{E} \left(1 - \frac{x^2}{a^2}\right)^{\frac{1}{2}} \quad (3.3)$$

Since the resultant displacements can be considered as the vectorial sum due to  $\sigma$  and  $\tau$ , equations (3.2) and (3.3) give

$$u_x(x,0) = \pm \frac{2\tau a}{E} \left(1 - \frac{x^2}{a^2}\right)^{\frac{1}{2}} - \frac{1-\nu}{E} \sigma x \quad (3.4)$$

and

$$u_y(x,0) = \frac{1-\nu}{E} \tau x \pm \frac{2\sigma a}{E} \left(1 - \frac{x^2}{a^2}\right)^{\frac{1}{2}} \quad (3.5)$$

where the second term of equation (3.5) is positive for the upper lip and negative for the lower lip.

Therefore the relative crack surface displacements are given by

$$u'_y(x,0) = \frac{1}{2} \left[ u_y(x,0)_{\text{upper}} - u_x(x,0)_{\text{lower}} \right]$$

$$u'_y(x,0) = 2 \frac{\sigma a}{E} \left(1 - \frac{x^2}{a^2}\right)^{\frac{1}{2}} \quad (3.6)$$

similarly



$$U'_x(x,0) = 2 \frac{\tau a}{E} \left(1 - \frac{x^2}{a^2}\right)^{\frac{1}{2}} \quad (3.7)$$

Substituting for  $\sigma$  and  $\tau$  from equations (3.6) and (3.7) respectively, equation (3.1) gives

$$K_I = \frac{U'_y(x,0)}{\left(1 - \frac{x^2}{a^2}\right)^{\frac{1}{2}}} \cdot \frac{E}{2a} (\pi a)^{\frac{1}{2}} \quad (3.8)$$

and

$$K_{II} = \frac{U'_x(x,0)}{\left(1 - \frac{x^2}{a^2}\right)^{\frac{1}{2}}} \cdot \frac{E}{2a} (\pi a)^{\frac{1}{2}} \quad (3.9)$$

Substitution of nodal displacements  $U'_y(x,0)$  and  $U'_x(x,0)$  into equation (3.8) and (3.9) from the finite element analysis, the stress intensity factors  $K^*$  can be obtained. From plots of  $K^*$  as a function of  $x/a$ , the estimates of the  $K$  values are then made by extrapolating the straight line portion of the  $K$  curve to  $x/a=1$ .

Woo et al (9) considered an angled edge crack in a finite plate subjected to uniform in-plane tension ( $\sigma_0$ ) as shown in Figure 3.7. A conic-section simulation model of crack surface was used in the finite element analysis. A coarse element mesh has been used and the smallest element measured at the crack tip was  $0.085a$  ( $a$  is the crack length). Both conventional isoparametric elements and distorted crack tip elements at the crack tip were employed. The geometric functions of  $P = K_I/\sigma_0(\pi a)^{\frac{1}{2}}$  and  $S = K_{II}/\sigma_0(\pi a)^{\frac{1}{2}}$  were compared with

Wilson's boundary collocation method (31). The convergence of the values of  $P$  and  $S$  are shown in Figure 3.8.

The accuracy of the values of  $P$  and  $S$  determined by the conic-section method with crack tip elements at the crack tip are within 5% and 9% respectively of the results reported by Wilson. The corresponding values obtained by the conventional isoparametric elements are within 6% and 16% of the Wilson results. This indicates that the conic-section simulation model can produce better estimates of  $K_I$  and  $K_{II}$  values with crack tip elements at the crack tip when a considerably coarser mesh is used.

It is seen that Chan et al (8) used a fine linear element mesh in a region near the crack tip. The linear dimensions of the elements were in the order of 0.001 of the crack length. It is expensive in computer time and data preparation effort to use such refined meshes. Woo et al (9) used a coarse 8-noded quadrilateral element mesh together with distorted crack tip elements at the crack tip. The smallest element used at the crack tip were in the order of 0.085 of the crack length.

It can be concluded that the Woo's method is better than the Chan's method because a coarse element mesh with crack tip elements around the crack tip can save computer time and represent the elastic stress singularity.

Since the Woo's method was not made available when this project was started, Chan's method was adopted to analyse the 100mm double-

notched cubes under compact shear loading. Subsequently the 100mm single-notched and 150mm double-notched cubes were analysed by using the Woo's method of the finite element analysis.

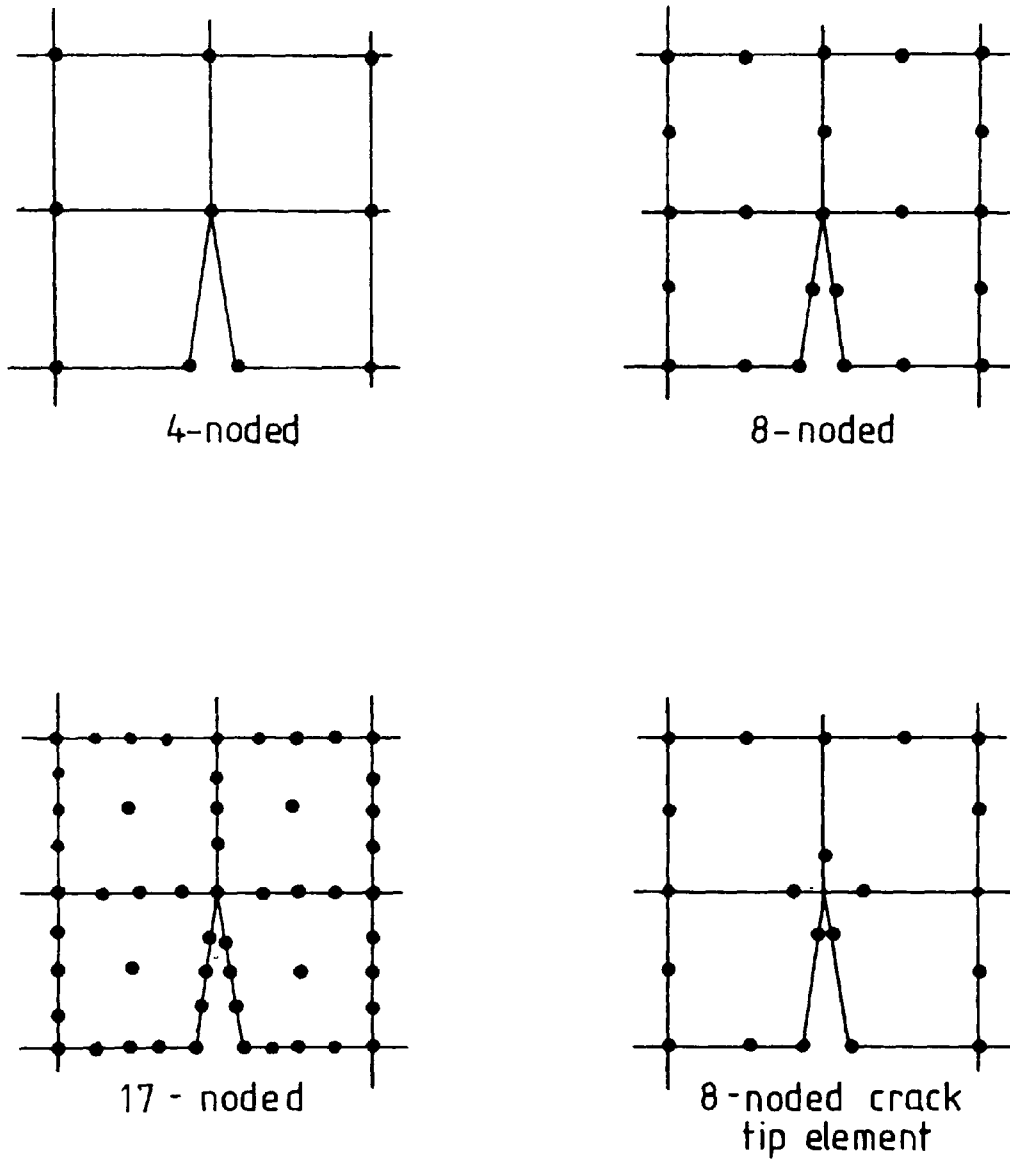


Fig. 3-1 Types of quadrilateral finite element

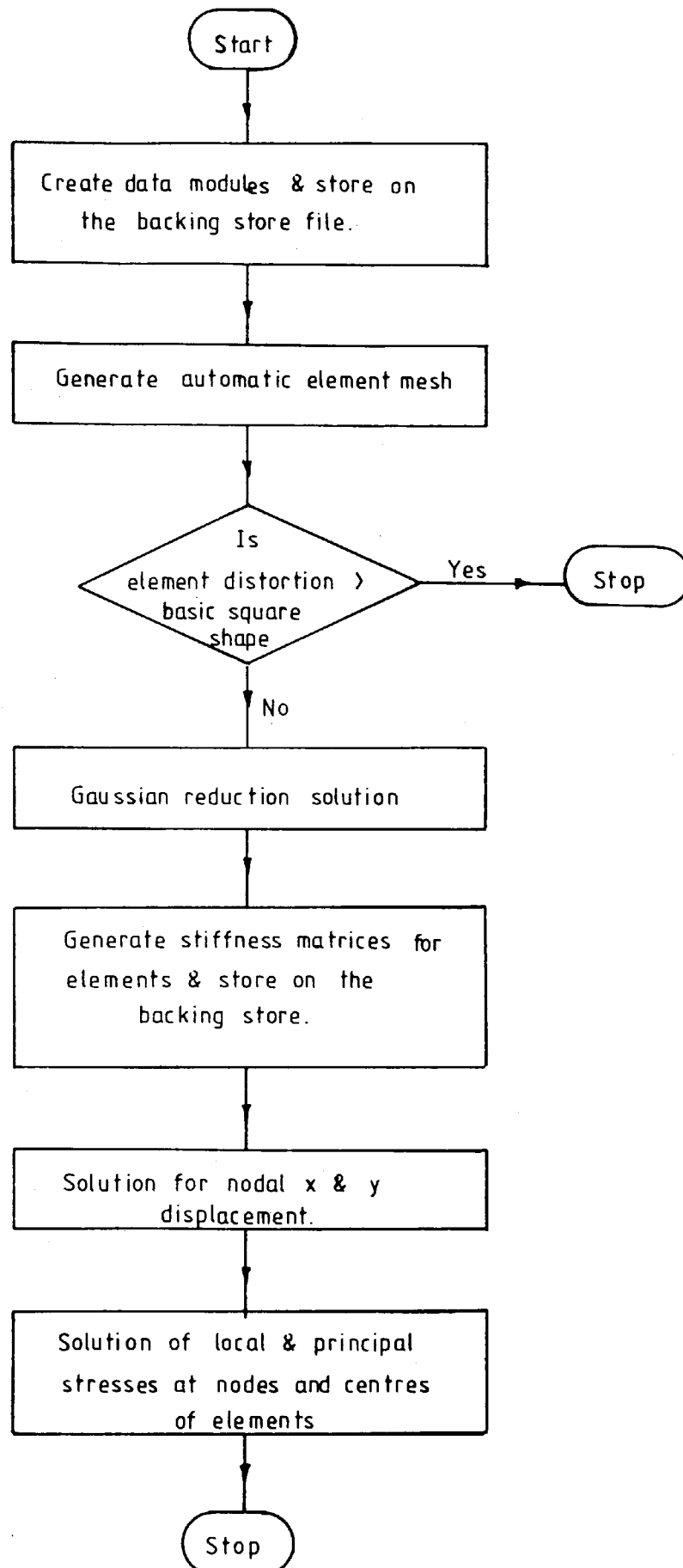


Fig. 3:2 The execution procedures of the PAFEC program

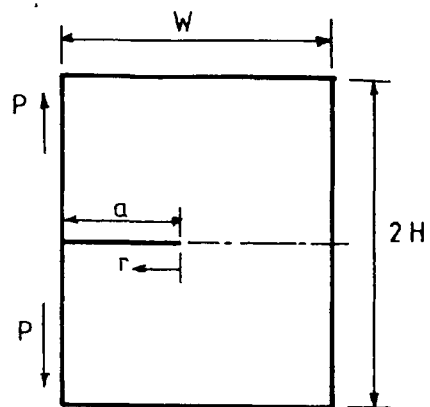


Fig. 3-3 CT geometry  $a/W=0.5$ ,  $H/W=0.6$

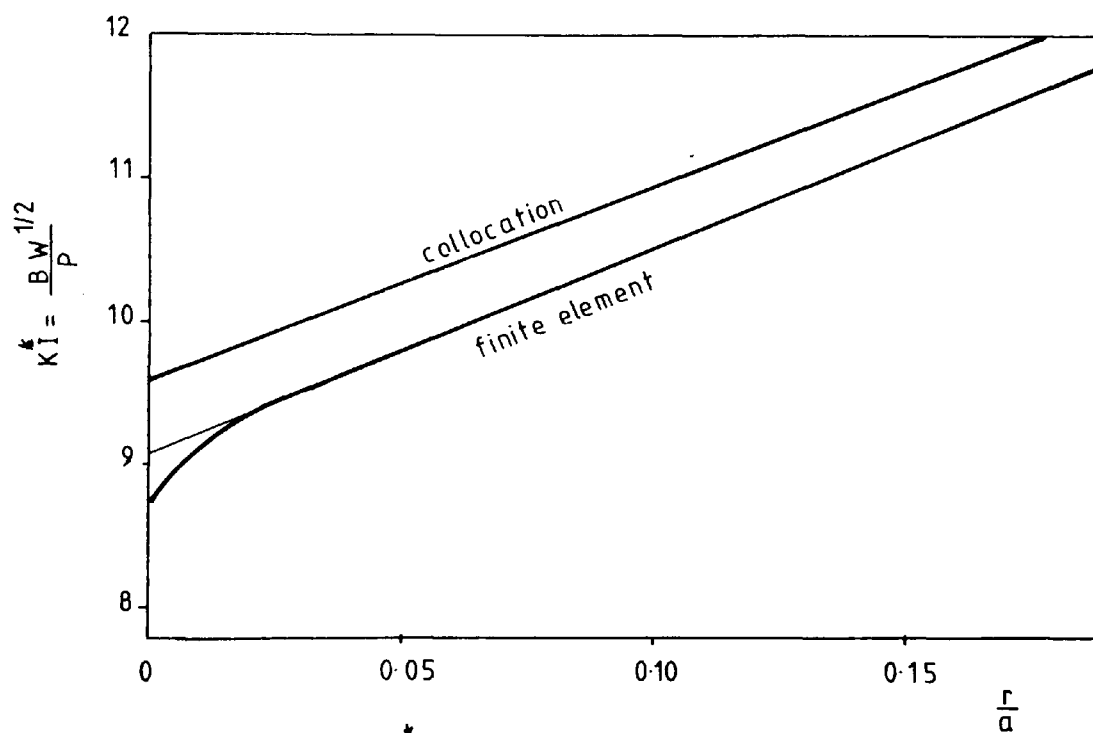


Fig. 3-4  $KI^*$  for displacement method.

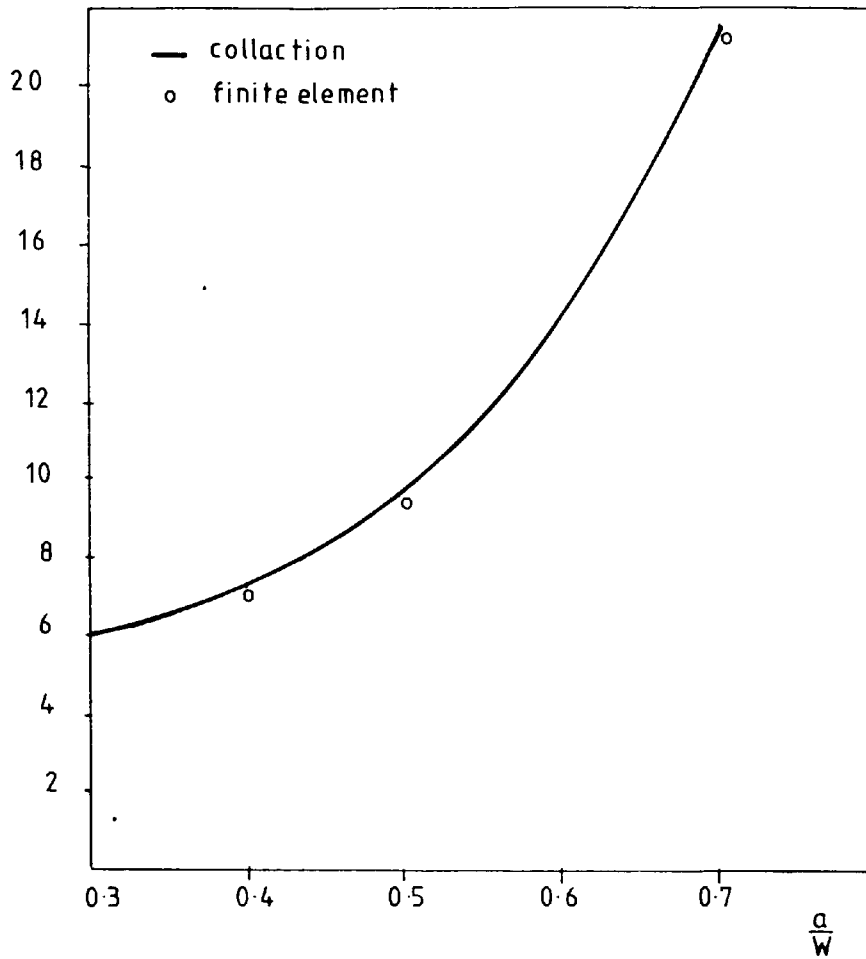


Fig. 3.5 Comparison of results of collocation and finite element solutions.

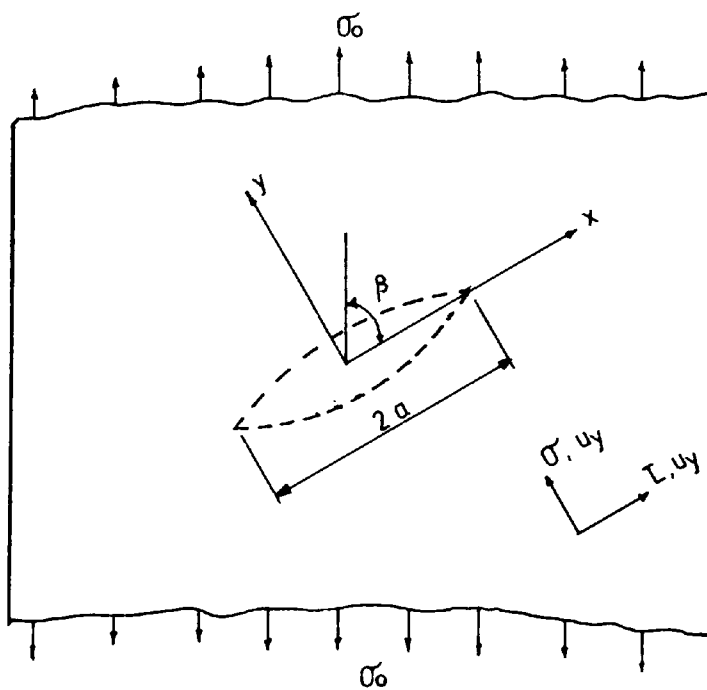


Fig. 3.6 Conic-section representation of a crack in combined opening & sliding modes.

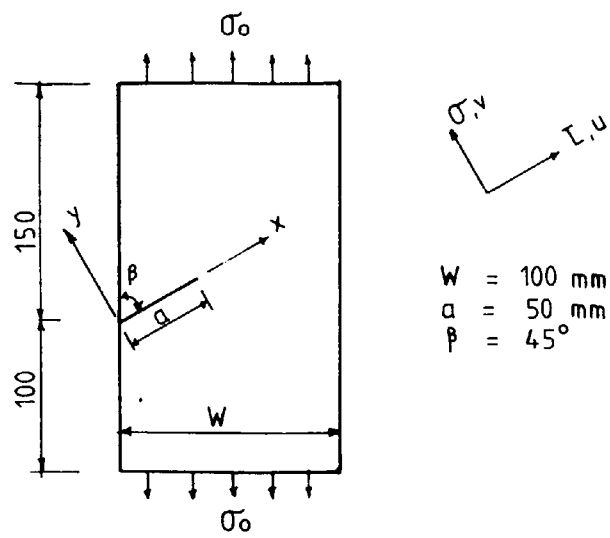


Fig. 3-7 An angled edge crack subjected to uniaxial tension.

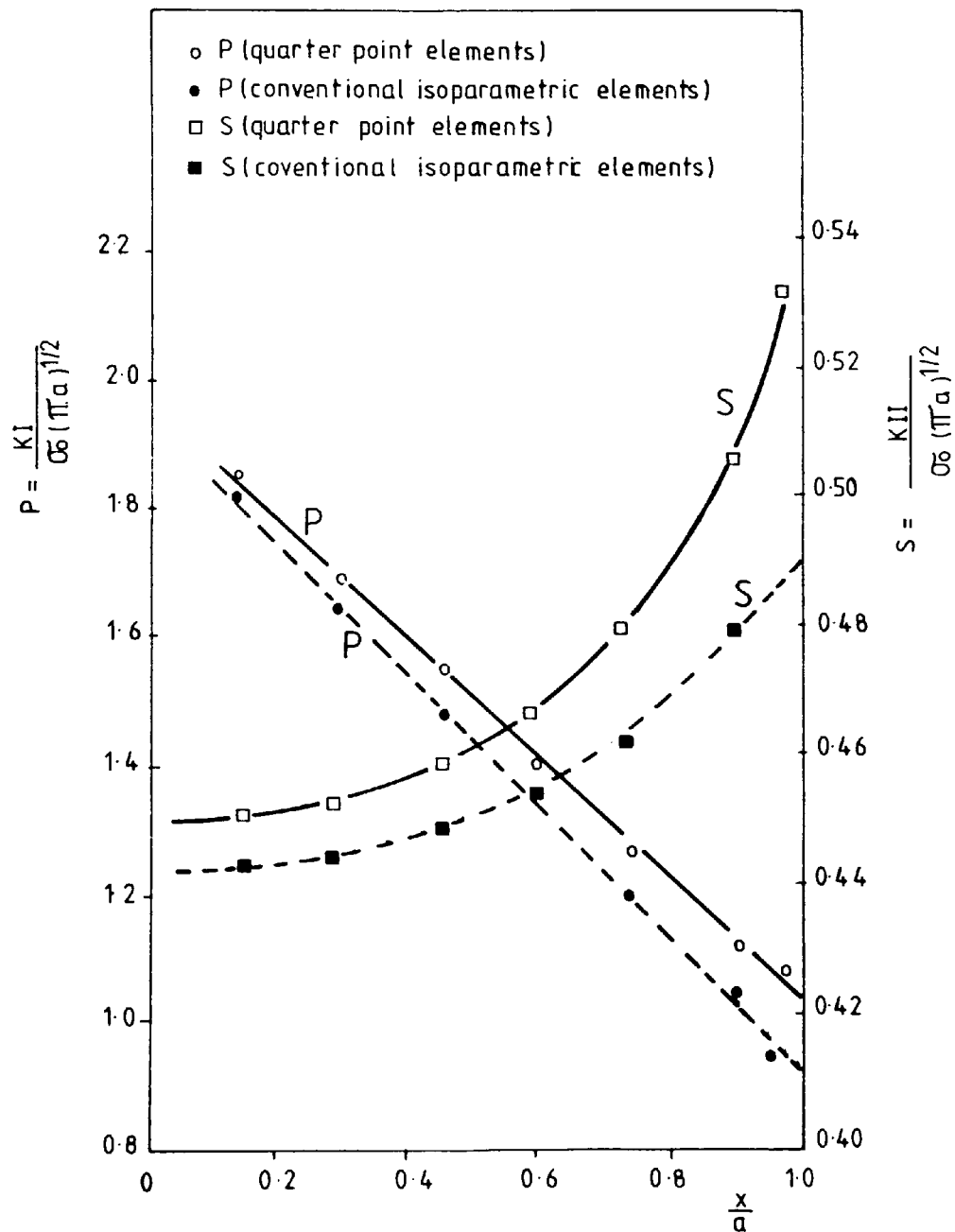


Fig. 3-8 Finite plate containing an angled edge crack and subjected to uniaxial tension.



## CHAPTER 4

### MATHEMATICAL MODELLING FOR 100mm CS SPECIMENS

#### USING PAFEC FINITE ELEMENT PROGRAM

##### 4.1 INTRODUCTION

Numerical analyses were made to study the possible Mode II type of fracture failure for the compact shear (CS) cubes. They were 100mm double-notched, 100mm single-notched and 150mm double-notched cubes. Since these cubes were made up of different notch spacing and depth, it was decided to establish a general model which can accommodate different geometrical shape as well as fulfilling the load and boundary conditions.

Chan's displacement approach (equation (2.25)) of the finite element method was chosen for the initial modelling of a 100mm double-notched cube. Instead of using a fine triangular element mesh around the crack tip area, a coarse quadrilateral isoparametric element was used. The analysis includes modelling the cube mathematically to study the stress profiles along the line of action of the load and to compare the Mode I and Mode II stress intensity factors under the shear loading conditions. Comparison was also made to study the accuracy of the boundary collocation and the two displacement approaches of the finite element methods used in determining the Mode II stress intensity factors.

In the modelling of 100mm single-notched, and 150mm double-notched cubes, Woo's displacement approach (equation (3.9)) was used. Since a coarse quadrilateral isoparametric element mesh with crack tip elements around the crack tip is recommended, it is of interest to verify it on the notched cubes. The analyses include the convergence study of element mesh size, the comparison of the Mode I and Mode II stress intensity factors and the determination of the calibration coefficients.

#### 4.2 FINITE ELEMENT MODELLING FOR 100mm DOUBLE-NOTCHED CUBES

The compact shear cubes have three basic geometries with notch spacing  $H = 50$ ,  $40$  and  $30\text{mm}$  as shown in Figure 4.1. Each geometry has eight variations by changing the crack length "a" from  $a = 25\text{mm}$  to  $60\text{mm}$  in  $5\text{mm}$  increments.

A general model was first established by considering a cube (of  $H/W = 0.5$ ,  $a/w = 0.35$ ) which was loaded by a compressive force of  $1000\text{N}$  at the centre of the top surface as shown in Figure 4.2(a). The cube is symmetrical about the centre line and a simplified geometry can thus be obtained by considering one half of the specimen as shown in Figure 4.2(b). The line of symmetry (or centre line) was modelled by a series of rollers so that vertical displacements only were allowed to take place. Vertical restraints were provided at the support thus assuring the shearing displacements at the crack tip required for Mode II fracture.

Initial analysis showed that the top free surface moved horizontally towards the crack while the support moved horizontally away from the crack thus producing a three-point bending as shown in Figure 4.2(c). This was not acceptable under the shear loading conditions and horizontal restraints were provided at the top and bottom corners of the cube as shown in Figure 4.2(d) to prevent the overlapping of the crack surfaces. This proved satisfactory (Figure 4.2(e)).

There are two main element geometries in two dimensional finite element analysis, triangular and quadrilateral. The simplest three noded triangular element, which has the lowest order of polynomial function is a constant strain triangle as the strains can be proved to be constant at every point within the element. The quadrilateral isoparametric element is one whose boundary surfaces are defined by polynomials of the same degree as their displacement expansion. The elements can be linear, quadratic, cubic or even higher order type. These higher order elements which possess linear, quadratic and cubic strain within the element respectively, can produce a more accurate result than the 3 noded constant strain triangular element. As a comparison of the element type, the number of constant strain triangular elements needed to give the same accuracy as the quadrilateral isoparametric element are listed in Table 4.1.

Various types of the quadrilateral isoparametric elements were used and comparison of their capabilities in analysing a cracked body was made. The types of quadrilateral isoparametric elements used in this study were :

- (a) The linear element (Figure 4.3(a)) with only four nodal points.
- (b) The quartic element (Figure 4.3(b)) with seventeen nodes, four corner nodes, three nodes are along each edge of the element and one node is located at the centre of the element.
- (c) The quadratic element (Figure 4.3(c)) with eight nodes, four corner nodes and four mid-side nodes.
- (d) The quarter-point (or special crack tip) element (Figure 4.3(d)) with eight nodes. This element can represent a crack tip singularity of  $r^{-\frac{1}{2}}$  of the strain field at the crack tip. The singularity in this element is achieved by placing the mid-side nodes near the crack tip at the quarter point.

For an initial model, a coarse mesh with sixty elements was assembled on a half cube using the above elements and the Mode II stress intensity factors were calculated for each model. Chan's displacement equations (2.25) as described in Chapter 3 were used to estimate the values of stress intensity factors. The result of this study is tabulated in Table 4.2.

It shows that the highest  $K_{II}$  value is obtained by using 17-noded elements and the crack tip elements (used at the crack tip only) yields a  $K_{II}$  value which is 0.5% less than the highest  $K_{II}$  obtained. The lowest  $K_{II}$  value is 6% smaller than the maximum value obtained using the 4 noded elements. Although 17 nodal elements can produce a higher  $K_{II}$  value, they do not possess the

crack tip singularity of  $r^{-\frac{1}{2}}$  of the strain field at the crack tip. The result of the  $K_{II}$  values are practically the same for both 17 noded elements and crack tip elements (used at the crack tip only). The 17 noded elements have about 2.5 times more degrees of freedom than the crack tip elements and this means 17 noded elements use more computer time and storage space.

It can be concluded that higher order elements are not necessarily best. The crack tip elements, (used at the crack tip only) which can represent the elastic crack tip singularity while using considerably less computer time are far more preferable in analysing cracked problems. The crack tip elements used at the crack tip only together with the 8 noded quadrilateral isoparametric elements were chosen for all finite element analysis in this project.

#### 4.2.1 A Convergence Study of Element-mesh Size

A convergence study of element mesh size was carried out on seven mesh-geometries as shown in Figure 4.4. The smallest size of an element used at the crack tip was about  $0.1a$  for 48, 60, 72 and 102 element-meshes and about  $0.07a$  for 144, 168 and 200 element-meshes respectively. Both 8-noded quadrilateral isoparametric and distorted elements (at the crack tip only) were used in this analysis. Initially, only 8-noded quadrilateral elements were used on all the element meshes. Secondly, the elements around the crack tip were replaced by the distorted elements. The  $K_{II}$  values were calculated from the vertical displacements on the crack surface using Chan's displacement equation (2.25).

Figure 4.5 shows a typical plot of  $K_{II}$  as a function of  $r/a$  for the 60 element-mesh with distorted elements around the crack tip. An estimate of  $K_{II}$  was obtained by extrapolating the straight line back to the vertical axis. Results of this study are shown in Table 4.3.

It can be seen from Table 4.3 that the element meshes which contain distorted elements at the crack tip show a quicker convergence than those with quadrilateral isoparametric elements only. Figure 4.6 shows a convergence graph for both undistorted and distorted elements (at the crack tip only) meshes. It is observed that when using as few as 60 elements (with distorted elements at the crack tip) there is only a difference of 1.0% in the  $K_{II}$  value when compared to the results from 144 elements.

It can be concluded that using a coarse mesh of 60 quadrilateral isoparametric elements (with distorted elements at the crack tip) is sufficiently accurate for the fracture analyses in mind.

#### 4.2.2 Stress Analysis of the Specimen

The boundary conditions for the CS cube (Figure 4.2(d)) has been shown to be satisfactory in producing vertical displacements along the crack surface required by the Mode II displacement condition. Further analysis has been carried out to confirm the dominance of a Mode II failure by studying the stress distribution along the line of action of the load for  $a/w = 0.3, 0.35, 0.40$  and  $0.45$  respectively.

For this a finite element analysis was carried out for each notch ratio using 8-noded quadrilateral isoparametric elements on a mesh of 200 elements as shown in Figure 4.4h. The smallest elements used around the crack tip were  $0.07a$ .

Numerical values of the nodal direct stresses  $\sigma_x$  and shear stresses  $\tau_{xy}$  along the line of action of the load obtained by this finite element analysis are illustrated in Table 4.4. The compressive stresses are represented by those with negative signs.

The direct and shear stress profiles plotted along the line of action of the load are shown in Figure 4.7. The magnitude of the stresses are shown on the horizontal axis and the crack surface is represented by the vertical axis. Clockwise shear stresses and direct stresses are shown positive.

A typical profile of the direct stress  $\sigma_x$  of  $a/W = 0.35$  shows that a maximum direct compressive stress of  $20.7\text{kN/m}^2$  is reached at the very tip of the top notch. This decreases sharply and reaches zero at a distance about half way between the two crack tips. The direct stress subsequently changes from a compressive to a tensile state and reaches a maximum of  $19.9\text{kN/m}^2$  at a point which is very close to the bottom of the crack tip. This high tensile stress zone at the tip of the bottom notch indicates that a tensile crack is likely to occur. The direct stress profile indicates that bending takes place at the tips of the top and bottom notches so that crack closing and opening occurs at the tips of the top and bottom notches respectively. (Table 4.4).

The profile of the shear stress  $\tau_{xy}$  of  $a/W = 0.35$  shows a maximum value of  $23.3\text{kN/m}^2$  at the tip of the top notch. Again this drops sharply when measured away from the top notch. At a distance where the direct stress reaches zero the shear stress levels out at  $5.6\text{kN/m}^2$ . It then increases sharply as it approaches the tip of the bottom notch until it reaches a maximum value of  $27.4\text{kN/m}^2$ . The shear stress profile shows high shear stresses occur at the tips of the top and bottom notches, thus encourages shear failure to take place.

Figure 4.7 also shows that similar direct stress and shear stress profiles are obtained for other notch ratio (i.e.  $a/W = 0.3$ ,  $0.4$  and  $0.45$ ). It can be seen that both the compressive stress and shear stress at the top notch increase with increasing notch depth. The tensile stress and shear stress at the bottom notch also increase with increasing notch depth, but they discontinue in the range  $0.35 \leq \frac{a}{W} \leq 0.4$ . This can be explained that a refinement of the element mesh at the bottom crack tip may be necessary in order to get more accurate stress results when the crack depth increases.

To summarise, when the CS cube is loaded bending takes place at the tips of the top and bottom notches. High compressive bending stresses at the tip of the top notch occur thus producing a crack closing action (Table 4.4). Subsequently a maximum shear stress is produced and plane sliding is encouraged along the line of action of the load. Mid-way between the two crack tips (i.e. at the neutral axis of the bending plane), the bending stress is zero and the shear



stress levels out. At the tip of the bottom notch bending again takes place and produces a crack opening action. Because of the horizontal restraints provided at the bottom corner of the cube, this opening action at the crack tip is stopped and changed into a hinge-effect. This effect pushes the crack surfaces to overlap each other and an apparent new crack tip is produced (Table 4.4). This explains why the maximum tensile bending stress and shear stress takes place not at the bottom crack tip but at an element size away from the crack tip. This high tensile stress zone indicates that a tensile crack may occur at the tip of the bottom notch but complete bending cannot take place due to the horizontal restraint at the bottom corners of the cube. Because of the high shear stress zones occur at both tips of the top and bottom notches, plane sliding or shear failure is likely to take place along the plane of the two vertical notches.

#### 4.2.3 Comparison of the Mode I and Mode II Stress Intensity

For  $H/W = 0.5$  ,  $0.4$  and  $0.3$

In order to investigate whether the Mode II type of failure is predominant under the CS loading conditions, both Mode I and Mode II stress intensity factors were calculated and compared. The cubes have three basic geometries with notch spacings  $H = 50$  ,  $40$  and  $30\text{mm}$  . Each geometry has eight variations by changing the crack length  $a = 25\text{mm}$  to  $a = 60\text{mm}$  in  $5\text{mm}$  increments. A constant 60 element mesh with distorted elements at the crack tip was used for all the finite element analyses. The smallest element size used at

the crack tip was  $0.2a$ ,  $0.167a$ ,  $0.14a$ ,  $0.125a$ ,  $0.111a$ ,  $0.1a$ ,  $0.09a$  and  $0.083a$  for the crack length changing from  $a = 25\text{mm}$  to  $a = 60\text{mm}$  in  $5\text{mm}$  increments respectively. Eight computer runs were made for each notch spacing  $H$  and a total of 24 computer runs were carried out. From each computer output the vertical and horizontal displacements along the crack  $U_y$ ,  $U_x$  were substituted into Chan's displacement equations (2.24) and (2.25) and the Mode I and Mode II stress intensity factors were evaluated. Figure 4.8 shows typical plots of  $K_{II}$  against  $r/a$  for  $H = 50$ ,  $40$  and  $30\text{mm}$  respectively with  $a/w = 0.35$ . The  $K_{II}$  estimates were obtained by extrapolating the straight line of the curve back to the  $K_{II}$  axis. Table 4.5 shows the  $K_I$  and  $K_{II}$  estimates and  $K_{II}/K_I$  ratios for various  $a/W$  and  $H/W$  values. The variations of  $K_{II}$  and  $K_{II}/K_I$  with  $a/W$  are expressed in graphical forms as shown in Figures 4.9 and 4.10 respectively.

Using the 60 element-mesh Figure 4.9 shows all three  $K_{II}$  values increase linearly with increasing  $a/W$  values in the range  $0.25 \leq a/w \leq 0.45$  and discontinue beyond  $a/w = 0.45$ .

Figure 4.10 shows the comparison of the  $K_{II}/K_I$  ratios for  $H = 50$ ,  $40$  and  $30\text{mm}$  with  $a/W$  ratios. All three  $K_{II}/K_I$  plots increase up to the range  $0.25 < a/W < 0.45$ , and beyond  $a/w = 0.45$  the sudden discontinuity occurred.

The discontinuity of the curves beyond  $a/W = 0.45$  was caused by inadequate element mesh near the crack tip. The re-arrangement of the element mesh was therefore made for crack length larger than

45mm as shown in Figure 4.9 and the corrected  $K_I$  and  $K_{II}$  values were obtained. The corrected results are tabulated in Table 4.6 and plotted in Figures 4.9 and 4.10. It can be seen that the  $K_{II}$  and  $K_{II}/K_I$  plots have improved. It is important to note that a cube with a smaller notch spacing  $H/W$  and higher  $a/W$  produces higher  $K_{II}/K_I$  ratios.

It can be concluded that the Mode II stress intensity factors are many times higher than the Mode I for a small notch spacing ratio  $H/W$ . (e.g.  $K_{II}/K_I = 124$  for  $H/W = 0.3$ ,  $a/W = 0.6$ ). This indicates that the Mode II type of failure is improving by reducing the notch spacing  $H$ .

#### 4.2.4 Determination of the Calibration Coefficients

##### of the Mode II Stress Intensity Factors for $H/W = 0.5$ , 0.4 and 0.3

In this section numerical work was carried out to determine the Mode II calibration coefficients for the 100mm CS cubes with a notch spacing  $H = 50$ , 40 and 30mm respectively.

The Mode II stress intensity factors for a finite plate is

$$K_{II} = Y\left(\frac{a}{W}\right) K_{II\infty} \quad (4.1)$$

where  $Y(a/W)$  is the calibration coefficient which depends upon the ratio of crack length to specimen width ( $a/W$ ),  $K_{II\infty}$ , the Mode II stress intensity factor for an infinite plate is

$$K_{II\infty} = \tau_{\infty} (\pi a)^{\frac{1}{2}} \quad (4.2)$$

where "a" is the crack length and the shear stress in an infinite plate is

$$\tau_{\infty} = \frac{P}{BW} \quad (4.3)$$

where "P" is the applied load as shown in Figure 4.1.

By substituting equation (4.2) into equation (4.1) it becomes

$$K_{II} = Y\left(\frac{a}{W}\right) \tau_{\infty} (\pi a)^{\frac{1}{2}} \quad (4.4)$$

and by substituting equation (4.3) into equation (4.4) it becomes

$$K_{II} = Y\left(\frac{a}{W}\right) \frac{P}{BW} (\pi a)^{\frac{1}{2}} \quad (4.5)$$

Re-arranging equation (4.1), it can be shown that the calibration coefficient is

$$Y\left(\frac{a}{W}\right) = \frac{K_{II}}{K_{II\infty}} \quad (4.6)$$

The Mode II stress intensity factors  $K_{II}$  obtained in previous sections were substituted into equation (4.6) in order to determine the calibration coefficients. These are tabulated in Table 4.7 for various ratios of  $a/W$  and  $H = 50, 40$  and  $30\text{mm}$  respectively. An empirical relation between the  $Y(a/W)$  values and the  $a/W$  ratios

was obtained using a least square method. Best fit curves are obtained for  $Y(a/W)$  values when  $0.25 \leq a/W \leq 0.60$  and equations of  $Y(a/W)$  expressed in polynomials of powers  $a/W$  as shown in Table 4.8.

The calibration coefficients for  $H = 50, 40$  and  $30\text{mm}$  are shown graphically in Figure 4.11. It is seen that the values of  $Y(a/W)$  for all three notch spacings are almost independent of crack length when  $0.30 \leq a/W \leq 0.45$ . The calibration coefficient for notch spacing is therefore reduced to a single value as shown in Table 4.8.

The Mode II stress intensity factors for the specific geometries were obtained by substituting the calibration coefficients into equation (4.4).

$$K_{II} = Y(a/W) \tau (\pi a)^{\frac{1}{2}} \quad (4.7)$$

The corresponding Mode II stress intensity factors are summarised in Table 4.8, they are

$$H=50\text{mm} \quad K_{II} = 1.19 \frac{P}{BW} (\pi a)^{\frac{1}{2}} \quad (4.8)$$

$$H=40\text{mm} \quad K_{II} = 1.02 \frac{P}{BW} (\pi a)^{\frac{1}{2}} \quad (4.9)$$

$$H=30\text{mm} \quad K_{II} = 0.89 \frac{P}{BW} (\pi a)^{\frac{1}{2}} \quad (4.10)$$

#### 4.2.5 Comparison of the Boundary Collocation Method to the Finite Element Methods

The capability of the displacement finite element method used by Chan et al (8) and Woo et al (9) as described in Chapters 2 and 3 respectively were compared by analysing a notched cube of  $H/W = 0.5$  under a load of 1000N as shown in Figure 4.12(a). Since there was no exact solution to compare the results, the expression derived by Chisholm and Jones (19) was used as a collocation process. Equation (2.41) gives the Mode II stress intensity factor for a compact shear specimen as

$$K_{II} = \frac{PW^{\frac{1}{2}}}{bh} \left(\frac{a}{W}\right)^{\frac{1}{2}}$$

The notation is illustrated in Figure 4.12(b).

The corresponding values of  $K_{II}$  were obtained by substituting various ratios of  $a/W$  into equation (2.43). Subsequently, the calibration coefficients  $Y(a/W)$  were obtained by using equation (4.6) as illustrated in Table 4.9. The finite element analysis for a cracked body from Chan's method (eq. (2.25)) gives

$$K_{II} = \frac{(2\pi)^{\frac{1}{2}} E}{4(1-\nu^2)} \cdot \frac{U_x}{r^{\frac{1}{2}}}$$

The notation is illustrated in Figure 4.12(c).

For the two finite element analyses, a constant mesh of sixty 8-noded quadrilateral isoparametric elements with crack tip elements at the crack tip was used. The smallest element used at the crack tip

was 0.2, 0.167, 0.14, 0.125, 0.111, 0.1, 0.09 and 0.083 of the crack length  $a = 25, 30, 35, 40, 45, 50, 55$  and  $60\text{mm}$  respectively. The  $K_{II}$  estimates and the calibration coefficients  $Y(a/W)$  obtained by Chisholm and Jones' method, Chan's method and Woo's method are tabulated in Tables 4.9 and 4.10 respectively. Results of  $K_{II}$  and  $Y(a/W)$  are shown graphically in Figures 4.13 and 4.14 respectively. Figure 4.13 shows that the  $K_{II}$  values obtained by the finite element methods are of similar values to those obtained by the boundary collocation method. Figure 4.14 shows the three calibration coefficient plots.

The  $Y(a/W)$  values obtained by the finite element methods using Chan's and Woo's approach are about 6% and 4% larger respectively than the collocative value and there is only 4% difference between the two finite element methods when  $0.3 \leq a/W \leq 0.45$ . Woo's finite element method appears to be more desirable in this analysis because (a) it has been shown that relatively coarse mesh could be used to obtain reasonably accurate results by using the elliptical displacement function and (b) the crack tip singularity is modelled by using distorted elements at the crack tip.

#### 4.2.6 Conclusions

The 100mm compact shear cube with a pair of double notches at the top and bottom faces was modelled. Because of symmetry about the centre line, only one half of the cube was analysed. The centre line of the cube was replaced by a series of rollers and horizontal restraints were provided at the top and bottom corners of the cube.

In the finite element analysis, four element types have been studied for the half cube of notch spacing  $H = 50\text{mm}$  and notch depth  $a = 35\text{mm}$ . They were 4-noded, 8-noded, 17-noded elements and distorted elements used at the crack tip together with the 8-noded elements. It was found that distorted elements (used at the crack tip only) were more preferable than other elements in analysing crack problems because they can represent the crack tip singularity of  $r^{-\frac{1}{2}}$  of the strain field (by moving their mid-side nodes to the quarter point positions), they also use less computer time.

Seven element meshes were constructed for a convergence study of element mesh for the half cube (because of symmetry one half of the cube was used) and the total number of elements used varied from 48 to 200. Two combinations of element types were used. Initially 8-noded quadrilateral isoparametric elements were used on the meshes and secondly distorted elements were used at the crack tip. In both cases, the  $K_{II}$  values converge with 144 elements. It seems reasonable to use the 60 element mesh when compared with the 144 element mesh because (a) it is economical to use less elements and (b) it is sufficiently accurate when the difference in the  $K_{II}$  value is only 1.0%.

Analysis was carried out to study the stress distribution along the line of action of the load under the CS load condition. The maximum direct compressive stress ( $\sigma = 20.7 \text{ KN/m}^2$ ) is obtained at



the top notch, the stress decreases to zero half way between the notches and reaches a maximum in tension ( $\sigma = 19.9 \text{ kN/m}^2$ ) at the bottom notch. This tensile stress zone at the tip of the bottom notch indicates that a tensile crack is likely to occur. The shear stress reaches a maximum of  $\tau = 23.3 \text{ kN/m}^2$  at the top notch and reduces to a minimum  $\tau = 5.6 \text{ kN/m}^2$  mid-way between the notches before reaching another maximum  $\tau = 27.4 \text{ kN/m}^2$  at the bottom notch. The high tensile stress and shear stress at the tip of the bottom notch indicate that fracture is initiated by the development of tensile stress, but rapidly changes to a shear type of failure.

Further analysis was carried out to support the claim of a Mode II failure under the CS loading by comparing the  $K_I$  and  $K_{II}$  values. The CS cubes have a notch spacing  $H = 50, 40$  and  $30 \text{ mm}$  and the crack length varies from  $a = 25 \text{ mm}$  to  $a = 60 \text{ mm}$  in  $5 \text{ mm}$  increments. 8 computer runs were made for each notch spacing, a total of 48 computer runs made to obtain the  $K_I$  and  $K_{II}$  values for the CS cubes. It was found that the  $K_{II}$  values are many times higher than the  $K_I$  as  $H/W$  ratio decreases and  $a/W$  increases (e.g.  $K_{II}/K_I = 124$  for  $H/W = 0.3, a/W = 0.6$ ). It can be concluded that a Mode II type of failure is improving by reducing the notch spacing  $H$ .

Calibration coefficients were determined for the  $100 \text{ mm}$  CS cube with notch spacings of  $H = 50, 40$  and  $30 \text{ mm}$  and expressed in a polynomial of powers  $a/W$  when  $0.25 \leq a/W \leq 0.6$ . Simplified calibration coefficients were obtained by averaging the  $Y(a/W)$

values since they were independent of  $a/W$  ratios when  $0.3 \leq a/W \leq 0.45$  .

Finally, the capability of the displacement finite element method used by Chan et al (8) and Woo et al (9) was compared with the boundary collocation method used by Chisholm and Jones (19). This was done so by analysing a notched cube of notch spacing  $H = 50\text{mm}$  under a compressive load of  $1000\text{N}$  . The results show that a good correlation is obtained using Woo's method.

#### 4.3 FINITE ELEMENT MODELLING FOR 100mm SINGLE-NOTCHED CUBES

It has been shown in Section 4.2.3 that a possible "pure" Mode II type of failure will occur if the notch spacing is reduced to  $H = 0$  . An attempt was therefore made to model a cube which has a single notch  $10\text{mm}$  deep on the top surface and a single notch  $30\text{mm}$  deep on the bottom surface as shown in Figure 4.15(a). The cube was loaded by a compressive force  $P = 1000\text{N}$  as shown in Figure 4.15(b). The deformed cube showed that a considerable amount of vertical displacement took place along the bottom notch indicating that a Mode II type of failure is possible under this loading and configuration.

##### 4.3.1 A Convergence Study of Element-mesh Size

A convergence study of element mesh size was carried out on four mesh geometries as indicated in Figure 4.15 for 100 , 240 , 640 and 1040 element-meshes.

The 8-noded quadrilateral isoparametric elements with distorted elements at the crack tip were used in this study. The smallest size of an element used at the crack tip was  $0.33a$ ,  $0.16a$ ,  $0.08a$  and  $0.04a$  for 100, 240, 640 and 1040 element-mesh respectively (where  $a$  is the crack length). The  $K_{II}$  values were calculated from the vertical displacements on the bottom notch using Woo's displacement equation (3.9).

Figure 4.16 shows a typical plot of  $K_{II}$  as a function of  $x/a$  for the 240 element-mesh. An estimate of  $K_{II}$  is obtained by extrapolating the straight line of the plot (at  $x/a = 0$  and  $x/a = 0.45$ ) to  $x/a = 1$ .

Results for other element-meshes are shown in Table 4.11 and plotted in Figure 4.17. It is seen that the curve converges at a value of  $K_{II} = 3.91\text{Nmm}^{-3/2}$  where the mesh contains 640 elements. It was observed that when using the 240 element-mesh there was only a difference of 1.1% in the  $K_{II}$  value when compared to the result from 640 element-mesh. The 240 element-mesh with distorted elements at the crack tip was therefore sufficient for the finite element modelling of the 100mm single-notched cube.

#### 4.3.2 Comparison of the Mode I and Mode II Stress Intensity Factors

An investigation was made to study the significance of a Mode II type of failure for the single-notched cube in compression as shown in Figure 4.15(a) by comparing both the Mode I and Mode II stress intensity factors. The cube has eight variations by changing the crack length  $a$  from  $a = 25\text{mm}$  to  $60\text{mm}$  in  $5\text{mm}$  increments.

A constant 240 element mesh with distorted elements at the crack tip was used for all the finite element analysis. The smallest element used at the crack tip was  $0.2a$  ,  $0.167a$  ,  $0.143a$  ,  $0.125a$  ,  $0.111a$  ,  $0.1a$  and  $0.083a$  for the crack length  $a = 25$  ,  $30$  ,  $35$  ,  $40$  ,  $45$  ,  $50$  ,  $55$  and  $60\text{mm}$  respectively. A total of 8 computer runs were carried out for all.

From each computer output the vertical and horizontal displacements along the bottom notch were substituted into Woo's equations (3.8) and (3.9) respectively so that the Mode I and Mode II stress intensity factors were evaluated. Results of the  $K_I$  ,  $K_{II}$  and  $K_{II}/K_I$  when  $0.25 \leq \frac{a}{W} \leq 0.6$  are summarised in Table 4.12.

Variation of  $K_{II}$  estimates and  $K_{II}/K_I$  ratios with different  $a/W$  ratios are shown graphically in Figures 4.18 and 4.19 respectively. Figure 4.18 shows that the  $K_{II}$  estimates increase linearly with the increasing  $a/W$  ratios. This indicates that a Mode II type of failure is dominant as the notch depth increases. Figure 4.19 shows that the  $K_{II}/K_I$  plot increases non-linearly with the increasing  $a/W$  ratios. Because the  $K_{II}/K_I$  ratio is not significantly high (e.g.  $K_{II}/K_I = 12$  for  $a/W = 0.6$ ) when compared with the double-notched cube of  $H/W = 0.3$  in Section 4.2.4 where  $K_{II}/K_I = 124$  for  $a/W = 0.6$  , the existing model of 100mm single-notched cube has failed to achieve a pure Mode II type of failure. Nevertheless, the analysis was continued to evaluate the calibration coefficients in the determination of the stress intensity factors in order to complete the study of this 100mm single-notched cube.

#### 4.3.3 Determination of the Calibration Coefficients of the Mode II Stress Intensity Factors

The calibration coefficients  $Y(a/W)$  were obtained as described in Section 4.2.5 using equation (4.6), the  $Y(a/W)$  values were obtained and tabulated in Table 4.12. Figure 4.20 shows the  $Y(a/W)$  values were dependent on the  $a/W$  ratios. An empirical relation between the  $Y(a/W)$  values and the  $a/W$  ratios was obtained by using a least square method. Best fit curve was obtained for  $Y(a/W)$  values when  $0.3 \leq a/W \leq 0.45$  and equation of  $Y(a/W)$  expressed in polynomials of powers  $a/W$  is shown in Table 4.12.

when  $0.3 \leq a/W \leq 0.45$ , the calibration coefficients

$$Y\left(\frac{a}{W}\right) = 6.062 - 9.192 \left(\frac{a}{W}\right) + 7.6 \left(\frac{a}{W}\right)^2 \quad (4.11)$$

Substituting equation (4.11) into (4.4) and (4.7) gives the Mode II stress intensity factor as

$$K_{II} = Y\left(\frac{a}{W}\right) \cdot \frac{P}{2BW} (\pi a)^{\frac{1}{2}}$$

#### 4.3.4 Conclusions

A single-notched cube was designed to produce a "pure" shear type of failure. The initial study showed that a coarse mesh of 240 elements with crack tip elements at the crack tip was sufficient to model the cube when Woo's displacement equation was used as there was a difference of only 1.1% in the  $K_{II}$  value when using 640 element mesh.

The comparison of the  $K_{II}$  and  $K_I$  values when  $0.25 \leq a/W \leq 0.60$  showed that  $K_{II}$  was not significantly higher than  $K_I$  at  $a/W = 0.6$  ( $K_{II}/K_I = 12$ ) when compared to double-notched cube (of  $H/W = 0.3$ ,  $a/W = 0.6$ ,  $K_{II}/K_I = 124$ ). As a high  $K_{II}/K_I$  ratio is expected for a "pure" shear type of failure, the 100mm single-notched cube failed to achieve this condition.

In the completion of the study on 100mm single-notched cubes, the calibration coefficients were evaluated and found to be dependent of  $a/W$  ratios. A least square method was used to evaluate the equation of the calibration coefficient expressed in polynomials of powers  $a/W$  when  $0.3 \leq a/W \leq 0.45$ .

#### 4.4 FINITE ELEMENT MODELLING FOR 150mm DOUBLE-NOTCHED CUBES

The study of 100mm compact shear (CS) cubes under the Mode II type of failure was completed with decreasing notch spacing and increasing notch depth. It was found that a significant Mode II type of failure improved by reducing the notch spacing  $H$  and increasing the notch depth  $a$ .

An attempt was made to study the 150mm compact shear cubes with proportional configuration to the 100mm compact shear cubes and examine whether similar conclusions can be shown between the two cubes that a Mode II failure is dominant with smaller notch spacing  $H$  and deeper notch depth  $a$ .

The 150mm double-notched cubes have three basic geometries with notch spacing  $H = 80, 60$  and  $40\text{mm}$ . Each geometry has eleven variations by changing the lower notch depth  $a$  from  $a = 30\text{mm}$  to  $80\text{mm}$  in  $5\text{mm}$  increments. The upper notch depth is always kept at  $15\text{mm}$ .

#### 4.4.1 A Convergence Study of Element-mesh Size

The CS cube shown in Figure 4.21(a) was loaded by a compressive force  $P = 1000\text{N}$ . Because of symmetry, only one half of the cube was used and vertical restraints were provided at the support thus assuming the shearing displacements at the crack tip required for Mode II fracture. The cube deformed in an identical manner to a  $100\text{mm}$  CS cube.

A convergence study of element mesh size was carried out on six mesh geometries as indicated in Figure 4.21. These are 180, 240, 294, 490, 686 and 930 element meshes. The 8-noded quadrilateral isoparametric elements with distorted elements at the crack tip were used in this study. The smallest size of an element used at the crack tip was  $0.11a$  for 180 and 240 element meshes  $0.055a$  for 294, 490 and 686 element meshes and  $0.027a$  for 938 element mesh. The  $K_{II}$  values were calculated from the vertical displacements on the bottom notch using Woo's displacement equation (3.9).

Figure 4.22 shows a typical plot of  $K_{II}$  as a function of  $\chi/a$  for the 294 element mesh. An estimate of  $K_{II}$  is obtained by extrapolating the straight line of the plot to  $\chi/a = 1$ .

Results for the element meshes are tabulated in Table 4.13 and shown graphically in Figure 4.23. It is seen that the curve converges at a value of  $K_{II} = 1.868 \text{Nmm}^{-3/2}$  where the mesh contains 686 elements. It was observed that when using the 294 element mesh there was only a difference of 1.5% in the  $K_{II}$  value when compared to the result from a 686 element mesh. The 294 element mesh with distorted elements at the crack tip was sufficient for the finite element modelling of the 150mm double-notched cubes.

#### 4.4.2 Comparison of the Mode I and Mode II Stress Intensity Factors

For  $H/W = 0.53, 0.4$  and  $0.26$

An investigation was made to study the significance of a Mode II type of failure for the 150mm double-notched cube in compression by comparing both the Mode I and Mode II stress intensity factors. The cubes have three basic geometries with notch spacing  $H = 80, 60$  and  $40\text{mm}$ . Each geometry has eleven variations by changing the crack length  $a = 30\text{mm}$  to  $80\text{mm}$  in  $5\text{mm}$  increments. A constant 294 element-mesh with distorted elements at the crack tip was used for all the finite element analysis. The smallest element used at the crack tip was  $0.083a, 0.071a, 0.063a, 0.056a, 0.05a, 0.045a, 0.042a, 0.038a, 0.036a, 0.033a$  and  $0.031a$  for crack length



$a = 30\text{mm}$  to  $a = 80\text{mm}$  in  $5\text{mm}$  increments respectively. A total of 33 computer runs were carried out.

From each computer output the vertical and horizontal displacements along the bottom notch were substituted into Woo's equations (3.8) and (3.9) respectively, so that the Mode I and Mode II stress intensity factors were evaluated. Figure 4.22 shows typical plots of  $K_{II}$  against  $\chi/a$  for  $H/W = 0.53$ ,  $0.4$  and  $0.26$  respectively. Table 4.14 shows the  $K_I$  and  $K_{II}$  estimates and  $K_{II}/K_I$  ratios for various  $H/W$  and  $a/W$  ratios. The variations of  $K_{II}$  and  $K_{II}/K_I$  with various  $a/W$  ratios are shown graphically in Figures 4.24 and 4.25 respectively.

Figure 4.24 shows all three  $K_{II}$  plots increasing linearly with increasing  $a/W$  values and also shows that the plot with a wider notch spacing ratio  $H/W$  produces higher  $K_{II}$  values than the one with a smaller  $H/W$  ratio.

Figure 4.25 shows the comparison of  $K_{II}/K_I$  ratio for various  $a/W$  ratios. It is seen that all three  $K_{II}/K_I$  plots increase non-linearly with the increasing  $a/W$  ratio, thus indicating a Mode II type of failure is dominant as the notch depth increases. It is also seen that a smaller  $H/W$  ratio produces a higher  $K_{II}/K_I$  ratio. In the case of  $H/W = 0.26$  and  $a/W = 0.53$ ,  $K_{II}/K_I$  reaches infinity. This result is extremely encouraging because it implies a pure shear type of failure occurs for the  $150\text{mm}$  double-notched cube of  $H/W = 0.26$  and  $a/W = 0.53$ .

By comparing the  $K_{II}/K_I$  ratios between 150mm and 100mm CS cubes for various  $H/W$  and  $a/W$  ratios (Table 4.14 and Table 4.6), it is observed that a  $K_{II}/K_I$  ratio of 150mm CS cube is about 1.5 times larger than 100mm CS cube for  $H/W = 0.53$  and 1.8 times larger for  $H/W = 0.4$ . For  $H/W = 0.26$  the  $K_{II}/K_I$  ratio of 150mm CS cube is about 3 times larger than the 100mm CS cube where  $0.2 \leq \frac{a}{W} \leq 0.35$  and increases rapidly to infinity at  $a/W = 0.53$ .

It can be concluded that the 150mm double-notched cubes are more suitable to achieve a Mode II type of failure than the 100mm double-notched cubes because  $K_{II}/K_I$  ratios of 150mm cubes are significantly higher than those of 100mm cubes when compared with the same notch spacing and depth ratios. A "pure" shear failure condition may be achieved when the notch spacing ratio  $H/W = 0.26$  and notch depth ratio  $a/W = 0.53$ .

The  $K_{II}$  stress intensity factors were found to be :

$$H = 80\text{mm} \quad K_{II} = \left[ 2.35 - 2.93\left(\frac{a}{W}\right) + 2.99\left(\frac{a}{W}\right)^2 \right] \frac{P}{BW} (\pi a)^{\frac{1}{2}} \quad (4.12)$$

$$H = 60\text{mm} \quad K_{II} = \left[ 1.91 - 2.35\left(\frac{a}{W}\right) + 2.36\left(\frac{a}{W}\right)^2 \right] \frac{P}{BW} (\pi a)^{\frac{1}{2}} \quad (4.13)$$

$$H = 40\text{mm} \quad K_{II} = \left[ 1.67 - 2.76\left(\frac{a}{W}\right) + 3.30\left(\frac{a}{W}\right)^2 \right] \frac{P}{BW} (\pi a)^{\frac{1}{2}} \quad (4.14)$$

#### 4.4.3 Determination of the Calibration Coefficient of Mode II Stress Intensity Factors for $H/W = 0.53, 0.4$ and $0.26$

The calibration coefficients were determined by using equation (4.6) as described in Section 4.2.5 and the results are tabulated in Table 4.15 for various  $a/W$  ratios and  $H/W$  ratios. The calibration coefficients  $Y(a/W)$  are shown graphically in Figure 4.26. It is seen that the  $Y(a/W)$  values for the three notch spacing  $H/W$  ratios do not produce smooth curves. This indicates that the constant 294 element mesh used for all analyses needs to be refined in order to produce better plots of  $Y(a/W)$ , these  $Y(a/W)$  values being independent of  $a/W$  ratios.

An empirical relation between the  $Y(a/W)$  values and the  $a/W$  ratios was obtained by using a least square method. Best fit curves for  $Y(a/W)$  values when  $0.3 \leq a/W \leq 0.53$  for  $H/W = 0.53$ ,  $0.4$  and  $0.26$  respectively and equations of  $Y(a/W)$  expressed in polynomials of powers  $a/W$  are shown in Table 4.16.

#### 4.4.4 Conclusions

It can be concluded that a 294 element-mesh is the best choice to analyse the 150mm half cube when 8-noded quadrilateral isoparametric elements with crack tip elements at the crack tip are used. Because (a) it is economical to use less elements and (b) it is sufficiently accurate when the difference in the  $K_{II}$  value is 1.5% when a 686 element-mesh is used.

The comparison of  $K_{II}/K_I$  ratios with various  $H/W$  and  $a/W$  ratios indicates that the  $K_{II}/K_I$  ratio increases rapidly with the decrease of  $H/W$  and increase of  $a/W$  ratios. In the case of  $H/W = 0.26$  and  $a/W = 0.53$ ,  $K_{II}/K_I$  reaches infinity. This implies that a "pure" Mode II failure may be obtained for 150mm CS cube with smaller notch spacing and deeper notch depth.

The calibration coefficients for the three notch spacings of the 150mm CS cubes were not constant when  $0.20 \leq a/W \leq 0.53$  and a refined element mesh is therefore necessary in order to produce  $Y(a/W)$  values which should be independent of  $a/w$  ratios.

It can be concluded that the 150mm double-notched cubes are more suitable to achieve a Mode II failure than the 100mm double-notched cubes because higher  $K_{II}/K_I$  values are obtained when using the same notch spacing and depth ratios.

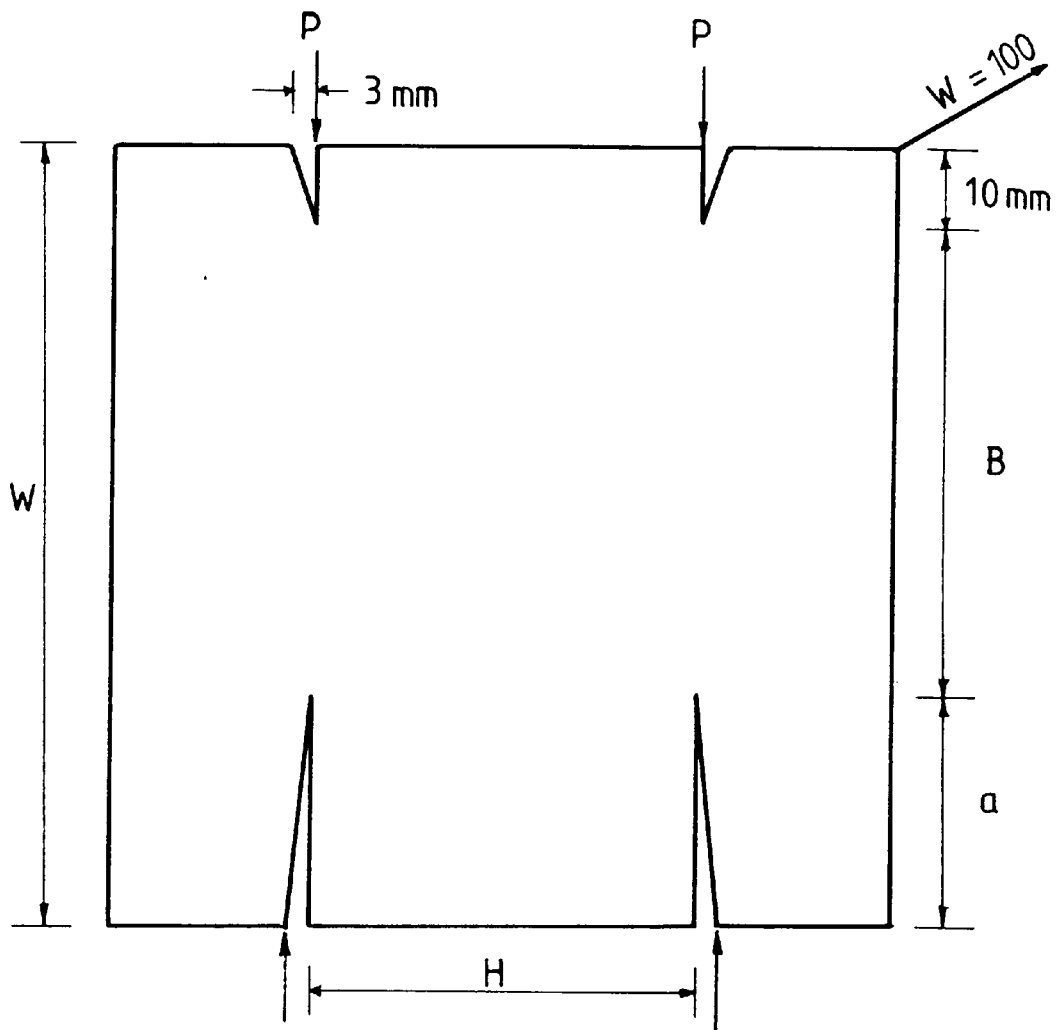


Fig. 4.1 Configuration for the double-notched cubes

H (mm)	a (mm)
50	25
	30
	35
40	40
	45
30	50
	55
	60

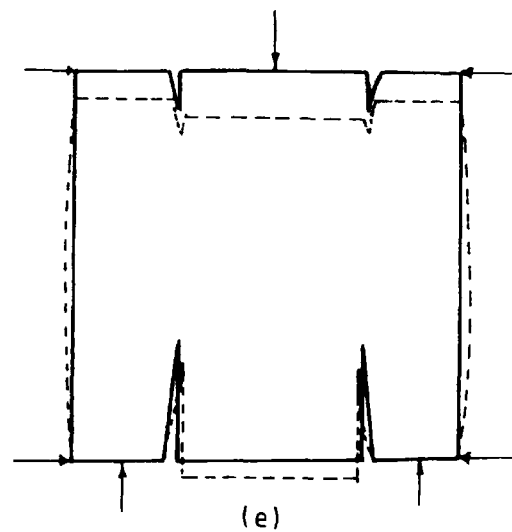
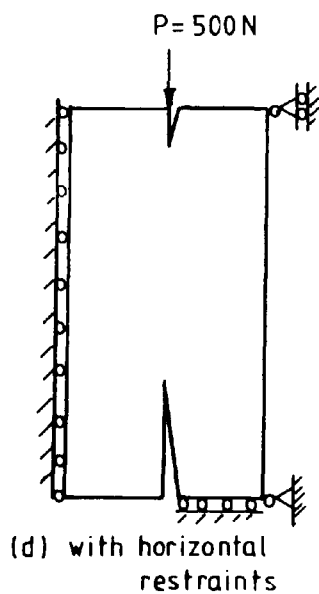
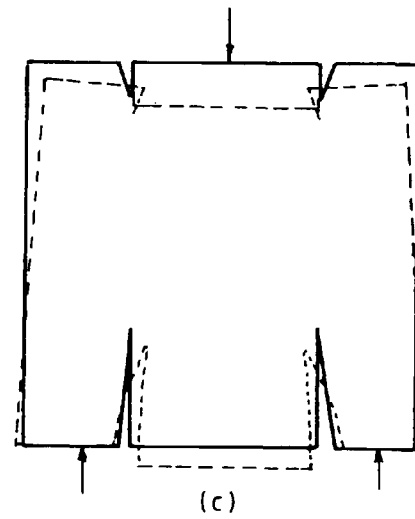
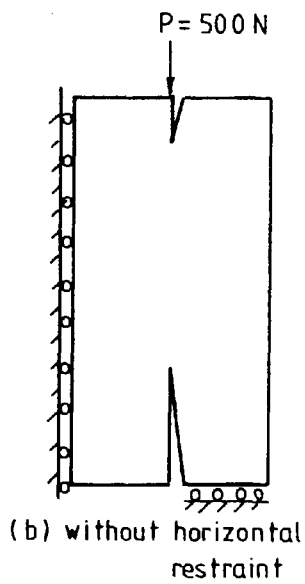
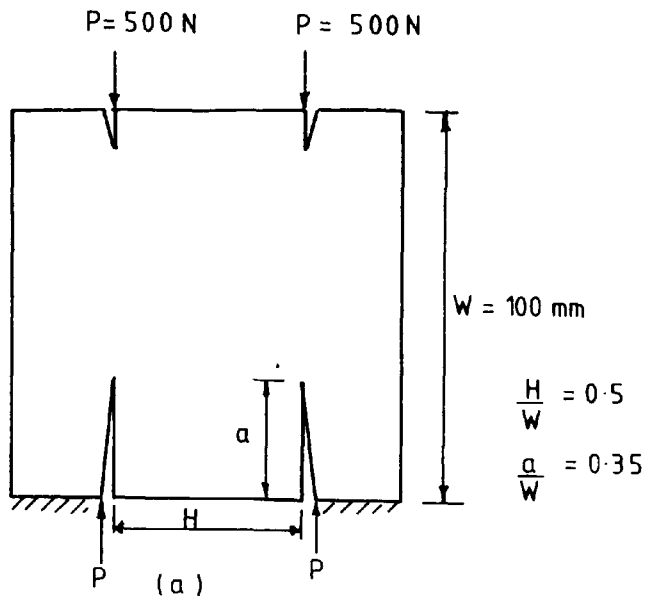


Fig.4-2 The deformed shape of the CS cube with and without horizontal restraints.

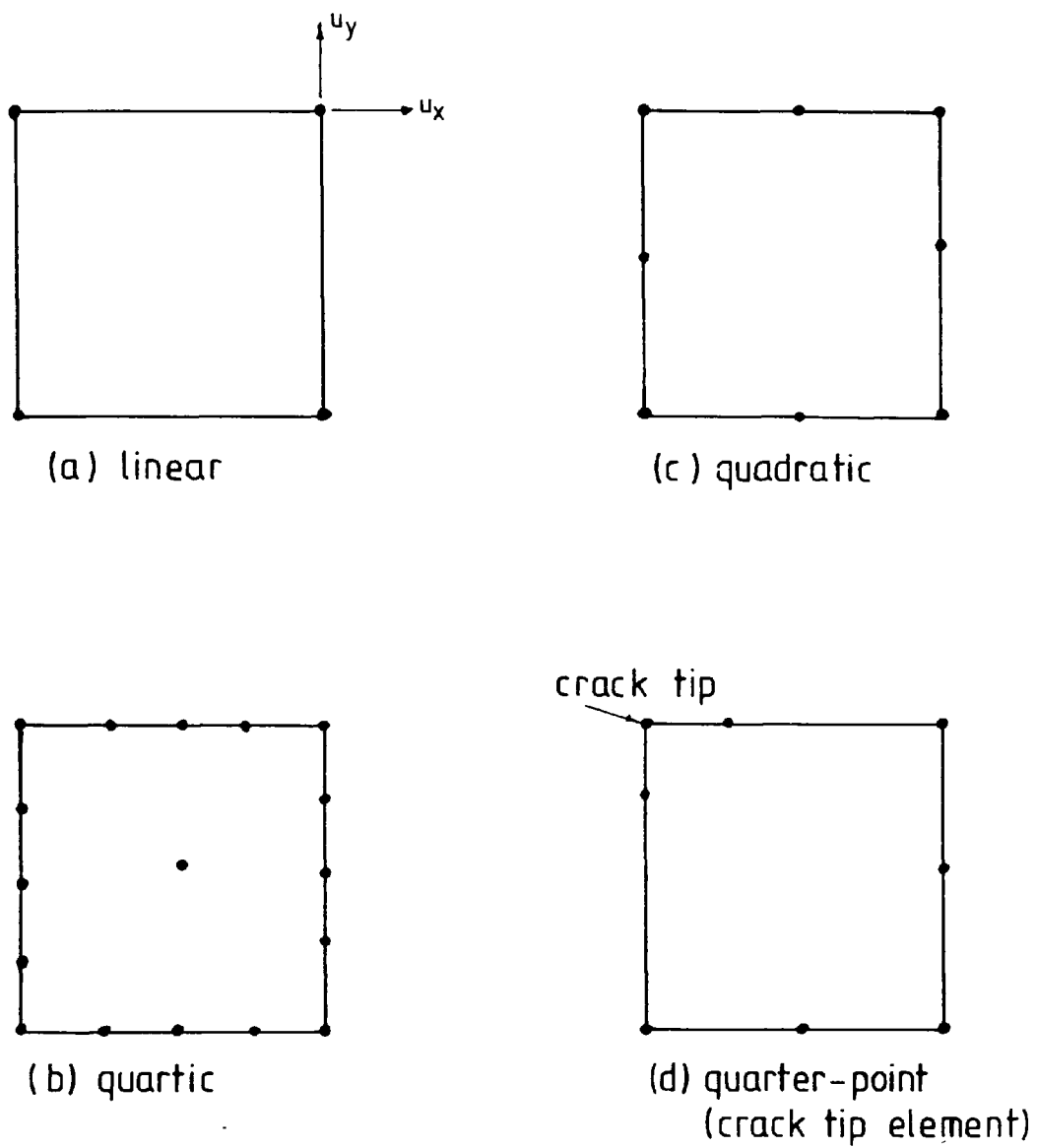


Fig. 4.3 Types of quadrilateral isoparametric element.

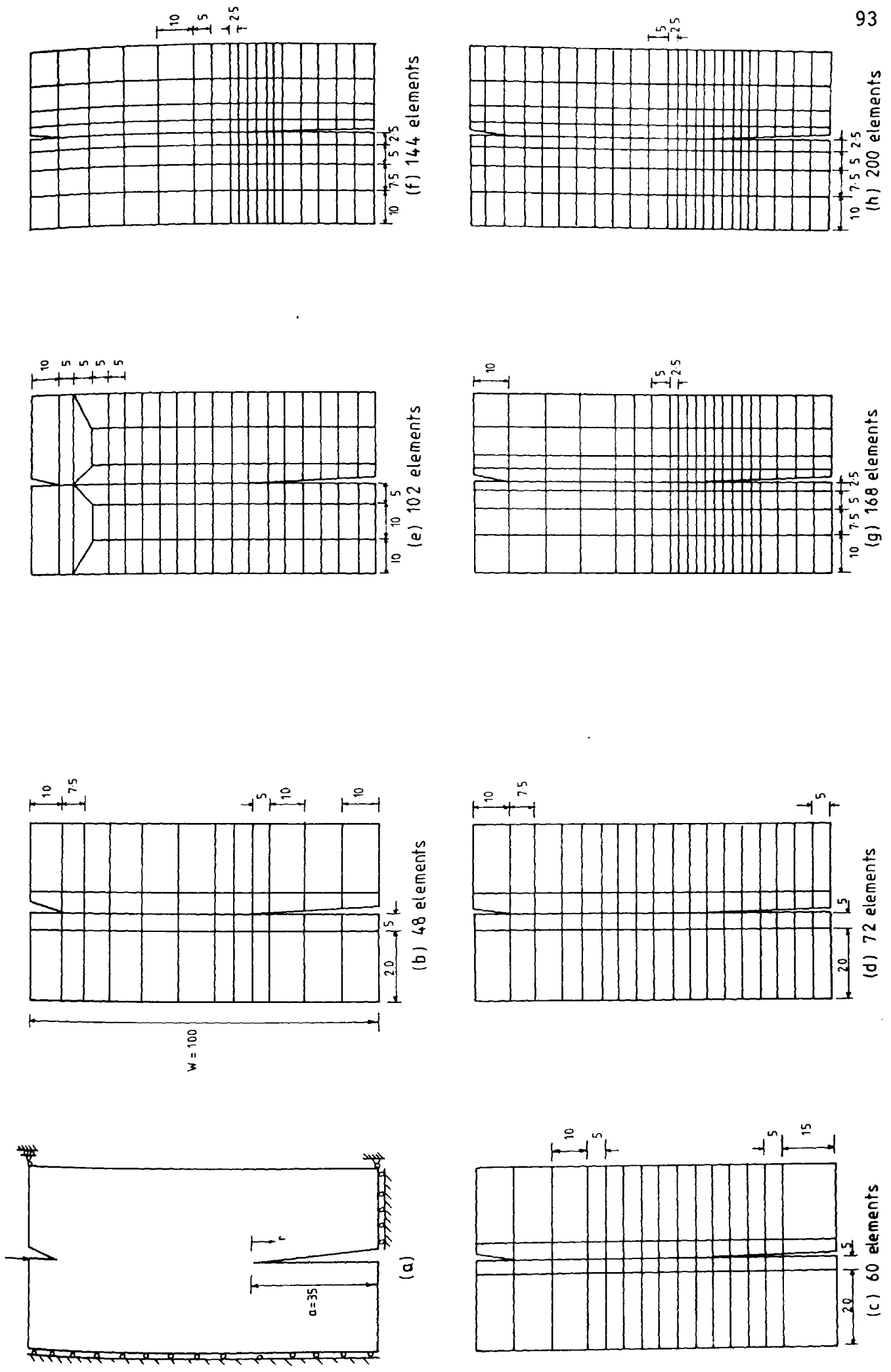


Fig. 4.4 Types of element mesh



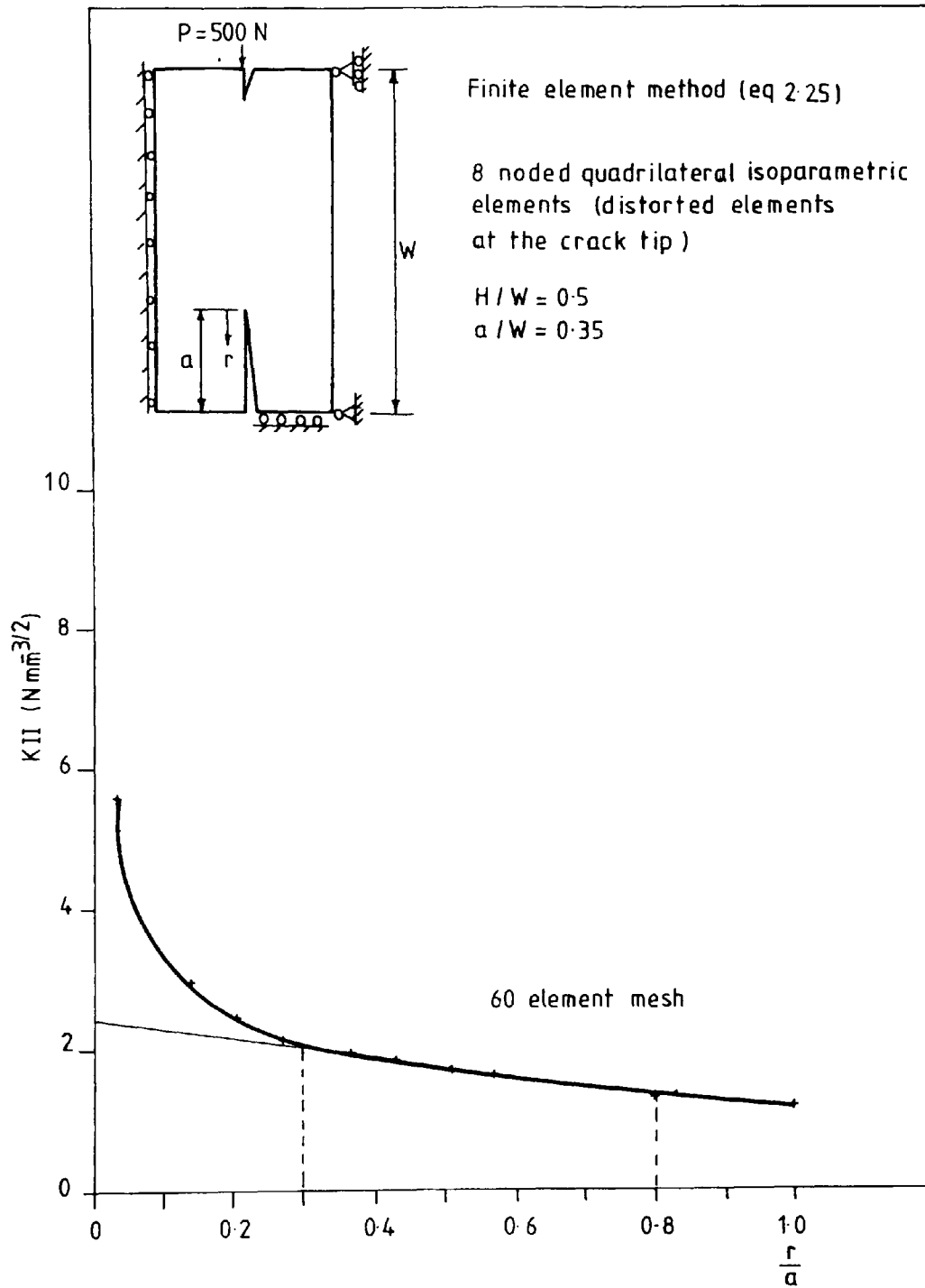


Fig. 4.5 Variation of  $K_{II}$  with  $r/a$

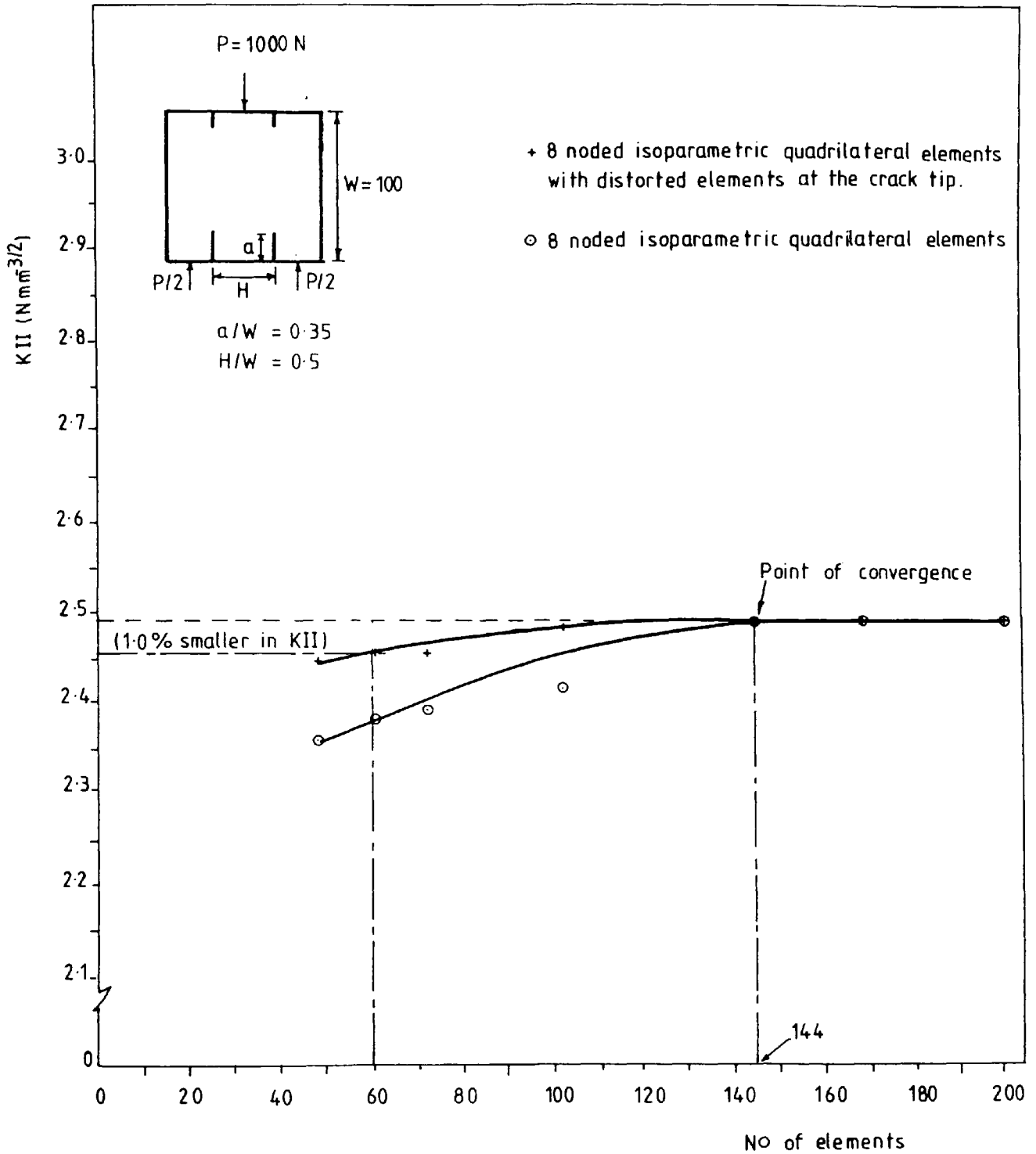


Fig.4.6 Convergence graph of element-meshes

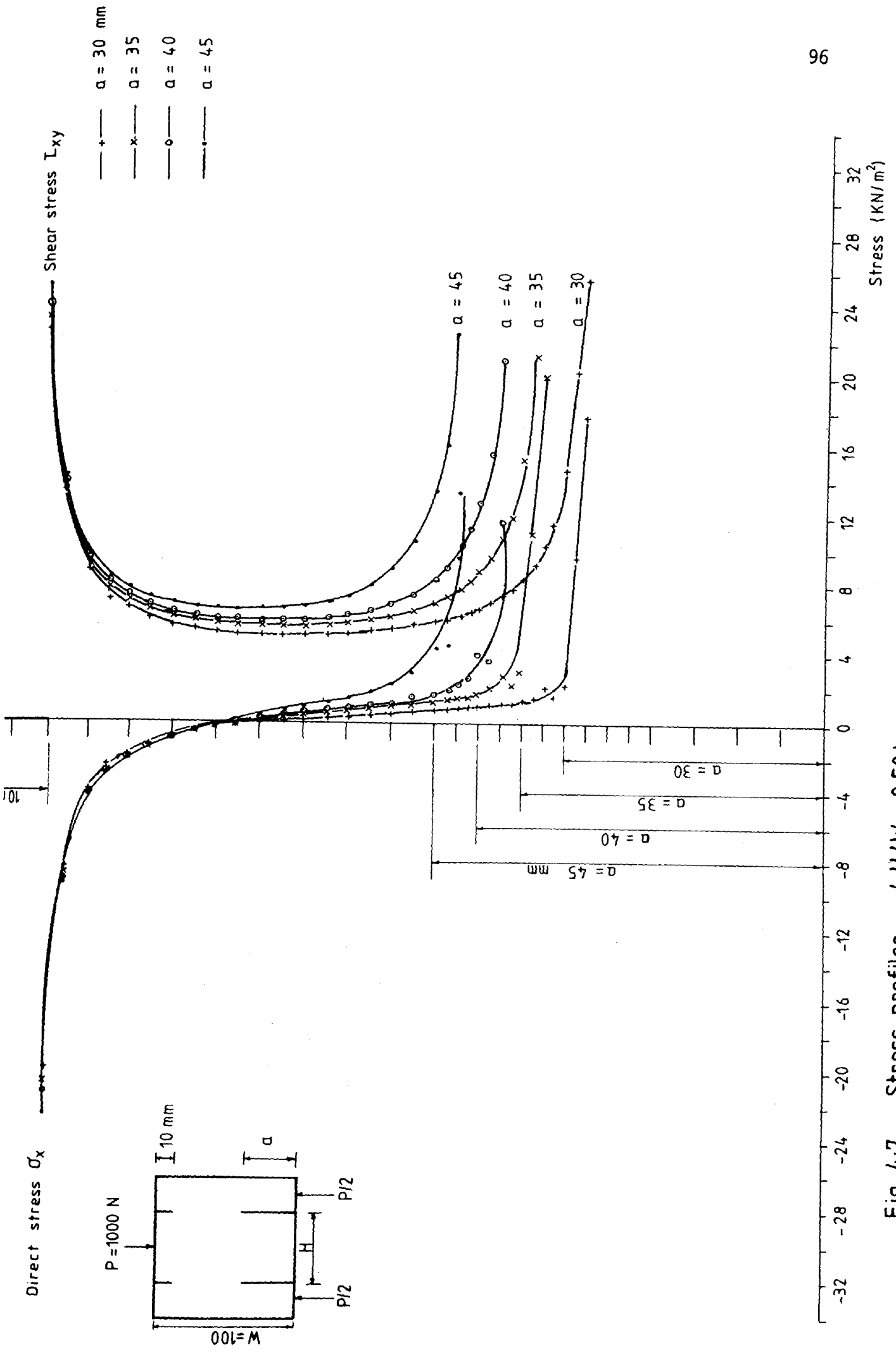


Fig. 4.7 Stress profiles (  $H/W = 0.50$  )

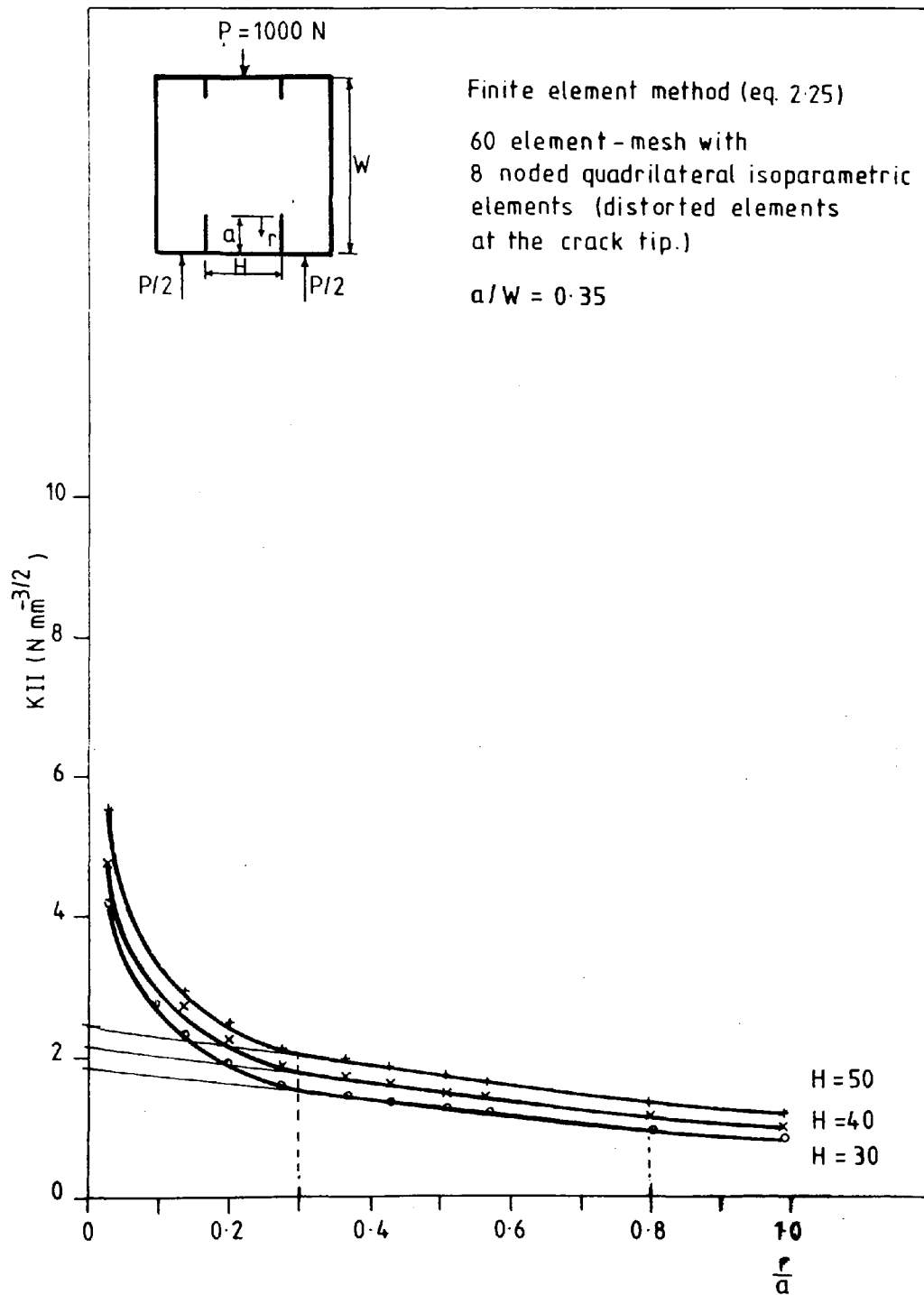


Fig. 4.8 Variation of  $K_{II}$  with  $r/a$

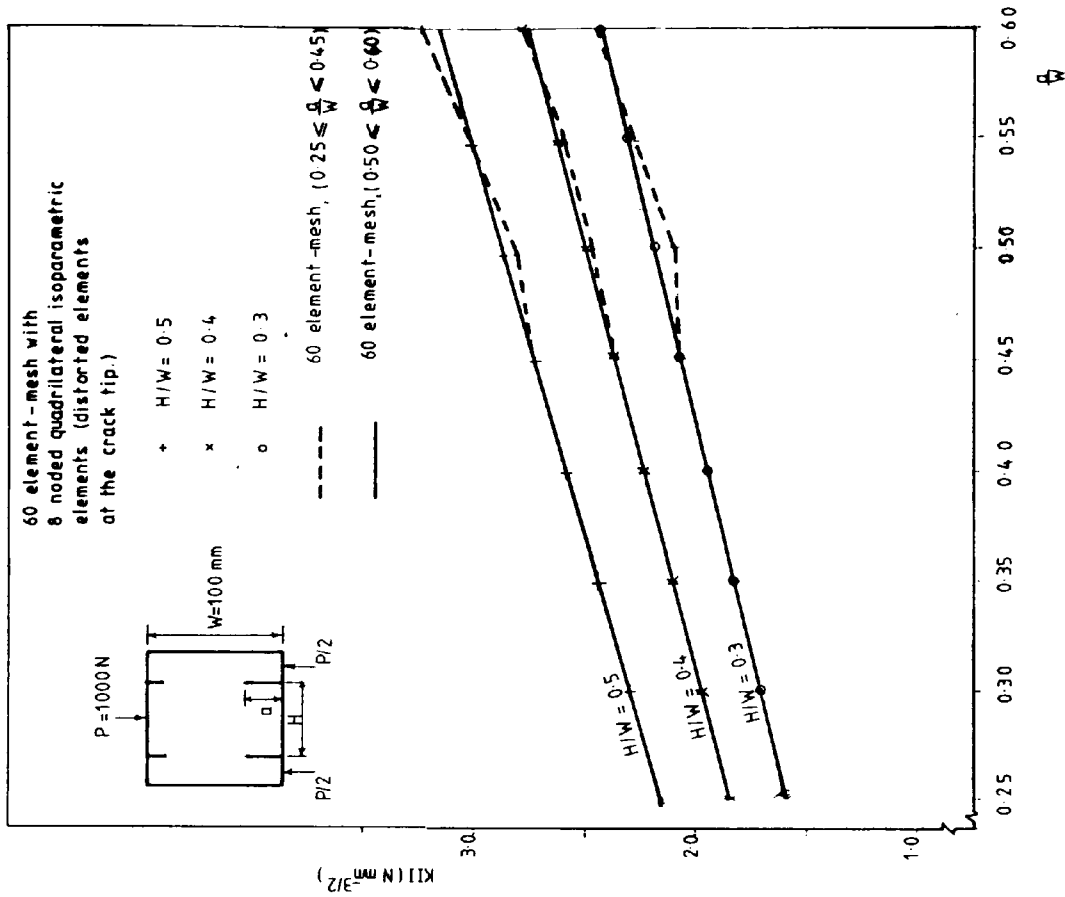
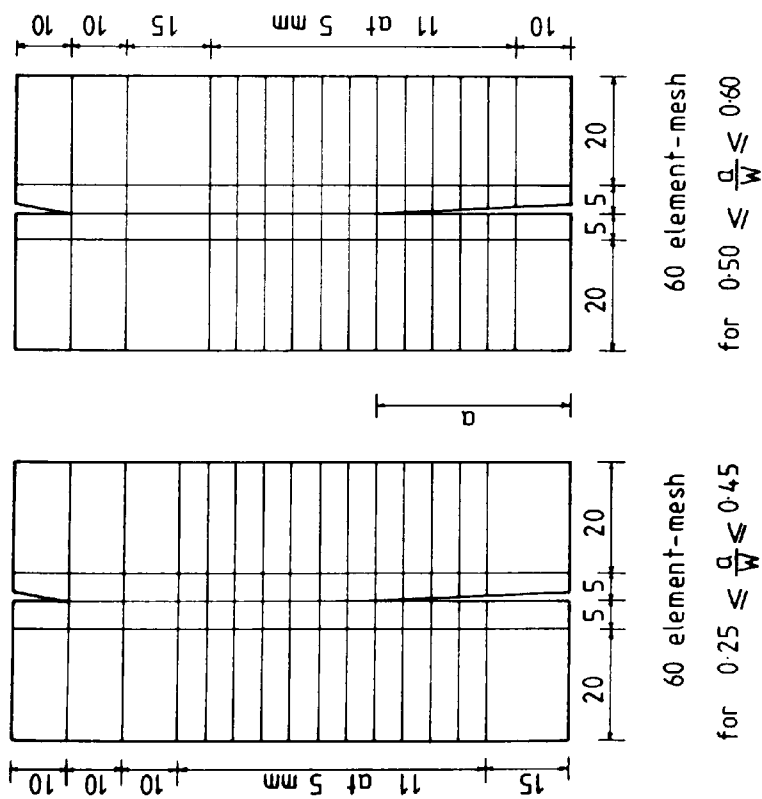


Fig. 4.9 Variation of KII with a/W





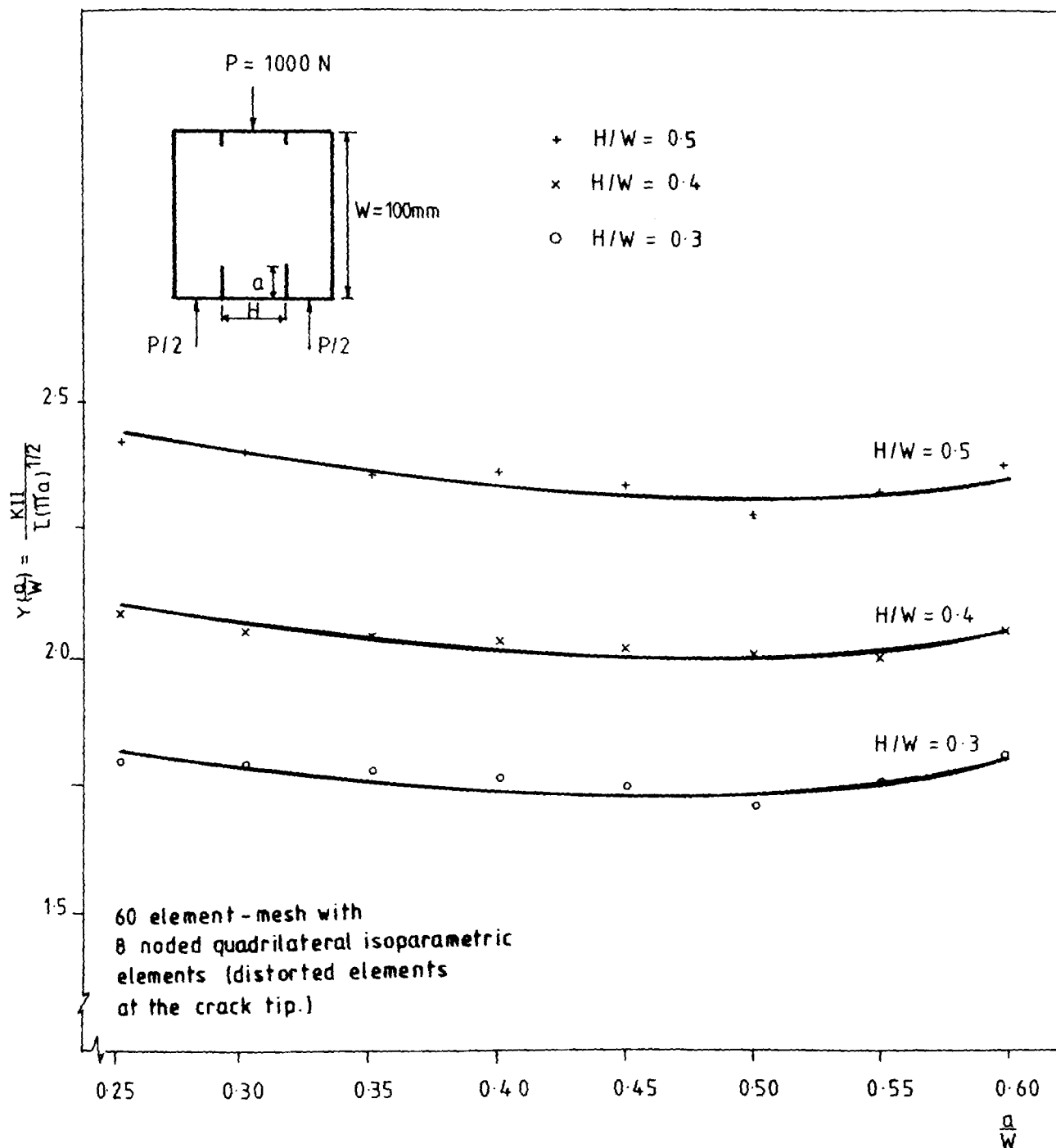


Fig. 4-11 Calibration coefficients in Mode II

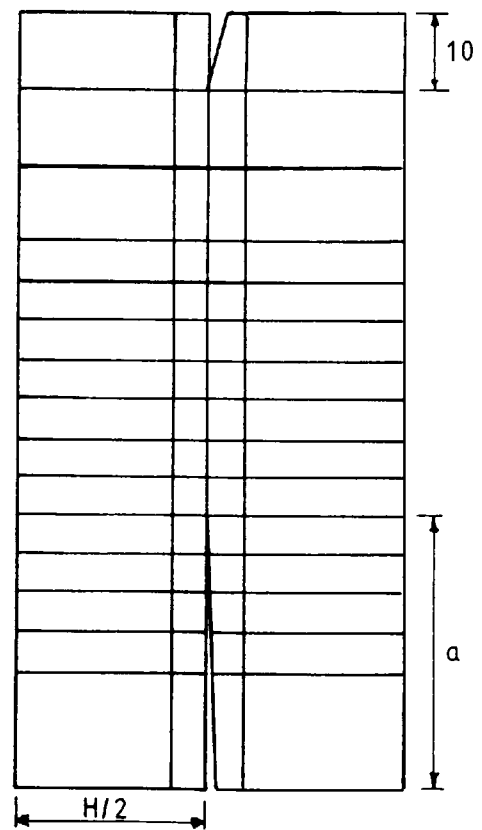
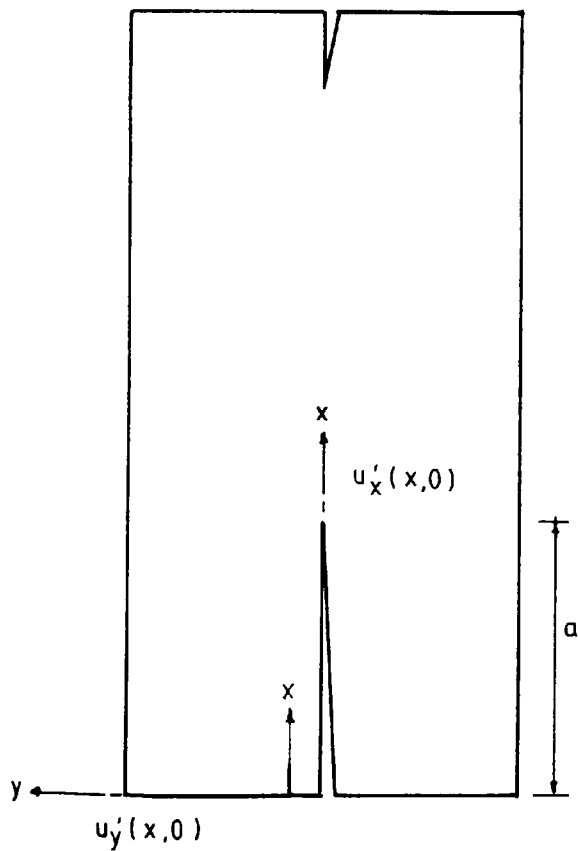
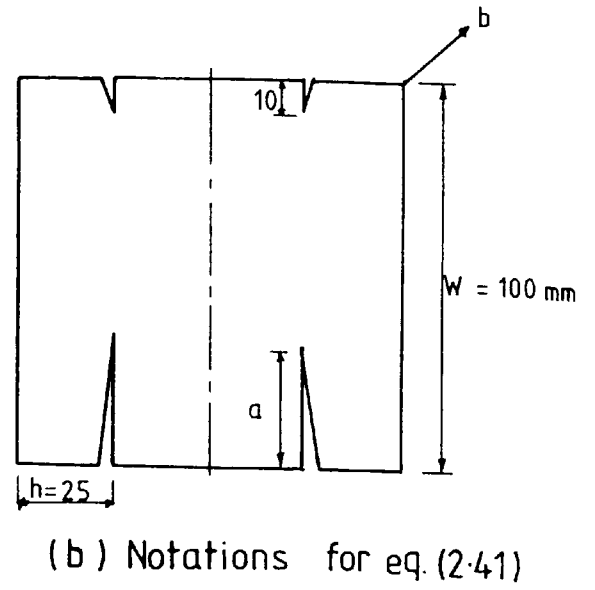
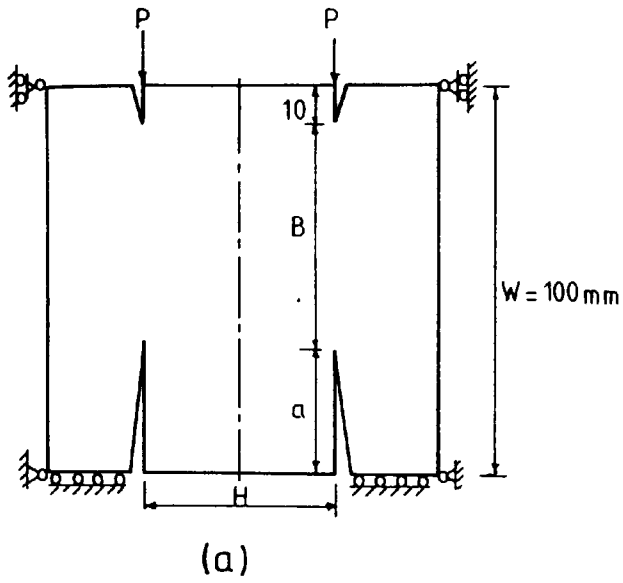


Fig 4.12 The CS cube used in the analysis



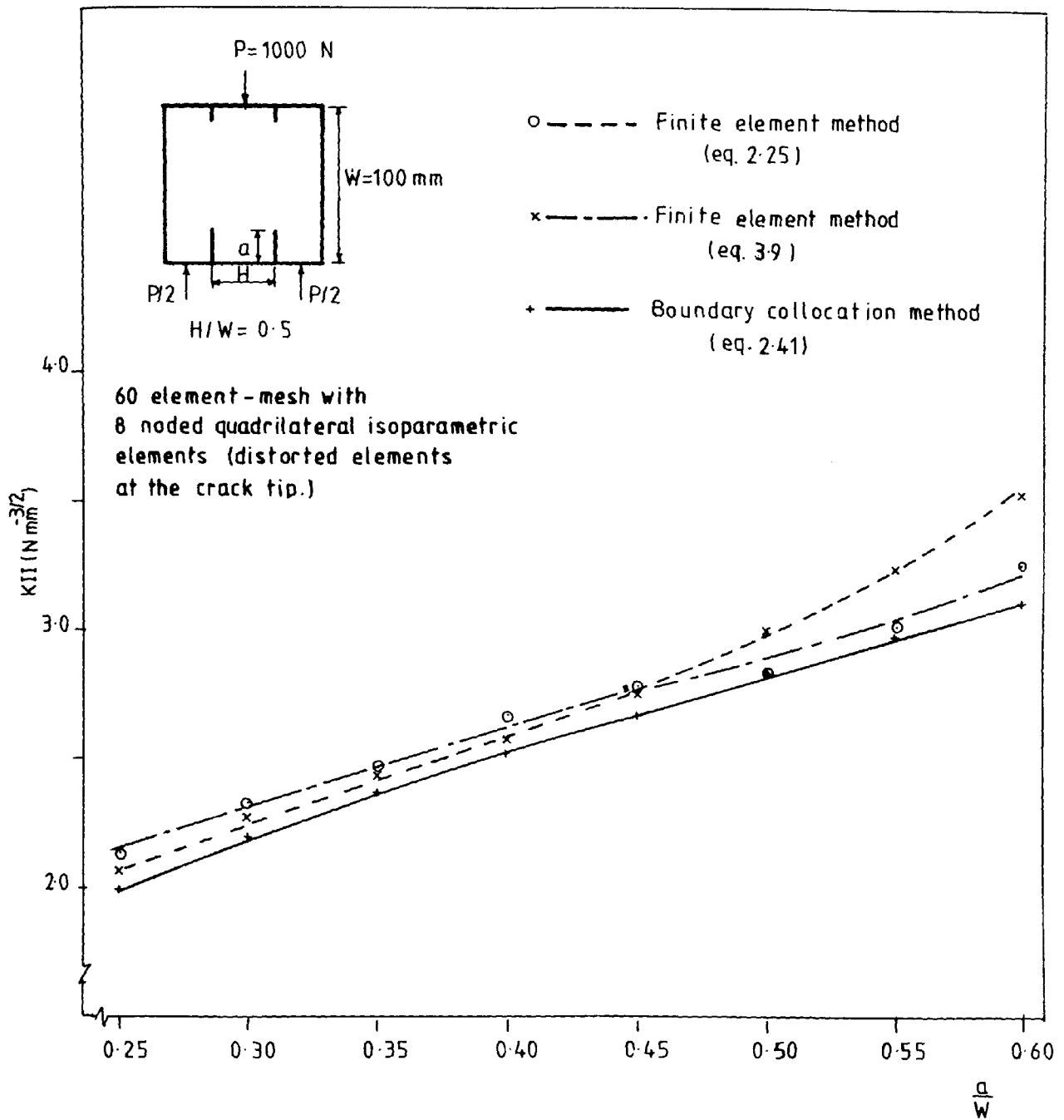


Fig. 4.13 Comparison of collocation and finite element solutions.

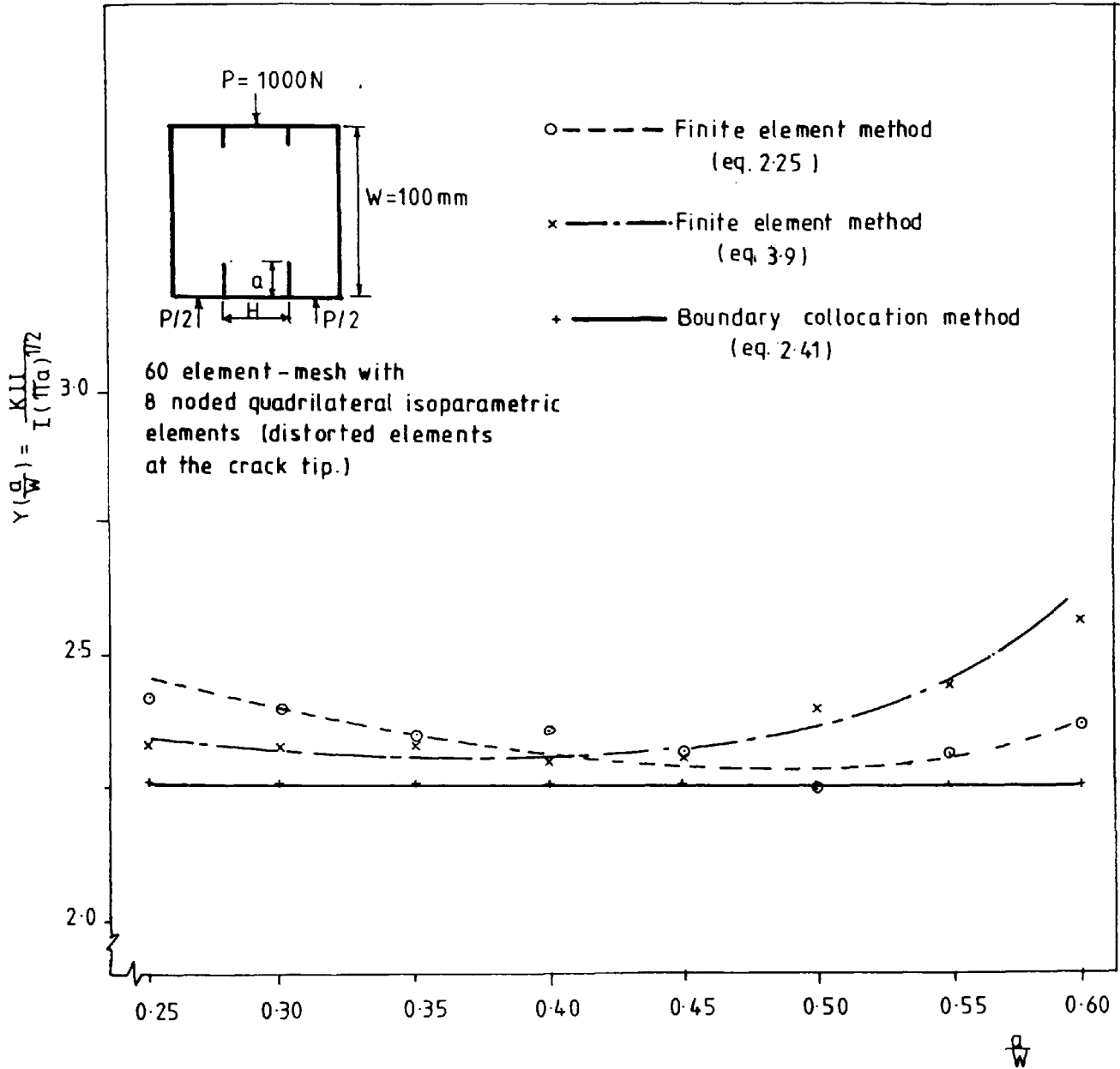


Fig. 4-14 Calibration coefficients in Mode II

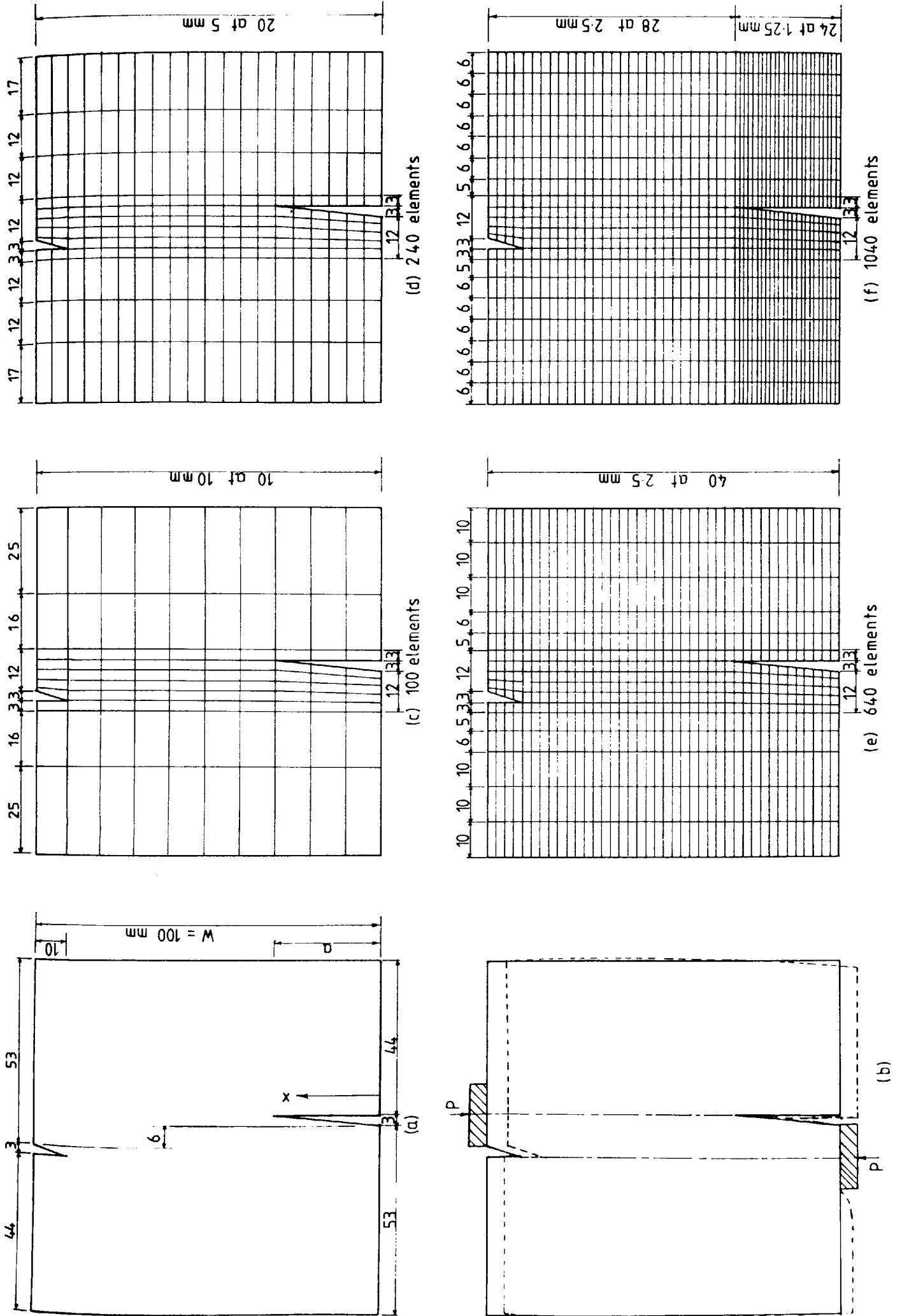
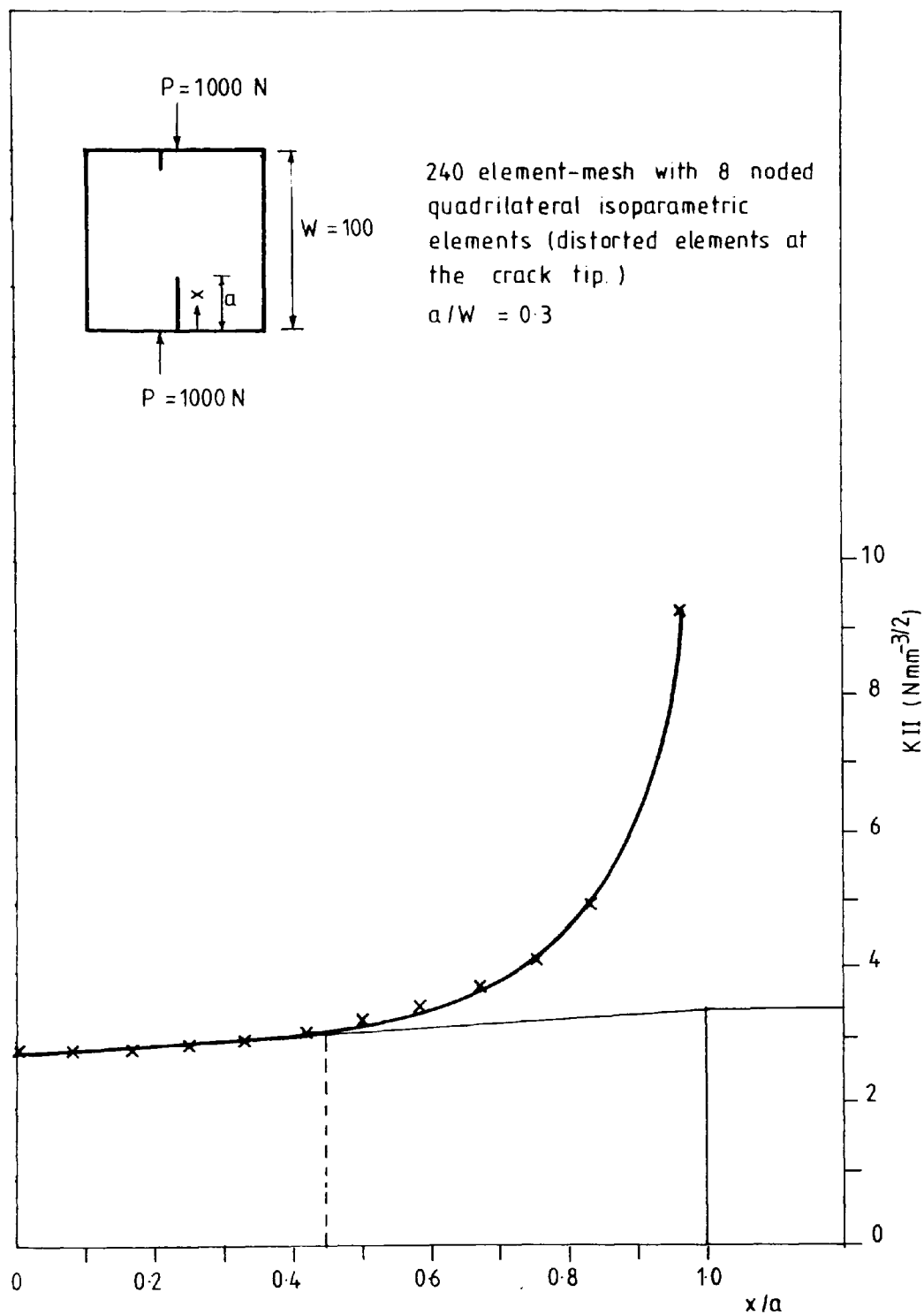
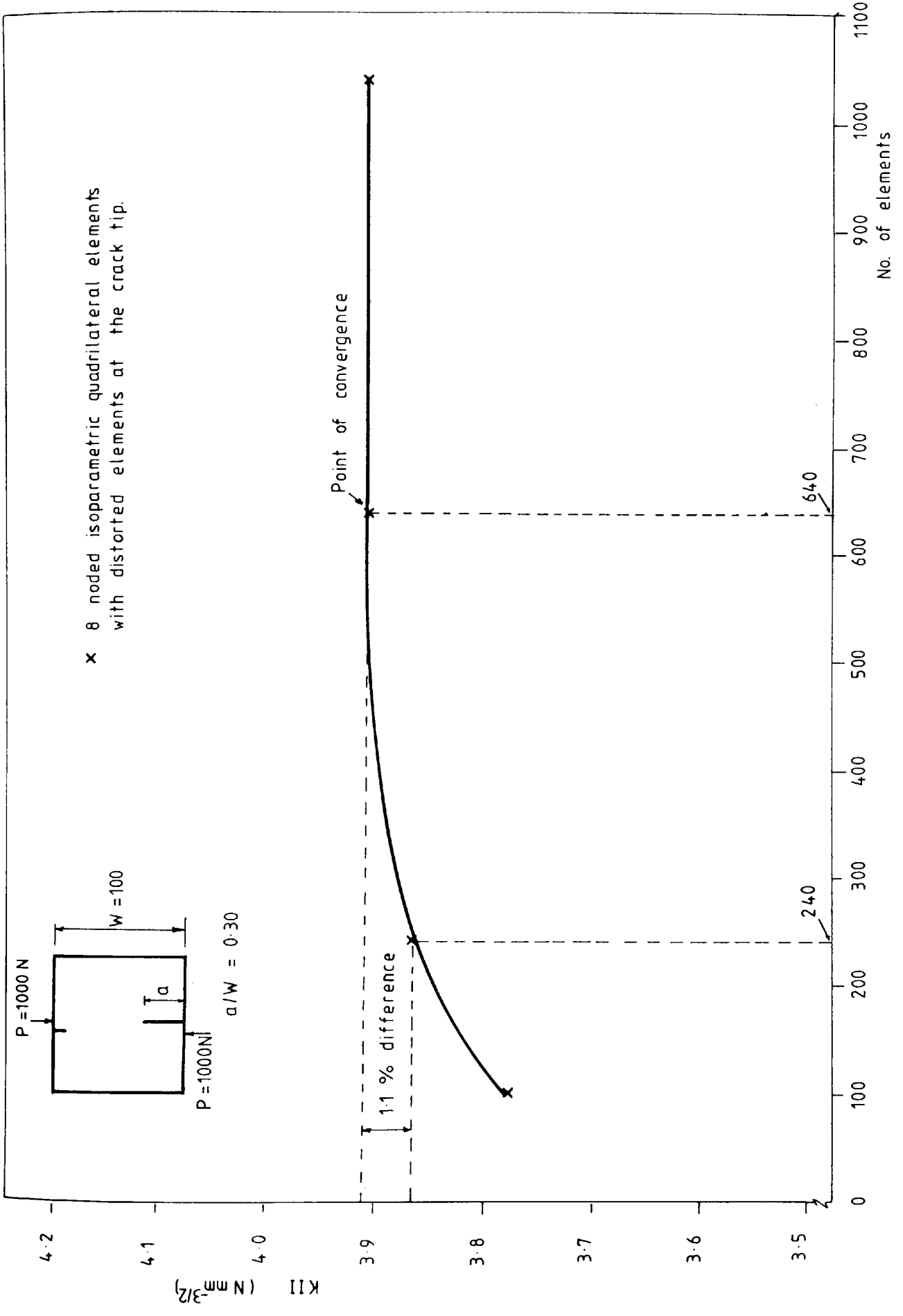


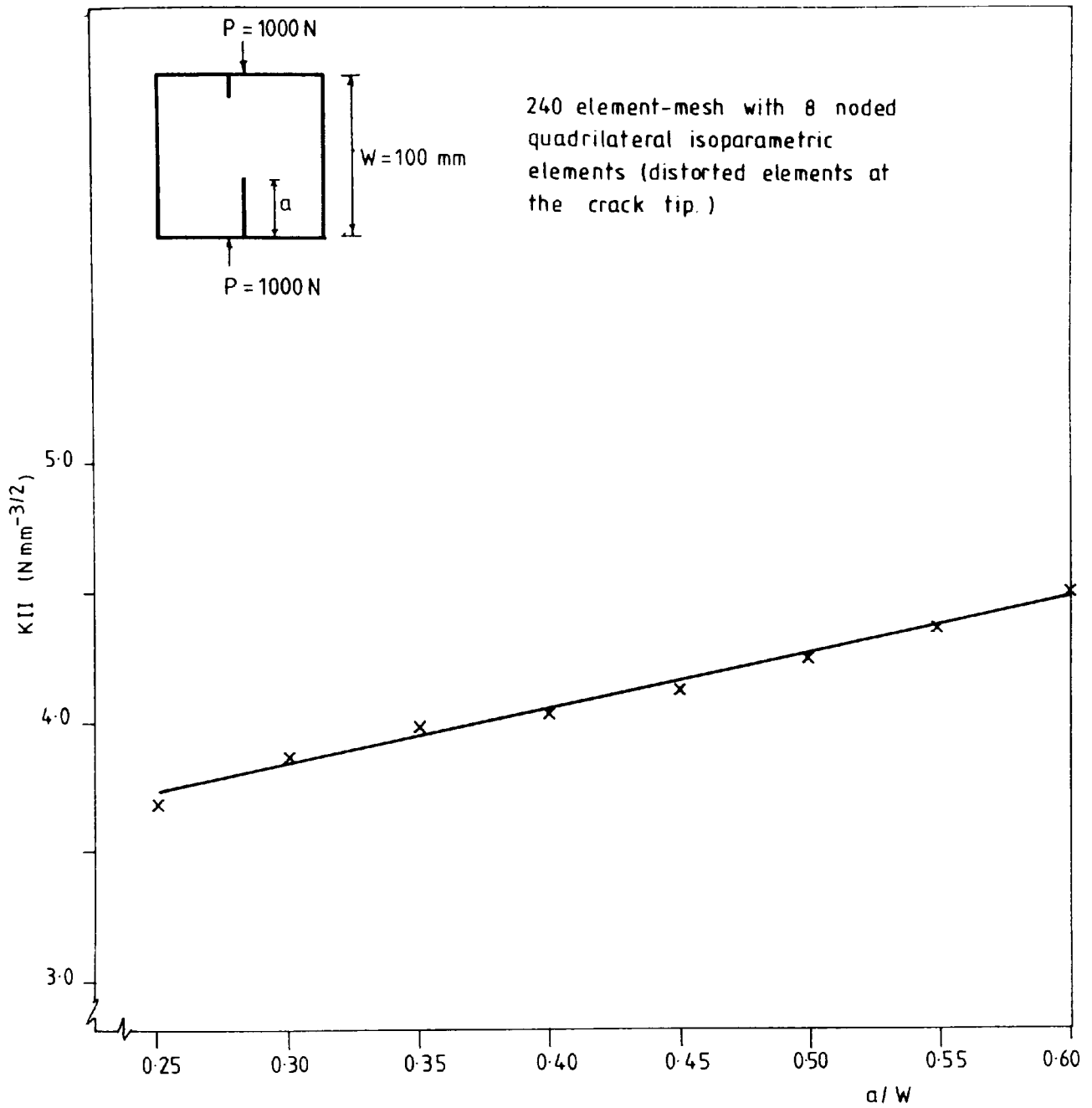
Fig. 4.15 Types of element mesh

Fig. 4.16 Variation of  $K_{II}$  with  $x/a$



x 8 noded isoparametric quadrilateral elements with distorted elements at the crack tip.

Fig. 4.17 Convergence graph of element-mesh

Fig. 4-18 Variation of  $K_{II}$  with  $a/W$

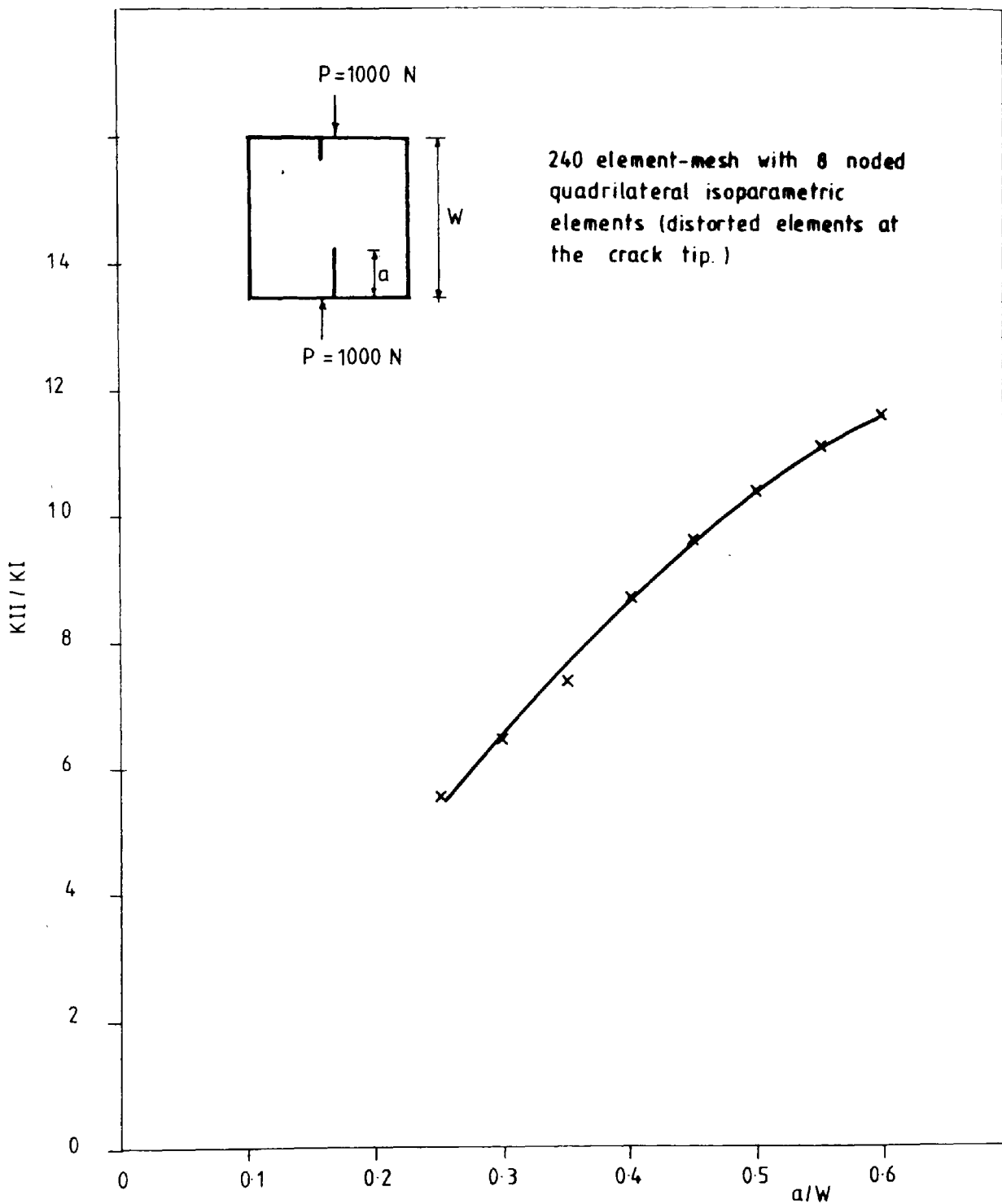


Fig. 4-19 Comparison of  $K_{II}/K_I$  ratios with  $a/W$

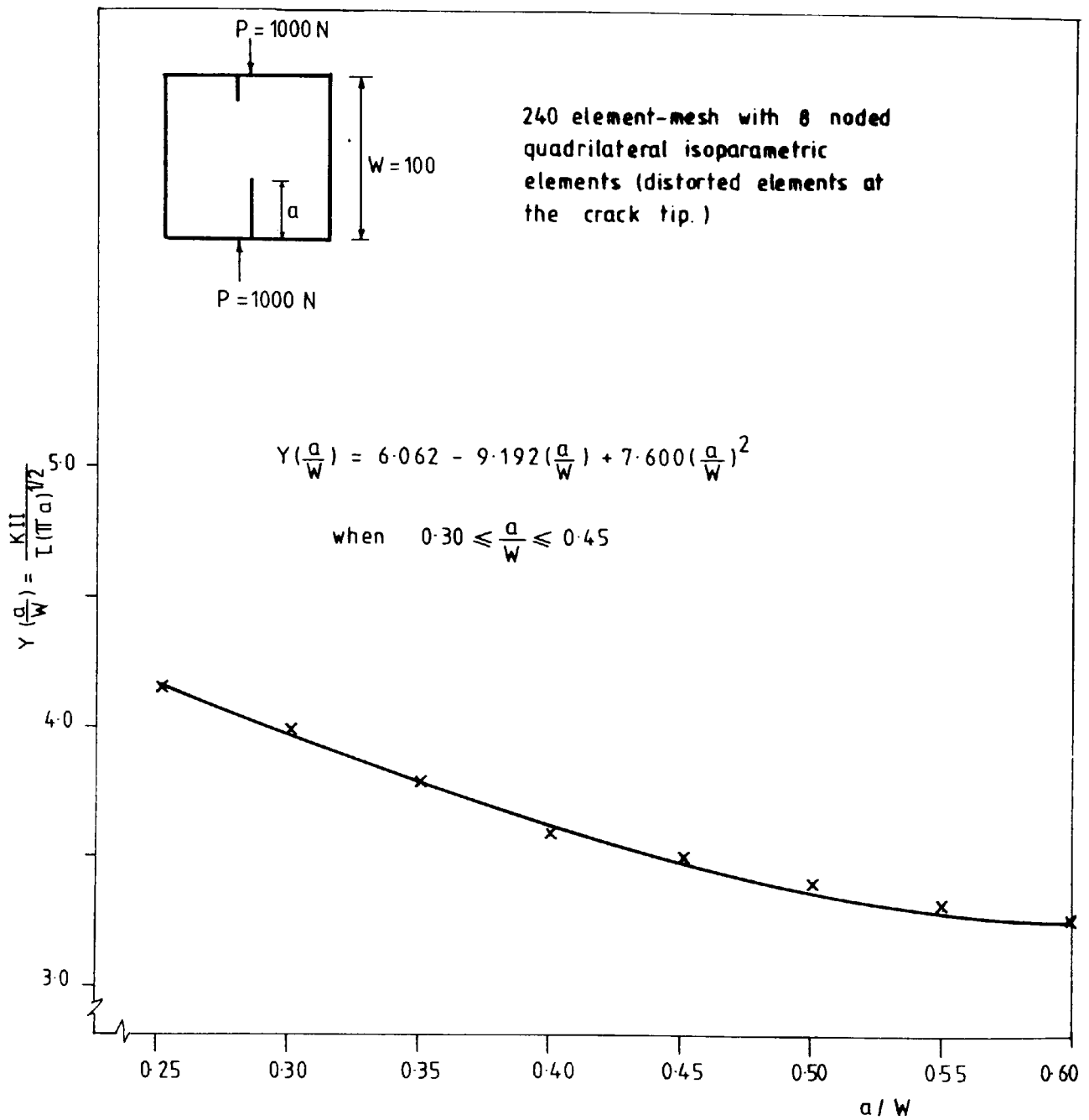
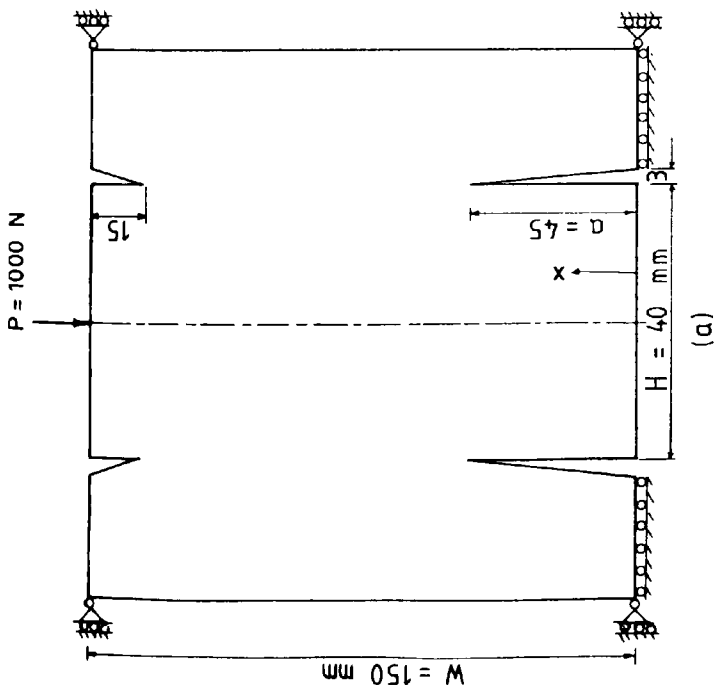
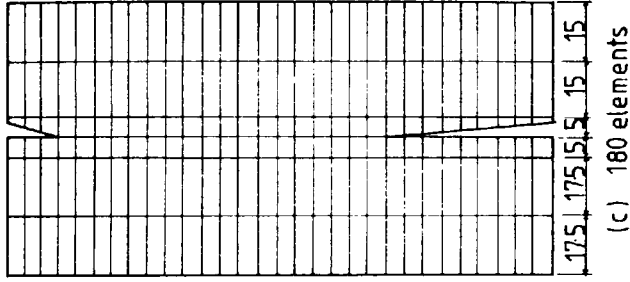


Fig. 4.20 Calibration coefficients  $Y\left(\frac{a}{W}\right)$  in Mode II

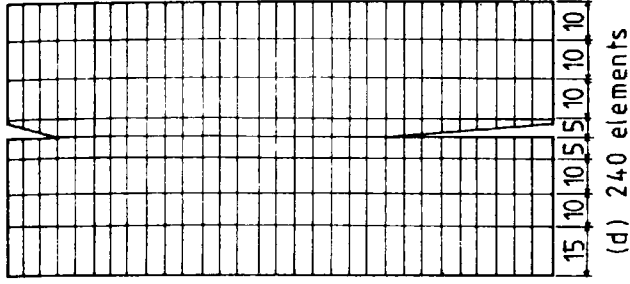




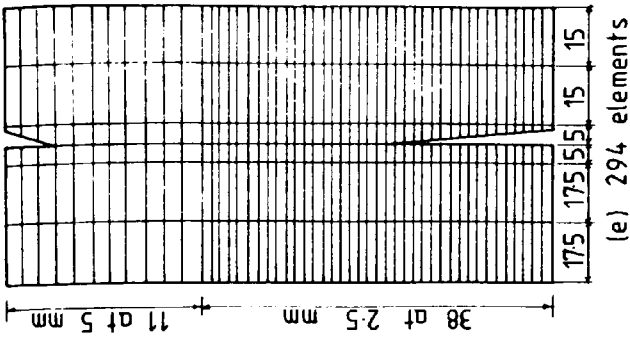
(a)



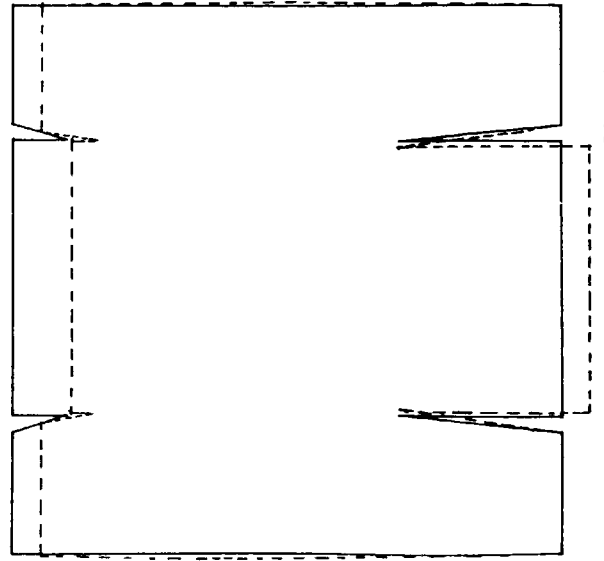
(c) 180 elements



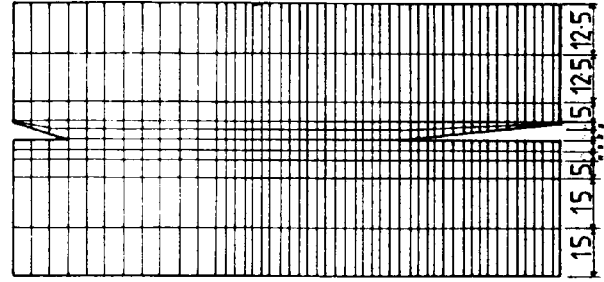
(d) 240 elements



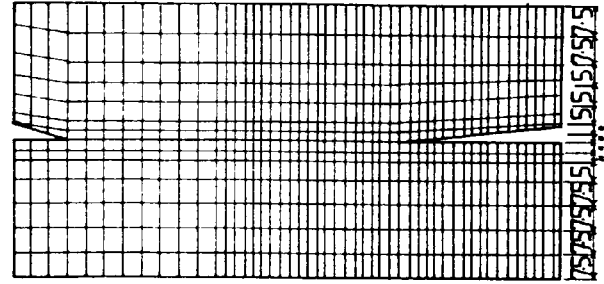
(e) 294 elements



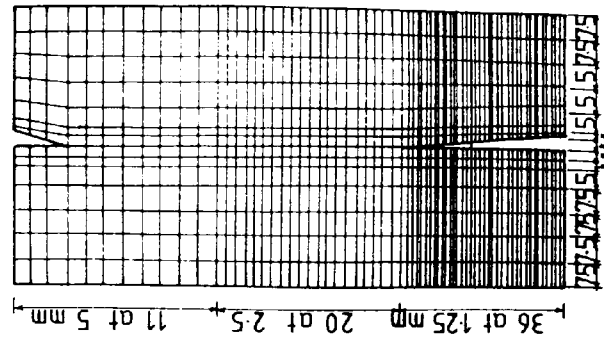
(b) Deformed CS cube



(f) 490 elements



(g) 686 elements



(h) 938 elements

Fig. 4.21 Types of element mesh

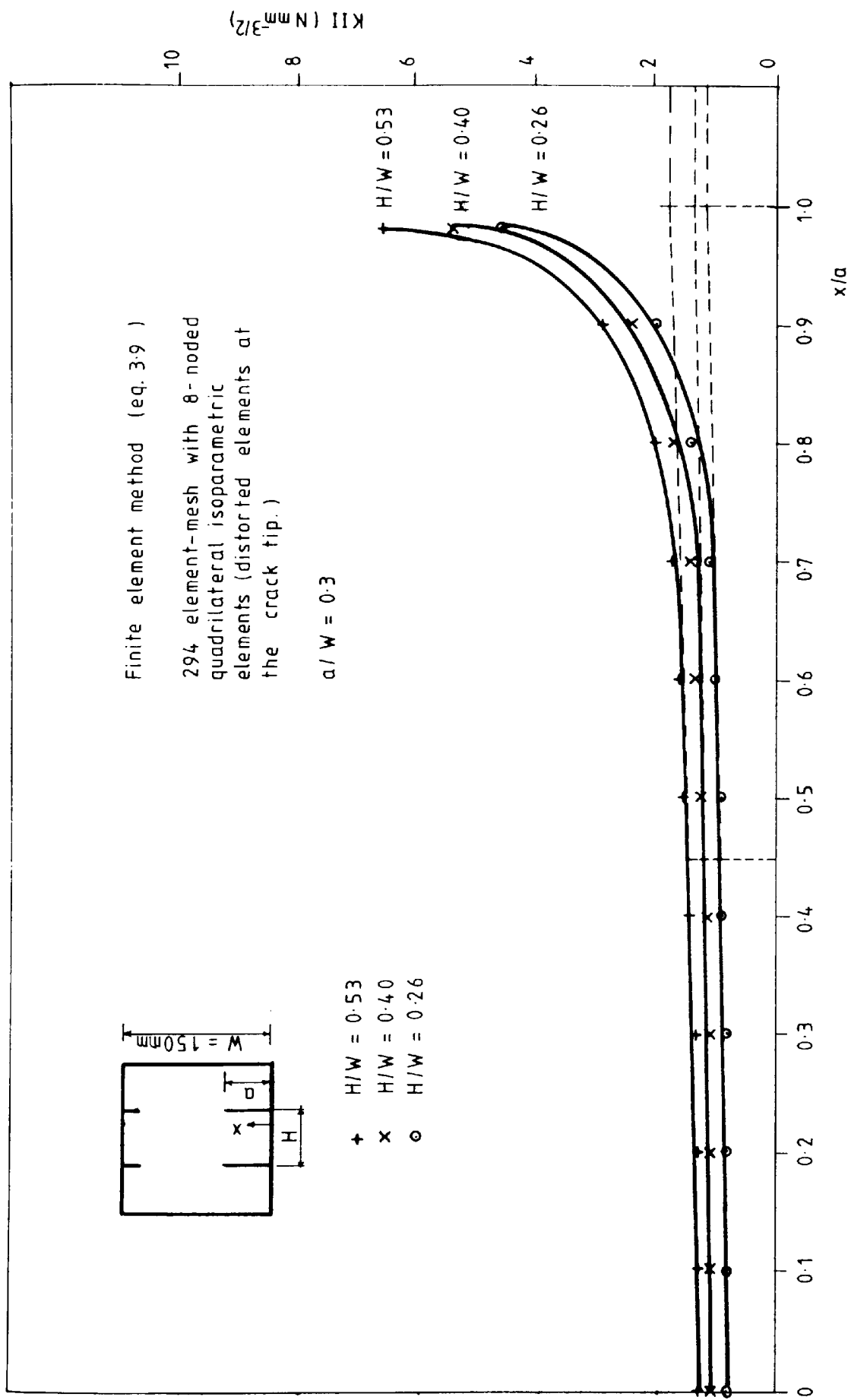


Fig. 4.22 Variation of  $K_{II}$  with  $x/a$

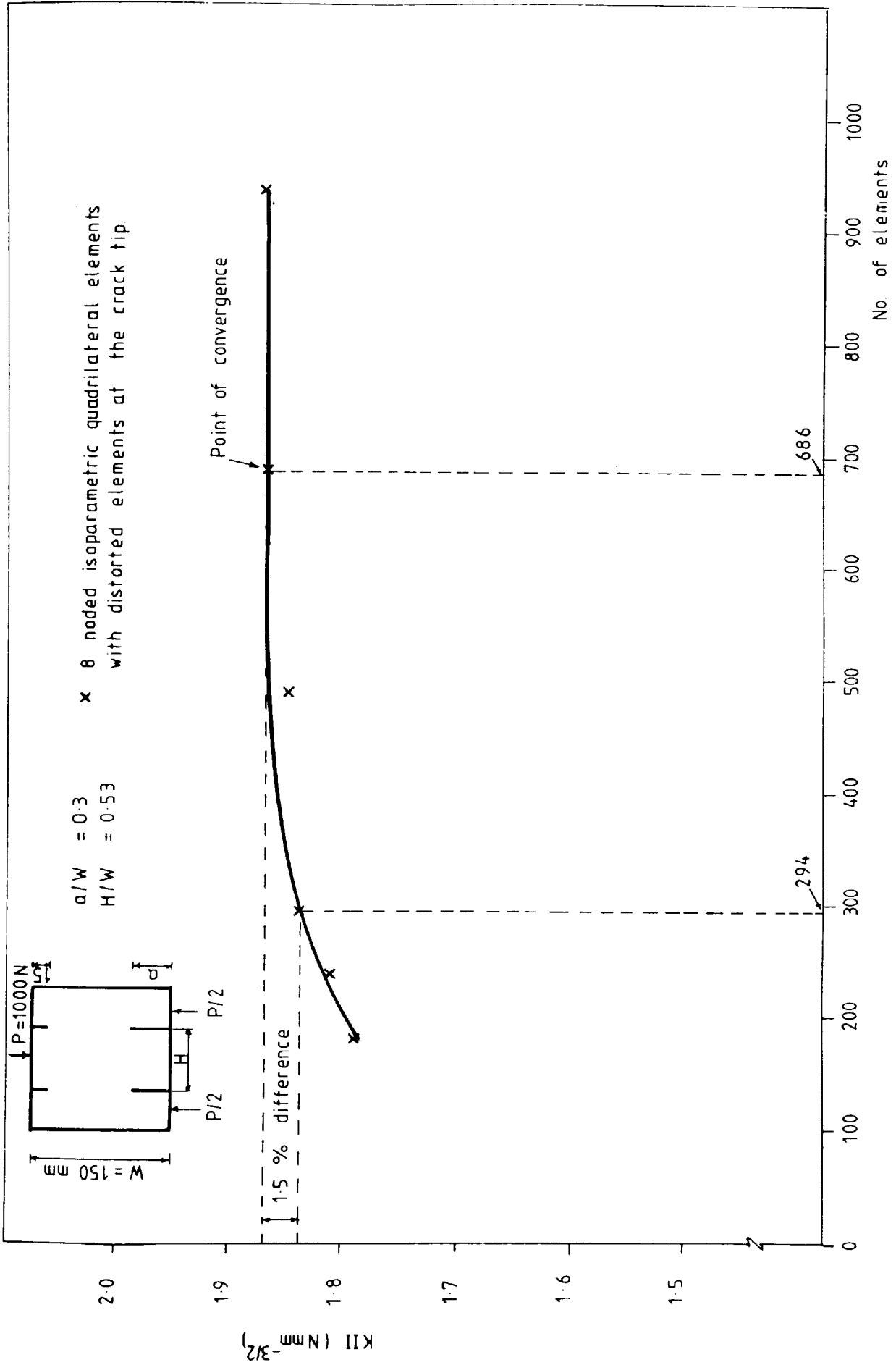


Fig. 4.23 Convergence graph of element-meshes

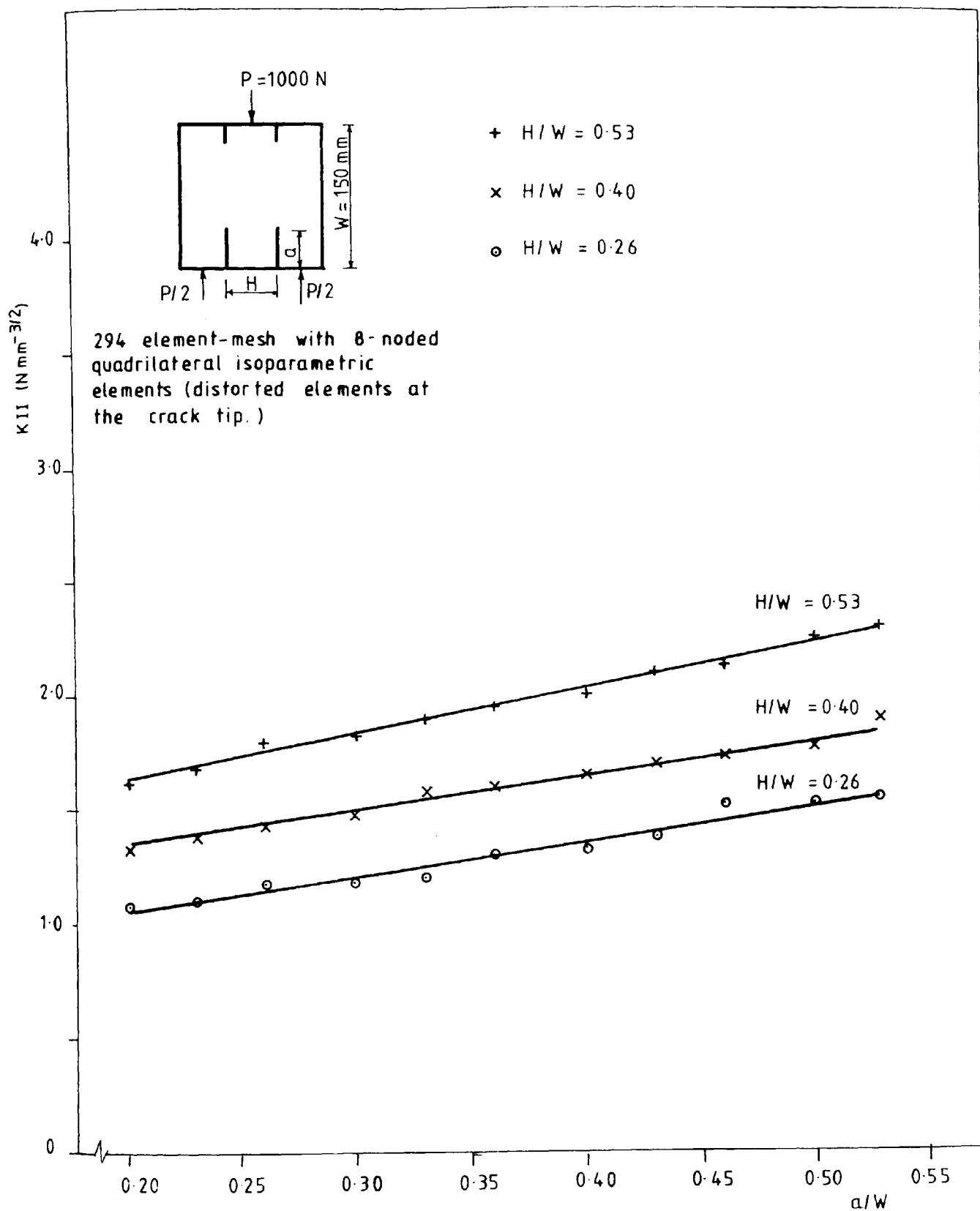


Fig. 4.24 Variation of  $K_{II}$  values with  $a/W$

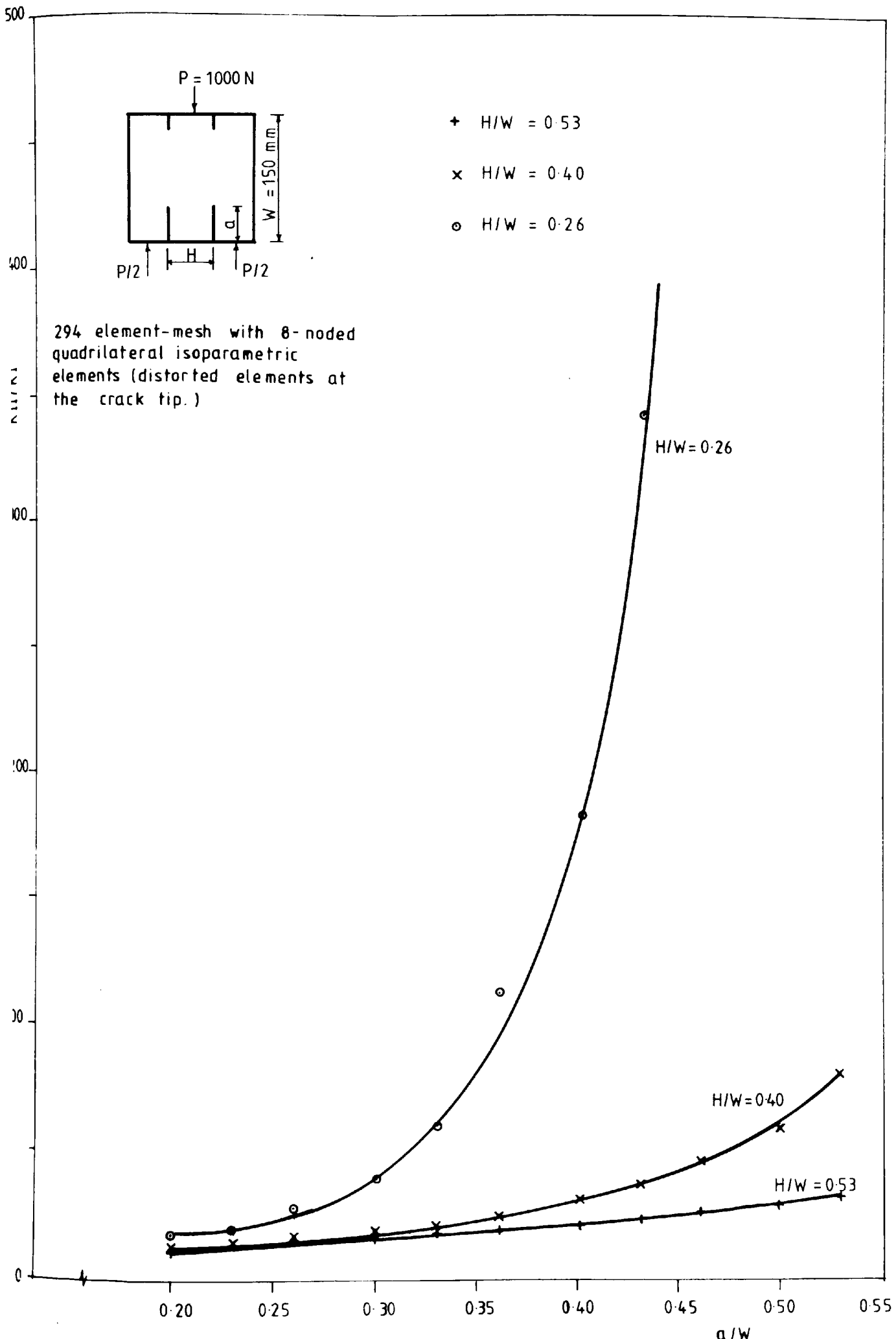


Fig. 4-25 Comparison of KII/KI ratios with a/W

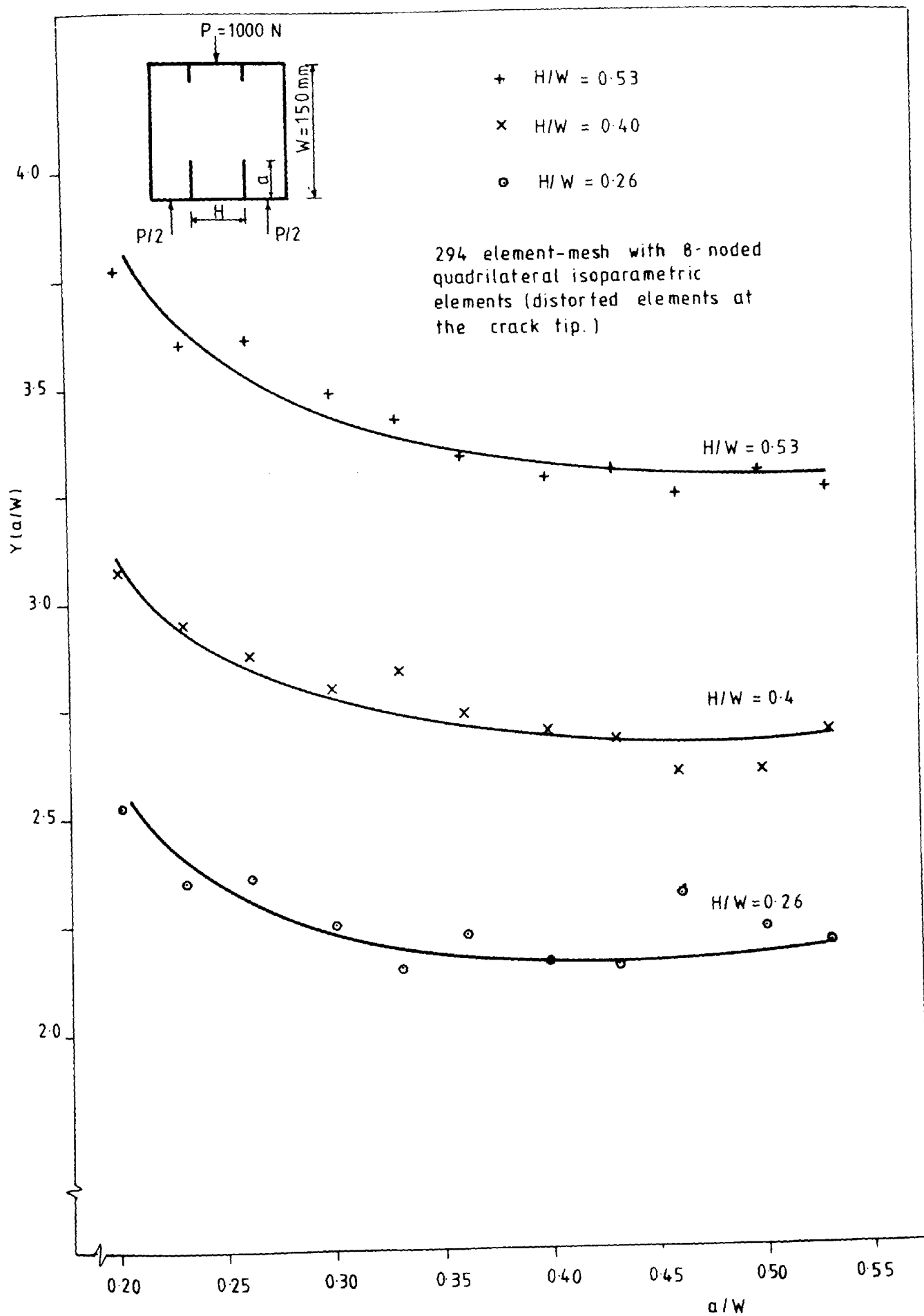


Fig. 4.26 Calibration coefficients in Mode II




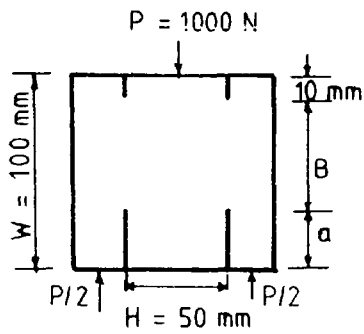
Quadrilateral isoparametric Element type	Equivalent number of constant strain triangular element
 <span data-bbox="502 907 630 952">Linear</span>	8
 <span data-bbox="502 1041 686 1086">Quadratic</span>	16
 <span data-bbox="502 1182 606 1227">Cubic</span>	32

Table 4-1 Comparison of quadrilateral elements with triangular elements



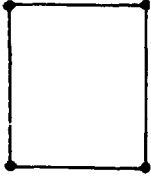
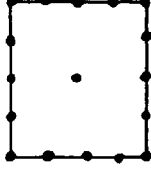
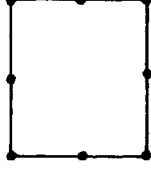
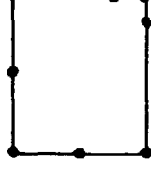
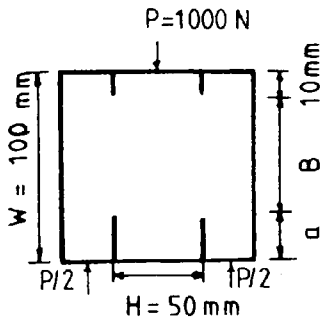
ELEMENT TYPE	NODES	DEGREE OF FREEDOM	$K_{II}$ ( $\text{N mm}^{-3/2}$ )
 Linear (4 nodes)	102	149	2.340
 Quartic (17 nodes)	588	1064	2.480
 Quadratic (8 nodes)	246	418	2.380
 1/4-point at crack tip (8 nodes)	246	418	2.468

Table 4.2 Comparison of the quadrilateral isoparametric elements in terms of  $K_{II}$  values for 60 element mesh ( $H/W = 0.5$  and  $a/W = 0.35$ )





Number of elements	$K_{II} \text{ (N mm}^{-3/2}\text{)}$	
	8-noded quadrilateral isoparametric element	8-noded quadrilateral isoparametric elements (distorted elements at the crack tip)
48	2.358	2.448
60	2.380	2.468
72	2.390	2.458
102	2.417	2.482
144	2.494	2.494
168	2.494	2.494
200	2.494	2.494

Table 4.3 The convergence study of element meshes (100 mm cube  $H/W=0.5$ ,  $a/W=0.35$ )

Distance measured from the top notch (mm)	$a/W = 0.3$		$a/W = 0.35$		$a/W = 0.40$		$a/W = 0.45$	
	Direct stress $\sigma_x$ (KN/m <sup>2</sup> )	Shear stress $\tau_{xy}$ (KN/m <sup>2</sup> )	Direct stress $\sigma_x$ (KN/m <sup>2</sup> )	Shear stress $\tau_{xy}$ (KN/m <sup>2</sup> )	Direct stress $\sigma_x$ (KN/m <sup>2</sup> )	Shear stress $\tau_{xy}$ (KN/m <sup>2</sup> )	Direct stress $\sigma_x$ (KN/m <sup>2</sup> )	Shear stress $\tau_{xy}$ (KN/m <sup>2</sup> )
Top notch								
0	-19.90	22.60	-20.700	23.300	-21.300	24.00	-22.500	25.10
5	-3.79	8.72	-4.010	9.100	-4.170	9.41	-4.430	9.95
10	-2.08	6.61	-2.230	6.980	-2.340	7.27	-2.470	7.78
15	-0.804	5.61	-0.899	5.960	-0.946	6.29	-0.962	6.80
20	-0.351	5.26	-0.393	5.660	-0.387	5.98	-0.289	6.54
25	-0.023	5.10	-0.013	5.540	0.088	5.90	0.315	6.53
30	0.171	5.08	0.291	5.580	0.454	5.99	0.864	6.77
35	0.320	5.15	0.556	5.750	0.820	6.28	1.450	7.38
40	0.477	5.36	0.855	6.140	1.250	6.89	2.220	8.67
45	0.672	5.77	1.200	6.930	1.810	8.23	4.440	13.20
47.5	0.789	6.11	1.440	7.620	2.070	9.51	13.200	22.40
50	0.926	6.58	1.660	8.680	4.020	12.50		
52.5	1.120	7.26	2.700	10.600	11.600	20.80		
55	1.280	8.32	2.860	15.100				
57.5	2.170	10.20	19.900	27.400				
60	2.180	14.60						
62.5	17.700	25.50						

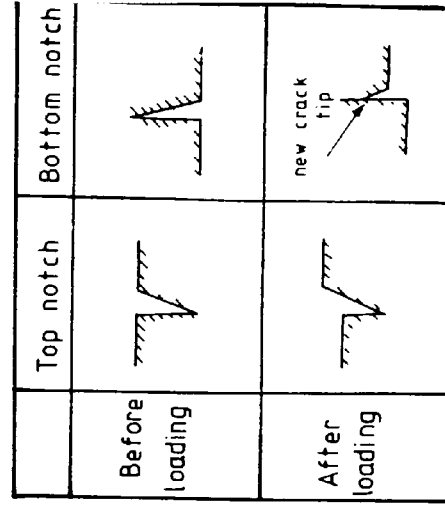
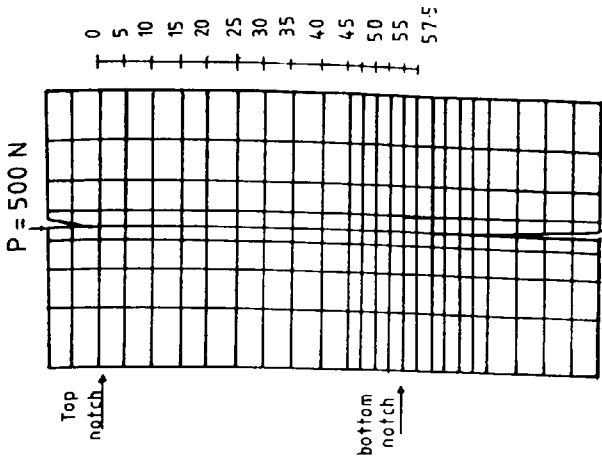
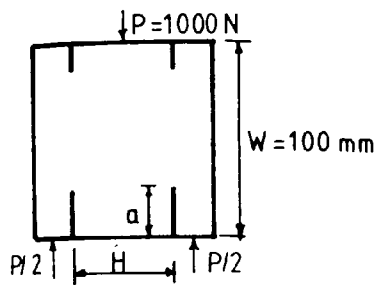
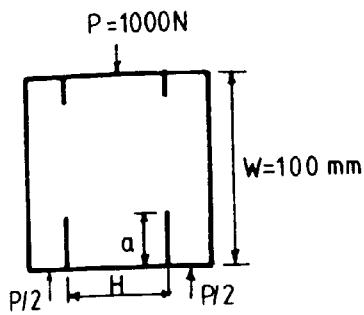


Table 4.4 Direct and shear stresses  
( $H/W = 0.5$ )  
(100 mm double-notched cubes)



$\frac{a}{W}$	H = 50 mm			H = 40 mm			H = 30 mm		
	KII (N mm <sup>-3/2</sup> )	KI (N mm <sup>-3/2</sup> )	$\frac{KII}{KI}$	KII (N mm <sup>-3/2</sup> )	KI (N mm <sup>-3/2</sup> )	$\frac{KII}{KI}$	KII (N mm <sup>-3/2</sup> )	KI (N mm <sup>-3/2</sup> )	$\frac{KII}{KI}$
0.25	2.141	0.216	9.9	1.839	0.185	9.9	1.590	0.132	12.0
0.30	2.329	0.214	10.9	1.993	0.170	11.7	1.733	0.114	15.2
0.35	2.468	0.198	12.5	2.142	0.152	14.1	1.860	0.093	20.0
0.40	2.656	0.169	15.7	2.280	0.124	18.4	1.972	0.066	29.9
0.45	2.786	0.162	17.2	2.416	0.112	21.6	2.085	0.054	38.6
0.50	2.930	0.185	15.8	2.530	0.134	18.9	2.180	0.074	29.5
0.55	3.100	0.173	17.8	2.670	0.116	23.0	2.300	0.056	41.1
0.60	3.250	0.159	20.4	2.820	0.106	26.6	2.140	0.047	51.3

Table 4.5 Estimates of KI, KII and KII/KI for various a/W  
100 mm double-notched cube — 60 element mesh



$\frac{a}{W}$	H = 50 mm			H = 40 mm			H = 30 mm		
	KII ( $\text{N mm}^{-3/2}$ )	KI ( $\text{N mm}^{-3/2}$ )	$\frac{KII}{KI}$	KII ( $\text{N mm}^{-3/2}$ )	KI ( $\text{N mm}^{-3/2}$ )	$\frac{KII}{KI}$	KII ( $\text{N mm}^{-3/2}$ )	KI ( $\text{N mm}^{-3/2}$ )	$\frac{KII}{KI}$
0.25	2.141	0.216	9.9	1.839	0.185	9.9	1.590	0.132	12.0
0.30	2.329	0.214	10.9	1.993	0.170	11.7	1.773	0.114	15.2
0.35	2.468	0.198	12.5	2.142	0.152	14.1	1.860	0.093	20.0
0.40	2.656	0.169	15.7	2.280	0.124	18.4	1.972	0.066	29.9
0.45	2.786	0.162	17.2	2.416	0.112	21.6	2.085	0.054	38.6
0.50	2.820	0.148	19.1	2.500	0.078	32.1	2.120	0.031	68.4
0.55	3.050	0.118	25.8	2.620	0.065	40.3	2.300	0.021	109.5
0.60	3.250	0.104	31.3	2.820	0.060	47.0	2.480	0.020	124.0

Table 4.6 Estimates of KI, KII and KII/KI for various  $a/W$   
 100 mm double-notched cube — 60 element mesh  
 when  $0.50 \leq \frac{a}{W} \leq 0.60$

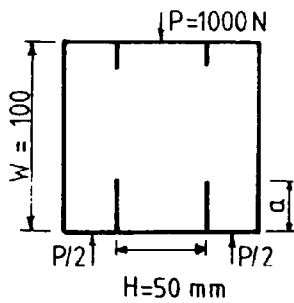
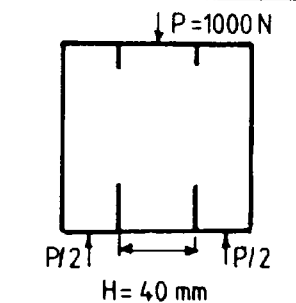
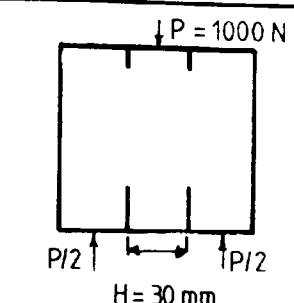
Finite element method (eq.2-25)								
$a$	$\frac{a}{W}$	$K_{II\infty} = \sqrt{\pi a}^{-1/2}$ ( $\text{Nmm}^{-3/2}$ )	KII ( $\text{Nmm}^{-3/2}$ )	$Y\left(\frac{a}{W}\right) = \frac{K_{II}}{K_{II\infty}}$	KII ( $\text{Nmm}^{-3/2}$ )	$Y\left(\frac{a}{W}\right) = \frac{K_{II}}{K_{II\infty}}$	KII ( $\text{Nmm}^{-3/2}$ )	$Y\left(\frac{a}{W}\right) = \frac{K_{II}}{K_{II\infty}}$
25	0.25	0.886	2.141	2.416	1.839	2.076	1.590	1.795
30	0.30	0.971	2.329	2.399	1.993	2.053	1.733	1.785
35	0.35	1.049	2.468	2.353	2.142	2.042	1.860	1.773
40	0.40	1.121	2.656	2.369	2.280	2.034	1.972	1.759
45	0.45	1.189	2.786	2.343	2.416	2.032	2.085	1.754
50	0.50	1.253	2.820	2.251	2.500	1.995	2.120	1.692
55	0.55	1.314	3.050	2.321	2.620	1.994	2.300	1.750
60	0.60	1.373	3.250	2.367	2.820	2.054	2.480	1.806

Table 4.7  $Y\left(\frac{a}{W}\right)$  & KII values for  
 $H = 50, 40, \& 30$  mm.

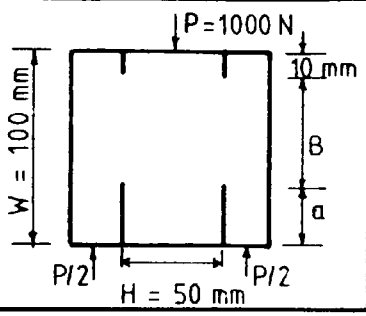
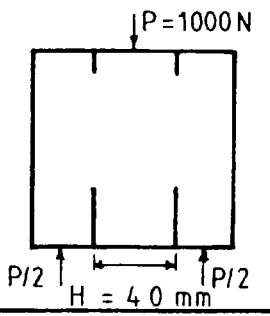
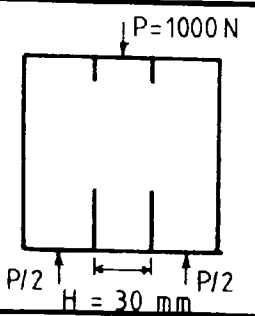
Finite element method (eq.2-25)			
$\frac{a}{W}$	Calibration coefficients $Y\left(\frac{a}{W}\right) = \frac{KII}{L\infty(\pi a)^{1/2}}$		
0.25	2.416	2.076	1.795
0.30	2.399	2.053	1.785
0.35	2.353	2.042	1.773
0.40	2.369	2.034	1.759
0.45	2.343	2.032	1.754
0.50	2.251	1.995	1.692
0.55	2.321	1.994	1.750
0.60	2.367	2.054	1.806
Range	The least square method		
$0.25 \leq \frac{a}{W} \leq 0.60$	$Y\left(\frac{a}{W}\right) = -175.57 + 2787.86\left(\frac{a}{W}\right) - 17824.70\left(\frac{a}{W}\right)^2 + 59571.13\left(\frac{a}{W}\right)^3$	$Y\left(\frac{a}{W}\right) = 0.65 + 25.10\left(\frac{a}{W}\right) - 161.52\left(\frac{a}{W}\right)^2 + 485.87\left(\frac{a}{W}\right)^3 - 696.64\left(\frac{a}{W}\right)^4 + 383.59\left(\frac{a}{W}\right)^5$	$Y\left(\frac{a}{W}\right) = 0.98 + 7.08\left(\frac{a}{W}\right) - 19.62\left(\frac{a}{W}\right)^2 + 16.85\left(\frac{a}{W}\right)^3$
$0.30 \leq \frac{a}{W} \leq 0.45$	Average value		
	$Y\left(\frac{a}{W}\right) = 2.37$	$Y\left(\frac{a}{W}\right) = 2.04$	$Y\left(\frac{a}{W}\right) = 1.77$
	Mode II stress intensity factor		
	$KII = 1.19 \frac{P}{BW} (\pi a)^{1/2}$	$KII = 1.02 \frac{P}{BW} (\pi a)^{1/2}$	$KII = 0.89 \frac{P}{BW} (\pi a)^{1/2}$

Table 4.8  $Y\left(\frac{a}{W}\right)$  values in polynomial & simplified forms  
for  $H = 50, 40 \text{ \& } 30 \text{ mm}$

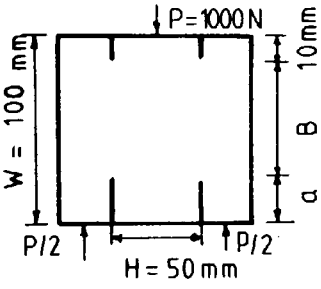
			Boundary collocation method (eq.2.41)		Finite element method (eq.2.25)		Finite element method (eq. 3.9)	
a	$\frac{a}{W}$	$K_{II\infty} = L_{\infty}(\pi a)^{1/2}$ (N mm <sup>-3/2</sup> )	K <sub>II</sub> (N mm <sup>-3/2</sup> )	$Y\left(\frac{a}{W}\right) = \frac{K_{II}}{K_{II\infty}}$	K <sub>II</sub> (N mm <sup>-3/2</sup> )	$Y\left(\frac{a}{W}\right) = \frac{K_{II}}{K_{II\infty}}$	K <sub>II</sub> (N mm <sup>-3/2</sup> )	$Y\left(\frac{a}{W}\right) = \frac{K_{II}}{K_{II\infty}}$
25	0.25	0.886	2.000	2.257	2.141	2.416	2.068	2.334
30	0.30	0.971	2.191	2.256	2.326	2.399	2.275	2.343
35	0.35	1.049	2.366	2.255	2.468	2.353	2.448	2.334
40	0.40	1.121	2.530	2.257	2.656	2.367	2.581	2.302
45	0.45	1.189	2.683	2.257	2.786	2.343	2.746	2.310
50	0.50	1.253	2.828	2.257	2.820	2.251	3.020	2.410
55	0.55	1.314	2.966	2.257	3.050	2.321	3.230	2.458
60	0.60	1.373	3.098	2.256	3.250	2.367	3.540	2.578

Table 4.9 K<sub>II</sub> &  $Y\left(\frac{a}{W}\right)$  values by the boundary collocation and finite element methods for H = 50 mm.

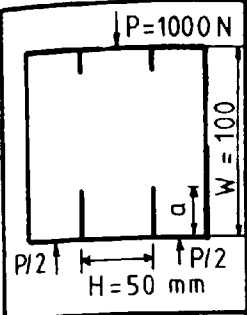
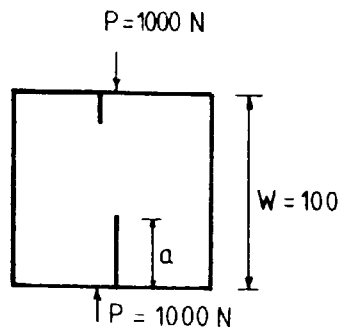
	Boundary Collocation method (eq. 2.41)	Finite element method (eq. 2.25)	Finite element method (eq. 3.9)
$\frac{a}{W}$	Calibration coefficients $Y\left(\frac{a}{W}\right) = \frac{KII}{\sqrt{\infty}(\pi a)^{1/2}}$		
0.25	2.257	2.416	2.334
0.30	2.256	2.399	2.343
0.35	2.255	2.353	2.334
0.40	2.257	2.369	2.302
0.45	2.257	2.343	2.310
0.50	2.257	2.251	2.410
0.55	2.257	2.321	2.458
0.60	2.256	2.367	2.578
Range	The least square method		
$0.25 \leq \frac{a}{W} \leq 0.60$	$Y\left(\frac{a}{W}\right) = 2.29 - 0.27\left(\frac{a}{W}\right) + 0.66\left(\frac{a}{W}\right)^2 - 0.53\left(\frac{a}{W}\right)^3$	$Y\left(\frac{a}{W}\right) = -175.57 + 2787.86\left(\frac{a}{W}\right) - 1782470\left(\frac{a}{W}\right)^2 + 59571.13\left(\frac{a}{W}\right)^3$	$Y\left(\frac{a}{W}\right) = 102.01 - 1574.95\left(\frac{a}{W}\right) + 10146.21\left(\frac{a}{W}\right)^2 - 34109.54\left(\frac{a}{W}\right)^3 + 63133.30\left(\frac{a}{W}\right)^4 - 61053.04\left(\frac{a}{W}\right)^5 + 24133.42\left(\frac{a}{W}\right)^6$
$0.30 \leq \frac{a}{W} \leq 0.45$	Average value		
	$Y\left(\frac{a}{W}\right) = 2.26$	$Y\left(\frac{a}{W}\right) = 2.37$	$Y\left(\frac{a}{W}\right) = 2.32$
	Mode II stress intensity factor		
$KII = 1.13 \frac{P}{BW} (\pi a)^{1/2}$	$KII = 1.19 \frac{P}{BW} (\pi a)^{1/2}$	$KII = 1.16 \frac{P}{BW} (\pi a)^{1/2}$	

Table 4.10  $Y\left(\frac{a}{W}\right)$  values in polynomial & simplified forms for  $H=50$  mm by the boundary collocation & finite element methods.

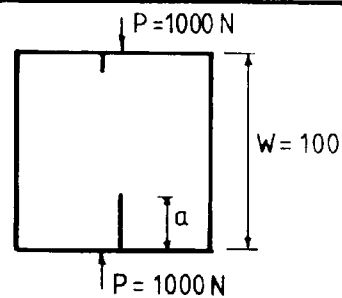




	KII ( $\text{N mm}^{-3/2}$ )
Number of elements	8 - noded quadrilateral isoparametric elements (distorted elements at the crack tip)
100	3.783
240	3.868
640	3.910
1040	3.910

Table 4.11 The convergence study of element meshes  
( $a/W = 0.30$ )

Finite element method  
(eq. 3.9)



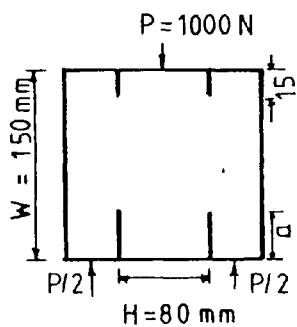
$\frac{a}{W}$	$K_{II\infty} = \sqrt{\pi a}$ ( $Nmm^{-3/2}$ )	KI ( $Nmm^{-3/2}$ )	KII ( $Nmm^{-3/2}$ )	$\frac{KII}{KI}$	$Y\left(\frac{a}{W}\right) = \frac{KII}{\sqrt{\pi a}}$
0.25	0.886	0.648	3.682	5.7	4.156
0.30	0.971	0.600	3.868	6.5	3.984
0.35	1.049	0.540	3.975	7.4	3.789
0.40	1.121	0.459	4.022	8.8	3.588
0.45	1.189	0.426	4.125	9.7	3.469
0.50	1.253	0.409	4.261	10.4	3.401
0.55	1.314	0.395	4.384	11.1	3.336
0.60	1.373	0.389	4.500	11.6	3.277

Range	Calibration coefficients
$0.30 \leq \frac{a}{W} \leq 0.45$	The least square method $Y\left(\frac{a}{W}\right) = 6.062 - 9.192 \left(\frac{a}{W}\right) + 7.600 \left(\frac{a}{W}\right)^2$
$0.25 \leq \frac{a}{W} \leq 0.60$	The least square method $Y\left(\frac{a}{W}\right) = 0.638 + 44.379 \left(\frac{a}{W}\right) - 1871.800 \left(\frac{a}{W}\right)^2 + 308.716 \left(\frac{a}{W}\right)^3 - 179.696 \left(\frac{a}{W}\right)^4$

Mode II stress intensity factor

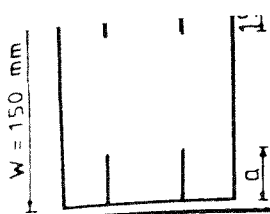
$$KII = Y\left(\frac{a}{W}\right) \frac{P}{2BW} (\pi a)^{1/2}$$

Table 4.12 Estimates of KI, KII, KII/KI & Y(a/W)  
for various a/W



Number of elements	KII ( $\text{Nmm}^{-3/2}$ ) 8-noded quadrilateral isoparametric elements (distorted elements at the crack tip)
180	1.790
240	1.810
294	1.841
490	1.848
686	1.869
938	1.869

Table 4.13 The convergence study of element meshes for 150 mm cube ( $a/W = 0.3$ )



$\frac{a}{W}$	H = 80 mm			H = 60 mm			H = 40 mm		
	K <sub>II</sub> (N mm <sup>-3/2</sup> )	K <sub>I</sub> (N mm <sup>-3/2</sup> )	$\frac{K_{II}}{K_I}$	K <sub>II</sub> (N mm <sup>-3/2</sup> )	K <sub>I</sub> (N mm <sup>-3/2</sup> )	$\frac{K_{II}}{K_I}$	K <sub>II</sub> (N mm <sup>-3/2</sup> )	K <sub>I</sub> (N mm <sup>-3/2</sup> )	$\frac{K_{II}}{K_I}$
0.20	1.630	0.145	11.2	1.330	0.100	13.3	1.090	0.065	16.8
0.23	1.680	0.128	13.1	1.380	0.090	15.3	1.100	0.048	22.9
0.26	1.800	0.120	15.0	1.430	0.083	17.2	1.180	0.033	35.8
0.30	1.841	0.118	15.6	1.480	0.078	19.0	1.190	0.030	39.7
0.33	1.900	0.108	17.6	1.580	0.068	23.2	1.200	0.020	60.0
0.36	1.950	0.100	19.5	1.600	0.062	25.8	1.300	0.012	113.0
0.40	2.010	0.095	21.2	1.650	0.050	33.0	1.320	0.007	183.3
0.43	2.100	0.090	23.3	1.700	0.045	37.8	1.370	0.004	342.5
0.46	2.140	0.080	26.9	1.720	0.035	49.1	1.520	0.002	800.0
0.50	2.250	0.075	30.0	1.780	0.027	50.9	1.530	0.001	1275.0
0.53	2.300	0.070	32.9	1.900	0.023	82.6	1.550	0.000	$\infty$

Table 4-14 Estimates of K<sub>I</sub>, K<sub>II</sub>/K<sub>I</sub> for various a/W

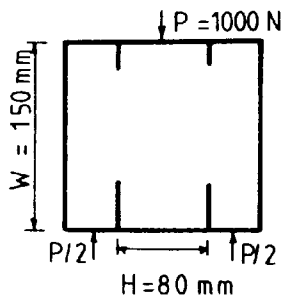
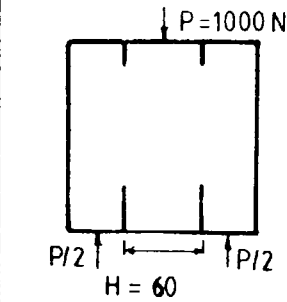
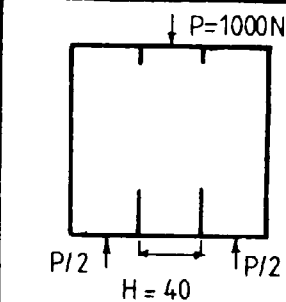
Finite element method (eq. 3-9)								
$a$	$\frac{a}{W}$	$K_{II\infty} = \sqrt{\pi a}$ ( $N\text{ mm}^{-3/2}$ )	$K_{II}$ ( $N\text{ mm}^{-3/2}$ )	$Y\left(\frac{a}{W}\right) = \frac{K_{II}}{K_{II\infty}}$	$K_{II}$ ( $N\text{ mm}^{-3/2}$ )	$Y\left(\frac{a}{W}\right) = \frac{K_{II}}{K_{II\infty}}$	$K_{II}$ ( $N\text{ mm}^{-3/2}$ )	$Y\left(\frac{a}{W}\right) = \frac{K_{II}}{K_{II\infty}}$
30	0.20	0.431	1.630	3.782	1.330	3.086	1.090	2.529
35	0.23	0.466	1.680	3.605	1.380	2.961	1.100	2.361
40	0.26	0.498	1.800	3.614	1.430	2.871	1.180	2.369
45	0.30	0.528	1.841	3.487	1.480	2.803	1.190	2.254
50	0.33	0.557	1.900	3.411	1.580	2.837	1.200	2.154
55	0.36	0.584	1.950	3.339	1.600	2.740	1.300	2.226
60	0.40	0.610	2.010	3.295	1.650	2.705	1.320	2.164
65	0.43	0.635	2.100	3.307	1.700	2.677	1.370	2.157
70	0.46	0.659	2.140	3.247	1.720	2.610	1.520	2.307
75	0.50	0.682	2.250	3.299	1.780	2.610	1.530	2.243
80	0.53	0.705	2.300	3.262	1.900	2.695	1.550	2.199

Table 4-15  $Y(a/W)$  &  $K_{II}$  values for  $H=80, 60$  &  $40$  mm.

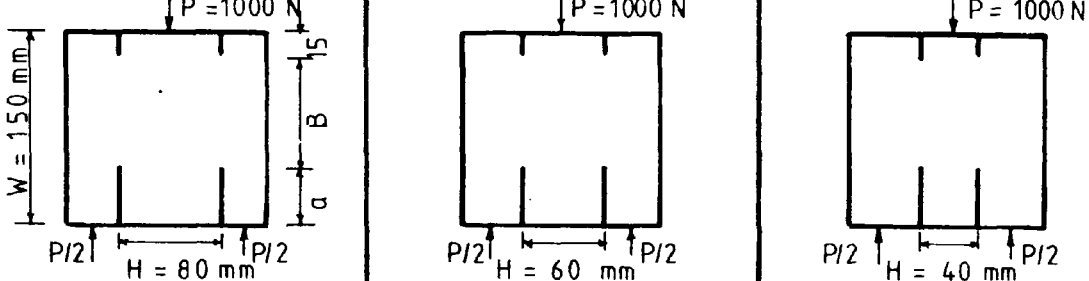
Finite element method (eq. 3-9)			
$\frac{a}{W}$	Calibration coefficients $Y\left(\frac{a}{W}\right) = \frac{K_{II}}{T_{\infty} (\pi a)^{1/2}}$		
0.20	3.782	3.086	2.529
0.23	3.605	2.961	2.361
0.26	3.614	2.871	2.369
0.30	3.487	2.803	2.254
0.33	3.411	2.837	2.154
0.36	3.339	2.740	2.226
0.40	3.295	2.705	2.164
0.43	3.307	2.677	2.157
0.46	3.247	2.610	2.307
0.50	3.299	2.610	2.243
0.53	3.262	2.695	2.199
Range	The least square method		
$0.30 \leq \frac{a}{W} \leq 0.53$	$Y\left(\frac{a}{W}\right) = 4.70 - 5.86\left(\frac{a}{W}\right) + 5.98\left(\frac{a}{W}\right)^2$	$Y\left(\frac{a}{W}\right) = 3.82 - 4.69\left(\frac{a}{W}\right) + 4.71\left(\frac{a}{W}\right)^2$	$Y\left(\frac{a}{W}\right) = 3.33 - 5.52\left(\frac{a}{W}\right) + 6.60\left(\frac{a}{W}\right)^2$
	Mode II stress intensity factor		
	$K_{II} = Y\left(\frac{a}{W}\right) \frac{P}{2BW} (\pi a)^{1/2}$	$K_{II} = Y\left(\frac{a}{W}\right) \frac{P}{2BW} (\pi a)^{1/2}$	$K_{II} = Y\left(\frac{a}{W}\right) \frac{P}{2BW} (\pi a)^{1/2}$

Table 4.16  $Y\left(\frac{a}{W}\right)$  values in polynomial & simplified forms  
for  $H = 80, 60$  &  $40$  mm

## CHAPTER 5

### AN EXPERIMENTAL INVESTIGATION INTO THE MODE II FRACTURE TOUGHNESS OF MORTAR AND SOIL-CEMENT

#### 5.1 INTRODUCTION

The application of fracture mechanics to the Mode I type of failure of concrete and cement composites has recently received considerable attention. Most of these investigations have been directed towards the determination of the fracture toughness of cementitious materials failing in tension and specimens with preformed notches. A considerable amount of work has also been done in studying the Mode II type of failure in cementitious materials as these materials are generally weak in shear. Debatable results, however, have been reported from these studies. Some investigations have concluded that linear elastic fracture mechanics is applicable to cementitious materials because the fracture toughness of these materials is independent of crack growth and specimen size. Others concluded that it is not applicable because the fracture toughness of such materials is dependent on notch size.

The aim of this study is to determine a suitable test geometry and consequently the fracture toughness,  $K_{IIC}$ , in the shear mode of failure for mortar and soil-cement. The  $K_{IIC}$  values were determined using both the stress intensity factor  $K$  approach and the strain energy release rate  $G$  approach. These are subsequently compared with other reported results.

The experimental work was divided into the following test series.

#### Development of test equipment in compression

- Test series one - Fracture tests on mortar cubes using compressive platens made in the Department of Civil Engineering and Building, The Polytechnic of Wales.
- Test series two - Using the INSTRON compressive platens and a simply designed load rig.

#### Determination of fracture toughness

- Test series three - 100mm double-notched mortar cubes using the INSTRON compressive platens and the load rig.
- Test series four - 100mm single-notched mortar cubes using the INSTRON compressive platens.
- Test series five - 100mm double-notched soil-cement cubes using the INSTRON compressive platens and the load rig.
- Test series six - 100mm single-notched soil-cement cubes using the INSTRON compressive platens



## 5.2 GENERAL PROPERTIES OF MORTAR AND COMPACT SHEAR FRACTURE TEST PROCEDURES

### Preparation of mortar

Mortars can be considered as composite materials in which sand particles are embedded in a matrix of hardened cement paste. The matrix composition of mortar used in this study was 1:3:0.45 (cement:sand:water) and the mix was

cement	=	10 Kg
sand	=	30 Kg
water	=	45 Kg

In order to maintain the same quality of mortar the following mixing procedures were adopted. The sand and cement were dry mixed in a 0.05 cubic metre pan mixer for one minute to ensure a thorough mix. The required amount of water was added gradually and mixed for a further two minutes.

100mm mortar cubes were prepared by placing the mortar into 100mm concrete cube moulds in two layers, each layer received one minute of compaction on a vibrating table. The specimens were stripped from the moulds after 24 hours and cured in water at a constant temperature of 22<sup>0</sup>C for 28 days.

Cylinders 150mm diameter x 300mm were cast vertically in three layers and each layer received one minute of compaction on a vibrating table. The specimens were cured as before.

### General properties of mortar

The general properties of the mortar used in this study were determined by finding the bulk density, compressive strength and static modulus of elasticity.

The bulk densities of the 100mm mortar cubes were found by weighing the cubes both in air and water using the following expression :

$$\text{bulk density} = \frac{(\text{cube mass in air}) \times (\text{water density})}{(\text{cube mass in air}) - (\text{cube mass in water})}$$

42 cubes which were taken in random from different mixes were tested and the results are shown in Table 5.2. The average density was taken as  $2164.3 \text{Kg/m}^3$  and the difference between the highest and lowest density was only 8% indicating that the quality of the mortar was fairly constant.

The compression tests on 100mm mortar cubes were carried out in an Avery-Denison 7226 testing machine. All the cubes were tested at a compression rate of  $150 \text{kN/mm}$  or  $0.25 \text{N/mm}^2/\text{s}$ . according to BS1881 (32). Results of the test are shown in Table 5.2 and the average compressive strength was  $41.83 \text{MN/m}^2$ .

Standard cylinders (150mm diameter x 300mm high) were tested in an Avery testing machine to determine the static modulus of elasticity according to BS1881 (33). The average modulus of elasticity of mortar was taken as  $33330 \text{N/mm}^2$  (see Table 5.2).

### Insertion of notches

For compact shear fracture test purposes, the 100mm mortar cubes were pre-notched (after 48 hours of curing) using a Clipper Masonry saw fitted with a 253mm diameter diamond-edge steel blade as shown in Plate 5.1. The notches were found to be 3mm wide.

The general configuration of the double-notched cube is shown in Figure 5.1 with the notch spacing  $H = 50$ , 40 and 30mm. For each notch spacing, the notch depths on the upper surface were kept at 10mm and the notch depths on the lower surface were varied from 30mm to 45mm in 5mm increments. The single-notched cubes which have only one notch on both the upper and lower surfaces were prepared in the same manner as the double-notched cubes.

### Compact shear fracture tests

The trial tests on 100mm mortar cubes and prisms with various notch depths and spacings were carried out in the Avery testing machine.

The compact shear fracture tests on 100mm double and single-notched cubes were carried out in the INSTRON 1251 materials testing machine. This is an electro-hydraulic closed-loop servo system consisting of three main units : a loading frame, an electronic control and measurement monitoring console and a hydraulic power pack. The load capacity is 100kN for the dynamic testing mode. All the tests were carried out at nominal room temperature using displacement control in the dynamic testing mode. The specimens were positioned

between the platens as shown in figure 5.1. The top platen was stationary while the bottom platen(which has a maximum stroke of 15mm) moved at a constant rate of 0.003mm/s upwards. The results of the compressive load against the displacement of the bottom platen were recorded autographically.

### 5.3 TRIAL TESTS ON 100mm MORTAR CUBES AND PRISMS

Research work in the Mode II shear type of failure of a double-notched cube has been initiated in the Department of Civil Engineering, Polytechnic of Wales. The present work is based on the initial study of finite element analysis on cubes with various notch spacings and depths. Before full scale experiments were carried out to verify the findings of the finite element analysis, trial tests were carried out to investigate if the shear type of failure occurred on the modified cubes and prisms. All the tests were carried out in the Avery testing machine.

Table 5.3a shows the failure patterns of the cubes with various notch arrangements. Drawings 1 to 3 show the cube with a single notch on opposite surfaces with the compressive load perpendicular to the notch depths. Drawing 1 shows a failure pattern with a crack joining the tips of the notches. Finite element analysis has to be employed to judge if the Mode II shear failure is dominant. Drawings 2 and 3 show complex failure patterns and shear failure was ruled out in this notch arrangement.

Drawings 4 and 5 show the cubes with a pair of double notches on opposite surfaces and the compressive load was perpendicular to the notch depth. No significant Mode II shear failure patterns were recorded in this notch arrangement.

Drawings 6 to 8 show the cubes with a single notch and the compressive load was in line with the notch depth. Crack patterns were recorded with different support conditions. Finite element analysis is necessary to study the mode of failure of these cubes, because the cubes were assumed to be under 3-point bending.

Table 5.3b shows the failure patterns of 100 x 100 x 250mm mortar prisms. Drawing 9 shows a prism with a single notch on one surface and the compressive load was in line with the notch depth. The prism was supported by two circular bars in order to initiate a crack from the notch tip. Finite element analysis has to be used to finalise the result.

Drawings 10 to 13 show the prisms with a pair of double-notched on both the upper and lower surfaces and the compressive load was in line with the notch depths. All the prisms failed with broken supports and no cracks were recorded joining the upper notches to the lower notches expected in this arrangement for a Mode II shear failure.

It can be concluded from the trial tests that the cubes shown in Table 5.3a appeared to produce desirable shear patterns for the Mode II type of failure except for the cubes with double notches

on opposite faces (drawings 4 and 5). Finite element analysis is necessary in order to obtain more information on whether a Mode II failure occurs. Likewise encouraging results were obtained from the prisms with one notch (shown in Table 5.3b). Again this is dependent on more numerical analysis before constructive conclusions can be drawn. This is not the case for the double-notched prisms which appeared to be broken at the supports when loaded.

#### 5.4 DEVELOPMENT OF TEST EQUIPMENT

##### 5.4.1 Test Series One - using Departmental made Compressive Platens

The aim of this work was to determine whether the test equipment was suitable to produce a Mode II type of shear failure.

The tests were carried out in the INSTRON testing machine using the compressive platens which were made in the Department of Civil Engineering, Polytechnic of Wales (see Figure 5.1). Displacement control in the dynamic testing mode was used. The 100mm mortar cubes used in the test included those with notch spacing  $H = 50$  , 40 and 30mm . For each notch spacing, the lower notch depth was varied from 30mm to 45mm in 5mm increments.

#### Discussion of test results

In the compact shear fracture tests on 100mm mortar cubes with notch spacing  $H = 50$  , 40 and 30mm and various lower notch depths, four types of failure pattern were recorded during the tests. They were as follows :

- (a) A small inclined crack first formed at the tip of a lower notch. This crack grew both in size and in length with increasing load until failure took place when the cube was split into two parts (Figure 5.2(a)).
- (b) A small inclined crack was located at the tip of a lower notch and propagated with increasing load. When failure occurred two cracks were found on the cube which was split into three parts. One of the cracks originated from the initial inclined crack, the other started from the tip of the lower notch and finished at the tip of the upper notch (Figure 5.2(b)).
- (c) A small inclined crack formed at the tip of a lower notch. The crack grew in size and length with the increase of load. When failure occurred the cube was broken into two parts connecting the tips of the upper notch and the lower notch (opposite to the one with an inclined crack, Figure 5.2(c)).
- (d) A small inclined crack formed at the tip of a lower notch. The crack grew in length and size as the load increased. When failure occurred the cube was broken into three parts which showed the shear cracks started from the tips of the lower notches and finished at the tips of the upper notches (Figure 5.2(d)). This type of failure was called double shear because two shear cracks were formed during testing.

Table 5.4 shows the details of the geometries and types of failure of the mortar cubes. The majority of the cubes failed in a similar manner to the split cube condition where the cubes were split into two halves and only 9.2% failed with double shear cracks under the shear loading condition. During the course of the tests, it was noticed that the compressive platens, manufactured in the Department, failed to provide an even load onto the cube, because once the upper and lower compressive platens were set parallel to each other, they would remain so, but the cubes did not always have absolutely parallel surfaces.

A typical plot of the compressive load against displacement for the cubes with double shear cracks is shown in Figure 5.3. The first peak on the trace shows a sudden 'pop-in' load  $P_1$  which showed the displacement increasing under decreasing load. The second peak represents the failure load. It is noticed that this load-displacement plot of mortar cubes has some similarity to the stress-strain curve of mild steel under tensile test and the load-displacement curve of the compact shear cube was taken as analogous to the one with compact tension specimen. The optimum load was determined by connecting the 5% secant line to the curve (indicated  $P_{(connected)}$  in Figure 5.3) as recommended by the ASTM (34).

The Mode II fracture toughness values were determined using equations (4.8-4.10) obtained from the finite element analysis as summarised in Table 5.5. Since 9.2% of the test failed with double



shear cracks, these results only provide a record of the test but do not have any significant value. It can be concluded that Mode II type of failure was not achieved under this load arrangement, mainly because the Departmental made compressive platens were not able to provide even load on cube surfaces.

#### 5.4.2 Test series two - using INSTRON compressive platens

The aim of this test was to improve the test equipment in order to produce Mode II type of failure for mortar cubes. It was shown in Test series one that the Departmental made compressive platens failed to provide even load and horizontal restraints were recommended at the cube supports in order to eliminate the "split-cube" condition.

These platens were replaced by two 300mm diameter steel INSTRON compressive platens which were specially purchased for this project (see Figure 5.4). Each platen is bolted to the main loading frame of the INSTRON testing machine. These platens not only provide secure surfaces, they can also be tilted individually to provide parallel surfaces to the cubes. A simply designed rig was also used in this test series to provide horizontal restraints at the cube supports (see Plate 5.3). The rig is made of five parts as numbered in Figure 5.4 and an isometric view of it is also shown. Part 2 can be adjusted for different notch spacings by sliding through the slots of parts 3 and 4.

The tests were again carried out using displacement control in the dynamic testing mode at a compression rate of 0.003mm/s.

### Discussion of test results

Work was carried out to test CS cubes for notch spacing  $H = 50\text{mm}$  with the notch depth varying from 30mm to 45mm in 5mm increments. 12 mortar cubes were tested for each notch depth, a total of 48 cubes tested in all. Two types of failure were recorded. These were single shear (Figure 5.2(c)) and double shear (Figure 5.2(d)) as summarised in Table 5.6. Around 60% of the cubes failed with double shear cracks. The load-displacement curves were plotted autographically with loads  $P_1$  (pop-in) and  $P_{\text{max}}$  (at failure) recorded. Figure 5.5 shows a typical load-displacement curve for a mortar cube with notch spacing  $H = 50$  and notch depth  $a = 30\text{mm}$ .

As described in Test series one, the corrected load  $P(5\%)$  was used as the critical load in the determination of fracture toughness. The stress intensity factor  $K$  approach and the strain energy release rate  $\mathcal{G}$  approach were employed in the determination of fracture toughness values for mortar.

For the stress intensity factor  $K$  approach, fracture toughness values were evaluated using equation (4.8) obtained from the finite element analysis.

$$K_{II} = 1.19 \frac{P}{BW} (\pi a)^{\frac{1}{2}}$$

where  $P$  is the  $P(5\%)$ . Other notations are shown in Figure 5.2(e). The fracture toughness values  $K_{IIC}$  for various notch ratios  $a/W$  are tabulated in Table 5.7.

For the strain energy release rate  $\mathcal{G}$  approach, fracture toughness values were evaluated from the equation

$$K_{II} \left( \frac{\mathcal{G} E}{1-\nu^2} \right)^{\frac{1}{2}} \quad (5.1)$$

where  $\mathcal{G}$  = energy release rate

$$= \frac{WD}{A}$$

WD = work done during crack propagation

= (area under  $P(5\%)$  of the load-displacement curve)

A = crack surface area

=  $2(B \times W)$  (see Figure 5.2(e))

E = Young's modulus

=  $10000\text{N/mm}^2$  (This value was taken prior experimentally determined E was available)

$\nu$  = Poisson's ratio

= 0.25

The fracture toughness values were determined and tabulated in Table 5.7 for mortar cubes using the  $K$  approach and the  $\mathcal{G}$  approach. A comparison of the results obtained by the two methods show that the  $K$  values by the finite element method are 26% to 38% larger than those obtained by the energy method.

It can be concluded from this test series that the cubes failing in double shear improved from 9.2% in test series one to 60% in this test series using the INSTRON compressive platens and the simply designed load rig.

The fracture toughness values were determined using both the stress intensity factor  $K$  approach (finite element method) and the strain energy release rate  $G$  approach. The results show a 26% to 38% difference in fracture toughness values between the two methods. This high percentage difference may be explained as follows :

- (a) The corrected load  $P(5\%)$  which is obtained by drawing a 5% secant line in a load-displacement curve is widely recommended as the critical load for a compact tension specimen, but may not be applicable to the load-displacement curves of a compact shear specimen because the failure mechanism in compression is more complicated than in tension. The 'pop-in' load  $P_1$  on the load-displacement curve when an inclined crack is formed may be used as the critical load in the determination of fracture toughness because this represents the appearance of the first crack.
- (b) The Young's Modulus  $E$  was assumed to be  $10000\text{N/mm}^2$  in the analyses. Since the energy method is directly influenced by this value, tests are recommended to determine the  $E$  value experimentally.

- (c) The specimen geometry of notch spacing  $H = 50\text{mm}$  used in this test may not be the best geometry to produce Mode II type of failure. Therefore different notch spacings and depths need to be tested.

#### 5.5 DETERMINATION OF FRACTURE TOUGHNESS FOR 100mm DOUBLE-NOTCHED MORTAR CUBES - TEST SERIES THREE

Tests were carried out on mortar cubes with notch spacing  $H = 50$ , 40 and 30mm. For each notch spacing, the lower notch depth was varied from 30mm to 45mm in 5mm increments. 12 cubes were used per notch depth, a total of 144 tested in all. The displacement control in the dynamic testing mode of the INSTRON testing machine was used with the compression rate kept at 0.003mm/s.

Fracture toughness values of the above specimen geometries were determined by the stress intensity factor  $K$  approach (finite element method) and the strain energy release rate  $\mathcal{G}$  approach. The evaluations were based on the 'pop-in' load  $P_1$  and the failure load  $P_{\max}$  and the results were compared using the equation derived by Chisholm and Jones (19).

### Discussion of test results

For all the tests, 58% failed in double shear for notch spacing  $H = 50 \text{ mm}$ , 80% for  $H = 40 \text{ mm}$  and 100% for  $H = 30 \text{ mm}$ . For a double shear failure, it was observed that a hairline inclined crack first developed at one of the bottom notches corresponding to the 'pop-in' load  $P_1$  (Figure 5.6) and subsequently the shear cracks, parallel with the line of loading, developed rapidly before sudden catastrophic failure ( $P_{\max}$ ). Plate 5.4 shows the typical crack patterns of the cubes and Plate 5.5 shows a typical crack surface of a cube.

The fracture toughness values of the specimens were determined using the stress intensity factor  $K$  approach (Finite Element Method FEM) and the strain energy release rate  $\mathcal{G}$  approach (EA) based on the load-displacement curves.

There is considerable difficulty in understanding the fracturing process in compression and it is known that fracture energy calculated under load-displacement curves without accounting for testing machine and sample stiffness characteristics, can lead to unrepresentative results. Two interpretations of the load  $P$  from the load-displacement curve were used in the determination of the fracture toughness values in order to clarify the fracturing process in compression. They were  $P_1$  and  $P_{\max}$ .  $P_1$  represents the 'pop-in' load  $P_1$  when the first crack occurs and  $P_{\max}$  represents the maximum failure load when extensive micro-cracking occurs beyond  $P_1$ . In view of the difficulties

where an energy approach is used, three interpretations of the load-displacement curves were used and the basic concepts used in evaluation of fracture toughness are summarised in Table 5.8.

#### Using $P_1$ ('pop-in' load)

In the EA1 method, the strain energy release rate was calculated using the energy approach outlined in Section 5.4.2 where the area under the 'pop-in' load  $P_1$  was used to determine the work done.

In the EA2 method, the area under the initial non-linear part of the plot was disregarded because it reflects machine/specimen interaction and the work done under this part of the curve does not contribute to the fracturing process. The work done used in fracture toughness calculation was obtained by measuring the area under the linear part of the plot.

In the EA3 method, the work absorbed by the testing machine based on its stiffness characteristics was evaluated and the strain energy release in EA1 accordingly reduced. The stiffness,  $k$ , of the testing machine is defined by

$$k = \frac{P}{d} \quad (5.2)$$

where  $P$  is the load applied to the testing machine and  $d$  is the deformation of the testing machine when load  $P$  is applied. The stiffness of the testing machine determines the work absorbed of the machine when the specimen is compressed a distance  $d$

$$ECM = \frac{1}{2} P d \quad (5.3)$$

Substituting  $d = \frac{P}{k}$  from eq. (5.2) into (5.3) gives

$$ECM = \frac{P^2}{2k}$$

To obtain the strain energy release of a sample the total strain energy release was reduced by this amount

$$EA3 = EA1 - ECM$$

The fracture toughness values calculated for the three geometries using the finite element solution and the three energy approaches using the load  $P_1$  are summarised in Table 5.9. As can be seen 100% double shear was achieved only for those samples with a notch spacing of  $H = 30\text{mm}$ . 80% of the cubes failed in double shear for  $H = 40\text{mm}$  and about 58% for  $H = 50\text{mm}$ . The remainder of samples failed in single shear or another mechanism. These results confirm the conclusions drawn from the finite element analysis that with decreasing notch spacing  $H$  and increasing  $a/W$  ratio, the shear failure mechanism assumes greater significance. The results of Table 5.10 are also shown graphically in Figures 5.7, 5.8 and 5.9 for  $H/W = 0.5$ , 0.4 and 0.3 respectively.

Figure 5.7 ( $H/W = 0.5$ ) shows a non-conclusive trend. In view of the fact that as many as 42% of specimens were wasted during testing, this group was not of practical use.



Figures 5.8 and 5.9 ( $H/W = 0.4$  and  $0.3$  respectively) clearly indicate that when the correction for machine specimen interaction (EA2) and particularly the correction for machine stiffness characteristics (EA3) was applied, a close correlation was achieved between the fracture toughness values predicted by the finite element method and the experimental values.

The fact that the experimental values obtained by EA3 are very consistent is encouraging as the fracture toughness value should be independent of specimen geometry. It is evident from these graphs that more flexible specimens required a smaller correction for the machine stiffness characteristics and therefore these are more suitable for the experimental determination of fracture toughness.

Since no other results are available for these geometries the boundary collocation equation derived by Chisholm and Jones, equation (2.41), was used to compare the results with those obtained using the finite element method. Table 5.11 shows the results for cubes with  $H = 30\text{mm}$ . The fracture toughness values are in good correlation between the two methods and identical results are obtained for notch ratio  $a/W = 0.35$ .

The fracture toughness values obtained for the specimen geometry with notch spacing  $H = 30\text{mm}$  and notch depth  $a = 45\text{mm}$  can be summarised as follows. The fracture toughness value  $K_{IIc}$  based on the stress intensity factor approach was found to be  $1.9 \text{ MN m}^{-3/2}$ , the  $K_{IIc}$  based on the strain energy release rate approach was found

to be in the order of 1.78 to 2.09 MN m<sup>-3/2</sup> and the fracture toughness based on the Chisholm and Jones' equation was 1.55 MN m<sup>-3/2</sup>. Desayi (16) reported fracture toughness values obtained from the centrally located inclined crack for prisms in compression which are in the range of 1.03 to 9.27 MN m<sup>-3/2</sup> for mortar and 3.65 to 10.84 MN m<sup>-3/2</sup> for concrete. These results correspond to those obtained in this study.

It can be concluded that a linear elastic fracture mechanics is applicable to this material because both the stress intensity factor approach and the strain energy release rate approach yield similar  $K_{IIC}$  values when correction is applied to experimental results for the machine/specimen interaction or the machine stiffness characteristics.

Using  $P_{(max)}$  failure load

The latent strength of the cubes after the initial 'pop-in' load  $P_1$  were estimated using equations (4.8-4.10) and the energy approaches as described previously. The failure load  $P_{(max)}$  was used in equations (4.8-4.10) and the three energy approaches described in Table 5.8 were used except the work done was obtained by measuring the area under  $P_{(max)}$  of the load-displacement curve for all cases.

Since cubes with spacing  $H = 30\text{mm}$  produced 100% failure in double shear, the latent toughness of this geometry were obtained and tabulated in Table 5.12. It is seen that large differences in

latent toughness  $K_{LT}$  values were obtained using the EA1 and EA2 methods. Good correlation was obtained between the finite element method and the EA3 method. This result shows that more flexible specimens required a smaller correction for the machine stiffness characteristics and therefore these are more suitable for the experimental determination of latent toughness.

The latent toughness values found from the finite element method using  $P_{(max)}$  were compared with those using the boundary collocation formula, eq. (2.43), derived by Chisholm and Jones. Table 5.13 shows the results obtained from both methods. It can be seen that a good correlation between the  $K_{LT}$  values were obtained.

The latent toughness values obtained for the specimen geometry with notch spacing  $H = 30\text{mm}$  and notch depth  $a = 45\text{mm}$  can be summarised as follows. The latent toughness value  $K_{LT}$  based on the stress intensity factor approach was found to be  $6.72 \text{ MN m}^{-3/2}$ , the  $K_{LT}$  based on the strain energy release rate approach was found to be in the order of  $6.42$  to  $8.47 \text{ MN m}^{-3/2}$  and the  $K_{LT}$  based on the Chisholm and Jones equation was  $5.47 \text{ MN m}^{-3/2}$ . These results indicate that both the stress intensity factor approach and the strain energy release rate approach yield similar  $K_{LT}$  values when correction is applied to experimental results for the machine/specimen interaction or the machine stiffness characteristics.

Table 5.14 shows the results of applied load and fracture toughness and latent toughness values for the specimen geometry of notch spacing  $H = 30\text{mm}$  using both the load at 'pop-in' and at

failure  $P_{(max)}$  respectively. It can be seen that the latent toughness values  $K_{LT}$  based on the finite element method and the EA3 method using  $P_{max}$  were about 3 times larger than the fracture toughness  $K_{IIC}$  using  $P_1$  while the failure load  $P_{max}$  was about 3 times the 'pop-in' load  $P_1$ . This indicates that the critical fracture toughness when the first crack occurs at the notch tip and the latent toughness at failure when extensive micro-cracking occurs correspond to the same order of the load at 'pop-in' and at 'failure'.

#### 5.6 DETERMINATION OF FRACTURE TOUGHNESS FOR 100mm SINGLE-NOTCHED MORTAR CUBES - TEST SERIES FOUR

Tests were carried out on 100mm mortar cubes with one notch on both the upper and lower surfaces. The upper notch depth was kept at 10mm and the lower notch depth varied from 30mm to 45mm in 5mm increments. 12 cubes were tested per notch depth, a total of 48 cubes in all. The INSTRON compressive platens were used with displacement control in the dynamic testing mode. The compressive rate kept at 0.003mm/s. Plate 5.6 shows the test arrangement of a single notched mortar cube.

Fracture toughness values of the single notched cubes were determined using the stress intensity factor  $K$  approach (finite element method) and the strain energy release rate  $\mathcal{G}$  approach. The evaluations were based on the 'pop-in' load  $P_1$  of the load-displacement curves.

### Discussion of test results

Details of the test results of single notched mortar cubes with various notch depths are shown in Table 5.15. Failure was achieved for 92% of cubes with notch ratio  $a/W = 0.3$  and  $0.45$ , about 75% for  $a/W = 0.35$  and  $0.4$ . The remainder of the cubes failed with a crushed support surface. These results contradict the conclusion drawn from the finite element analysis for single notched cubes that with increasing  $a/W$  ratio the shear failure mechanism assumes the greater significance.

Observations were made for the cubes which failed in single shear and the corresponding load-displacement curves were recorded autographically. It was observed that a hairline crack, parallel with the line of action of load, developed at the tip of the upper notch corresponding to the 'pop-in' load  $P_1$ . Subsequently another hairline crack developed at the tip of the bottom notch. When sudden catastrophic failure occurred it was found that the cube was broken in two from the tip of the upper notch to the lower notch tip. Plate 5.7 shows the cubes after failure for various notch depth ratios.

The fracture toughness values  $K_{IIC}$  were obtained using the finite element method (FEM) and the three energy approaches (EA) as discussed in Section 5.5. In the finite element method, the fracture toughness values were calculated by substituting the 'pop-in' load  $P_1$  into equation (4.11). (See Table 5.8).

The work done obtained for the 3 energy approaches (EA) was based on measuring the area under the 'pop-in' load  $P_1$ . Corrections were

made on the load-displacement curves for the effect of machine specimen interaction (EA2) and machine stiffness characteristics (EA3). The corresponding  $K_{IIC}$  values are tabulated in Table 5.16 and shown graphically in Figure 5.10. Table 5.16 shows that the best results were obtained for the notch ratio  $a/W = 0.3$ . These inconsistent results confirm the findings from the finite element analysis that this geometry failed to produce the shear type of failure and most probably the mixed mode of failure is taking place.

## 5.7 GENERAL PROPERTIES OF SOIL-CEMENT AND COMPACT SHEAR FRACTURE TEST PROCEDURES

The aim of this work was to determine the general properties of soil-cement which is generally weak in shear.

### Preparation of soil-cement

The cement stabilized soil used in this work was termed soil-cement. The soil was a red marl (Keuper) from Leckwith, Cardiff, South Wales. The marl had been dried in the oven and pulverised into a powder form and 8% by weight of ordinary Portland cement was added. Since moisture content is an important factor in soil properties it was necessary to determine the moisture content.

The standard Proctor compaction test was used to determine the optimum dry density and moisture content of the soil-cement according to BS1924 (35). The details of the test are summarised in Table 5.17 and 5.18. Figure 5.11 shows the plot of dry density against moisture content and the optimum moisture content was found to be 16.6% at a dry density of  $1.78 \text{ (Mg/m}^3\text{)}$  as tabulated in Table 5.19(a).

In order to maintain consistency the following mix procedures were adopted :

red marl : 4 Kg  
 cement (8%) : 0.32 Kg  
 water (18%) :  $4.32 \times 0.18 = 0.778$  Kg

Time (minute)		Mix condition
dry mix	2	low speed
	1	blended
wet mix	2	low speed
	1	blended
	2	low speed
	1	blended

The required amount of red marl and cement were placed into the bowl of a soil mixer and thoroughly blended together as shown in the above table. The required amount of water was then gradually added while the mixer was operating at a low speed. The soil-cement was mixed and blended for the time scale shown in order to achieve a thorough mix.

The correct mixing of this material was an important element of the sample preparation and in particular the control of moisture content had an important bearing on the quality of compaction in the samples. In fact 18% by weight of water was used instead of 16.6% (as was determined) in order to allow for loss of moisture.



### Compaction

The soil-cement was compacted in standard 100mm concrete cube moulds with a "collar", made by removing the base from another mould attached to the top by means of two "G" clamps. The soil - cement was broken up into granular form before being carefully placed into the bottom of the mould. This first procedure proved to be of vital importance since lumps of the material at the bottom of the mould did not compact well. The cubes were filled and hand compacted gently with a 5mm diameter steel bar in five equal layers (Plate 5.8) A 100mm square x 300mm long piece of timber was then placed onto the top of the material and struck with a 4.5Kg rammer falling from a height of 500mm. 12 , 15 ,18 and 20 blows were tried initially to determine the best compaction. Plate 5.9 shows the compaction with the 4.5Kg rammer. It was found that the cubes were under-compacted after 12 and 15 blows because uneven surfaces were found on the cube. Whereas 20 blows was found to over-compact as hair cracks were found on the cubes. It was found that 18 blows gave the best compaction when the cube surfaces were found to be smoothly finished with no hair cracks.

Another attempt was made to produce a constant compaction by using a "Kango 900" demolition hammer which gives 2000 blows/min. (Plate 5.10). It was found that 15 seconds operating time was as good as 18 blows by a 4.5Kg rammer. This compaction method speeded up the operation considerably. After the compaction the collar was removed and the extra material was levelled off with a spatula (Plate 5.11).

### Curing

It is known that moisture content control during curing is extremely important if the material is to obtain its maximum strength. Therefore precautions were taken to control the moisture content. The soil-cement cubes in their moulds were enclosed in sealed polythene bags for 24 hours. The moulds were stripped and the cubes were first wrapped in cling film then in tin foil and sealed in polythene bags for 28 days.

### General properties of soil-cement

The compressive strength of 100mm soil-cement cubes were found using the Avery Denison 7226 testing machine. All the cubes were tested at a compression rate of 80KN/mm or  $0.13\text{N/mm}^2/\text{s}$ . The average compressive strength was  $4.96\text{ MN/m}^2$  as shown in Table 5.19(a). The elastic modulus and Poisson's ratio were taken as  $1200\text{ N/mm}^2$  and 0.25 .

### Insertion of notches

For compact shear fracture test purposes, the 100mm soil-cement cubes were notched(after 21 days of curing) using a circular lathe mounted with a diamond edge cutting blade. This enables the insertion of slots (2mm wide) to be controlled to the desired degree of accuracy. Plate 5.1 shows the lathe machine.

### Compact shear fracture tests

The compact shear fracture tests on 100mm double-notched and single-notched cubes were carried out in the INSTRON 1251 testing

machine using displacement control in the dynamic testing mode. INSTRON compressive platens were used for both double and single-notched cubes. The load rig was used for double-notched cubes only.

#### 5.8 DETERMINATION OF FRACTURE TOUGHNESS FOR 100mm DOUBLE-NOTCHED SOIL-CEMENT CUBES - TEST SERIES FIVE

Tests were carried out on cubes with notch spacing  $H = 50$  , 40 and 30mm. For each notch spacing, the upper notch depths were kept at 10mm and the lower notch depth varied from 30mm to 45mm in 5mm increments. 8 cubes were used per notch depth, a total of 96 cubes.

Fracture toughness values of the above geometries were determined using the stress intensity factor  $K$  approach (finite element method) and the strain energy release rate  $G$  approach. The evaluations were based on the 'pop-in' load  $P_1$  and the results were compared using the equation derived by Chisholm and Jones (19).

#### Discussion of test results

Details of the test results of double-notched cubes are shown in Table 5.20. 59% failed in double shear for notch spacing  $H = 50$ mm, 75% for  $H = 40$ mm and 100% for  $H = 30$ mm . These results confirm the conclusions drawn from the finite element analysis that with decreasing notch spacing  $H$  and increasing  $a/W$  ratio, the shear failure mechanism assumes greater significance.

For a double shear failure it was observed that a hairline inclined crack first developed at one of the bottom notches corresponding to the 'pop-in' load  $P_1$  (Figure 5.12) and subsequently the shear cracks, parallel with the line of loading, developed very steadily but slowly. After failure occurred, the cubes were found to be greatly deformed but intact. The load-displacement curve shows a gradual decrease in load after the peak load (Figure 5.12).

Plate 5.13 shows the cubes after failure for various notch depths.

The fracture toughness values  $K_{IIC}$  were obtained using the finite element method (FEM) and the three energy approaches (EA) as discussed in Section 5.5 where the 'pop-in' load  $P_1$  was used in all cases. The corresponding  $K_{IIC}$  values for the specimen geometries are tabulated in Table 5.21 and shown graphically in Figures 5.13, 5.14 and 5.15 for  $H = 50\text{mm}$ , 40 and 30mm respectively.

It can be seen in Figure 5.13 ( $H/W = 0.5$ ) that the  $K_{IIC}$  values obtained using the energy approaches are smaller than those when the finite element method is used. Since only 59% of specimens failed in double shear, this group is not of practical use.

Figure 5.14 ( $H/W = 0.4$ ) shows that similar  $K_{IIC}$  values are obtained using the EA1 and EA3 methods. The best correlated result between the finite element method and the EA1 and EA3 methods was obtained when the notch depth ratio  $a/W = 0.4$ . The fracture toughness value  $K_{IIC}$  based on the stress intensity factor was found

to be  $0.43 \text{ MN m}^{-3/2}$ , the  $K_{IIC}$  based on the strain energy release rate approach was found to be in the order of 0.37 to  $0.42 \text{ MN m}^{-3/2}$ .

Figure 5.15 ( $H/W = 0.3$ ) shows good correlation in fracture toughness values are obtained when the finite element method and the EA1 and EA3 methods are used. The most suitable geometry for shear fracture test was found to be of notch depth ratio  $a/W = 0.35$ . The fracture toughness value  $K_{IIC}$  based on the stress intensity factor approach was found to be  $0.43 \text{ MN m}^{-3/2}$ , the  $K_{IIC}$  based on the strain energy release rate approach was found to be in the order of 0.40 to  $0.44 \text{ MN m}^{-3/2}$ . Since no other results are available for these geometries for comparison, the boundary collocation equation (2.41) derived by Chisholm and Jones (19) was used to compare the  $K_{IIC}$  values with those obtained using the finite element method. Table 5.22 shows the fracture toughness values were in good correlation between the two methods and identical results were obtained for a notch depth ratio  $a/W = 0.35$ .

It can be concluded from these tests that good correlation was obtained between the finite element method and the EA1 and EA3 methods in the determination of fracture toughness values based on the 'pop-in' load  $P_1$ . The  $K_{IIC}$  values were underestimated when the EA2 method was used. This indicated that the correction was not necessary for the machine/specimen interaction because the fracture behaviour was not significantly masked by the experimental set up.

5.9 DETERMINATION FRACTURE TOUGHNESS FOR 100mm  
SINGLE-NOTCHED SOIL-CEMENT - TEST SERIES SIX

Tests were carried out to test 100mm soil-cement cubes with one notch on both the upper and lower surfaces. The upper notch was kept at 10mm and the lower notch depth varied from 30mm to 45mm in 5mm increments. 7 cubes were used per notch depth, a total of 28 in all. The INSTRON compressive platens were used with displacement control in the dynamic testing mode at a compression rate of 0.003 mm/s.

Fracture toughness values were determined using the stress intensity factor  $K$  approach (finite element method) and the strain energy release rate  $\mathcal{G}$  approach.

### Discussion of test results

Details of the test results of the single-notched soil-cement cubes with various notch depths are shown in Table 5.23. 100% shear failure was achieved for a notch depth ratio of  $a/W = 0.3$  and  $0.45$ , 86% for  $a/W = 0.35$  and  $0.40$ . According to the finite element analysis, the shear failure mechanism was not significantly increased with increasing  $a/W$  ratio. The experimental results confirm this statement and it can be concluded that this test geometry is not suitable for the Mode II shear test.

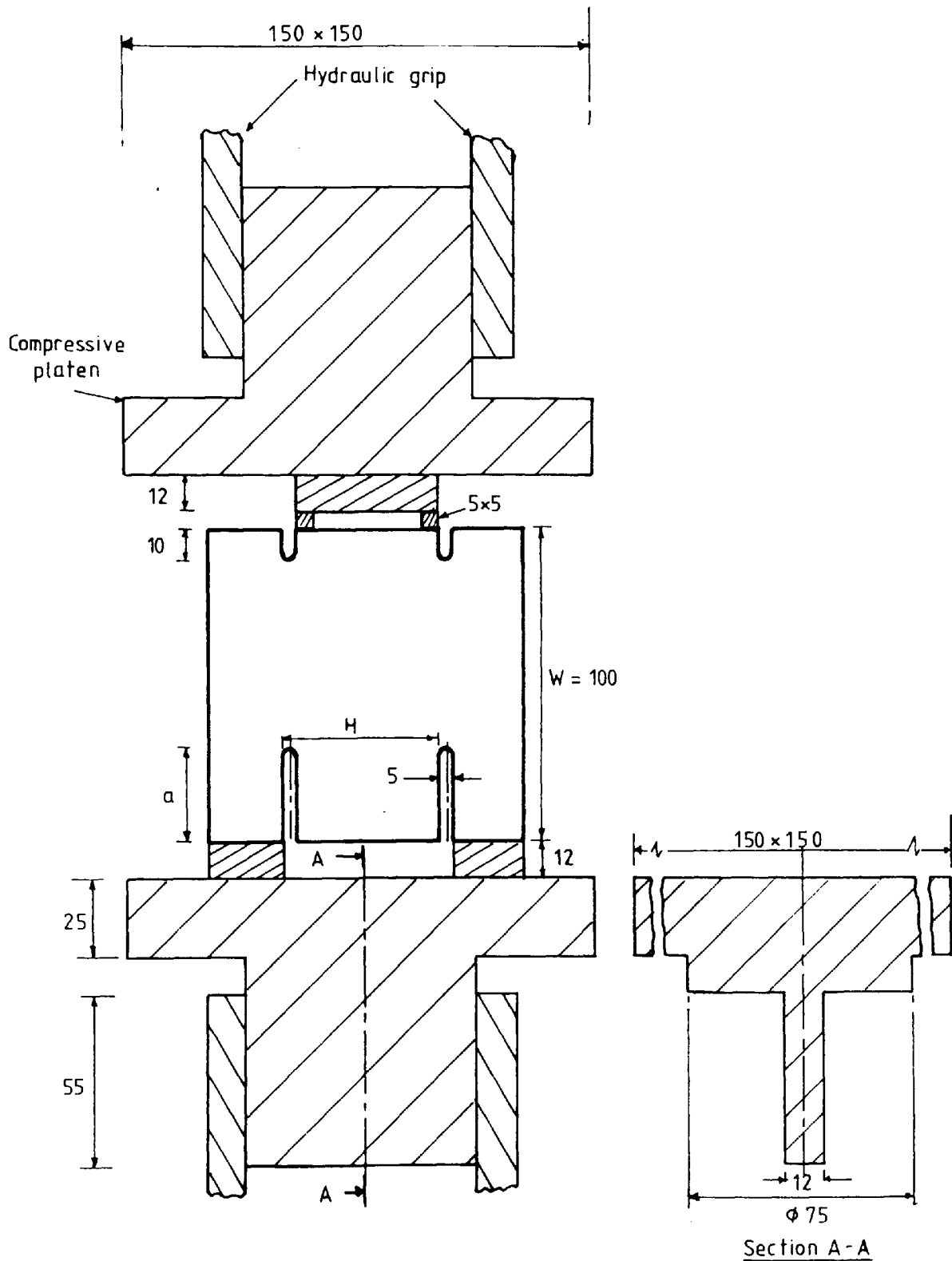
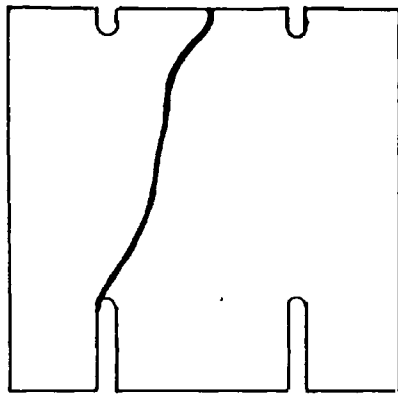
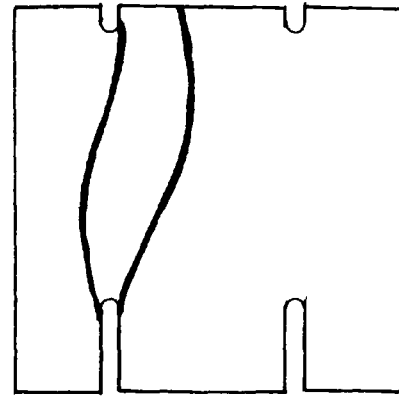


Fig 51 Test series one  
The hydraulic gripped compressive  
platens of the fracture test arrangement.

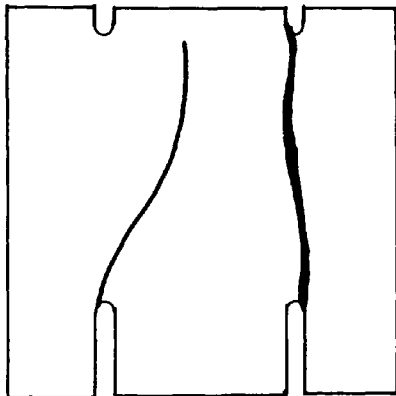




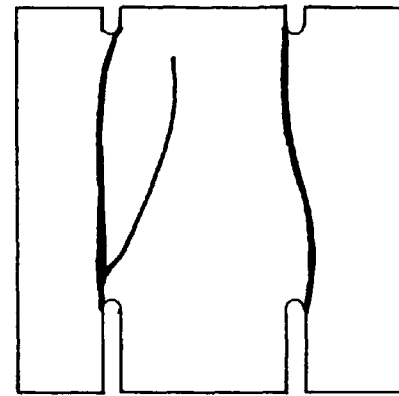
(a) Tension



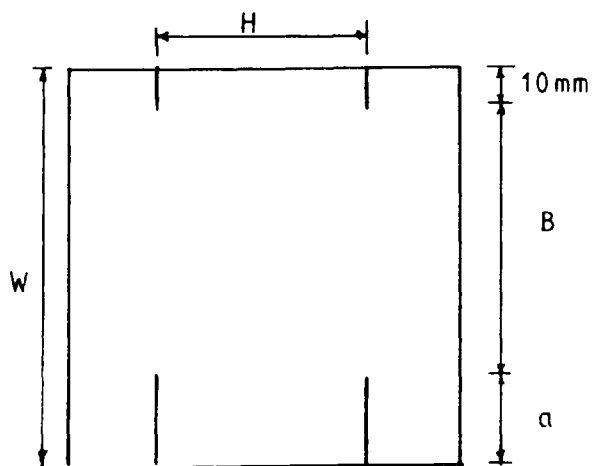
(b) Tension &amp; single shear



(c) Single shear



(d) Double shear



(e)

Fig.5:2 Types of failure of the tested cubes. Test series one

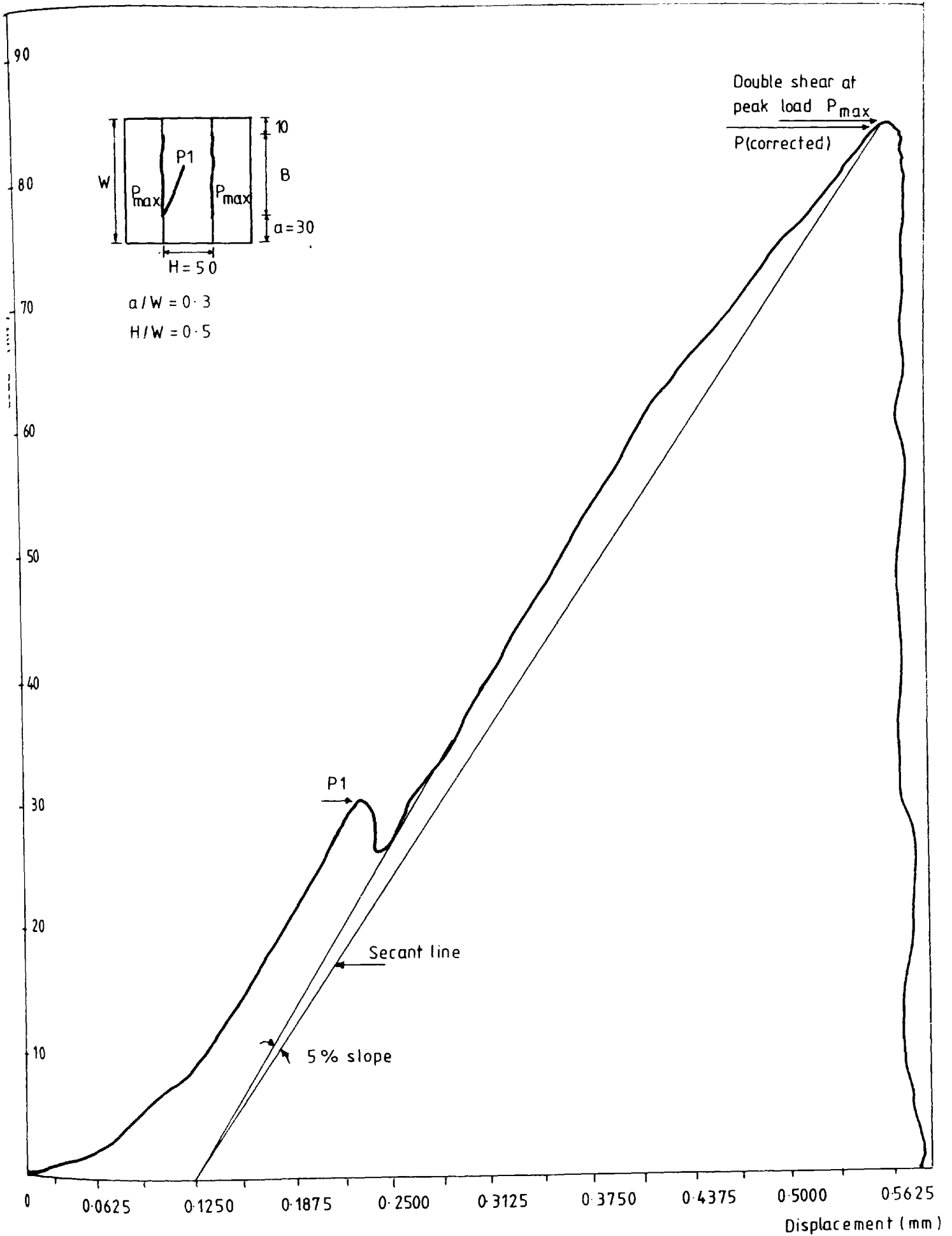


Fig 5.3 Test series one  
 Load - displacement curve.

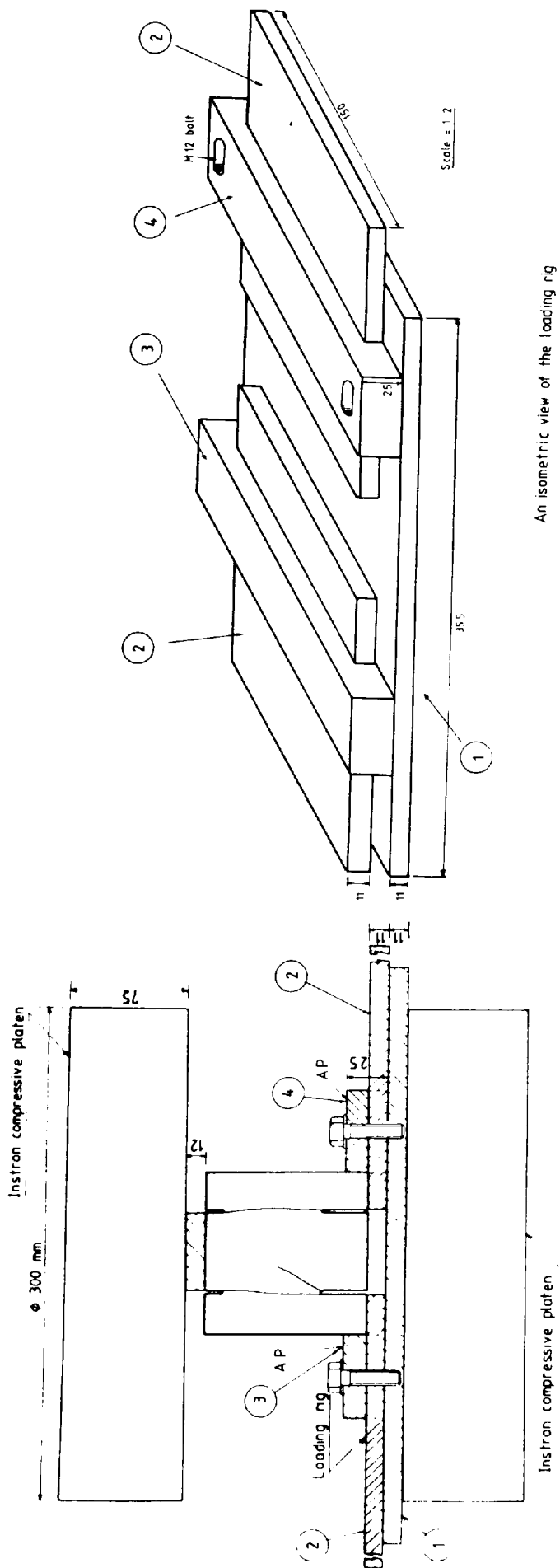


Fig 5.4 The INSTRON compressive platens and the load rig of the fracture test arrangement.

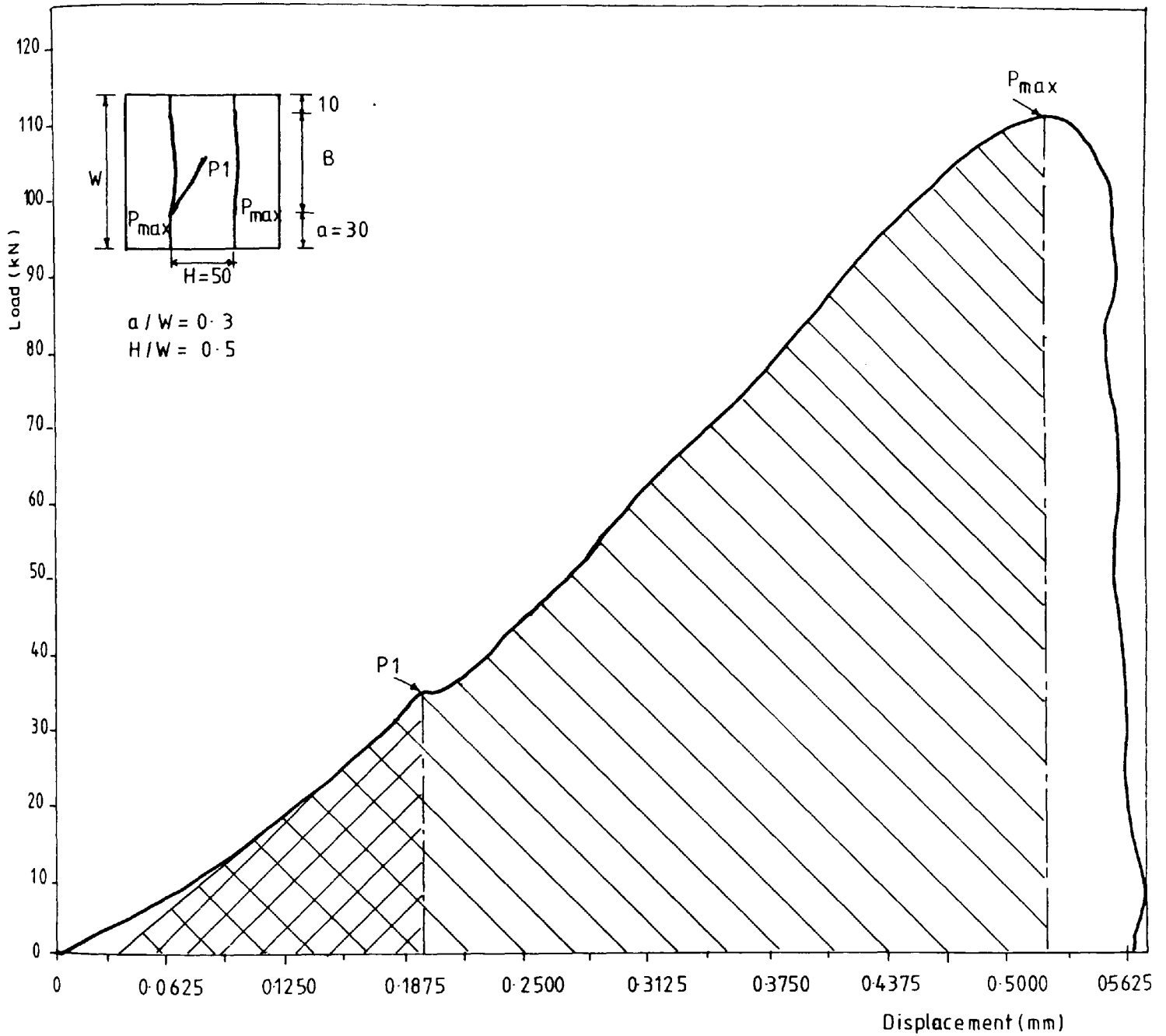


Fig. 55 Test series two  
Load-displacement curve.

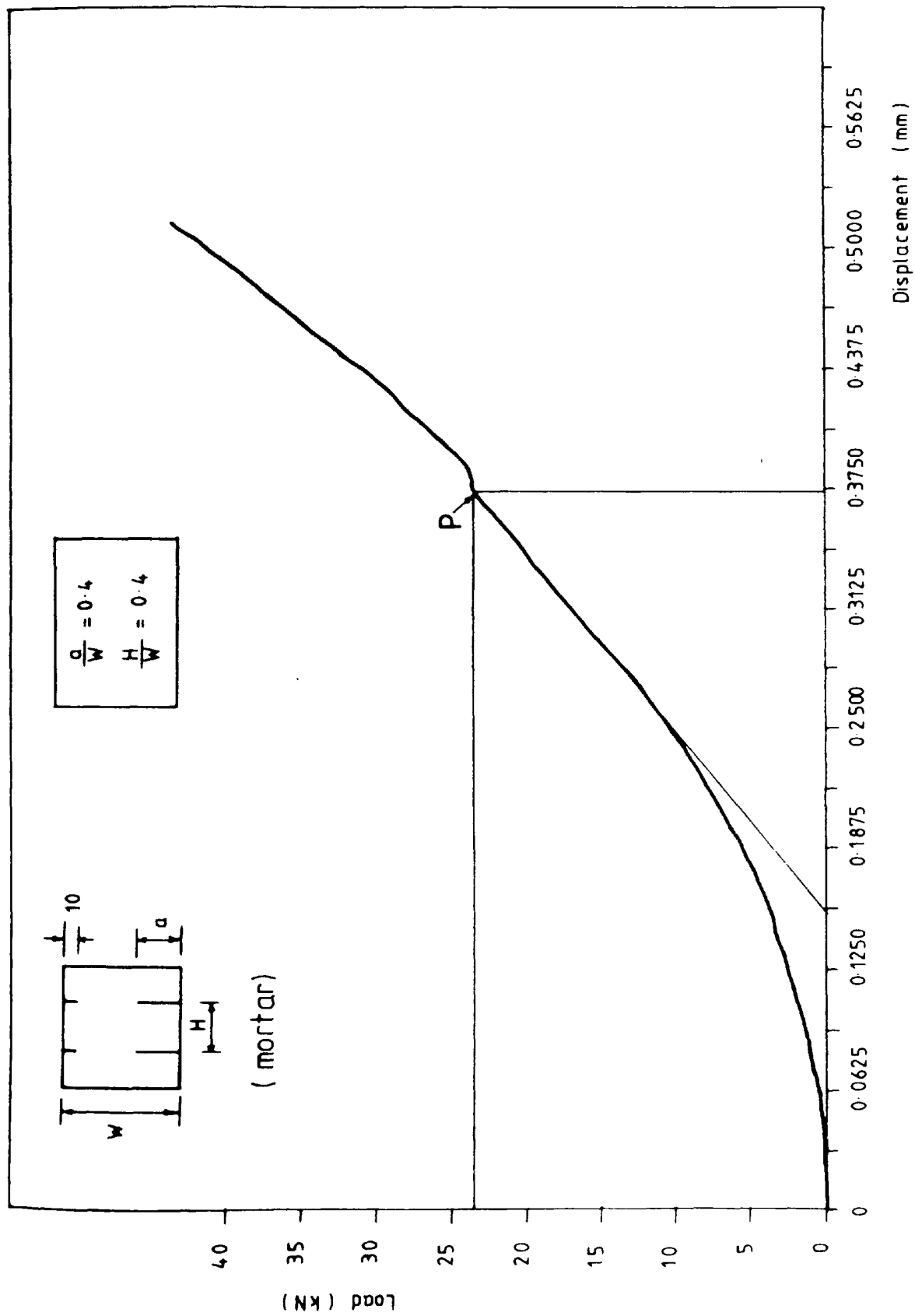


Fig. 5.6 Test series three  
Load-displacement curve

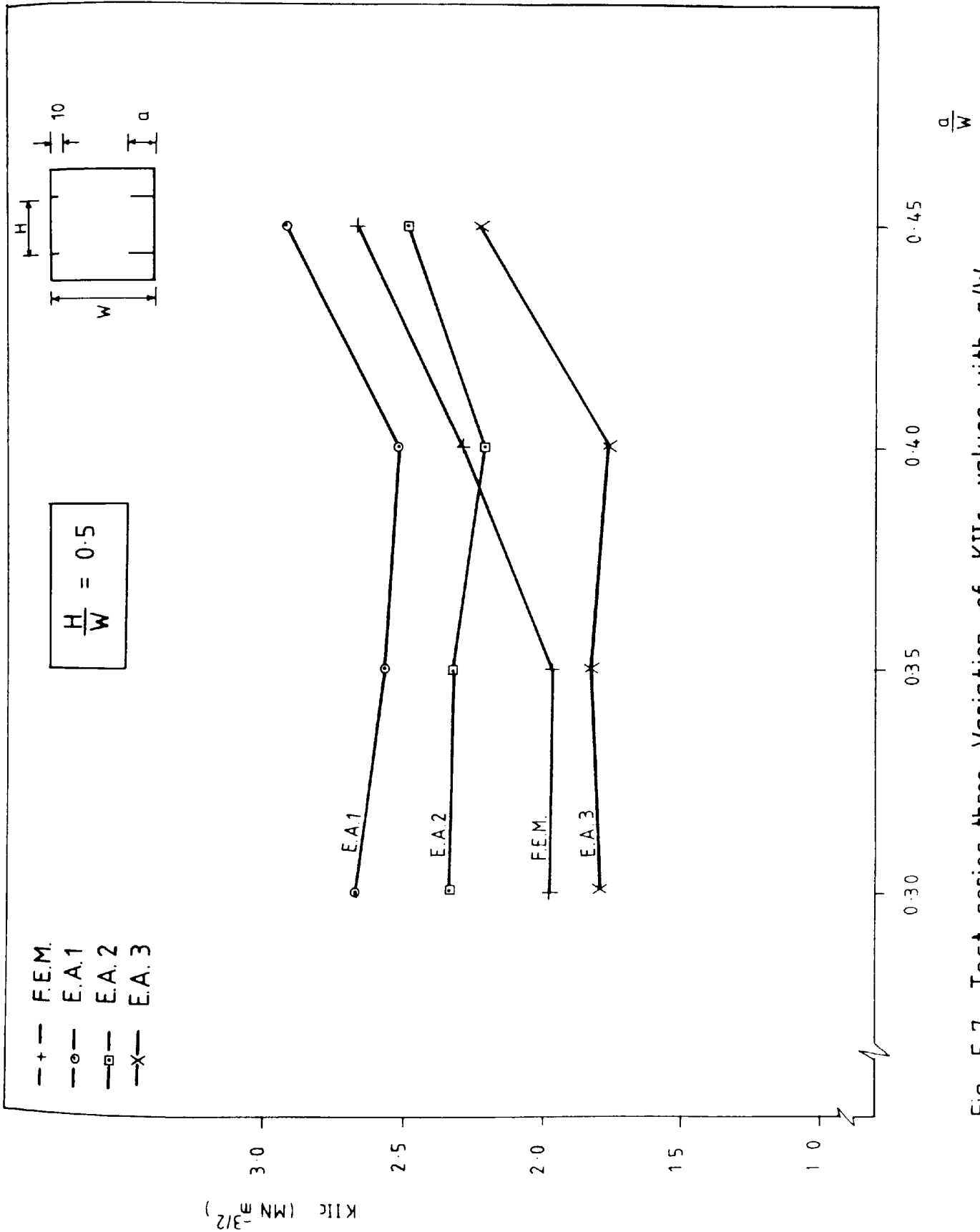


Fig. 5.7 Test series three: Variation of KIIC values with  $a/W$  (mortar cubes)

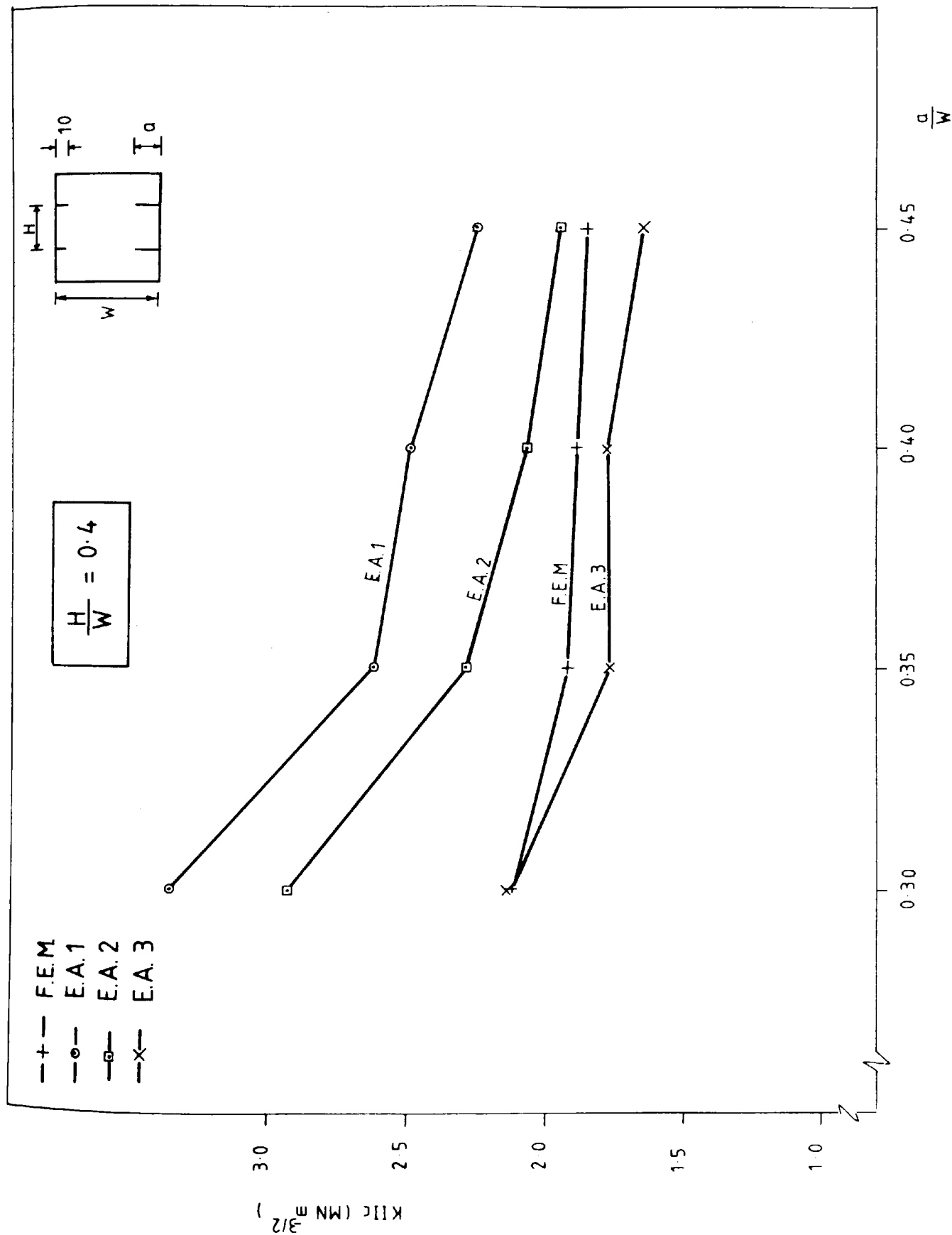


Fig. 5.8 Test series three: Variation of KIIC values with a/W (mortar cubes)

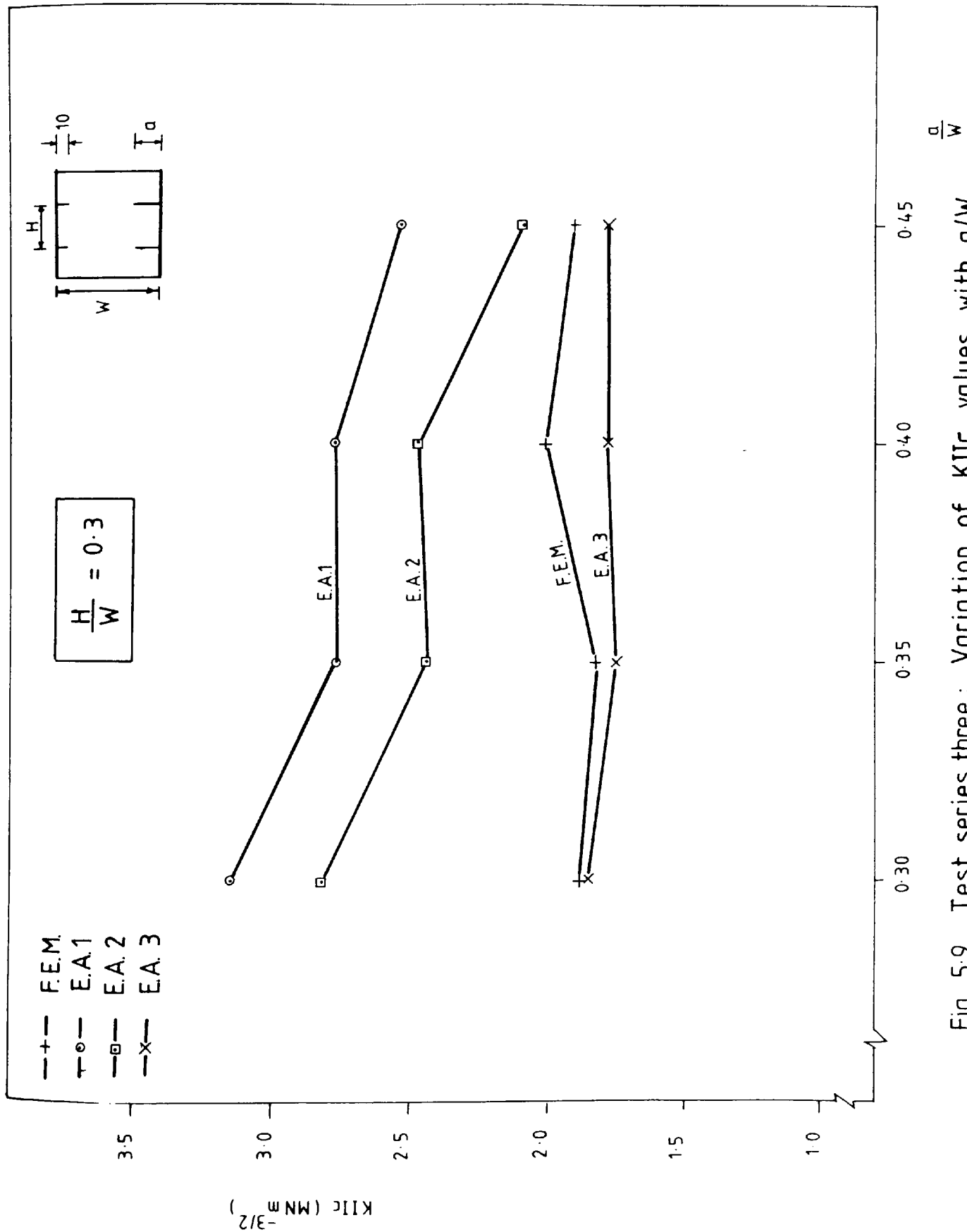


Fig. 5.9 Test series three: Variation of KIIC values with  $a/W$  (mortar cubes)



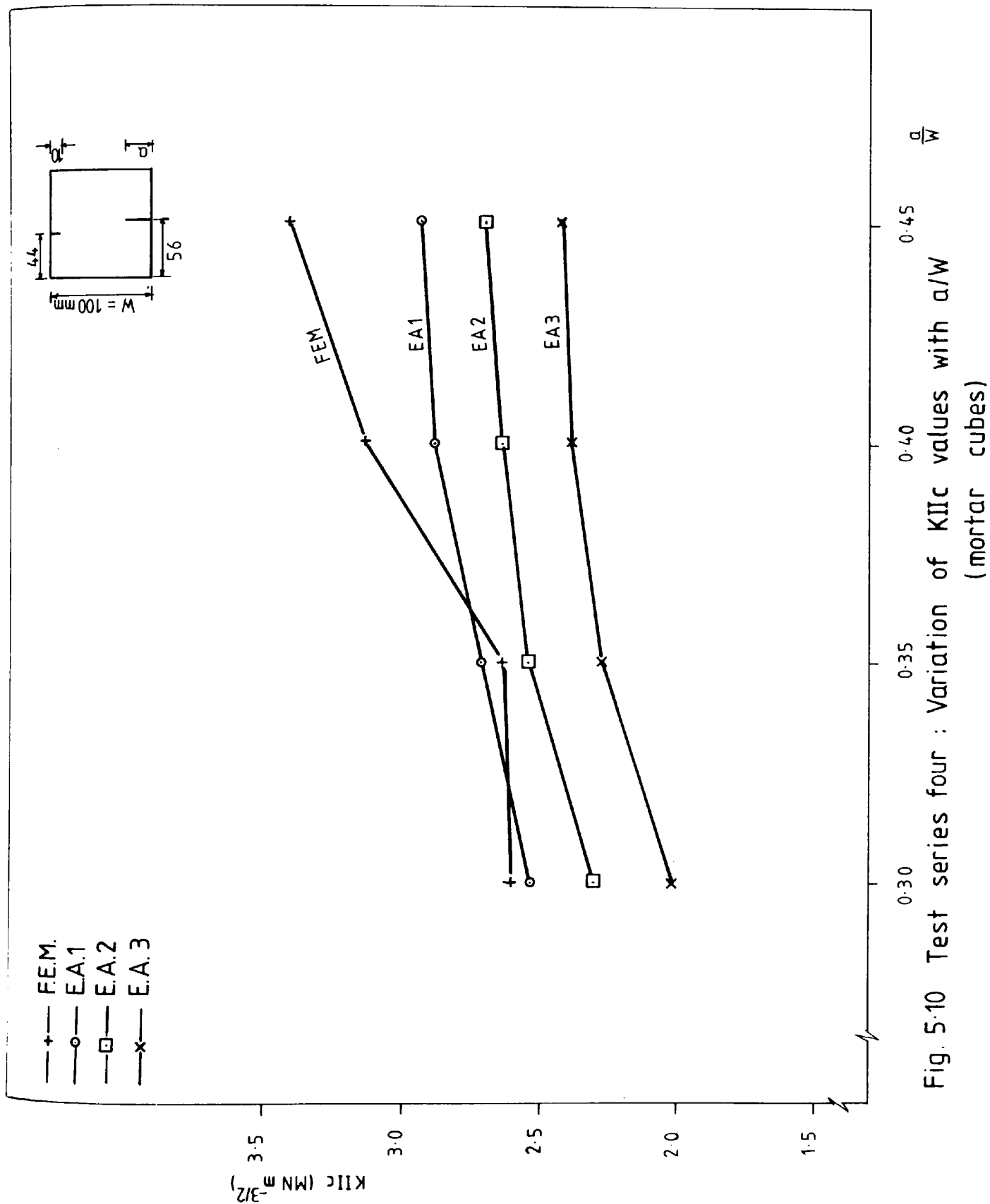


Fig. 5.10 Test series four : Variation of KIIC values with a/W (mortar cubes)

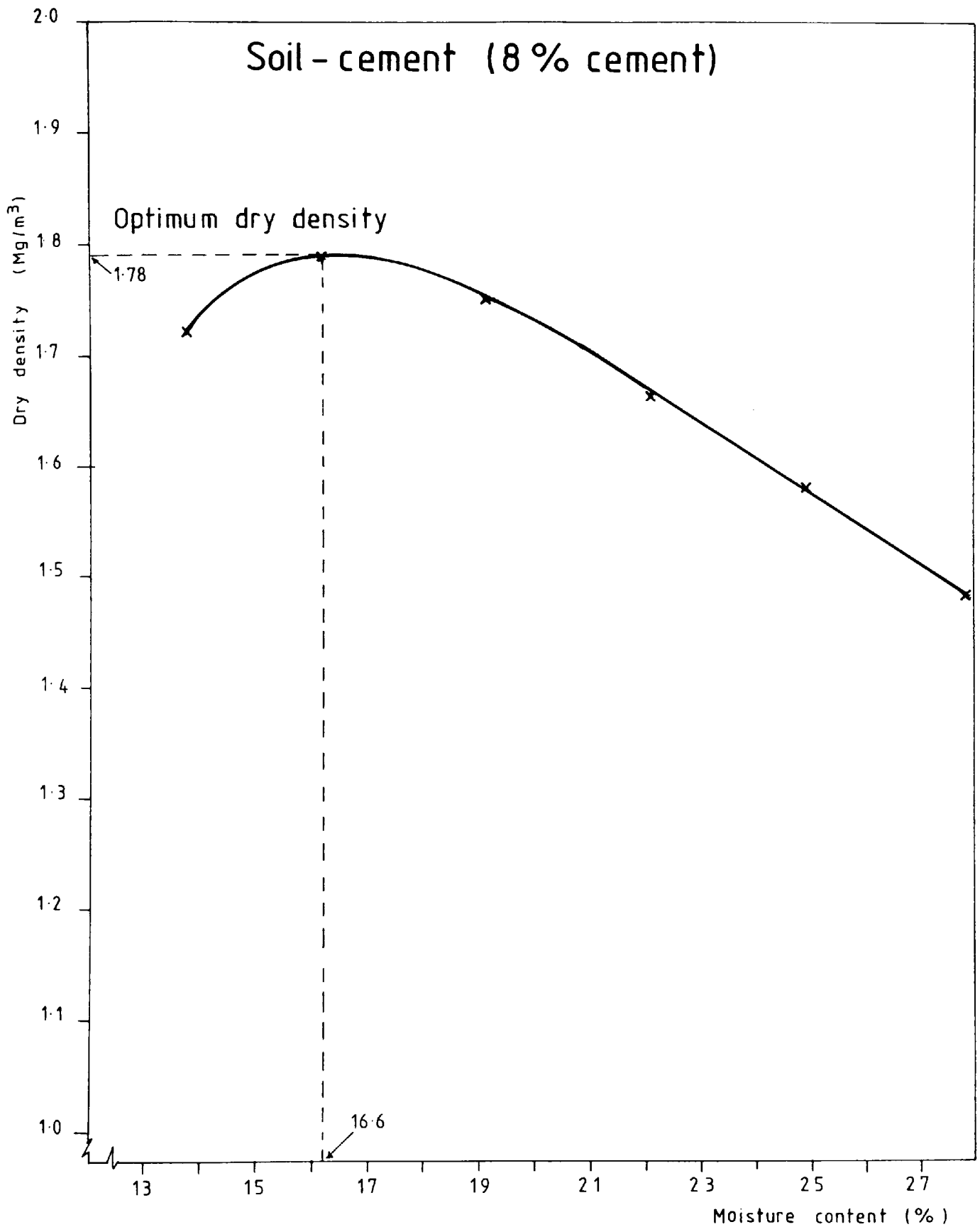


Fig. 5.11 Plot of dry density—moisture content  
of soil-cement  
(4.5 Kg rammer method)

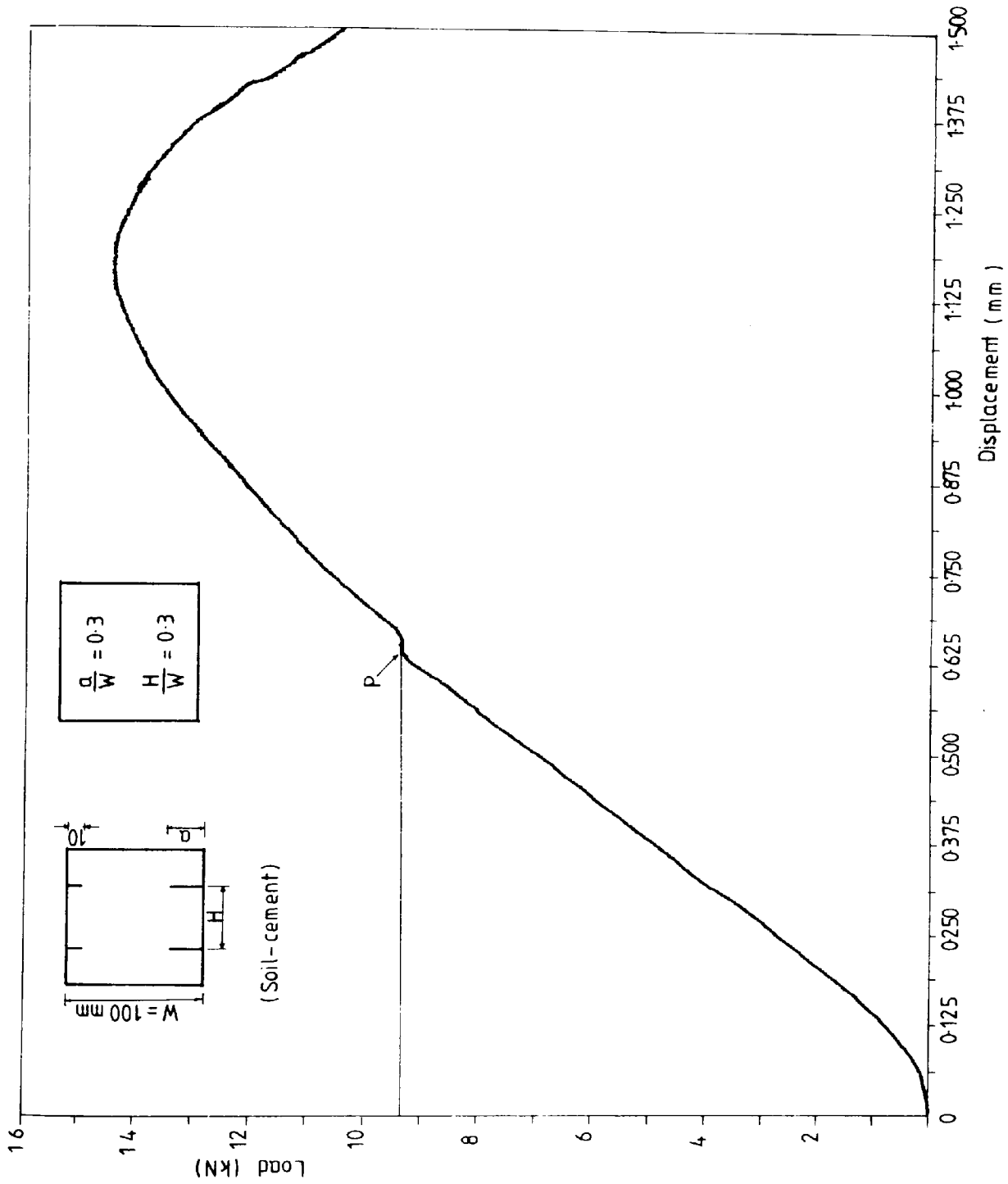


Fig. 5.12 Test series five  
load-displacement curve

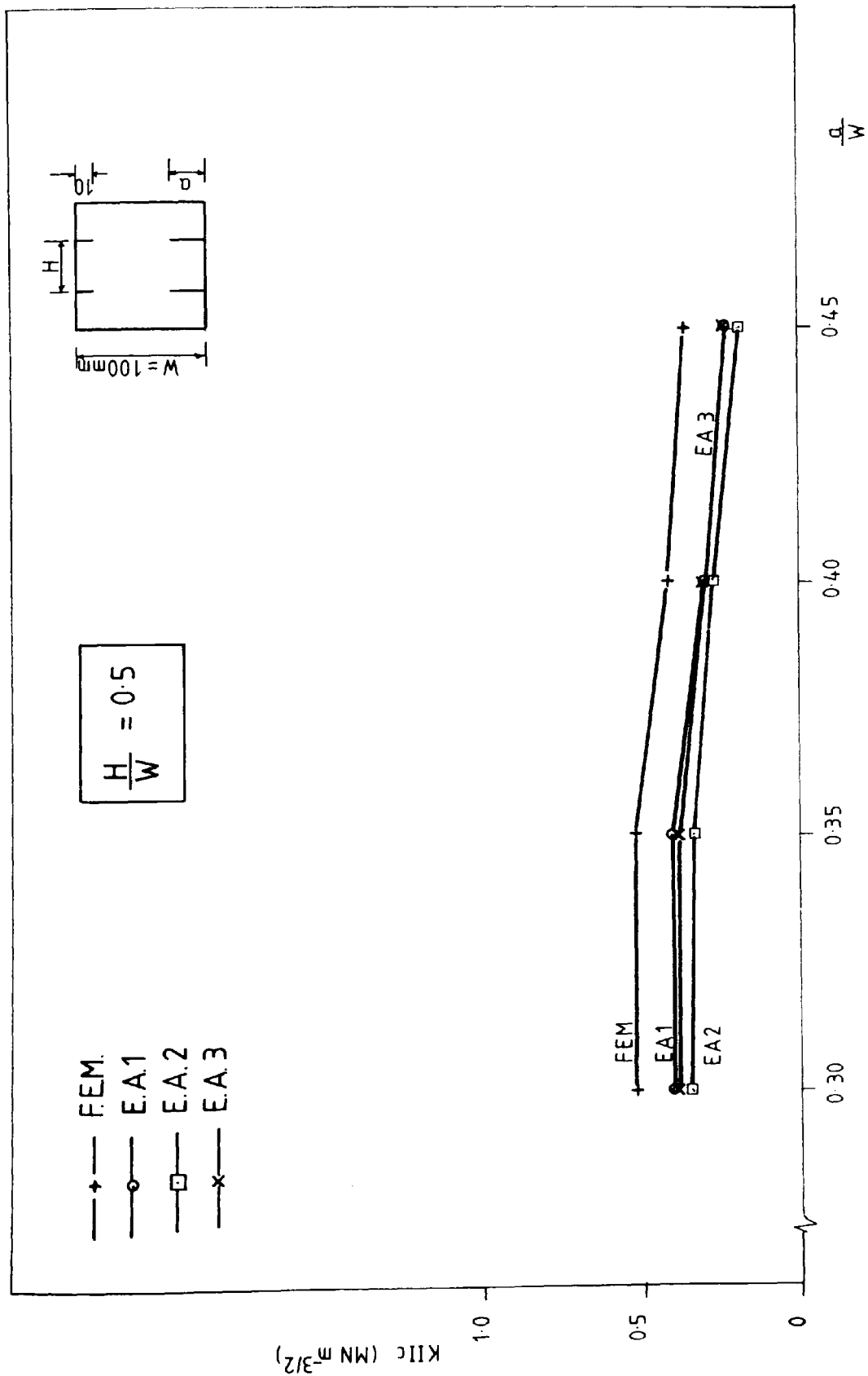


Fig. 5.13 Test series five : Variation of KIIC values with  $a/W$  for  $H/W=0.5$   
(soil-cement cubes)

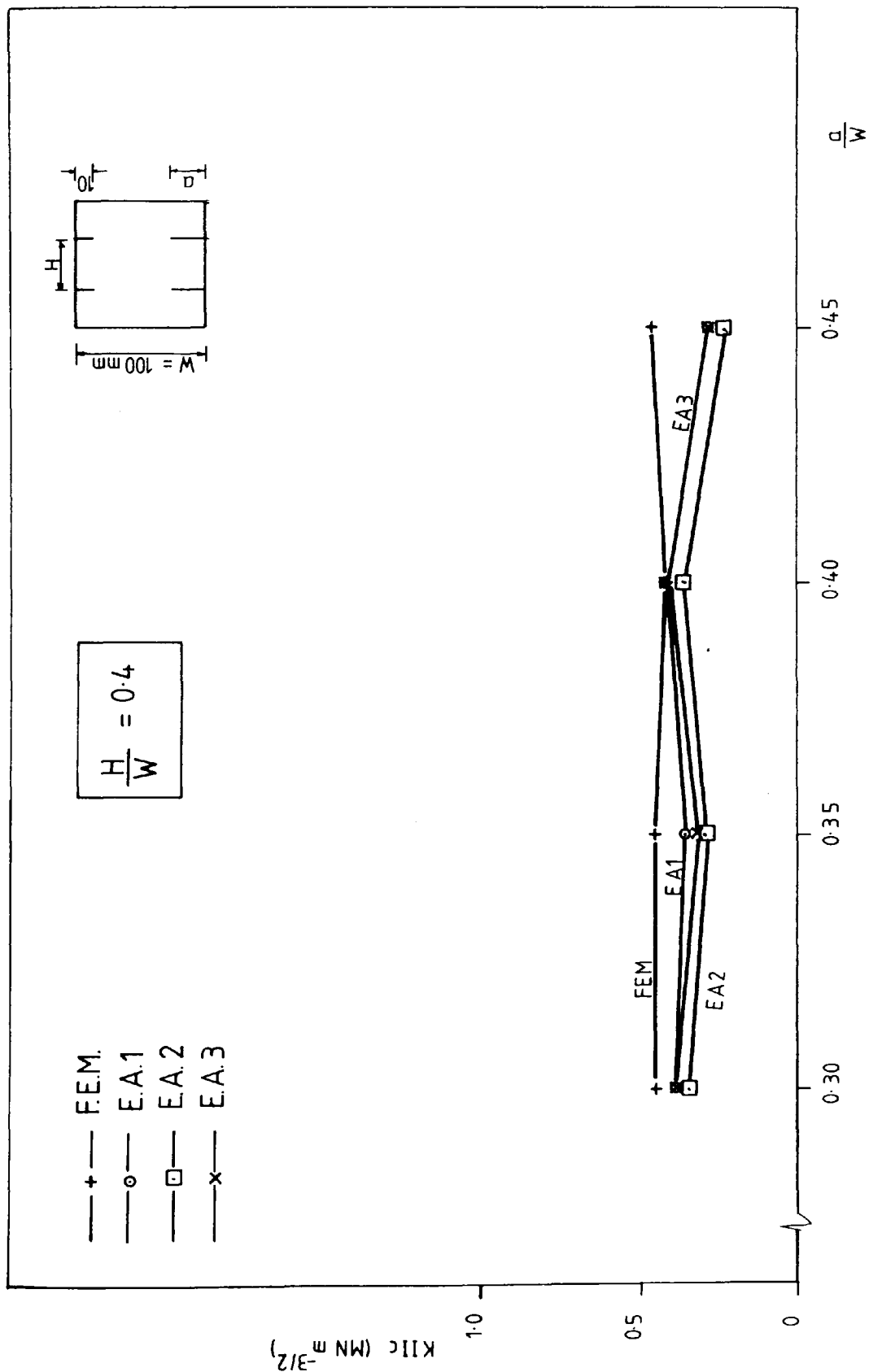


Fig 5.14 Test series five : Variation of KIIC values with  $a/W$  for  $H/W=0.4$   
(soil - cement cubes)

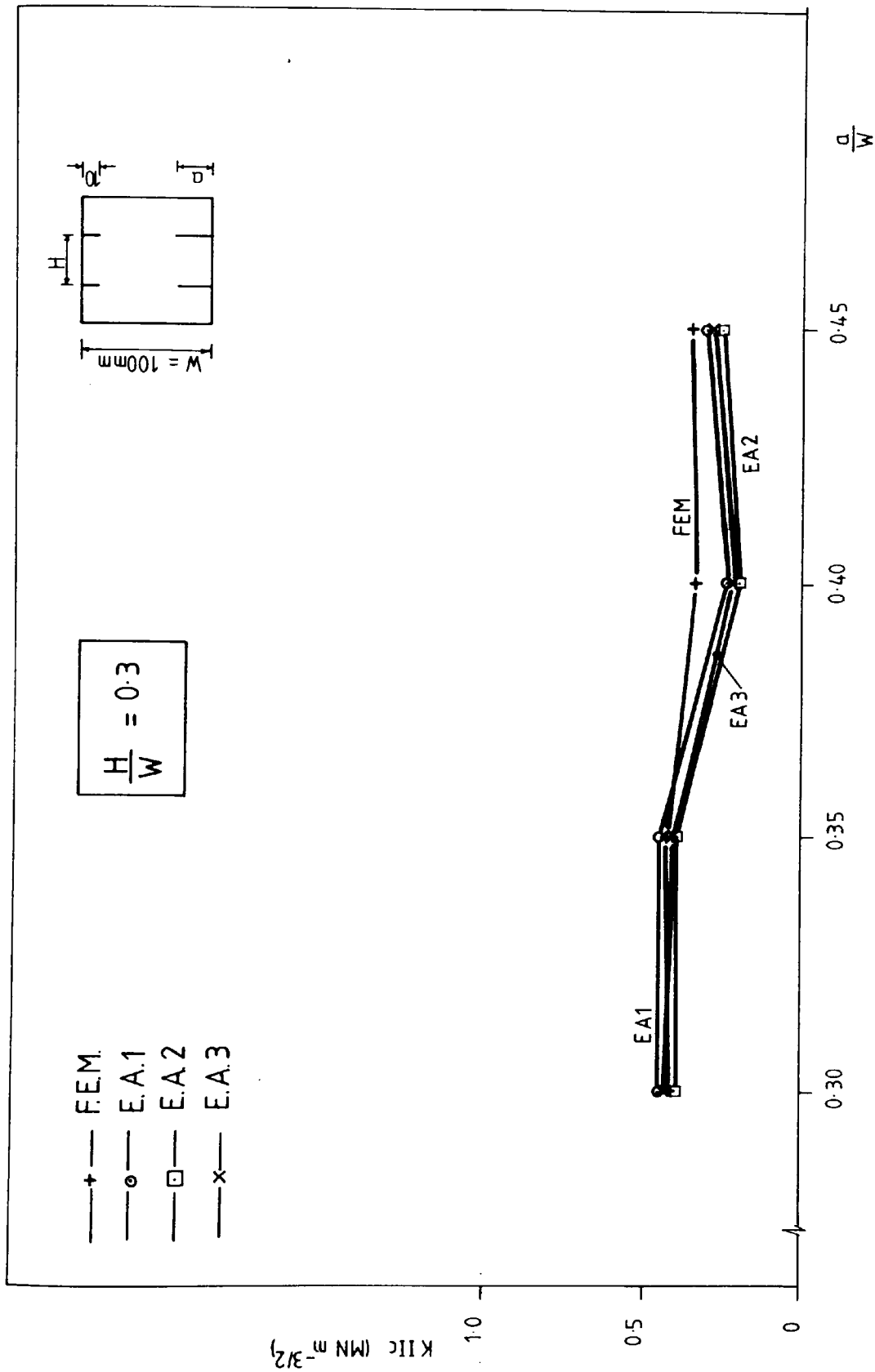


Fig. 5.15 Test series five : Variation of KIIC values with a/W for H/W = 0.3 (soil-cement cubes)

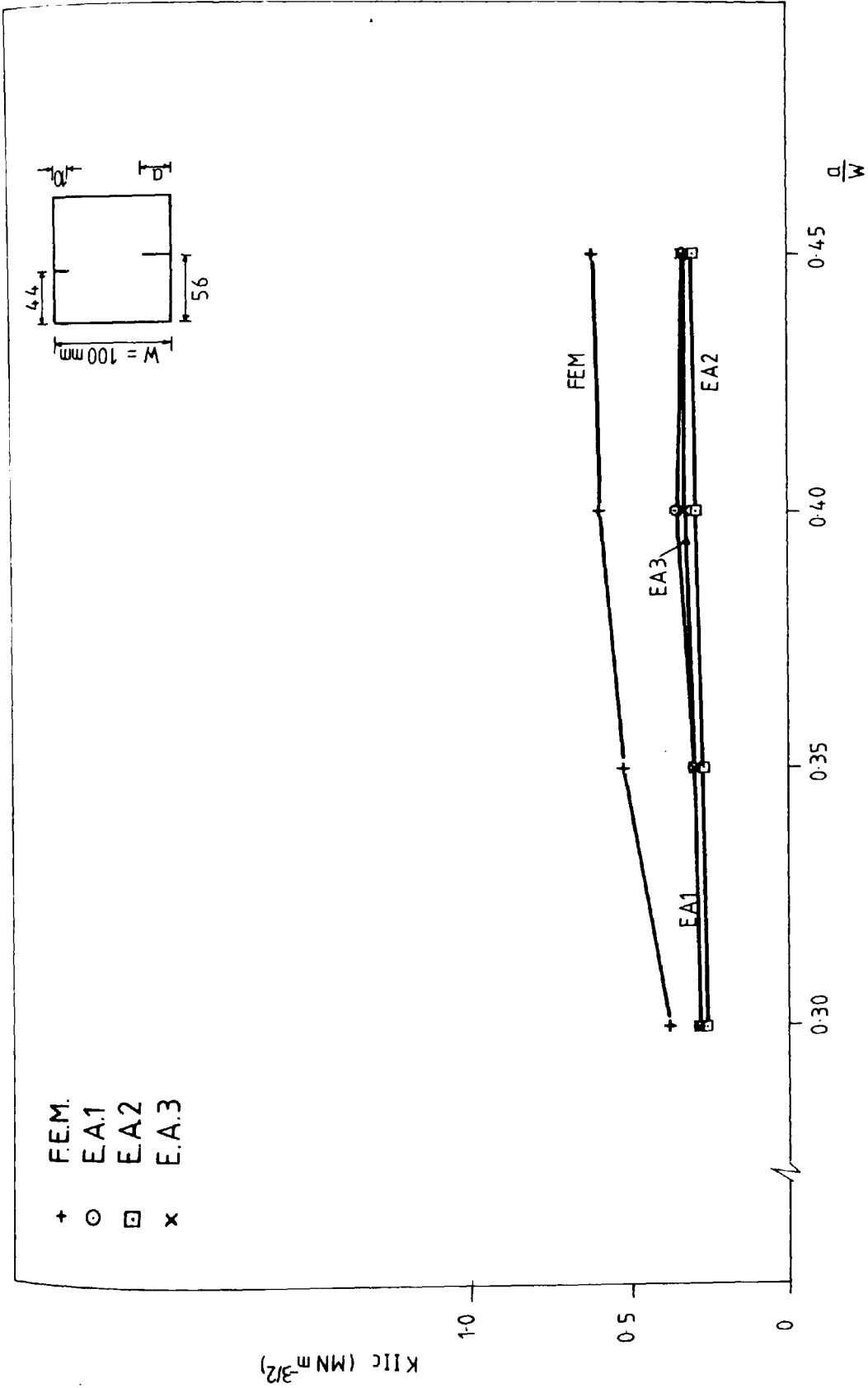


Fig. 516 Test series six : Variation of KIIC values with a/W  
(soil-cement cubes)

Test series	Material	Geometry	Load-arrangement	Load-condition	Load used	Methods used to obtain K <sub>Ic</sub>
One	Mortar	Double - notched $H = \begin{cases} 50 \\ 40 \text{ mm} \\ 30 \end{cases}$ $a = 30, 35, 40 \text{ \& } 45 \text{ mm}$	Departmental made compressive platens	Displacement control	P (-5%)	F.E.M.
Two	Mortar	Double-notched $H = 50 \text{ mm}$ $a = 30, 35, 40 \text{ \& } 45 \text{ mm}$	Instron platens + Load rig	Displacement control	P (-5%) & P <sub>1</sub>	F.E.M, E.A. E.A.1 & B.C
Three	Mortar	Double -notched $H = \begin{cases} 50 \\ 40 \text{ mm} \\ 30 \end{cases}$ $a = 30, 35, 40 \text{ \& } 45 \text{ mm}$	Instron platens + Load rig	Displacement control	P <sub>1</sub>	F.E.M, E.A.1 E.A.2 & E.A.3
Four	Mortar	Single-notched $a = 30, 35, 40 \text{ \& } 45 \text{ mm}$	Instron platens	Displacement control	P <sub>1</sub>	F.E.M, E.A.1 E.A.2 & E.A.3
Five	Soil-cement	Double -notched $H = \begin{cases} 50 \\ 40 \text{ mm} \\ 30 \end{cases}$ $a = 30, 35, 40 \text{ \& } 45 \text{ mm}$	Instron platens + Load rig	Displacement control	P <sub>1</sub>	F.E.M. , E.A.1 E.A.2 & E.A.3
Six	Soil-cement	Single - notched $a = 30, 35, 40 \text{ \& } 45 \text{ mm}$	Instron platens	Displacement control	P <sub>1</sub>	FEM, E.A1 E.A.2 & E.A.3

Table 5.1 Summary of fracture tests



Mix proportions by weight cement:sand:water = 1:3:0.45						Total number	Average
Density of 100 mm cubes (Kg/m <sup>3</sup> )	2229.5	2207.1	2091.3	2234.6	2180.0	42 cubes	2164.3
	2194.4	2093.8	2220.8	2095.5	2170.0		
	2207.9	2098.7	2222.2	2089.9	2190.0		
	2061.9	2115.2	2160.8	2180.0	2230.6		
	2068.4	2083.9	2146.0	2180.0	2203.7		
	2066.0	2084.8	2139.0	2180.0	2215.5		
	2169.0	2191.3	2169.1	2207.1	2183.3		
	2162.7	2202.6	2202.8	2212.5	2201.8		
	2169.6	2187.8					
Compressive strength of 100 mm cubes (MN/m <sup>2</sup> )	46.51	42.72	46.99	44.40	43.50	42 cubes	41.83
	45.43	44.28	43.61	44.29	43.00		
	48.00	44.73	42.14	44.73	43.50		
	35.33	39.79	43.50	41.00	47.50		
	37.08	38.44	41.38	40.00	43.08		
	31.22	38.92	42.29	40.50	44.29		
	38.83	39.70	35.93	45.05	39.43		
	39.35	43.45	40.10	42.18	40.40		
	39.87	40.34					
Elastic modulus of 150 $\phi$ x 300 mm 'E' x 10 <sup>3</sup> (N/mm <sup>2</sup> )	33.68	33.54	32.36	36.96	31.37	7 cylinders	33.33
	32.12	32.81					

Table 5.2 Properties of mortar at 28 days.

Before test	After test	Condition	Failure load (KN)	Before test	After test	Condition	Failure load (KN)
<p>1</p> <p>W = 100 mm</p> <p>30</p> <p>20</p>		Load control	275 270	<p>5</p> <p>20</p> <p>20</p>		Strain control	60
<p>2</p> <p>20</p> <p>20</p>		Load control	270 270	<p>6</p> <p>30</p> <p>30</p>		Load control	35 35
<p>3</p> <p>20</p> <p>20</p>		Strain control	305 328	<p>7</p> <p>40</p> <p>40</p>		Load control	60
<p>4</p> <p>20</p> <p>20</p>		Load control	220 220	<p>8</p> <p>20</p> <p>20</p>		Load control	18

Table 5.3a Trial tests on 100mm mortar cubes

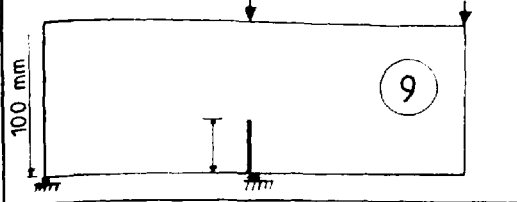
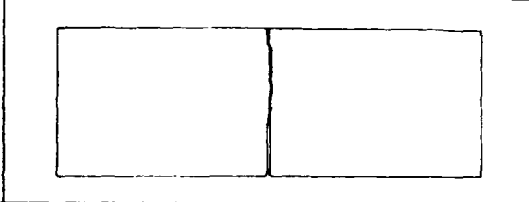
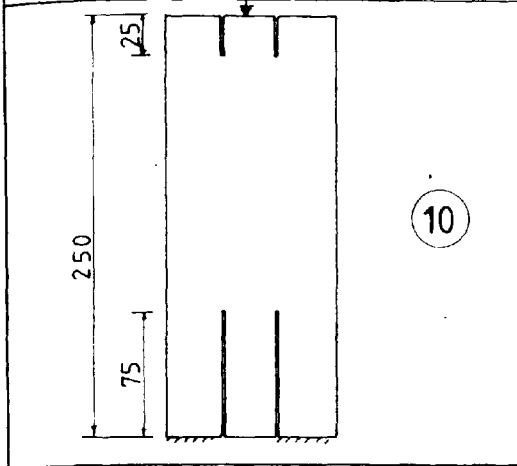
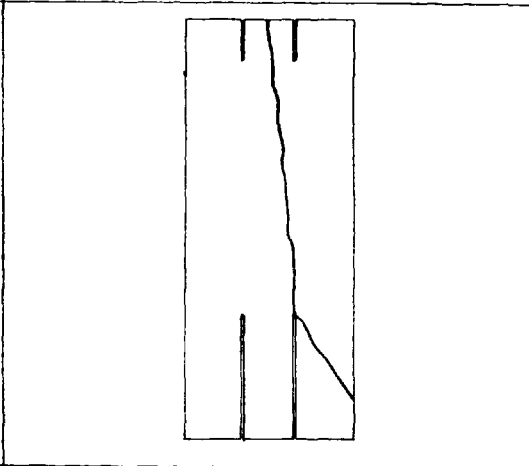
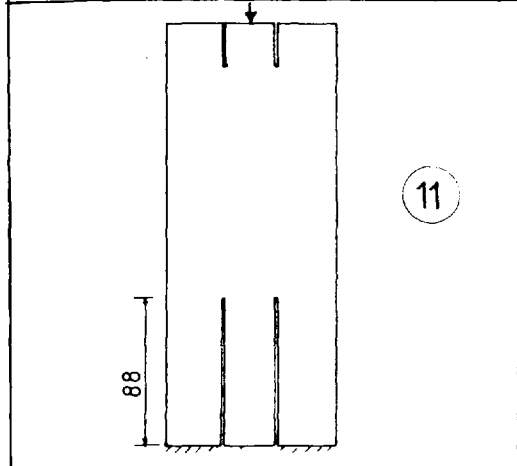
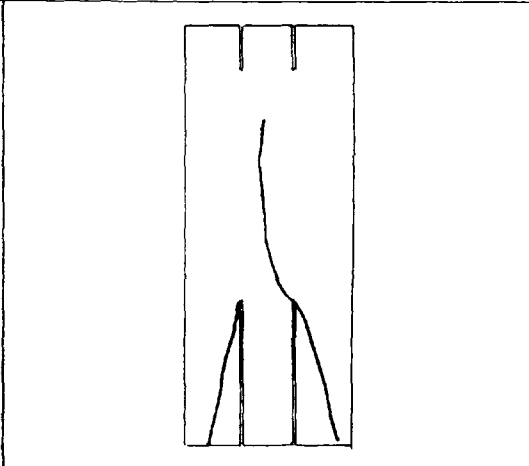
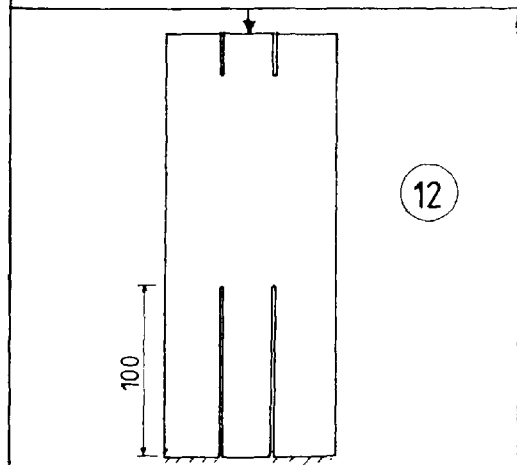
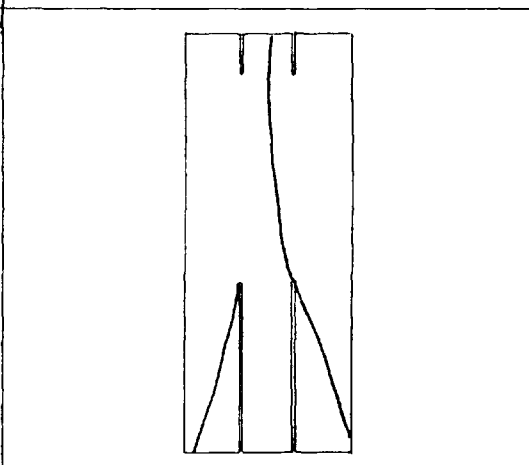
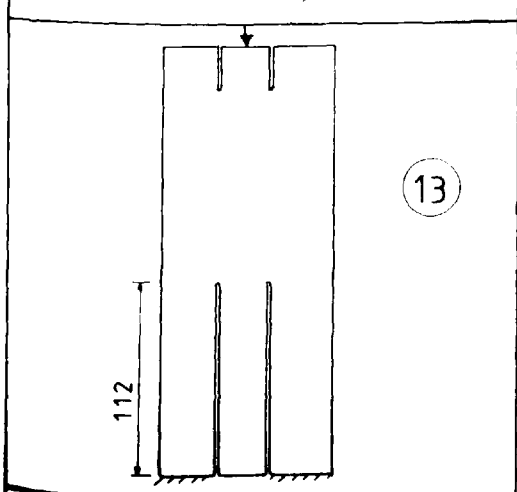
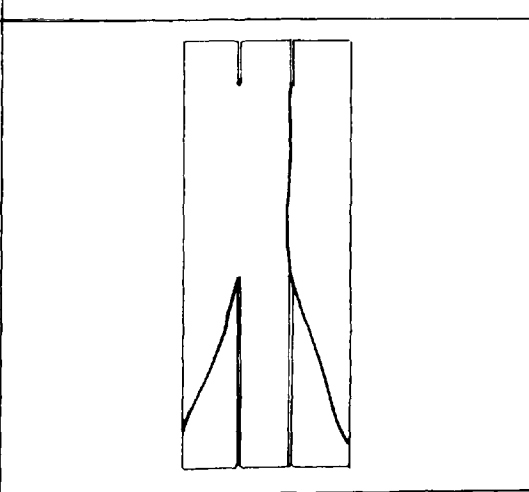
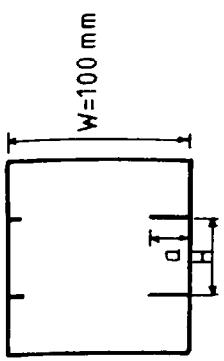
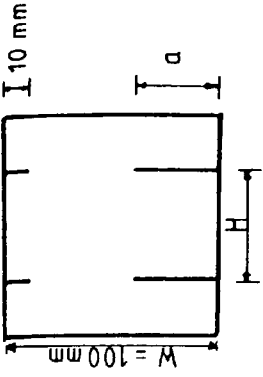
Before test	After test	Condition	Failure load (KN)
 <p>100 mm</p> <p>9</p>		Load control	6 8 14 18
 <p>250</p> <p>75</p> <p>25</p> <p>10</p>		Load control	142.2 140.2 140.0
 <p>88</p> <p>11</p>		Load control	117.3
 <p>100</p> <p>12</p>		Load control	116.0
 <p>112</p> <p>13</p>		Load control	109.8

Table 5.3b Trial tests on 100 x 100 x 250 mm mortar prisms



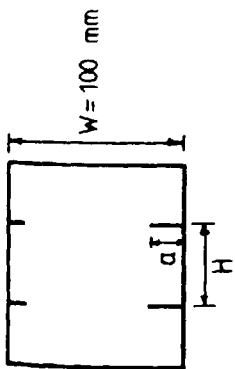
H (mm)	α (mm)	Number of samples		Double shear (%)	Test temp. (°C)	P <sub>1</sub> × 10 <sup>3</sup> (N)	P <sub>max</sub> × 10 <sup>3</sup> (N)
		total	failed in other mechanism shear				
50	30	16	3	18.8	205	30.60	81.80
	35	12	3	25.0	230	34.86	56.25
	40	12	1	8.3	240	29.50	60.20
	45	12	—	—	220	16.40	37.02
40	30	12	—	—	238	34.31	51.44
	35	12	2	16.6	228	25.80	47.50
	40	12	—	—	235	25.42	39.75
	45	12	—	—	220	20.70	35.44
30	30	12	1	8.3	2220	32.80	50.80
	35	12	3	25.0	220	33.82	45.80
	40	12	—	—	2420	25.26	42.68
	45	12	1	8.3	2600	16.20	52.80
		total: 148					

Table 5.4 Test series one : Details of the experiment for the 100 mm double-notched mortar cubes after 28 days.



H (mm)	a (mm)	Number of samples		P $\times 10^3$ (-5% slope) (N)	Mode II stress intensity factors KIIc ( $\text{MN m}^{3/2}$ ) F.E.M.
		total	used in analysis		
50	30	16	3	7937	4.81
	35	12	3	5531	3.95
	40	12	1	5850	5.50
	45	12	—	—	—
40	30	12	—	—	—
	35	12	2	4615	2.84
	40	12	—	—	—
	45	12	—	—	—
30	30	12	1	5000	2.26
	35	12	3	4340	2.31
	40	12	—	—	—
	45	12	1	5280	3.90

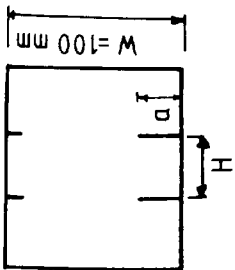
Table 5.5 Test series one : Fracture toughness KIIc for the 100 mm double-notched mortar cubes after 28 days.



H (mm)	a (mm)	Number of samples failed in		Double shear (%)	Test temp (°C)	P <sub>1</sub> × 10 <sup>3</sup> (N)	P <sub>max</sub> × 10 <sup>3</sup> (N)	L (N/mm <sup>2</sup> )	L <sub>max</sub> (N/mm <sup>2</sup> )
		total	other mechanism						
50	30	12	4	66.7	18.5	32.70	109.50	2.72	9.12
	35	12	5	58.3	19.5	27.50	90.70	2.50	8.25
	40	12	8	33.3	13.5	27.20	84.70	2.72	8.47
	45	12	3	75.0	15.0	27.00	78.10	3.00	8.68

total : 48

Table 5.6 Test series two : Details of the experiment for the 100 mm double-notched mortar cubes after 28 days.



H (mm)	a (mm)	Number of samples		P (-5% slope) $\times 10^3$ (N)	KIIc (MNm <sup>3/2</sup> )		%diff of KIIc P (-5%) FEM & EA
		total	used in analysis		P (-5% slope) F.E.M.	EA	
50	30	12	8	110.6	6.71	4.92	26.7
	35	12	7	90.6	6.47	4.58	29.2
	40	12	4	84.7	7.12	4.41	38.1
	45	12	9	76.0	6.96	4.60	33.9

Table 5.7 Test series two : Fracture toughness KIIc for the 100 mm double-notched mortar cubes after 28 days.

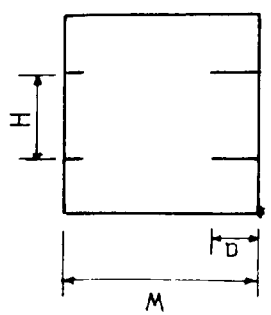
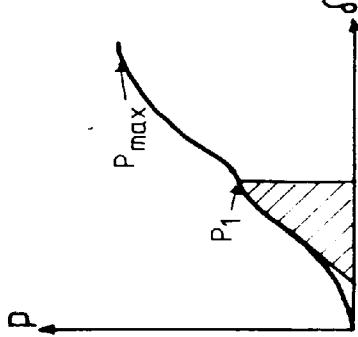
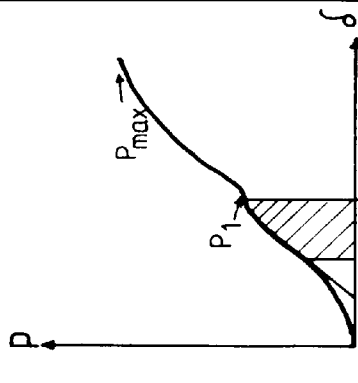
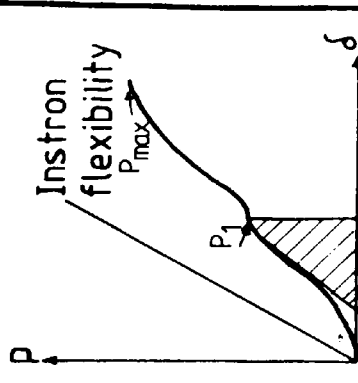
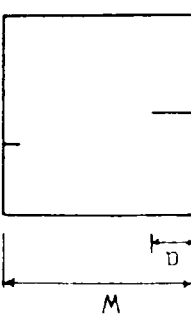
Geometry	Finite element method F.E.M.	Energy Approach			
	H/W=0.5	KII = 119 $\frac{P}{BW} (\pi a)^{1/2}$	E. A. 1	E. A. 2	E. A. 3
	H/W=0.4	KII = 102 $\frac{P}{BW} (\pi a)^{1/2}$			
	H/W=0.3	KII = 89 $\frac{P}{BW} (\pi a)^{1/2}$	<p>WD1 = shaded area</p> $G1 = \frac{WD1}{A}$ $KII = \left( \frac{G1 E}{1 - \nu^2} \right)^{1/2}$	<p>WD2 = shaded area</p> $G2 = \frac{WD2}{A}$ $KII = \left( \frac{G2 E}{1 - \nu^2} \right)^{1/2}$	<p>WD3 = Correction for Instron flexibility</p> $G3 = \frac{WD3}{A}$ $KII = \left( \frac{G3 E}{1 - \nu^2} \right)^{1/2}$
	$Y\left(\frac{a}{W}\right) = 6.062 - 9.192 \left(\frac{a}{W}\right) + 7.600 \left(\frac{a}{W}\right)^2$ $KII = Y\left(\frac{a}{W}\right) \frac{P}{BW} (\pi a)^{1/2}$				

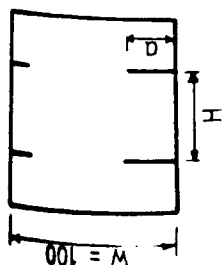
Table 5.8

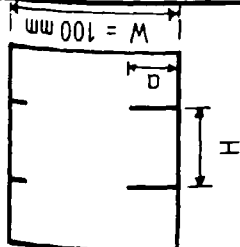


H (mm)	a (mm)	Number of samples failed in		Test temp. (°C)	P <sub>1</sub> × 10 <sup>3</sup> (N)	P <sub>max</sub> × 10 <sup>3</sup> (N)	L (N/mm <sup>2</sup> )	L <sub>max</sub> (N/mm <sup>2</sup> )
		total	other mechanism shear					
50	30	12	4	18.5	32.70	109.50	2.72	9.12
	35	12	5	19.0	27.50	90.70	2.50	8.25
	40	12	8	13.5	27.20	84.70	2.72	8.47
	45	12	3	15.0	27.00	78.10	3.00	8.68
40	30	12	1	17.0	40.50	111.90	3.35	9.23
	35	12	2	20.0	31.30	92.90	2.71	8.04
	40	12	2	20.0	26.10	88.20	2.61	8.82
	45	12	4	21.0	21.70	75.70	2.41	8.41
30	30	12	0	21.5	41.50	105.80	3.46	8.82
	35	12	0	23.0	34.10	103.30	3.07	9.33
	40	12	0	22.0	32.30	102.10	3.23	10.21
	45	12	0	22.0	25.60	90.30	2.85	10.03

total: 144

Table 5.9 Test series three: Details of the experiment for the 100 mm double-notched mortar cubes after 28 days.





H (mm)	a (mm)	Number of samples		$P_1$ $\times 10^3$ (N)	Mode II stress intensity factors KIIc ( $\text{MN m}^{-3/2}$ )			% difference of KIIc values from F.E.M.			
		total	used in analysis		F.E.M.	E.A. 1	E.A. 2	E.A. 3	FEM&EA1	FEM&EA2	FEM&EA3
50	30	12	8	32.7	1.98	2.68	2.34	1.80	-35.4	-18.2	9.1
	35	12	7	27.5	1.97	2.58	2.33	1.83	-31.0	-18.3	7.1
	40	12	4	27.2	2.29	2.53	2.21	1.77	-10.5	3.5	22.7
	45	12	9	27.0	2.67	2.93	2.49	2.23	-9.7	6.7	16.5
40	30	12	9	40.5	2.12	3.35	2.93	2.13	-58.0	-38.2	-0.5
	35	12	10	31.3	1.92	2.63	2.29	1.78	-37.0	-19.3	7.3
	40	12	10	26.1	1.89	2.49	2.07	1.78	-31.7	-9.5	5.8
	45	12	7	21.7	1.85	2.25	1.95	1.65	-21.6	-5.4	10.8
30	30	12	11	41.5	1.88	3.15	2.82	1.86	-67.6	-50.0	1.1
	35	12	12	34.1	1.82	2.77	2.44	1.75	-52.2	-34.1	3.8
	40	12	12	32.3	2.03	2.78	2.47	1.78	-36.9	-21.7	12.3
	45	12	11	25.6	1.90	2.53	2.09	1.78	-33.2	-10.0	6.3

Table 5.10 Test series three : Fracture toughness KIIc for the 100 mm double-notched mortar cubes after 28 days.

H (mm)	a (mm)	P <sub>1</sub> × 10 <sup>3</sup> (N)	K <sub>IIC</sub> (MNm <sup>-3/2</sup> )		% difference of K <sub>IIC</sub> from F.E.M
			F.E.M.	B. C.	
30	30	41.5	1.88	2.05	- 9.0
	35	34.1	1.82	1.82	0
	40	32.3	2.03	1.85	8.9
	45	25.6	1.90	1.55	18.4

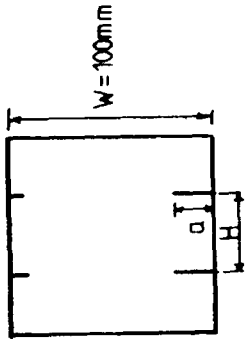


Table 5.11 Test series three : Fracture toughness K<sub>IIC</sub> for the 100 mm double-notched mortar cubes after 28 days.

H (mm)	a (mm)	$P_{max}$ $\times 10^3$ (N)	Latent toughness $K_{LT}$ ( $MN m^{-3/2}$ )					% difference of $K_{LT}$ from F.E.M.		
			F.E.M.	E.A.1	E.A.2	E.A.3	FEM&E.A.1	FEM&E.A.2	FEM&E.A.3	
30	30	105.8	4.82	8.46	8.34	5.59	-75.5	-73.0	-16.0	
	35	103.3	5.54	8.82	8.72	6.10	-59.2	-57.4	-10.1	
	40	102.1	6.44	9.04	8.99	6.00	-40.4	-39.6	6.8	
	45	90.3	6.72	8.58	8.47	6.42	-27.7	-26.0	4.5	

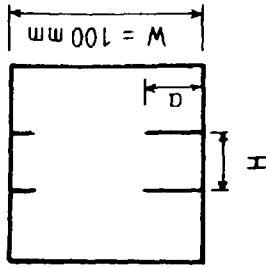
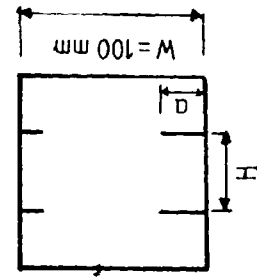


Table 5.12 Test series three : Latent toughness  $K_{LT}$  for the 100 mm double-notched mortar cubes after 28 days.

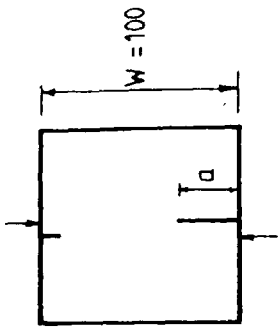


H (mm)	a (mm)	$P_{\max}$ $\times 10^3$ (N)	$K_{LT}$ ( $MNm^{-3/2}$ )		% difference of $K_{LT}$ from F.E.M. F.E.M. & B.C.
			F.E.M.	B.C.	
30	30	105.8	4.82	5.24	- 8.7
	35	103.3	5.54	5.52	0.4
	40	102.1	6.44	5.83	9.5
	45	90.3	6.72	5.47	18.6

Table 5.13 Test series three: Latent toughness  $K_{LT}$  for the 100 mm double-notched mortar cubes after 28 days.

H (mm)	a (mm)	$P_1$ $\times 10^3$ (N)	KIIC		% difference FEM & EA3	$P_{max}$ $\times 10^3$ N	$K_{LT}$ ( $MN \bar{m}^{-3/2}$ )		% difference FEM & EA3
			F.E.M.	E.A.3			F.E.M.	E.A.3	
30	30	41.5	1.88	1.86	1.1	105.8	4.82	5.59	-16.0
	35	34.1	1.82	1.75	3.8	103.3	5.54	6.10	-10.1
	40	32.3	2.03	1.78	12.3	102.1	6.44	6.00	6.8
	45	25.6	1.90	1.78	6.3	90.2	6.72	6.42	4.5
average :		33.4	1.91	1.79		100.4	5.88	6.03	

Table 5.14 Test series three : Comparison of  $K_{LT}$  with KIIC for the 100 mm double-notched mortar cubes after 28 days.



a (mm)	Number of samples failed in		shear (%)	Test temp (°C)	$P_1 \times 10^3$ (N)	$P_{max} \times 10^3$ (N)	L (N/mm <sup>2</sup> )	L <sub>max</sub> (N/mm <sup>2</sup> )
	total	other mechanism shear						
30	12	1	91.7	16.0	25.40	37.90	2.12	3.16
35	12	3	75.0	19.5	23.10	33.20	2.10	3.02
40	12	3	75.0	18.0	24.40	34.20	2.44	3.42
45	12	1	91.7	17.5	23.40	32.60	2.60	3.63

total : 48

Table 5.15 Test series four: Details of the experiment for the 100 mm single-notched mortar cubes after 28 days.

a (mm)	Number of samples		$P_f \times 10^3$ (N)	Mode II stress intensity factors KIIc ( $\text{MN m}^{-3/2}$ )			% difference of KIIc values from F.E.M.			
	total	used in analysis		F.E.M.	E.A.1	E.A.2	E.A.3	FEM & EA1	FEM & EA2	FEM & EA3
30	12	11	25.4	2.60	2.54	2.31	2.02	2.3	11.2	22.3
35	12	9	23.1	2.64	2.72	2.55	2.28	-3.0	3.4	13.6
40	12	9	24.4	3.14	2.88	2.64	2.39	8.3	15.9	23.9
45	12	11	23.4	3.41	2.93	2.70	2.42	14.1	20.8	29.0

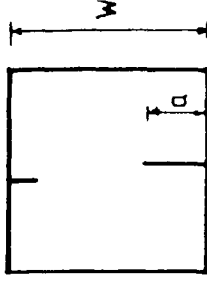


Table 5-16 Test series four: Fracture toughness KIIc for the 100 mm single-notched mortar cubes after 28 days.



Percentage of water (%)	Weight of water (g)	Increment of water (g)
14	453.6	453.6
17	550.8	97.2
20	648.0	97.2
23	745.2	97.2
26	842.4	97.2
29	939.6	97.2

Table 5-17 Weight of water required for the Procter compaction test

Container number	8	17	19	23	72	88
% of water	14	17	20	23	26	29
Mass of container (m1) g.	9.44	9.42	16.14	10.15	9.98	10.10
Mass of wet soil + container (m2) g.	48.24	47.77	49.30	54.19	48.26	67.14
Mass of dry soil + container (m3) g.	43.54	42.41	43.98	46.22	40.61	54.72
Mass of moisture (m2 - m3) g.	4.70	5.36	5.32	7.97	7.65	12.42
Mass of dry soil (m3 - m1) g.	34.10	32.99	27.84	36.07	30.63	44.62
Moisture content $W = \frac{(m2 - m3)}{m3 - m1} \times 100\%$	13.78	16.25	19.11	22.10	24.98	27.84
Mass of mould + base (m1) g	3017	3017	3017	3017	3017	3017
Mass of mould + base + compacted soil (m2) g.	4979	5096	5104	5043	4993	4904
Mass of compacted soil (m2 + m1) g.	1962	2079	2087	2026	1976	1887
Bulk density $\rho = \frac{(m2 - m1)}{1000}$ (Mg/m <sup>3</sup> )	1.962	2.079	2.087	2.026	1.976	1.887
Dry density $= \frac{100\rho}{100+W}$ (Mg/m <sup>3</sup> )	1.72	1.79	1.75	1.66	1.58	1.48

Table 5.18 Values obtained from the Procter compaction test.

Liquid limit	22.4 % M.C.
Plastic limit	15.2 % M.C.
Moisture content	16.6 %
Optimum dry density	1.78 (Mg/m <sup>3</sup> )
Elastic modulus 'E'	1200.0 (N/mm <sup>2</sup> )
Poisson's ratio 'γ'	0.25
Compressive strength	4.96 (MN/m <sup>2</sup> )

(a) General properties of soil-cement (8 %)

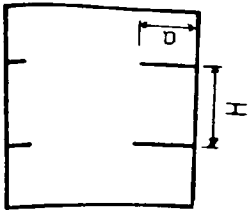
Method of compaction		Density of 100mm soil-cement cubes (8% cement) (kg/m <sup>3</sup> )	Average (kg/m <sup>3</sup> )
4.5 Kg rammer	Number of blows		
	12	2021 2040 2014 2027 1965	2013
	15	2113 2106 2096 2110 2074	2100
	18	2100 2111 2093 2090 2110 2094 2108 2111	2109
		2097 2125 2128 2136 2157 2116 2133 2087	
		2168 2108 2139 2140 2139 2130 2118 2118	
2167 2161 2172 2170 2080 2141 2059 2132			
2064 2095 2092 2102 2113 2082 2095 2089			
20	2085 2079 2082 2078 2108 2107 2109 2058	2127	
	2083 2054 2120 2042		
Electrical Kango hammer	15 seconds	2191 2155 2159 2172 2178	2171

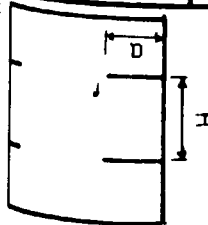
(b) Variation of density of 100 mm soil-cement cube with methods of compaction.

H (mm)	a (mm)	Number of samples failed in		Double shear (%)	Test temp (°C)	$P_i \times 10^3$ (N)	$P_{max} \times 10^3$ (N)	$\tau$ (N/mm <sup>2</sup> )	$\tau_{max}$ (N/mm <sup>2</sup> )
		total	other mechanism						
50	30	8	2	75.0	19.5	8.61	16.07	0.72	1.34
	35	8	1	87.5	19.5	7.23	12.26	0.66	1.11
	40	8	3	62.5	12.5	4.98	9.84	0.50	0.98
	45	8	7	12.5	14.5	3.70	15.60	0.41	1.73
40	30	8	2	75.0	17.5	8.70	15.50	0.72	1.29
	35	8	3	62.5	16.0	7.40	16.50	0.68	1.50
	40	8	—	100.0	17.0	6.00	11.80	0.56	1.12
	45	8	3	62.5	20.0	5.50	14.50	0.61	1.60
30	30	8	—	100.0	17.0	9.20	15.80	0.76	1.30
	35	8	—	100.0	17.5	8.00	14.50	0.72	1.30
	40	8	—	100.0	17.0	5.40	13.20	0.54	1.32
	45	8	—	100.0	18.0	4.90	11.70	0.54	1.30

total: 96

Table 5.20 Test series five : Details of experiment for the 100 mm double-notched soil-cement cubes after 28 days.





H (mm)	a (mm)	Number of samples		$P_1$ $\times 10^3$ (N)	Mode II stress intensity factors KIIc ( $\text{MN m}^{-3/2}$ )				% difference of KIIc values from F.E.M.		
		total	used in analysis		F.E.M.	E.A.1	E.A.2	E.A.3	FEM & EA1	FEM & EA2	FEM & EA3
50	30	8	6	8.61	0.52	0.40	0.35	0.39	23.1	32.7	25.0
	35	8	7	7.23	0.52	0.40	0.34	0.39	23.1	34.6	25.0
	40	8	5	4.98	0.42	0.30	0.28	0.30	28.6	33.3	28.6
	45	8	1	3.70	0.37	0.23	0.20	0.23	37.8	45.9	37.8
40	30	8	6	8.70	0.45	0.39	0.34	0.38	13.3	24.4	15.6
	35	8	5	7.40	0.46	0.36	0.29	0.35	21.7	37.0	23.9
	40	8	8	6.00	0.43	0.41	0.37	0.42	4.7	14.0	2.3
	45	8	5	5.50	0.47	0.29	0.24	0.28	38.3	48.9	40.4
30	30	8	6	9.20	0.41	0.45	0.40	0.44	- 9.8	2.4	- 7.3
	35	8	6	8.00	0.43	0.44	0.40	0.42	- 2.3	7.0	2.3
	40	8	6	5.40	0.34	0.24	0.21	0.23	29.4	38.2	32.4
	45	8	7	4.90	0.36	0.31	0.26	0.30	13.9	27.8	16.7

Table 5.21 Test series five : Fracture toughness KIIc for the 100 mm double-notched soil-cement cubes after 28 days.

H (mm)	a (mm)	P <sub>1</sub> × 10 <sup>3</sup> (N)	K <sub>IIc</sub> (MNm <sup>-3/2</sup> )		% difference of K <sub>IIc</sub> from F.E.M.
			F.E.M.	B.C.	
30	30	9.2	0.41	0.46	-12.2
	35	8.0	0.43	0.43	0
	40	5.4	0.34	0.31	8.8
	45	4.9	0.36	0.30	16.7

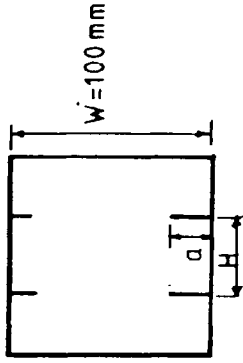
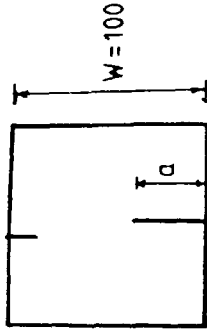


Table 5.22 Test series five: Fracture toughness K<sub>IIc</sub> for the 100 mm double-notched soil-cement cubes after 28 days.

a (mm)	Number of samples failed in		shear (%)	Test temp (°C)	$P_1 \times 10^3$ (N)	$P_{max} \times 10^3$ (N)	L (N/mm <sup>2</sup> )	$L_{max}$ (N/mm <sup>2</sup> )
	total	other mechanism						
30	7	—	100.0	17.0	3.74	5.66	0.31	0.47
35	7	1	85.7	19.5	4.57	6.42	0.42	0.58
40	7	1	85.7	19.0	4.58	7.08	0.46	0.70
45	7	7	100.0	19.0	4.21	7.76	0.47	0.97

total : 28

Table 5.23 Test series six : Details of the experiment for the 100 mm single-notched soil-cement cubes after 28 days.



a (mm)	Number of samples		P <sub>i</sub> × 10 <sup>3</sup> (N)	Mode II stress intensity factors KIIc (MN m <sup>-3/2</sup> )				% difference of KIIc values from F.E.M.		
	total	used in analysis		F.E.M.	E.A.1	E.A.2	E.A.3	FEM & EA1	FEM & EA2	FEM & EA3
30	7	7	3.74	0.38	0.28	0.26	0.28	26.3	31.6	26.3
35	7	6	4.57	0.52	0.30	0.28	0.30	42.3	46.2	42.3
40	7	6	4.58	0.59	0.35	0.30	0.34	40.7	49.2	42.4
45	7	7	4.21	0.61	0.33	0.31	0.33	45.9	49.2	45.9

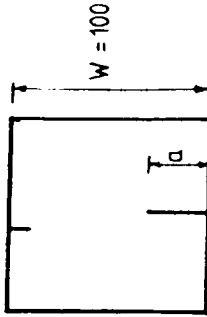


Table 5.24 Test series six : Fracture toughness KIIc for the 100 mm single-notched soil-cement cubes after 28 days.





Plate 5.1 Insertion of notches on mortar cubes using a Clipper masonry saw

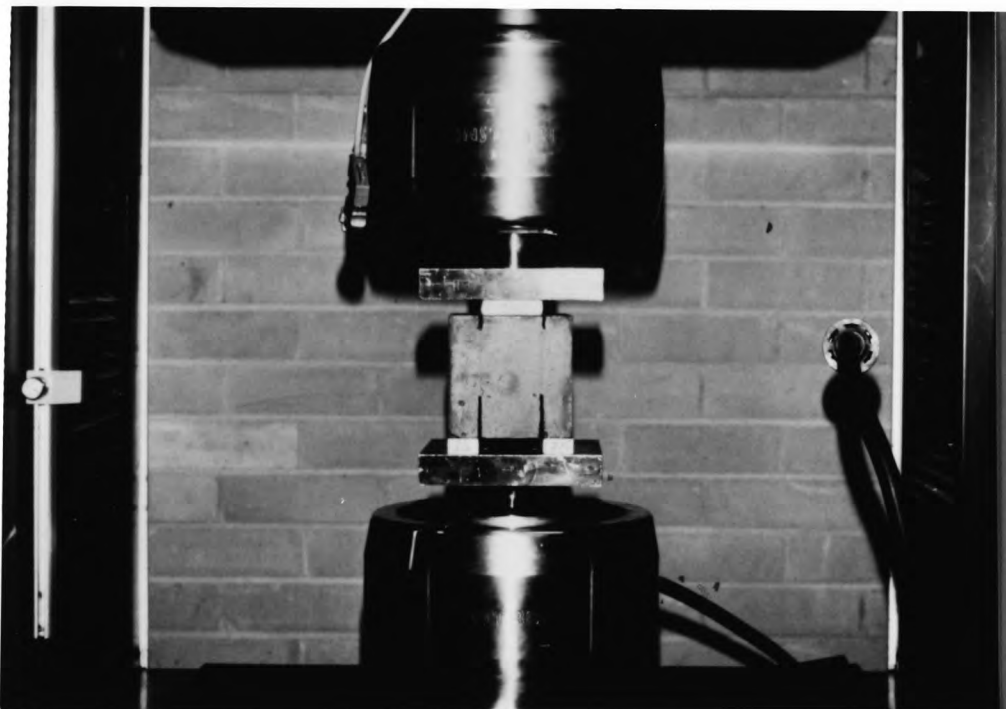


Plate 5.2 Fracture test on double-notched mortar cube using Departmental made compressive platens

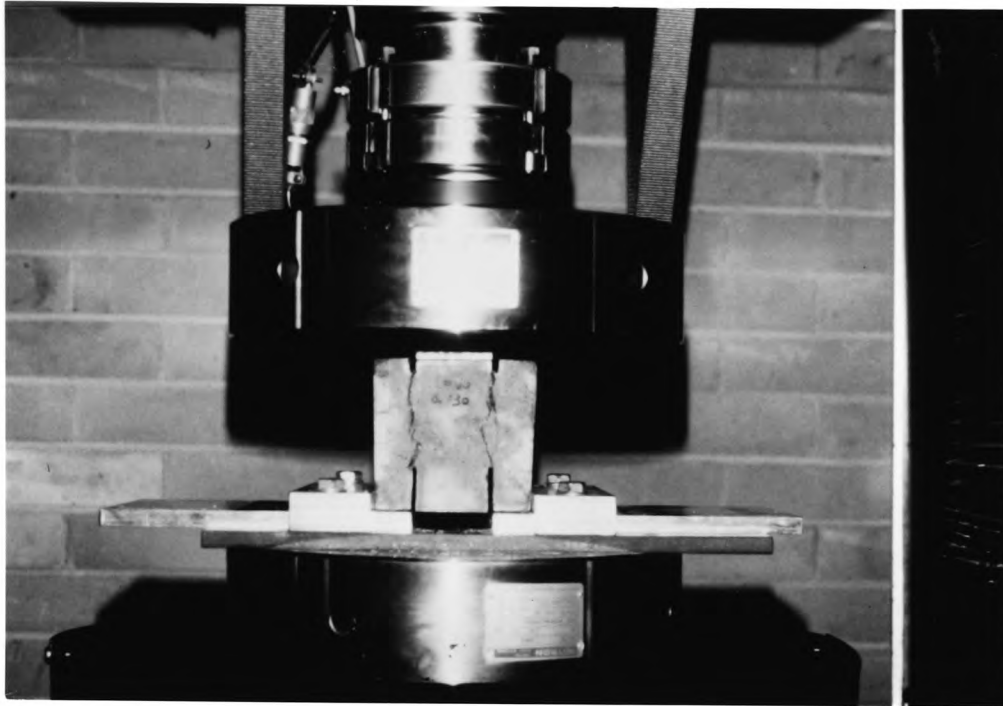


Plate 5.3 Fracture test on double-notched mortar cubes using INSTRON compressive platens

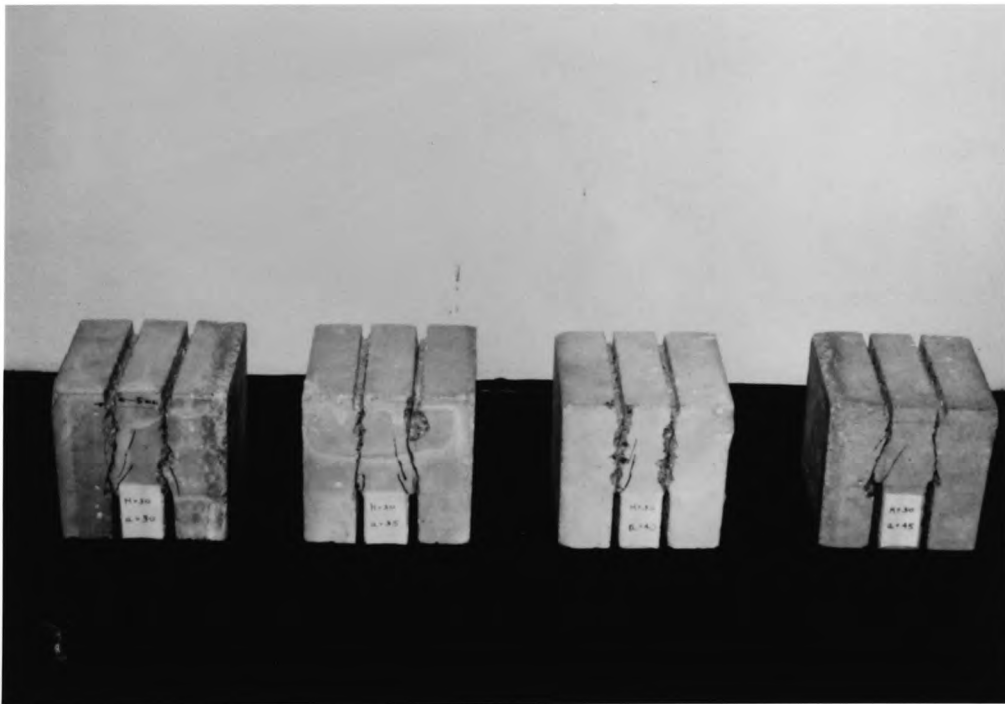


Plate 5.4 Typical double shear failure patterns of mortar cubes of  $H = 30\text{mm}$ ,  $a = 30, 35, 40$  and  $45\text{mm}$



Plate 5.5 Typical fracture surface of a cube  $a_1$  and  $b_1$  correspond to the shear particles  $a_2$  and  $b_2$

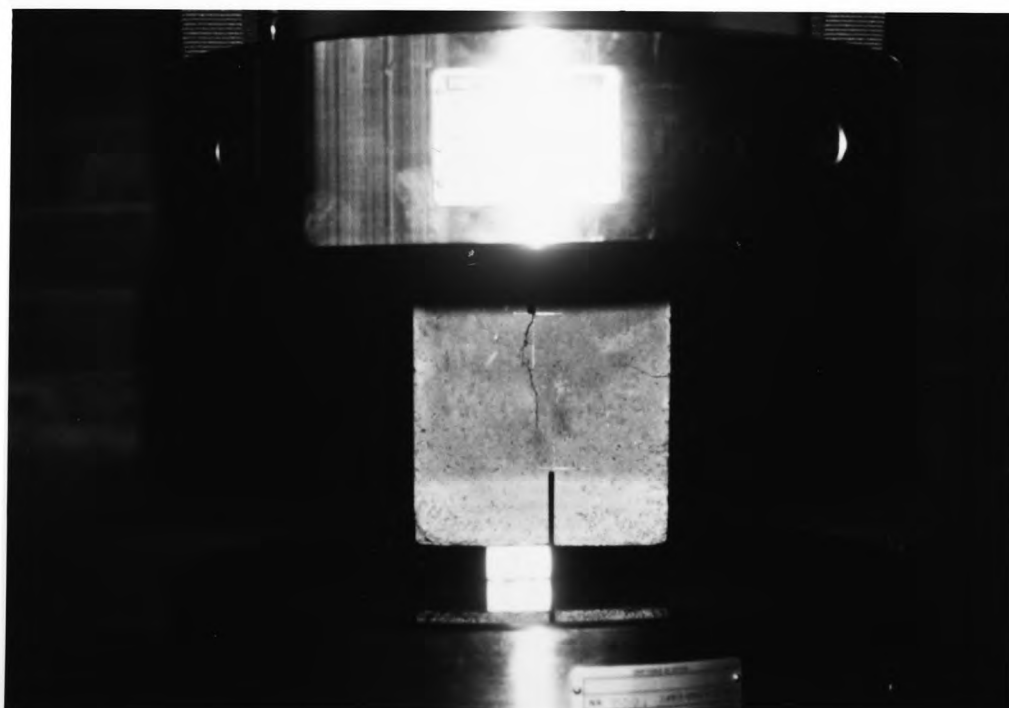


Plate 5.6 Fracture test on single-notched mortar cube



Plate 5.7 Typical single shear failure patterns of mortar cubes of  $a = 30$  ,  $35$  and  $40\text{mm}$



Plate 5.8 Hand-compacted in 5 equal layers of soil cement



Plate 5.9 4.5Kg rammer for 18 blows of compaction

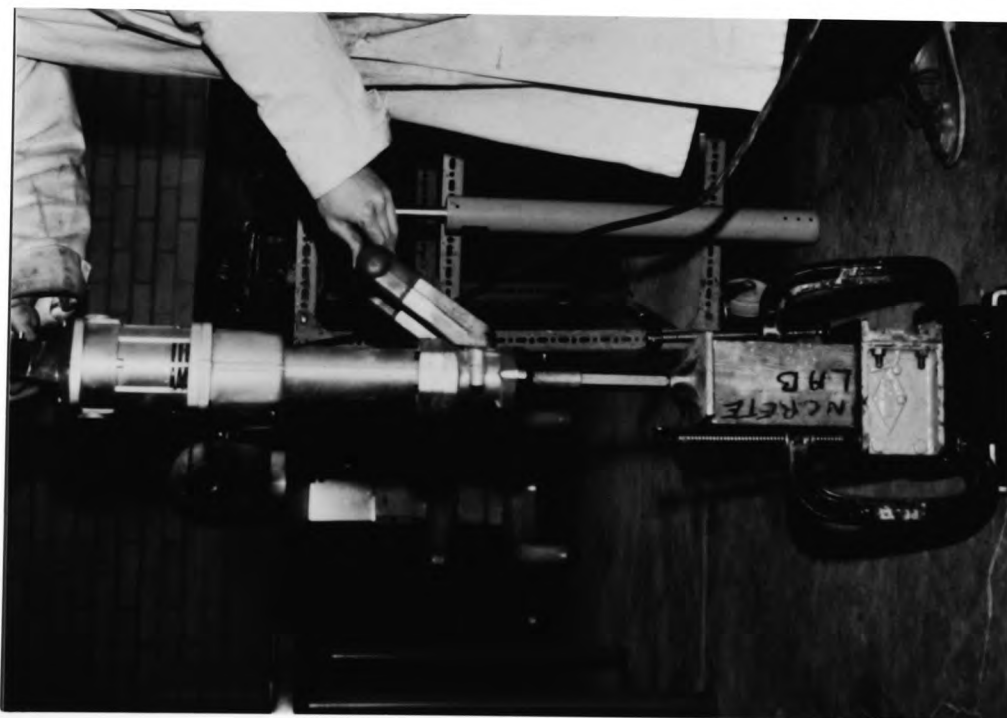


Plate 5.10 Kango "900" demolition hammer for 15 seconds of compaction



Plate 5.11 Level off a soil-cement cube



Plate 5.12 Insertion of notches on soil-cement cubes using a specially mounted circular lathe

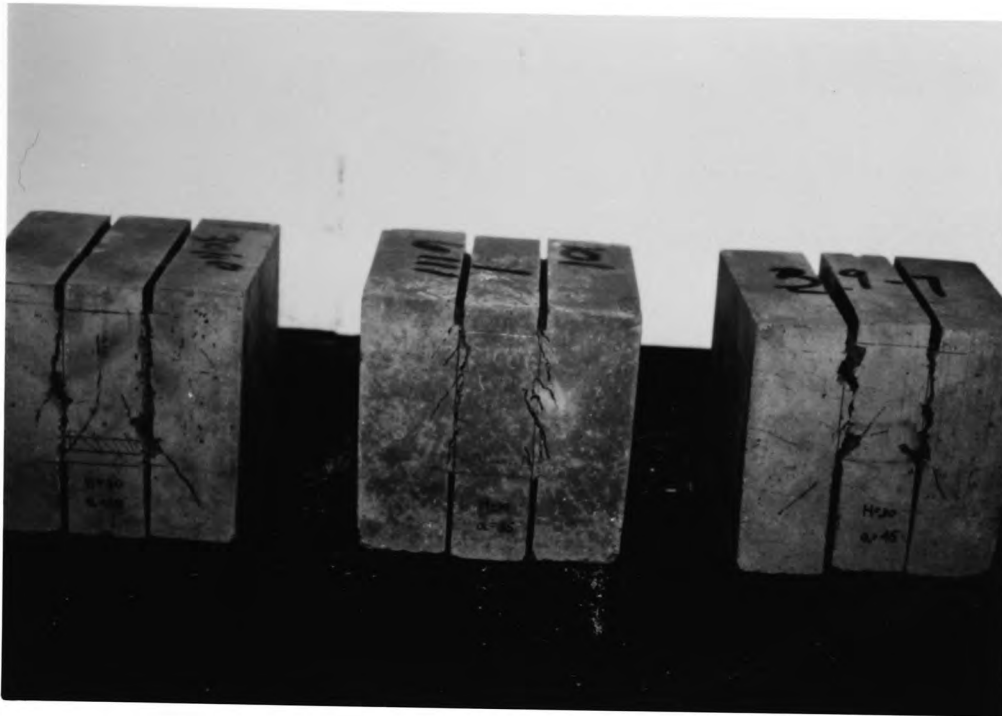


Plate 5.13 Typical double shear failure patterns of soil-cement cubes of  $H=30\text{mm}$ ,  $a=30,35$  and  $45\text{mm}$



Plate 5.14 Typical single shear failure patterns of soil-cement cubes of  $a=30,35,40$  and  $45\text{mm}$

## CHAPTER 6

### CONCLUSIONS AND FUTURE WORK

#### 6.1 CONCLUSIONS

The main aim of this project was to determine the Mode II fracture toughness of mortar and soil-cement using both the stress intensity factor  $K$  approach and the strain energy release rate  $G$  approach. The work was divided into two main areas :

- (a) The finite element modelling of 100mm double-notched, 100mm single-notched and 150mm double-notched cubes.
- (b) The determination of fracture toughness values for 100mm double-notched and single-notched cubes in compression using the INSTRON testing machine. Both mortar and soil-cement were used.

##### 6.1.1 Finite Element Modelling for 100mm Double-Notched Cubes

In the finite element analysis all the work was carried out on a VAX 11/785 computer using the PAFEC computer program suite.

The main aim was to model a Mode II type of failure occurring on a compact shear cube with a pair of double notches on the top and bottom face. Because of symmetry about the centre line of the cube, only one half of the cube was represented by a mathematical



model satisfying both the boundary and loading conditions. Four types of quadrilateral isoparametric elements were compared; they were 4-noded, 8-noded, 17-noded and distorted elements used at the crack tip together with the 8 noded elements. It was found that the latter combination produced sufficiently accurate results for the desired engineering application. This is because crack tip elements at the crack tip can represent the elastic crack tip singularity which is required in the elastic fracture analysis and have the advantage of using considerably less computer time than higher order elements.

The convergence study of the stress intensity factor  $K_{II}$  was carried out using several mesh designs and it was found that the 60 element-mesh produced a desirable accuracy of  $K_{II}$  values.

In order to determine which mode of failure is predominant under the shear load condition, a comparison of the  $K_I$  and  $K_{II}$  values was made. The compact shear cubes have a notch spacing  $H = 50, 40$  and  $30\text{mm}$  with the upper notch depth being kept at  $10\text{mm}$  and the lower notch depth varies from  $25\text{mm}$  to  $60\text{mm}$  in  $5\text{mm}$  increments. A 60 element-mesh with crack tip elements at the crack tip was used in the analysis and a total of 24 computer runs were made. Chan's displacement equations were employed to evaluate the  $K_I$  and  $K_{II}$  values. It was found that the  $K_{II}$  values are many times higher than  $K_I$  (e.g.  $K_{II}/K_I = 124$  for  $H = 30\text{mm}$ ,  $a = 60\text{mm}$ ) when the notch spacing decreases and notch depth increases, thus indicating

that a Mode II type of failure is predominant

The calibration coefficients for the 100mm compact shear cubes were determined and the equations for  $K_{II}$  stress intensity factors were obtained as follows :

$$(a) \quad H = 50\text{mm} \quad K_{II} = 1.19 \frac{P}{BW} (\pi a)^{\frac{1}{2}}$$

$$(b) \quad H = 40\text{mm} \quad K_{II} = 1.02 \frac{P}{BW} (\pi a)^{\frac{1}{2}}$$

$$(c) \quad H = 30\text{mm} \quad K_{II} = 0.89 \frac{P}{BW} (\pi a)^{\frac{1}{2}}$$

#### 6.1.2 Experimental Investigation (mortar)

The compact shear fracture for 100mm double-notched mortar cubes were conducted in compression. All the fracture tests were carried out in the INSTRON testing machine using displacement control mode at a rate of 0.003 mm/s .

The first test series was unsuccessful due to the inadequacy of both the machine loading platens and the loading rig.

In the second test series the improved experimental set-up has been used. This consisted of the special INSTRON compressive platens ensuring the uniform load application and also a simple loading rig ensuring that the shear loading condition was maintained during testing.

Double-notched mortar cubes of notch spacing  $H = 50$  ,  $40$  and  $30\text{mm}$  and the lower notch depth varying from  $30\text{mm}$  to  $45\text{mm}$  in  $5\text{mm}$  increments were tested; a total of 144 cubes in all. It was found that 58% of the cubes failed in double shear for notch spacing  $H = 50\text{mm}$  , 80% for  $H = 40\text{mm}$  and 100% for  $H = 30\text{mm}$  . The results confirmed the conclusions drawn from the finite element analysis that with decreasing notch spacing  $H$  and increasing notch depth a the shear mechanism assumes greater significance. The fracture toughness values were determined using the stress intensity factor  $K$  approach and the strain energy release rate  $G$  approach.

In view of the difficulty in understanding the fracturing process in compression three interpretations of the load-displacement curves were used in calculating the fracture energies. They were EA1 , EA2 and EA3 . In the EA1 method, the work done was calculated by measuring the area under the load-displacement curve. In the EA2 method, the area under the initial non-linear part of the plot, was disregarded because it reflects machine/specimen interaction and the work done under this part of the curve does not contribute to the fracturing process. The work done used in fracture toughness calculation was obtained by measuring the area under the linear part of the plot. In the EA3 method, the work done obtained in the EA1 method was corrected for the machine stiffness characteristics.

It was found that the finite element method and the energy methods produced similar fracture toughness  $K_{IIC}$  when  $P_1$  was used provided corrections for machine/specimen interaction and machine stiffness characteristics were made. The most suitable geometry appeared to be of  $H = 30\text{ mm}$  and  $a = 45\text{ mm}$  for the Mode II shear test. The average  $K_{IIC}$  using the finite element method was found to be  $1.9\text{ MN m}^{-3/2}$ , the  $K_{IIC}$  based on the strain energy release rate was found to be in the order of 1.78 to  $2.09\text{ MN m}^{-3/2}$  and the average  $K_{IIC}$  based on the Chisholm and Jones equation was  $1.55\text{ MN m}^{-3/2}$ . Desayi (16) reported the fracture toughness values obtained from the centrally located inclined crack for mortar prisms in compression are in the range of 1.03 to  $9.37\text{ MN m}^{-3/2}$  which correspond to those obtained in this study.

Close correlation between the finite element method and the energy methods was again obtained when failure load  $P_{\max}$  was used in determining the latent toughness  $K_{LT}$ . The average  $K_{LT}$  based on the finite element method was found to be  $6.72\text{ MN m}^{-3/2}$ , the  $K_{LT}$  based on the strain energy release rate was found to be in the order of 6.42 to  $8.47\text{ MN m}^{-3/2}$  and the  $K_{LT}$  based on the Chisholm and Jones equation was  $5.47\text{ MN m}^{-3/2}$ .

It was found that the latent toughness  $K_{LT}$  based on the maximum load (at failure) was about three times of the fracture toughness  $K_{IIC}$  based on the 'pop-in' load  $P_1$  (when the first crack appeared) using both the finite element method and the EA3 method.

The failure load  $P_{max}$  was also found to be three times the load  $P_1$ . This indicates that the critical fracture toughness  $K_{IIC}$  when the first crack occurs at the notch tip and the latent toughness when failure occurs correspond to the same order of the load at  $P_1$  and at 'failure'  $P_{max}$ .

### 6.1.3 Experimental Investigation (soil-cement)

In the determination of the fracture toughness for 100mm soil-cement cubes, the same experimental set-up was used as for mortar. The notches of the cubes were spaced at  $H = 50$ , 40 and 30mm and the lower notch depth varied from 30mm to 45mm in 5mm increments, a total of 96 cubes were tested.

It was found that 59% failed in double shear for notch spacing  $H = 50$ mm, 75% for  $H = 40$ mm and 100% for  $H = 30$ mm. These results confirmed the conclusions drawn from the finite element analysis that with decreasing notch spacing  $H$  and increasing notch depth  $a$ , the shear failure mechanism assumes the greater significance.

The fracture toughness values were determined using the stress intensity factor  $K$  approach (finite element method) and the strain energy release rate  $G$  approach where the 'pop-in' load  $P_1$  was used in all cases. Three energy approaches were used in the determination of fracture energy from the load-displacement curve, they were EA1, EA2 and EA3. The work done in the EA1

method obtained by measuring the area under the load-displacement curve, the work done in the EA2 method was corrected for the machine/stiffness interaction and correction was made for the machine stiffness characteristics in the EA3 method.

It was found that a good correlation in  $K_{IIC}$  values was obtained between the finite element method and the EA1 method. This indicated that correction for the machine/specimen interaction was not necessary because the specimen geometry was sufficiently flexible.

The best geometries for the Mode II fracture test appeared to be of notch spacing  $H = 30\text{mm}$ , notch depth  $a = 35\text{mm}$  and  $H = 40\text{mm}$ ,  $a = 40\text{mm}$ . The average fracture toughness  $K_{IIC}$  using the finite element method for  $H = 30\text{mm}$ ,  $a = 35\text{mm}$  was found to be  $0.43 \text{ MN m}^{-3/2}$ , the  $K_{IIC}$  based on the strain energy release rate was found to be in the order of  $0.40$  to  $0.42 \text{ MN m}^{-3/2}$  and the average  $K_{IIC}$  based on Chisholm and Jones equation  $0.43 \text{ MN m}^{-3/2}$ , which corresponds to those obtained in this study. For  $H = 40\text{mm}$ ,  $a = 40\text{mm}$ , the average  $K_{IIC}$  based on the finite element method was  $0.43 \text{ MN m}^{-3/2}$ , the  $K_{IIC}$  based on the strain energy release rate was in the order of  $0.37$  to  $0.42 \text{ MN m}^{-3/2}$  and the average  $K_{IIC}$  based on Chisholm and Jones equation was  $0.40 \text{ MN m}^{-3/2}$ .

#### 6.1.4 Finite Element Modelling for 100mm Single-Notched Cubes

It was found in the analysis of double-notched cubes that

a Mode II type of failure assumes greater significance with decreasing notch spacing, therefore a single notch of 10mm deep on the top surface and a single notch of 30mm deep on the bottom surface of a cube was modelled.

The convergence study of the stress intensity factor  $K_{II}$  was carried out using several mesh designs and crack tip elements (at the crack tip only) together with 8 noded quadrilateral iso-parametric elements were used. Woo's Mode II displacement equation was used to determine  $K_{II}$ . It was found that the 240 element-mesh was sufficiently accurate for the  $K_{II}$  value determination.

In order to determine which mode of failure is predominant under the shear load, a comparison was made to study the  $K_I$  and  $K_{II}$  values. The upper notch depth of the cube was kept at 10mm, the lower notch depth varied from 25 to 60mm in 5mm increments, a total of 8 computer runs were made. It was found that the  $K_{II}$  values were not significantly larger than  $K_I$ . The highest  $K_{II}/K_I = 1.2$  for  $a/W = 0.6$ . The calibration coefficients were obtained for  $0.25 \leq a/W \leq 0.6$  and found to be dependent on  $a/W$  ratios.

#### 6.1.5 Experimental Investigation (mortar)

Experiments in the determination of fracture toughness for 100mm single-notched mortar cubes were carried out using the INSTRON compressive platens. The upper notch which was off-set at 6mm to the lower notch, was kept at 10mm and the lower notch depth varied from 30mm to 45mm in 5mm increments, a total of 48 cubes were tested.

It was found that there was no significant correlation between the fracture toughness  $K_{IIC}$  when the finite element method and the strain energy release rate were used. Therefore this geometry was not suitable for the Mode II fracture test.

#### 6.1.6 Experimental Investigation (soil-cement)

In the determination of fracture toughness for 100mm single-notched soil-cement cubes, a total of 28 cubes were tested. It was found that 100% shear failure was achieved for notch depth ratios  $a/W = 0.30$  and  $0.45$  and 86% for  $a/W = 0.35$  and  $0.4$ .

It was found that high percentage differences in  $K_{IIC}$  values were obtained between the finite element method and the fracture energy methods, therefore the single-notched soil-cement cube were not suitable for Mode II fracture test purposes.

#### 6.1.7 Finite Element Modelling for 150mm Double-Notched Cubes

The main aim was to model a Mode II type of failure occurring on a 150mm compact shear cube with a pair of double notches on the top and bottom surfaces. Because of symmetry about the centre line of the cube, only one half of the cube was represented by a mathematical model satisfying both the boundary and loading conditions.

The convergence study of the stress intensity factor  $K_{II}$  was carried out using several mesh designs and it was found that the 294 element-mesh produced a desirable accuracy of  $K_{II}$  value.



In order to determine which mode of failure is predominant under the shear load, a comparison was made to study the  $K_I$  and  $K_{II}$  values. The compact shear cubes have a notch spacing  $H = 80, 60$  and  $40\text{mm}$  with the upper notch depth kept at  $15\text{mm}$  and the lower notch depth varied from  $30\text{mm}$  to  $80\text{mm}$  in  $5\text{mm}$  increments. A 294 element-mesh with crack tip elements at the crack tip was used in the analysis and a total of 33 computer runs were made. Woo's displacement equations were employed to evaluate the  $K_I$  and  $K_{II}$  values. It was found that  $K_{II}/K_I$  ratio increases rapidly with the decrease of notch spacing  $H$  and increase of notch depth  $a$ . In the case of  $H = 40\text{mm}$  and  $a = 80\text{mm}$ ,  $K_{II}/K_I$  reaches infinity. This implies that a "pure" Mode II type of failure can be obtained with a smaller notch spacing and a deeper notch depth of  $150\text{mm}$  double-notched cube.

The calibration coefficients for the three notch spacings were obtained using a least square method and the equations for  $K_{II}$  stress intensity factors were obtained as follows :

$$(a) \quad H = 80\text{mm} \quad K_{II} = \left[ 2.35 - 2.93\left(\frac{a}{W}\right) + 2.99\left(\frac{a}{W}\right)^2 \right] \frac{P}{BW} (\pi a)^{\frac{1}{2}}$$

$$(b) \quad H = 60\text{mm} \quad K_{II} = \left[ 1.91 - 2.35\left(\frac{a}{W}\right) + 2.36\left(\frac{a}{W}\right)^2 \right] \frac{P}{BW} (\pi a)^{\frac{1}{2}}$$

$$(c) \quad H = 40\text{mm} \quad K_{II} = \left[ 1.67 - 2.76\left(\frac{a}{W}\right) + 3.30\left(\frac{a}{W}\right)^2 \right] \frac{P}{BW} (\pi a)^{\frac{1}{2}}$$

In conclusion it can be said that the linear elastic fracture mechanics is applicable to the 100mm double-notched mortar cubes provided correction is applied to experimental results for the machine/specimen interaction or the machine stiffness characteristics; because both the stress intensity factor  $K$  approach (finite element method) and the strain energy release rate  $G$  approach yield very similar fracture toughness  $K_{IIC}$  for  $H = 30\text{mm}$  and  $a = 45\text{mm}$ . The linear elastic fracture mechanics is also applicable to the 100mm double-notched soil-cement cubes for  $H = 40\text{mm}$ ,  $a = 40\text{mm}$  and  $H = 30\text{mm}$ ,  $a = 35\text{mm}$  with no correction is needed for the experimental results because the specimen geometries were sufficiently flexible to produce similar  $K_{IIC}$  values when both the finite element method and the energy methods were used.

## 6.2 FUTURE WORK

Finite element modelling has been established for the Mode II type of failure for 100mm double-notched 100mm single-notched and 150mm double-notched cubes. Experimental works have been done to verify the finite element analyses on 100mm double-notched and single-notched cubes, both mortar and soil-cement were used. Most of the works have shown a good correlation between the finite element analysis and the experimental verification in the determination of fracture toughness values. It is considered that further investigations should be carried out in order to improve the results.

In the finite element modelling for 100mm double-notched cubes it has been shown that the Mode II shear failure assumes the greater significance with the decrease of notch spacing and increase of notch depth. Therefore further reduction in notch spacing  $H$  should be carried out for  $H = 20\text{mm}$  and  $10\text{mm}$ , the upper notch depth should be kept at  $10\text{mm}$  for consistency and the lower notch depth should have bigger ranges to study the shear effect on the cube. It is hoped that this would be confirmed in future.

In the finite element modelling for 100mm single-notched cubes it has been shown that a "pure" shear failure was not obtained because  $K_{II}/K_I$  ratio was not significantly high. This could be the result of inadequate arrangement of the notches since the upper notch was off-centre at  $6\text{mm}$  to the lower notch and a mixed Mode I and Mode II displacement condition was likely to occur. The single-notched cube should be re-arranged so that the top notch is in line with the bottom notch. Again the upper notch depth should be kept at  $10\text{mm}$  and the bottom notch depth should have a bigger range as in the case of the proposed double-notched cubes so that direct comparison can be made to these two geometries.

In the finite element modelling of 150mm double-notched cubes direct stress and shear stress profiles should be plotted along the line of action of the compressive load for  $H = 40\text{mm}$  in order to support the claim of a "pure" shear condition (as has been shown that  $K_{II}/K_I$  ratio equals infinity at  $a = 80\text{mm}$ ). It has been shown that

the calibration coefficients obtained using a constant element-mesh of 294 elements of the finite element method scatter when  $0.2 \leq a/W \leq 0.53$  for  $H = 80, 60$  and  $40\text{mm}$  respectively. Re-arrangement of element-mesh when the notch depth increases should be carried out in order to improve the accuracy of the analyses. Trial tests should be carried out in order to obtain the range of failure loads on different notch ratios for further analysis.

In the experimental works of determining fracture toughness of mortar and soil-cement, it has been shown that it is rather easy to prepare and control the quality of mortar but not soil-cement. Since the desired moisture content and compaction bear an important structural property on the soil-cement, therefore it is of interest to use different moisture content and degree of compaction in comparing the  $K_{IIC}$  value.

For all the energy approaches, the work done under the load-displacement curves has been measured manually using a planimeter. The work was time consuming and inaccurate. A data logging system should be assembled and an associated software programme written to record the displacement of the loading platen and the load. This will assist the calculation of the experimental stress intensity factors as the area under the load-displacement curve can be readily measured.

REFERENCES

1. Griffith, A.A.  
'Proceedings of the 1st International Congress for Applied Mechanics'.  
Delft, 1924, pp. 55.
2. Irwin, G.R.  
'Fracture dynamics, fracturing of metals'  
American Society of Metals, Cleveland, 1948,  
pp. 147-166.
3. Orowan, E.  
'Fracture and strength of solids'  
Prog. Physics, vol. 12, 1949, pp. 185-232.
4. Irwin, G.R.  
'Analysis of stresses and strains near the end of a crack transversing plate'  
Transactions of the A.S.M.E. Journal of Applied Mechanics, vol. 24, 1957, pp. 361-364.
5. Paris, P.C. and Sih, G.C.  
'Stress analysis of cracks'  
American Society of Testing and Materials, STP 381,  
1965, pp. 30-81.
6. Westergaard, H.M.  
'Bearing pressure and cracks'  
Transactions of the A.S.M.E. Journal of Applied Mechanics, vol. 61A, 1939, pp. 49-53.

7. Rice, J.R.  
'A path independent integral and the approximate analysis of strain concentration by notches and cracks'.  
Journal of Applied Mechanics, vol. 35, 1968, pp. 379.
8. Chan, S.K., Tuba, I.S. and Wilson, W.K.  
'On the finite element method in linear fracture mechanics'.  
Engineering Fracture Mechanics, vol. 2, 1970. pp. 1-17.
9. Woo, C.W. and Kuruppu, M.D.  
'Use of finite element method for determining stress-intensity factors with a conic-section simulation model of crack surface'.  
International Journal of Fracture, vol. 20, No. 3,  
Nov. 1982, pp. 163-179.
10. Chow, C.L. and Lau, K.J.  
'A conic-section simulation analysis of two-dimensional fracture problems using the finite element method'.  
International Journal of Fracture, vol. 12, No. 5,  
Oct. 1978, pp. 669-683.
11. Glucklich, J.  
'Fracture of plain concrete'.  
Journal of the Engineering Mechanics Division, A.S.C.E.  
vol. 89, No. EM6, Paper No. 3715, Dec. 1968, pp. 127-138.
12. Kaplan, M.F.  
'Crack propagation and fracture of concrete'.  
Journal Am.Con.Inst., vol. 58, (28), 1961, pp. 591-610.

13. Swamy, R.N.  
'Fracture toughness applied to concrete'.  
Developments in concrete technology, Edited by Lydon, F.D.  
Applied Science Publishers Ltd. London, 1979, pp. 221-281.
14. Visalvanich, K. and Naaman, A.E.  
'Fracture methods in cement composites'.  
Proceedings of the American Society of Civil Engineering,  
Engineering Mechanics, vol. 107, EM6, Dec. 1981, pp. 1155-1171.
15. Knox, W.R.A.  
'Fracture mechanics in plain concrete under compression'.  
Iron and Steel Institute London, Publication 20,  
1970, pp. 158-162.
16. Desayi, P.  
'Fracture of concrete in compression'.  
Materials and Structures, RILEM, Vol. 10, No. 57, May-June  
1977, pp. 139-143.
17. Watkins, J.  
'Fracture toughness test for soil-cement samples in Mode II'.  
International Journal of Fracture, vol. 23, 1983, pp. R135-R138.
18. Dixon, J.R. and Strannigan, J.S.  
'Determination of energy release rates and stress intensity  
factors by the finite element method'. Journal of Strain  
Analysis, vol. 7, No. 2, 1972.
19. Chisholm, D.B. and Jones, D.L.  
'An analytical experimental stress analysis of a practical  
Mode II fracture test specimen'. Experimental Mechanics,  
vol. 17, 1977, pp. 7-13.

20. Liu, K.L.W.  
'The fracture toughness of fibre concrete'.  
A thesis submitted for the degree of Doctor of Philosophy  
C.N.A.A., London, 1982.
21. Watkins, J. and Liu, K.L.W.  
'A finite element study of the short beam test specimen  
under Mode II loading'. The International Journal of  
Cement Composites and Lightweight Concrete, vol. 7, No. 1,  
Feb. 1985, pp. 39-47.
22. Williams, M.L.  
'On the stress distribution at the base of a stationary  
crack'. Transactions of the A.S.M.E. vol. 79, 1957,  
pp. 109-114.
23. Agarwal, B.D. and Giare, G.S.  
'Fracture toughness of short fibre composites in Mode II  
and Mode III'. Engineering Fracture Mechanics, vol. 15,  
No. 1-2, 1981, pp. 219-230.
24. Richard, H.A.  
'A new compact shear specimen'.  
International Journal of Fracture, vol. 17, 1981, pp.R105-R107.
25. Leslie-Banks-Sills and Arcan, M.  
'Toward a pure shear specimen for  $K_{IIC}$  determination'.  
International Journal of Fracture, vol. 22, 1983, pp. R9-R14.
26. Riddle, R.A., Streit, R.D. and Finnie, I.  
'An evaluation of the compact shear specimen for mixed  
mode function studies'.  
Transactions of the A.S.M.E., Journal of Engineering Materials  
and Technology, vol. 105, Oct. 1983, pp. 268-272.



27. Jones, D.L. and Chisholm, D.B.  
'An investigation of the edge-sliding Mode in fracture mechanics'.  
Engineering Fracture Mechanics, vol. 7, 1975, pp. 261-270.
28. Anandarajah, A. and Vardy, A.E.  
'Mode I and II fracture of adhesive joints'.  
Journal of strain analysis, vol. 19, No. 3, 1984,  
pp. 173-183.
29. Wang, S.S., Goetz, D.P. and Corten, H.T.  
'Fracture of random short-fibre SMC composite under shear loading'.  
International Journal of Fracture, vol. 26, 1984,  
pp. 215-227.
30. PAFEC  
User's data preparation and theory manuals, 1985.
31. Wilson, W.K.  
'Research Report 69-1E7-FMECH-R1'.  
Westinghouse Research Laboratories, Pittsburgh, 1969.
32. BS1881 : Part 116 : 1983 Testing Concrete  
'Method for determination of compressive strength of concrete cubes'.
33. BS1881 : Part 116 : 1983 Testing Concrete  
'Method for determination of static modulus of elasticity in compression'.
34. Fracture Toughness Evaluation by R- curve methods  
American Society for Testing and Materials, STP 527, 1973.

35. BS1924 : 1975  
Methods of test for stabilized soils, Test 4.  
Determination of the dry density/moisture content  
relationship of stabilized soils.
36. Broek, D.  
'Elementary Engineering Fracture Mechanics'.  
Noordhoff International Publishing (1974), The Netherlands.
37. Knott, J.F.  
'Fundamentals of Fracture Mechanics'.  
Butterworths (1973), London.
38. Ewalds, H.L. and Wanhill, R.J.H.  
'Fracture Mechanics'.  
Edward Arnold Publishers Ltd (1984), London.
39. Davies, J., Morgan, T.G. and Yim, C.W.A.  
'The finite element analysis of a punch-through shear  
specimen in Mode II'.  
International Journal of Fracture, vol. 28, June, 1985.  
pp. R47-R48.
40. Yim, C.W.A., Davies, J. and Morgan, T.G.  
'An experimental study of a punch-through shear specimen  
in Mode II'.  
The International Journal of Cement Composites and Lightweight  
Concrete.  
(Accepted for publication).

APPENDIX (PUBLICATIONS)

1. Davies, J., Morgan, T.G. and Yim, C.W.A.  
'The finite element analysis of a punch-through shear specimen in mode II'.  
International Journal of Fracture, Vol. 28, Part 2,  
June 1985, pp. R47-R48.
2. Yim, C.W.A., Davies, J. and Morgan, T.G.  
'An experimental study of fracture parameters of a punch-through shear specimen'.  
International Journal of cement composites and lightweight concrete.  
(Accepted for publication)